

QUANTUM PHASE TRANSITIONS IN COLD ATOMS
AND LOW TEMPERATURE SOLIDS

A Dissertation

Presented to the Faculty of the Graduate School

of Cornell University

in Partial Fulfillment of the Requirements for the Degree of

Doctor of Philosophy

by

Kaden Richard Alan Hazzard

May 2010

© 2010 Kaden Richard Alan Hazzard

ALL RIGHTS RESERVED

QUANTUM PHASE TRANSITIONS IN COLD ATOMS AND LOW
TEMPERATURE SOLIDS

Kaden Richard Alan Hazzard, Ph.D.

Cornell University 2010

This thesis describes how to create and probe novel phases of matter and exotic (non-quasiparticle) behavior in cold atomic gases. It focuses on situations whose physics is relevant to condensed matter systems, and where open questions about these latter systems can be addressed. It also attempts to better understand several experimental anomalies in condensed matter systems.

The thesis is divided into five parts. The first section or chapter of each part gives an introduction to the motivation and background for the physics of that part; the last section or chapter gives an outlook for future studies. **Parts 1-4 (Chapters 1, 2, 3, 4, 5, 6, 7, 8, 9, 10, 11, 12, 13, 14, and 15)** introduce and show different facets of how to learn about novel physics relevant to condensed matter using cold atomic systems. **Part 5 (Chapters 16, 17, 18, and 19)** constrains explanations of several ill-understood phenomena occurring in low-temperature quantum solids and condensed matter systems and attempts to construct mechanisms for their behavior.

Part 1 (Chapters 1 and 2) generally motivates and introduces condensed matter, cold atoms, and many-body physics. **Part 2 (Chapters 3, 4, 5, 6, and 7)** introduces optical lattice physics and describes ways of spectroscopically probing many-body physics, especially dynamics, near quantum phase transitions in these systems. **Part 3 (Chapters 8, 9, 10, 11, and 12)** discusses the effects of rotation and how this can create exotic states, as well as alternative methods of

creating exotic states. This leads us to study optical lattices where particles possess non-trivial correlations between particles even within a site in **Chapters 10 and 11**. **Part 4 (Chapters 13, 14, and 15)** introduces another route to studying exotic physics in cold atoms: examining finite temperature behavior near second order quantum phase transitions. In the “quantum critical regime” occurring near these transitions, non-quasiparticle behavior generically manifests. This behavior has been hidden in previous analyses of data, but **Chapter 14** introduces a set of tools required to extract universal quantum critical behavior from standard observables in cold atoms experiments. **Chapter 15** discusses near-term opportunities to use these tools to impact fundamental, open questions in condensed matter physics. **Part 5 (Chapters 16, 17, 18, and 19)** introduces several anomalous or interesting experimental results from low-temperature and solid state physics, constrains possible explanations, and attempts to construct mechanisms for their behavior. **Chapter 17** shows that collisional properties between quasi-two-dimensional spin-polarized hydrogen atoms are dramatically modified by the presence of a helium film, on which they are invariably adsorbed in present experiments. **Chapter 18** constrains theories regarding recent observations on atomic hydrogen defects in molecular hydrogen quantum solids. Finally, **Chapter 19** proposes a mechanism for supersolidity that could account for the experimental observations at that time. Since then, it probably has been falsified, but still contains an intriguing mechanism for coexistence of superfluidity and solidity that involves disorder.

BIOGRAPHICAL SKETCH

Kaden Hazzard was born January 11, 1982; that night, he started things off right by breaking the window in his parents' car (the subzero temperatures may have also contributed). After graduating high school in 2000, he pursued B.S. degrees in physics, mathematics, and a minor in chemistry at the Ohio State University, leaving in August 2004 for graduate study at Cornell. (Later, he decided it would be a good idea to fill out the paperwork for his Ohio State degrees and was officially awarded his degree in 2008.) He obtained his master's degree in theoretical physics from Cornell University in 2009, and will complete his PhD in May 2010. In May 2010, he will start a postdoctoral research fellowship at JILA and the University of Colorado-Boulder working and collaborating with Ana Maria Rey, Victor Gurarie, Michael Hermele, Leo Radzihovsky, and the other faculty there.

To my Mom and Dad

ACKNOWLEDGEMENTS

I start by thanking the people who first introduced me to the professional world of physics. Foremost is John Wilkins, who graciously entertained inquiries regarding his research from me — a senior in high school — and invited me already to participate in conferences and in his research at *The Ohio State University*. To this day, John’s generosity, immense knowledge, indefatigable work ethic, and helpful advice resonate with me; he was my first role model as a physicist.

Also, the rest of the Wilkins group deserve recognition, especially Jeongnim Kim, Seongwon Lee, David Richie, Dallas Trinkle, Richard Hennig, Erik Welch, and Joe Gorse, in no particular order. Each of them spent many hours (days, weeks, ...) of their life discussing physics and life, and this was tremendously enlightening and enjoyable. Also at Ohio State, a number of other professors profoundly influenced my view of physics: Richard Furnstahl, Thomas Lemberger, Cirayam Japaprakash, and Samir Mathur stand out.

After my second year as an undergraduate, I spent the summer doing experiments at Los Alamos National Labs with Joe Thompson, who exposed me to a whole new side of physics. It was at this time that I developed some knowledge of experimental physics, strongly correlated systems, and (to my current officemates’ chagrin) an interest in quantum criticality. Seeing the importance of this later topic to understand real materials and the deep theoretical issues it raises is what has motivated me to try to bring its study to cold atoms.

During my time at Cornell, wonderful colleagues have been constantly present. My advisor Erich Mueller has been an inspiration: his ability and desire to approach problems with a “whatever-works,” rather than a “whatever-we-know-how-to-do” or “what-is-fashionable” attitude stands out. So do his familiarity with both deep theoretical approaches and the dirty details of particular experiments. I cer-

tainly have learned more physics from him than any other single person. Moreover, he has allowed me a rare degree of freedom and flexibility, for which I am grateful.

Through conversations and lectures, the Cornell physics faculty has been as diverse and exciting as one could wish for. Also, a number of faculty at other institutions have been welcoming and willing to converse, collaborate, and entertain. I particularly enjoyed John Shumway and Nikolay Prokof'ev's sabbatical visits. Also, thanks to Cheng Chin and the rest of his group, especially Nate Gemelke, for being so generous with their experimental data. I wish to thank Cornell's condensed matter faculty — naming them all would quickly turn into a laundry list. However, two deserve special recognition: Dave Lee who, despite his eminence, befriends year after year of nameless graduate students, and who has shared countless wisdom with me; and Mukund Vengalattore for spending an immense amount of his time sharing his expertise and advice with me, and having a fearless willingness to allow me near his optics tables, not to mention bravely offering to let me bench press him.

A number of friends and companions enriched my life and made it more fun. Again, a comprehensive list would be impossible to construct, so I will name a few that have been particularly important to me. The Mueller group have been my closest companions: Dan “betes” Goldbaum, Sourish “Tandoori-in-my-house” Basu, Stefan “Lil 'Bau Wau” Baur, Stefan “Naughty” Natu (D2), and Eliot Kapit. Dan and the Stefans in particular: the amount of time we spent talking physics, eating (half of the time meals far out of our price range, compensating with the other half by eating barely edible leftovers found on the floors of various College-town institutions), watching football, playing Wii, making strangers cry at CTB, and making fun of each other is simply unfathomable. Dan, I especially want to thank you for that magical night in San Francisco.

Outside of the Mueller group, but staying in the physics department, thanks to Watson, Sumiran Pujari, JoJo Heinonen, Joern Kupferschmidt, Ben Machta, Phil Kidd, Dave Bernat, and about 50 unnamed others for putting up with me and generally being awesome. Frisbee Girl, as punishment for your resistance to letting me bench press you, I hope you are not offended by your demotion to a “friendly acknowledgement.”

Thanks to a few more friends for keeping me company and challenging me in far ranging manners, Angela and Sophie in particular. Over most of the last year, thanks to Betty (aka Debbie Martin) for having been one of my best friends and always putting a smile on my face. Most importantly, thank you Anna for your “jokes” at CTB, nursing me through two bouts of flu, removing the cholera from my apartment, interesting talks, travels, skydiving, and so on.

I have a similar (and not always unrelated) affection for all the baristas in Collegetown, the Commons, the Mall, and downtown for keeping a steady stream of caffeine in my veins! You were great diversions from the onslaught of physics and physicists.

Thanks to my family: Caley and Bradley, you’re my favorite niece and nephew. Caley, this thesis would have been incomplete without your brilliant and profoundly deep insights into quantum mechanics.

Thank you, especially, mom and dad for the phone calls, trips to Ithaca (and elsewhere), a place to sleep when I visit, and your support in general. I’ve had the fortune of always knowing that if anything happened, you would be there.

There are too many important people in my life to recognize them all. All who I have left off will be unsurprised by my incomprehensiveness — and should certainly accost me the next time we meet, so I can acknowledge them (possibly with food and drink) in person.

Finally, I thank the American taxpayer for funding this research. Erich Mueller's contribution was partially performed at the Aspen Center for Physics. This material is based upon work supported by Cornell's special graduate fellowship, the GAANN Award No. P200A030111 from the US Department of Education, by National Science Foundation grant Nos. PHY-0456261 and PHY-0758104, and by ARO Award W911NF-07-1-0464 with funds from the DARPA OLE Program.

TABLE OF CONTENTS

Biographical Sketch	iii
Dedication	iv
Acknowledgements	v
Table of Contents	ix
List of Tables	xv
List of Figures	xvi
1 Introduction to many-body physics in ultracold atomic gases	1
1.1 Motivation: many-body physics	1
1.2 Motivation: general atomic physics	6
1.3 History and introduction to many-body physics in cold atomic systems	8
1.3.1 Background and achievements.	8
1.3.2 Challenges.	10
2 Theoretical and experimental techniques used to explore many-body physics in cold atoms, especially optical lattices	13
2.1 Experimental techniques	13
2.1.1 Common experimental techniques for all cold atoms experiments: trapping and cooling	13
2.1.2 Optical lattice experimental techniques	17
2.1.3 Detection	20
2.2 Theoretical techniques	22
2.2.1 Interactions in cold atom systems	22
2.2.2 Weak interactions: Mean field theory and fluctuations	29
2.2.3 Bosons in an optical lattice and the Bose-Hubbard model	31
2.2.4 Gutzwiller mean field	34
2.2.5 Fluctuations in strong lattice potentials: beyond Gutzwiller	37
2.2.6 Extracting information about homogeneous systems from trapped systems	39
3 Radio-frequency spectroscopy: background and motivation	42
3.1 Motivation and background	42
3.2 Two differing pictures of RF spectroscopy	43
4 RF spectra: a sum rule approach to trapped bosons in an optical lattice	45
4.1 Abstract	45
4.2 Introduction	45
4.3 Spectrum of harmonically trapped gas	48
4.3.1 Hamiltonian and approximations	48
4.3.2 Homogeneous clock shifts	50
4.3.3 Calculation of spectrum in a trap	52

4.3.4	Analytic Results	55
4.3.5	Intermediate Coupling	56
4.4	Refinements	58
4.4.1	Anharmonicity	59
4.4.2	Alternative explanations of enhanced low-density spectral weight	60
4.5	Summary	63
5	RF spectra: multiple peaked spectrum in a homogeneous system	65
5.1	abstract	65
5.2	Introduction	66
5.2.1	RF Spectroscopy	67
5.3	Bose-Hubbard Model	69
5.3.1	Model and RF spectra	69
5.3.2	Sum Rules	71
5.4	Random phase approximation	72
5.4.1	General setup and solution	72
5.4.2	Limiting Cases and Dependence on Final State Interactions	74
5.4.3	Inhomogeneous spectrum	77
5.5	Conclusions and discussion	78
5.6	Acknowledgements	79
6	Radio-frequency spectra at finite temperature and other applications and theoretical developments of rf spectra	80
6.1	Abstract	80
6.2	Introduction	80
6.3	Clock shift diagrams.	81
6.4	Finite temperature superfluid	83
6.5	Applications	86
6.5.1	Thermometry with the Mott insulator	86
6.5.2	Number correlations and local compressibility.	94
6.6	“Inverse clock diagram” calculation	98
6.6.1	Inverse diagram when clock shift energy is proportional to the density plus a constant	98
6.6.2	Inverse clock shift diagram in the general case	100
6.6.3	Cooling and quantum register initialization	100
6.6.4	Measuring spatial correlations; quantum computer readout	101
6.7	Conclusions	110
7	RF spectra: summary, conclusions, and the future	112
8	Rotation, inducing gauge fields, and exotic states of matter in cold atoms	115
8.1	Physics of rotating particles/particles in gauge fields	116

8.1.1	Vortices	117
8.1.2	Vortices in lattices: Hofstadter butterfly	119
8.1.3	Quantum Hall effect	120
8.2	Rotation	122
8.2.1	Rotation and angular momentum boosts — principles and experimental techniques	122
8.2.2	Rotation leads to effective magnetic field (gauge field) and limitations for exotic states	123
8.3	Other methods of inducing gauge fields	124
8.4	On-site correlations	125
9	Stirring up fractional quantum Hall puddles	126
9.1	Abstract	126
9.2	Introduction	126
9.3	Summary	133
10	Incorporating arbitrarily strong on-site correlations into lattice models	137
10.1	Abstract	138
10.2	Body	139
11	Quantitative calculation of parameters for a model sufficiently general to capture all on-site correlations	149
11.1	Background	149
11.2	Introduction, notation, and set up	150
11.3	Quantitative estimates of the Hamiltonian parameters with quantum Monte Carlo	151
11.3.1	General idea	151
11.3.2	Relating response to correlation functions	152
11.3.3	Implementation of correlation function in PIMC	153
11.4	Solutions for various values of $t^{(mn)}$ and E_m	153
11.4.1	Non-interacting case	154
11.4.2	Strong coupling $t/U \rightarrow 0$ limit	159
11.4.3	General — correlation functions from exact diagonalization	168
11.5	Note on temperature dependence of response functions.	169
12	Summary, conclusions, and the future of induced gauge fields and lattices with on-site correlations	170
13	Quantum criticality: introduction	171
14	Quantum criticality in cold atoms	175
14.1	General criteria to observe cold atomic quantum criticality	175
14.2	General construction to eliminate unmeasurable non-universal parameters	182

14.2.1	Universal scaling functions from feasible cold atoms observables: density profiles	182
14.2.2	Universal collapse between different universal curves associated with varying values of effective quantum critical parameters	184
14.2.3	Most general observables	186
14.3	Simple example: non-interacting fermi liquid to vacuum quantum phase transition and verification of LDA results explicitly for non-interacting fermions	186
14.3.1	Universal scaling collapse for finite particle number and with a trap	187
14.4	Dilute Bose gas vacuum to superfluid phase transition	189
14.5	Bose-Hubbard model	193
14.5.1	Bose-Hubbard model in general quantum critical context and relating quantum critical fields to microscopic variables	197
14.5.2	$d = 1$	198
14.5.3	$d \geq 2$	202
15	The next steps in exploring quantum criticality in cold atoms	210
15.0.4	Other observables: spectroscopy	210
15.0.5	Other phase transitions	212
16	Part 5: Systems other than cold atoms	215
17	Film mediated interactions alter correlations and spectral shifts of hydrogen adsorbed on helium films	216
17.1	Abstract	216
17.2	Results	217
18	Molecular hydrogen solids	227
18.1	Abstract	227
18.2	Introduction and motivation	227
18.3	Experiments	228
18.3.1	General introduction: physics of atomic hydrogen embedded in solid hydrogen	228
18.3.2	Anomalies and experimental results	231
18.4	Scenarios	233
18.4.1	Bose statistics and Bose-Einstein condensation	233
18.4.2	<i>Local</i> Bose-Einstein condensation	238
18.4.3	Nuclear spin dependent Density-of-states	239
18.5	Other observations and speculations	241
18.6	Summary	242

19 Helium and hydrogen (super?)solids	244
19.1 Background	244
19.2 Abstract	245
19.3 Introduction	245
19.4 Torsional oscillator NCRI.	247
19.5 Two supersolid features.	247
19.6 Blocked annulus torsional oscillators	248
19.7 Dissipation peaks	249
19.8 H ₂ experiments.	250
19.9 Annealing	255
19.10 Frequency dependence	256
19.11 Thermodynamics: specific heat & pressure	257
19.12 ³ He doping	258
19.12.1 Frozen link model	259
19.12.2 Dynamic link model	260
19.13 Anomalous critical velocity	261
19.14 dc flow	263
19.15 Shear	263
19.16 Implications for mechanism	264
19.17 Future directions	264
19.18 Discussion	265
A RELATING SCATTERING AMPLITUDES AND <i>T</i>-MATRIX	269
B WARD IDENTITIES IN THE RF SPECTRUM FOR THE BOSE-HUBBARD MODEL: VERTEX CORRECTIONS, SYMMETRIES, AND CONSERVATION LAWS.	271
B.1 Abstract	271
B.2 Introduction and motivation	271
B.3 Homogeneous gas: no lattice	272
B.3.1 Setup	272
B.3.2 Showing covariance of kinetic energy	274
B.3.3 Partition function in path integral representation, including sources	276
B.3.4 Partition function under <i>SU</i> (2) transformations	276
B.3.5 Consequences of <i>SU</i> (2) invariance of the partition function	280
B.3.6 Connected Green's functions and effective action	282
B.3.7 Real space Ward identities	285
B.3.8 Fourier space Ward identities	287
B.4 Lattice (single band)	291
B.4.1 Setup	291
B.4.2 Showing covariance of kinetic energy	292
B.4.3 Partition function in path integral representation, including sources	293

B.4.4	Action under $SU(2)$ transformations	294
B.4.5	Consequences of $SU(2)$ invariance of the partition function .	296
B.4.6	Effective action	298
B.4.7	Real space Ward identities	299
B.4.8	Fourier space Ward identities	301
B.5	Rf spectra	305
B.5.1	Rf spectra in terms of exact single particle Green's functions and interaction vertex	306
B.5.2	Non-interacting gas	306
B.5.3	Dilute gas: condensed and non-condensed	307

Bibliography		310
---------------------	--	------------

LIST OF TABLES

- 8.1 Behavior of rotating lattice bosons in the simplest limits for *homogeneous* systems. The various length scales characterize interactions (scattering length a), the trap (oscillator length ℓ), the lattice spacing (d), and rotation (rotational length ℓ_R). Here \wedge represents logical “AND” and \vee the logical “OR.” One sees that even for the homogeneous system there are a remarkable variety of limits: the ordinary Bose-Hubbard model is arguably the simplest of all the limits, and it already displays the highly non-trivial physics of the superfluid physics. Each of the limits is an areas of study in its own right. The references are representative, not comprehensive. . . . 118

LIST OF FIGURES

4.1	Theoretical spectra showing the number of ^{87}Rb atoms transferred from hyperfine state $ a\rangle = F = 1, m_F = -1\rangle$ to state $ b\rangle = F = 2, m_F = 1\rangle$ when excited by light detuned from resonance by the frequency $\delta\nu$. The $N = 9 \times 10^4$ atoms are confined by a harmonic potential with $\bar{\omega} = (\omega_x\omega_y\omega_z)^{1/3} = 2\pi \times 100\text{Hz}$ and a three-dimensional periodic potential with lattice depth $V_0 = 5, 10, 25, 35E_{\text{rec}}$ (from top to bottom).	47
4.2	(a) Gutzwiller Mean Field phase diagram with constant density contours. The vertical dashed lines show the spatial dependence of the chemical potential for a trapped gas in the LDA: from left-to-right these correspond to the deep Mott limit, the ‘‘corrugated superfluid’’ situation appropriate to Fig. 4.4(b), and the dilute superfluid. (b) Phase diagram with contours of constant $\langle n \rangle g_2 = \langle n(n-1) \rangle / \langle n \rangle$. Contours are spaced by 0.1, with additional lines at $m \pm 0.01$, for integer m , to emphasize the Mott regions.	54
4.3	Analytically calculated spectra for the harmonically trapped system in the deep Mott limit (solid line), plotted as a function of $\delta\omega/(U_{ab} - U_a)$. Superimposed is the spectrum of the superfluid (dashed line) with the same parameters, but horizontally shifted to the left by $-(\delta\omega/2)(U_{ab} - U_a)$. The central density is $n_s(0) = [\mu_0 - \epsilon(0)]/U_a = 5.8$. This illustrates that the envelope of the spectral line in the Mott insulating state has the same shape as the superfluid spectrum, shifted horizontally.	57
4.4	(a) The density as a function of distance from the trap center for a harmonic trap in units of the Thomas-Fermi radius ℓ_{TF} , defined as $\ell_{\text{TF}} \equiv \sqrt{(\mu_0 - \epsilon_0) / (m \omega^2 / 2)}$. The density profile corresponds to the LDA contour at $t/U_a = 0.018$ of Fig. 4.2(a). The corrugation of the density is observable, but not dramatic; it would be particularly difficult to image in experiments looking at columnar integrated densities. (b) The hyperfine spectra arising from the density plotted in (a).	58
4.5	(a) A slice of the anharmonic potential $V_{\text{trap}}(\mathbf{r})$ similar to the one found in experiments. (b) Contour lines of constant density in the x-y plane for $n = 1, 2, \dots, 5$ in the anharmonic trap at $V_0 = 35E_{\text{rec}}$. (c) Corresponding spectra (using the ‘‘spherical trap model’’ discussed in text) for $V_0 = 5, 10, 25, 35E_{\text{rec}}$ with $N = 1.4 \times 10^7$ particles.	61

- 5.1 (Color online) Illustration of two types of RF-active excitations of the lattice superfluid near the Mott transition. Open (blue) circles are atoms in the $|a\rangle$ state, filled (red) circles are atoms in the $|b\rangle$ state, and the arrows indicate a delocalized particle while other particles are localized. (a) Illustrates the initial superfluid state, consisting of a dilute gas of atoms moving in a Mott background. Final states in (b) and (c), show the excitation of a core or delocalized atom. 68
- 5.2 (Color online) Homogeneous system's spectral density as a function of ω/U_{aa} and t_a/U_{aa} (whiter indicates larger spectral density) compared with sum rule prediction (red, single line). Delta functions are broadened to Lorentzians for visualization purposes. (a) Ground state phase diagram within the Gutzwiller approximation, for reference. (b,c) We take $U_{ba} = 1.2U_{aa}$ and $t_b = t_a$, with (b) $\mu = 1.98U_{aa}$ and (c) $\mu = 2.02U_{aa}$. (d,e) We take parameters corresponding to typical ^{87}Rb experiments: $U_{ba} = 0.976U_{aa}$ and $t_b = t_a$, and take (d) $\mu = 2.000U_{aa}$ and (e) $\mu = 2.004U_{aa}$. In both cases, a double peak structure is visible, but the region of the phase diagram in which it is important is much smaller for ^{87}Rb parameters than for Fig. (b,c)'s parameters. 70
- 5.3 (Color online) (a) Density n as a function of distance to trap center rescaled by the lattice spacing, r/d , in a local density approximation. For all subfigures, we take $t_a/U_{aa} = 0.004$, which is moderately smaller than the tip of the first Mott lobe. (b-e) Left: spectrum of a homogeneous gas with density $n(r)$, representing the spatially resolved spectrum observed in an experiment on a trapped gas. Horizontal axis is position, vertical is frequency, color from dark to light represents increasing spectral density. Continuous (red) curve denotes sum rule result for $\langle\omega\rangle$. We round the δ -functions to Lorentzians for visualization. Right: trap-averaged spectrum for a 3D trap within our RPA (black, solid line) compared with sum rule (red, dashed line). (b) $U_{ab} = 1.2U_{aa}, t_b = t_a$ (c) $U_{ab} = U_{aa}, t_b = t_a + 0.1U_{aa}$ (d) $U_{ab} = 1.2U_{aa}, t_b = t_a + 0.1U_{aa}$ (e) ^{87}Rb parameters: $U_{ab} = 0.976U_{aa}, t_b = t_a$ 76
- 6.1 (a) Condensate and excitation densities of a finite temperature superfluid at a temperature of 30 in units of the coupling constant U_α , the radial displacement is in units of the thermal de Broglie wavelength λ_T , and the trapping potential is αr^2 with $\alpha = 10^{-2}U_\alpha/\lambda_T^2$. The excitation density is rescaled to make it more visible. (b) Corresponding clock shift diagram at temperatures $T = 1, 30$ for the solid and dashed curves respectively. (b) The peak at low densities comes from the normal fluid tail. 86

6.2	Finite temperature clock shift diagrams in the deep Mott limit for a <i>homogeneous system</i> , at temperatures $T = 0.05, 0.2, 0.8$ in units of U_a , from bottom to top. The appearance of multiple peaks signals the occupation of states with different site fillings. The chemical potential is $\mu = 1.8$ (corresponding to a $n = 2$ site filling at zero temperature).	88
6.3	Finite temperature clock shift diagrams in the deep Mott limit for a harmonically trapped system. The temperatures are $T = 0.01, 0.7, 1.5$ in units of U_a from bottom to top. Vertical offsets are for clarity only. The chemical potential is $\mu = 1.4, 5.7$ (corresponding to $n = 2, 6$ zero-temperature site fillings at the trap center) in (a) and (b) respectively.	90
6.4	Deep Mott clock shift diagram with dipolar interactions for the state given in the text. The correspondence between peak and spatial variation is indicated, where a string “ $n_1n_2n_3$ ” indicates n_1 particles in the first neighbor site, n_2 in the second neighbor, and n_3 in the third neighbor. The labels instruct how to read-off the probabilities for each state.	105
9.1	(Color Online) Transferring small clusters from non-rotating ground state to $\nu = 1/2$ Laughlin state using rotating quadrupolar ($m = 2$) deformations. Left: Interaction energy (in units of $U/2$) of quantum states of harmonically trapped two dimensional clusters as a function of total angular momentum projection L in units of \hbar . Excitation paths are shown by arrows. Central: squared overlap (fidelity) of $ \psi(t)\rangle$ with the initial (solid) and final (dashed) states as a function of the duration of a square pulse. Right: Fidelities as a function of time for an optimized Gaussian pulse of the form $e^{-(t-t_0)^2/\tau^2}$. Time is measured in units of $\tau_0 = \hbar/U \sim 10^{-4}$ s. For $n = 2$, the peak perturbation amplitude is $V_p = 0.05(U/2)$, $\omega - \Omega_p = 2.0(U/2)$, and a Gaussian pulse time of $\tau = 24\tau_0$. For $n = 3$, $\tau = 102\tau_0$ and $\omega - \Omega_p = 2.046(U/2)$ and $2.055(U/2)$ for the Gaussian and square cases, respectively. For $n = 3$, nonlinear effects (coupling with near-resonant levels) shifted the optimal frequency away from the linear response expectation, $\omega - \Omega_p = 2(U/2)$	130

- 9.2 (Color Online) Using a rotating m -fold symmetric perturbation to drive $n = 3$ particle clusters from $L = 2$ to the $\nu = 1/2$ Laughlin state. Left: path on the energy level diagram. Center: second-order process coming from a deformation with $m = 2$. Right: direct transition produced with $m = 4$. Solid (dashed) lines are fidelities with the initial (Laughlin) state. In both cases the peak deformation is $V_p = 0.05(U/2)$. Both use a Gaussian pulse. The frequencies and pulse times τ we used for $m = 2, 4$ were $\omega - \Omega_p = (3.00/2)(U/2), 3.035(U/2)$ and $\tau/\tau_0 = 218, 21$. Note how much more rapid the direct process is. 134
- 9.3 (Color Online) Transferring atoms using multiple pulses. Left: paths from initial to Laughlin states for $n = 3, 4$. Right: Solid line is the fidelity with the initial state, dotted with the intermediate $(L, E) = (2\hbar, 3(U/2))$ state, and the dashed line with the Laughlin state. All pulses are Gaussians. Despite using multiple pulses, this technique is faster than using a higher order $m = 2$ pulse. The frequencies (Ω_p) , shape (m) , and pulse times (τ) for the $N = 3$ sequence were $\hbar(\omega - \Omega_p)/(U/2) = 3.00, 3.035$, $m = 2, 4$, and $\tau/\tau_0 = 16.95, 19.2$. For both, $V_p = 0.05(U/2)$. For $N = 4$, using two pulses with $m = 2$ and $V_p = 0.2(U/2)$, we achieve $> 98\%$ fidelity after a total two-pulse sequences with $\hbar(\omega - \Omega_p)/(U/2) = 3.130, 1.0376$ and $\tau/\tau_0 = 82.5, 87.0$ 135
- 10.1 (color online) (a) On-site energy with non-interacting energies subtracted off, $I_n = E_n - (3\hbar\omega/2 - \mu)n$, and energies scaled by $E_R = \hbar^2\pi^2/(2md^2)$, using typical ^{87}Rb parameters: lattice spacing $d = 532\text{nm}$, scattering length $a = 5.32\text{nm}$. Dashed: neglecting on-site correlations, solid: including correlations. Bottom to top curve: $n=2,3,4,5$. (b) Representative hopping matrix elements with on-site correlations, relative to those neglecting on-site correlations, $\tau^{(mn)} \equiv t^{(mn)}/(t\sqrt{(m+1)n})$, as a function of lattice depth V_0 on a scale. Bottom to top line: $t^{(03)}, t^{(31)}, t^{(05)}, t^{(35)}$. (c) For comparison, $t^{(01)}/E_R$ calculated from the exact Wannier states (upper curve) along with our Gaussian approximation to it with and without non-orthogonality corrections (second and third highest, respectively); also shown is the next-nearest neighbor hopping matrix element (bottom curve). The effective Hamiltonian parameters are calculated perturbatively in a/d for a Gaussian ansatz. 143

- 10.2 (color online) Left: On-site two-particle energy as a function of scattering length a rescaled by the on-site harmonic oscillator energy $\hbar\omega = 2\sqrt{V_0 E_R}$, for the two lowest energy branches. The corresponding characteristic length is $\ell = \sqrt{\hbar/m\omega}$. Right: Log plot of rescaled hopping matrix elements $\tau^{(mn)} \equiv t^{(mn)}/(t\sqrt{(m+1)n})$. Solid and dashed curves are $t^{(11)}/(\sqrt{2}t)$ and $t^{(12)}/(2t)$, respectively. We have chosen the lattice depth $V_0 = 15E_R$; this affects only the horizontal scale. In the ordinary Bose-Hubbard model, $t^{(mn)}/(\sqrt{(m+1)n}t) = 1$ for all m, n , as confirmed by this figure's $a = 0^-$ lowest (red) branch and $a = 0^+$ second (blue) branch limits. The resonance at $-d/a = 0$ separates the molecular side (left), from the atomic side (right). Note that $t^{(10)}/t$ (not shown) is universally equal to unity regardless of interaction strength, since interatomic correlations are absent when there is a single particle per site. . . . 144
- 10.3 (color online) Representative Gutzwiller mean-field theory phase diagrams, showing constant density (black, roughly horizontal) and constant $\xi \equiv \zeta_1 + \zeta_2 + \zeta_3$ (red, roughly vertical) contours: ξ , similar to the condensate density, is a combination of the mean fields ζ_m , defined after Eq. (10.5). Density contours are $n = \{0.01, 0.2, 0.5, 0.8, 0.99, 1.01, 1.2, \dots\}$ and order parameter contours are $\xi = \{0.2, 0.4, \dots\}$, except (d) where we take contours $\xi = \{0.02, 0.04, \dots\}$. The phase diagrams are functions of $\mu_{\text{eff}} \equiv \mu/E_R$ and $t_{\text{eff}} \equiv \exp\left(-\sqrt{V_0/E_R}\right)$, where the lattice depth V_0 is the natural experimental control parameter. We plot versus t_{eff} , instead of V_0 , as this is closer to the Hamiltonian matrix elements and more analogous to traditional visualizations of the Bose-Hubbard phase diagram. (a) Ordinary Bose-Hubbard model for $a = 0.01d$, (b) lattice bosons restricted to fillings $n = 0, 1, 2$ with $a = 0.01d$, on the next to lowest energy branch on the $a > 0$ side of resonance, (c) lattice boson model with $a = d$, and (d) FQH puddle array model taking $\omega - \Omega = 0.1E_R$ (see text for details). Parts (b,c) use the Hamiltonian parameters from the exact two-particle harmonic well solution. 146
- 10.4 Single lobe of the Mott insulator/superfluid boundary. Complete characterization of the mean-field lobe shape in the $z\bar{t}-\bar{\mu}$ plane for all possible t^\pm 's (see Eq. (10.7) for definitions). (a) Fix $t^- = 0.5$, vary t^+ from 1 (outer curve) to 21 (inner curve) in steps of 2. (b) Fix $t^+ = 1.5$, vary t^- from 0 (outer curve) to 1 (inner curve) in steps of 0.15. 147

11.1	Thermal expectation values $\overline{\langle s P_m s\rangle}$ versus inverse temperature $\beta\Delta$. At high temperature, all states are equally likely, while at high temperature they tend to a binomial distribution, indicated by the dashed red lines. Top to bottom: $N = 3, 5, 7$. It should be clear from the graphs which curves correspond to which m	158
11.2	Representative diagrams for the slave boson perturbation theory at low order in “ t/U ”.	163
11.3	Representative diagrams for the two-site slave boson perturbation theory at low order in “ t/U ”.	165
14.1	(a) Zero-temperature phase diagram illustrating Mott and superfluid phases computed within a finite-temperature extension of Gutzwiller mean field theory; constant density contours are phase transitions at temperature $T/U = (0, 0.06, 0.12, \dots, 0.96)$, from smallest to largest “lobes.” (b) Finite-temperature slice of phase diagram demonstrating the normal fluid and quantum critical regimes, the classical critical regime (a region near the SF/NF transition line), and the superfluid and Mott regimes. Note that all of the energy scales — the quantum critical crossover, the width of the classical critical region, and the superfluid transition temperature all scale in the same universal manner, as $\left \frac{t-t_c}{t_c}\right ^{z\nu}$ where $z = 2$ generically and $z = 1$ for the transition at fixed density at the tip of the Mott lobe and ν is the critical exponent associated with the most relevant scaling variable (although this last property isn’t preserved in the Gutzwiller approximation to the finite temperature phase diagram).	176
14.2	(a) Density, for temperatures $T = 2, 6, 10\omega$ and (b) compressibility for $d = 1$ non-interacting fermions as a function of μ , for temperatures $T = 2, 6, 10, 14\omega$. (c) Exact $N = 5$ particle density profile $n(r)$, in harmonic oscillator units $\ell \equiv \sqrt{1/(m\omega)}$ with m the fermion mass and ω the trap frequency (setting $k_B = \hbar = 1$ as usual), for temperatures $T = 0, 4, 8, 12, 16\omega$ compared with (d) LDA (Thomas-Fermi). (e,f) Same as (c,d) but with rescaled densities $\beta^{-1/2}n(r)$ replacing $n(r)$ to show universality near the $\mu = 0$ quantum critical point, for temperatures $T = 4, 8, 12, 16\omega$. (g) Exact $N = 5$ particle compressibility profile $\kappa(r)$ rescaled by $\kappa_0 \equiv 1/(\omega\ell)$ for temperatures $T = 2, 4, 6, \dots, 16\omega$ compared with (h) LDA. (i) Exact $N = 5$ particle κ vs n , demonstrating shape and temperature dependence of this curve for temperatures $T = 2, 4, \dots, 12\omega$, compared with LDA. (j) Exact $\kappa\beta^{1/2}$ for $N = 5$ particles, showing universal scaling collapse at every temperature (solid lines), compared with the thermodynamic limit (red dashed), for temperature $T = 2, 4, 6\omega$	190

14.3	The intricate quantum critical crossovers near the Mott lobe tip, governed by the “ $O(2) + \mu$ ” model of Eq. (14.23) physics. Near the tip, the dilute gas of quasiparticles — on the larger μ side of the tip — and the dilute gas of quasiholes — on the lower μ side of the tip — can both be important. Very near each of the transitions, the system is described by the corresponding dilute Bose gas quantum phase transition of quasiparticles or quasiholes, in the universality class of Eq. (14.21). At intermediate temperatures, both excitations occur and are symmetric on the relevant energy scales, with quantum criticality there described by the $O(2)$ model of Eq. (14.22).	193
14.4	Left to right: n vs r , κ vs. r , and κ vs. n for $t = 0$ at various temperatures. From top to bottom, the plots are for $T/U = 0.06, 0.1,$ and 0.25 . This represents the non-universal, non-critical contributions to the density that must be subtracted to give an appropriate quantum critical analysis.	195
14.5	Thermodynamics and universal scaling analysis of quantum criticality, applicable to density profiles, of the 1D Bose-Hubbard model. Figs. (a) and (b) show density and compressibility versus the chemical potential for temperatures $\bar{T} \equiv T/t = 0.01, 0.06, 0.11, \dots, 0.46$, which is clearly non-universal. Figs. (c) and (d) show $\bar{\kappa}\bar{T}^{1/2}$ versus $n/\bar{T}^{1/2}$. A universal window at low densities and low temperatures is made apparent by this analysis. The shape of this curve is controlled by the universal quantum critical theory. The exponents necessary to collapse also reveal the dynamic critical exponent. There is an additional universal region near $n = 1$, and the universal scaling analysis can be applied there as well by plotting $\kappa T^{1/2}$ vs $(1 - n)T^{-1/2}$. We omit this analysis because this problem possesses a symmetry so that it is exactly equivalent to the analysis near $n = 0$ shown here. Here, \bar{x} is the variable x rescaled by the appropriate power of t to make it dimensionless. (e) Logarithmic derivative $\frac{1}{n} \frac{dn}{dT}$ — roughly the “power” characterizing the temperature dependence — in the μ - T plane, showing a quantum critical fan of constant power corresponding to power law dependence of the density in the quantum critical fan. This is a standard type of plot when examining quantum critical materials.	199

- 14.6 Same as Fig. 14.6, but with $t = 0$ densities subtracted off prior to analysis to reveal only universal contributions (here only, we use the same symbols — e.g., n and κ — to denote the quantities with the $t = 0$ parts subtracted off). Thermodynamics and universal scaling analysis of quantum criticality, applicable to density profiles, of the 1D Bose-Hubbard model. Figs. (a) and (b) show density and compressibility versus the chemical potential for temperatures $\bar{T} \equiv T/t = 0.01, 0.06, 0.11, \dots, 0.46$, which is clearly non-universal. Figs. (c) and (d) show $\bar{\kappa}\bar{T}^{1/2}$ versus $n/\bar{T}^{1/2}$. A universal window at low densities and low temperatures is made apparent by this analysis. The shape of this curve is controlled by the universal quantum critical theory. The exponents necessary to collapse also reveal the dynamic critical exponent. We omit the analysis near $n = 1$ because this problem possesses a symmetry so that it is exactly equivalent to the analysis near $n = 0$ shown here. Here, \bar{x} is the variable x rescaled by the appropriate power of t to make it dimensionless. 200
- 14.7 Density profiles, compressibility profiles, and compressibility versus density, conventional experimental visualizations extracted from density profiles. Top to bottom: $t/U = 0.01, 0.014, 0.0585, 0.0593$. Each graph shows temperature $T = t/4, t/2, t, 2t$, and $4t$ in black (solid), red (solid), blue (solid), black (dashed), and red (dashed), respectively. See Fig. 14.8 for an analysis bringing out and comparing the universal behavior. 203
- 14.8 Rescaled compressibility versus density scaling curves. Top to bottom: $t/U = 0.01, 0.04, 0.0585, 0.0593$. The tip of the Mott lobe is $(t/U)_c = 0.0593$ in the thermodynamic limit [1]. Left to right: (i) rescaling appropriate to DBG transition near $n = 0$, (ii) rescaling appropriate to $O(2)$ transition near $n = 0$, (iii) rescaling appropriately to DBG near $n = 1$, and (iv) rescaling appropriate to $O(2)$ near $n = 1$. Universality persists to temperatures $T \sim t \sim 2t$, and over a more limited regime of the scaling curve at higher temperatures, as is expected. Each graph shows temperature $T = t/4, t/2, t, 2t$, and $4t$ in black (solid), red (solid), blue (solid), black (dashed), and red (dashed), respectively. The universal collapse or lack thereof is able to distinguish between the $O(2)$ and DBG universality classes, and the $O(2)$ emerges near the tip of the Mott lobe. 204

- 14.9 Density profiles, compressibility profiles, and compressibility versus density, conventional experimental visualizations extracted from density profiles, with contributions from $t = 0$ subtracted off to yield only the density contribution from low energy, universal fluctuations. Beware: we use identical symbols here (and only here and in Fig. 14.10 to indicate the quantities after subtraction. Top to bottom: $t/U = 0.01, 0.014, 0.0585, 0.0593$. Each graph shows temperature $T = t/4, t/2, t, 2t$, and $4t$ in black (solid), red (solid), blue (solid), black (dashed), and red (dashed), respectively. See Fig. 14.8 for an analysis bringing out and comparing the universal behavior. Note that except for the subtraction, this figure is identical to Fig. 14.7, except the last column has been split into two columns, for the transitions near $n = 0$ ($\mu \in (-0.35, 0.0)$, left) and $n = 1$ ($\mu \in (0.0, 1.0)$, right), to avoid clutter. 206
- 14.10 Rescaled compressibility versus density scaling curves. Top to bottom: $t/U = 0.01, 0.04, 0.0585, 0.0593$. The tip of the Mott lobe is $(t/U)_c = 0.0593$ in the thermodynamic limit. Left to right: (i) rescaling appropriate to DBG transition near $n = 0$, (ii) rescaling appropriate to $O(2)$ transition near $n = 0$, (iii) rescaling appropriately to DBG near $n = 1$ ($\mu \in (-0.35, 0.0)$), and (iv) rescaling appropriate to $O(2)$ near $n = 1$ ($\mu \in (0.0, 1.0)$). Universality persists to temperatures $T \sim t \sim 2t$, and over a more limited regime of the scaling curve at higher temperatures, as is expected. Each graph shows temperature $T = t/4, t/2, t, 2t$, and $4t$ in black (solid), red (solid), blue (solid), black (dashed), and red (dashed), respectively. The universal collapse or lack thereof is able to distinguish between the $O(2)$ and DBG universality classes, and the $O(2)$ emerges near the tip of the Mott lobe. Note that except for the subtraction, this figure is identical to Fig. 14.8. 207
- 17.1 (a) Rescaled mediated potential as a function of interparticle separation divided by λ , as given by Eq. (17.9), with $\xi = 1, 4, 15$ from top to bottom. (b) Scattering amplitudes f as a function of mediated potential depth factor $V_d \equiv (2\delta^2)/(\pi^3\lambda_0^2MC_3^2) = V_0(\lambda/\lambda_0)^2$ with $\lambda_0 \equiv 50\text{\AA}$, for the triplet (dashed) and singlet (solid) scattering channels. Vertical lines indicate V_d for the typical parameters given in the text (dashed line) and for $V_d = 0$ (solid). The divergences near $V_d = 0$ have been rounded off for display. (c) Contour plot of the factor by which V_{med} reduces the frequency shift as a function of λ and V_d . Typical values of parameters are shown by the black dot, while factor of two variations comprise the interior of the black rectangle. The contour plot is hidden in the white “resonance” region (far away from the relevant regime), where the scattering amplitude diverges. 222

18.1	Hyperfine level diagram for hydrogen atom in a strong magnetic field, where $\theta = 3 \times 10^{-3}$. Arrows denote electron (no-slash arrow) and nuclear (slashed arrow) spin projections.	229
18.2	The polarization versus temperature for the Boltzmann case (solid line) and the Bose-condensed case (dashed line), from Eq. 18.8.	237
19.1	Our model's basic idea. (a) The solid at $T > T_2$ before any superflow develops. There are two distinct types of regions: those that support superflow at low temperatures (SF) and those that will not (NSF). It is likely that T_2 is larger than the solidification temperature so that the domains are <i>always locally superfluid</i> in the solid. (b) The state of the system after cooling through one phase transition to a temperature $T_1 < T < T_2$: within each of the SF regions, a superflow develops. However, no global phase coherence is present. (c) The state of the system after cooling to $T < T_1$: global phase coherence has developed, and superflow occurs throughout the system.	246
19.2	The critical temperature (in mK) versus ^3He concentration (in parts per billion) on a log-log plot. Solid line: $x = 1/4$ static links prediction (see text); Dashed line $x = 1/6$ static links prediction. (Points are copied by hand out of Moses's proposal.) The color figure is from Kim <i>et al.</i> and compares various experimental T_c 's with Eq. (19.8), our prediction for T_c (solid pink line).	262
19.3	A schematic review of the Bose-Hubbard model: The phase diagrams for the Hubbard or coupled Josephson junction model. Here t is the tunneling rate, μ is the chemical potential, U is a measure of the interaction strength between particles on the same site, and T is the temperature. The " $n = x$ " states are the x -particle per lattice site Mott insulating states. (a) Zero-temperature phase diagram, consisting of Mott insulating lobes with integer fillings and a superfluid phase; presumably the supersolid phase is far from the Mott lobes. (b) The finite temperature phase diagram, with a normal fluid and a superfluid phase. While $A \rightarrow B$ would be a cooling path for a system directly described by the Hubbard model, our theory associate a more indirect path in t/U with the experimental cooling, as illustrated by the path $C \rightarrow D$	265

Chapter 1

Introduction to many-body physics in ultracold atomic gases

1.1 Motivation: many-body physics

“Today we cannot see whether Schrodinger’s equation contains frogs, musical composers, or morality — or whether it does not.” –Richard Feynman

Many of the most important, interesting, and vexing problems we encounter are questions about the behavior of large collections of objects: How do atoms organize themselves to form diverse materials such as plastics, metals, fluids, magnets? How do connected neurons collectively result in intelligence? How do competing organisms give rise to ecosystems? How do humans organize themselves into groups, economies, and societies? Each of these questions shares the common thread of being a question about how entities come together to give rise to behavior not obviously connected to the underlying entities. In physics, the study of large collections of interacting objects is referred to as “many-body physics.”

There are several reasons that condensed matter and ultracold atomic physics are wonderful areas in which to study this emergence. Firstly, unlike many other fields, we have a good understanding of the constituent pieces — they obey Schrodinger’s equation referenced above by Feynman — and we can specifically focus on the means by which the individual pieces’ behaviors turn into the collective behavior. Secondly, it is possible to do reproducible, tunable, quantitative experiments — in contrast, you can’t repeatedly create human societies in test tubes. Remaining firmly grounded in experimental consequences is extremely useful when developing reliable theories for many-body systems, since these theories almost invariably involve uncontrolled or untested approximations. Physics of-

fers us a grounded way to develop new methodologies for understanding emergent behavior.

Example of emergence in many-body physics.—For a concrete example, consider a gold atom, a tiny, basically spherical, transparent speck. None of metallic gold’s properties are readily apparent — its shine and color, its large heat capacity (think of a cold winter, when a metal doorknob feels much cooler than wood at the same temperature), and its low electrical resistance have no direct counterparts in the individual gold atom. Understanding how atoms collectively form metals was an early coup of solid state physics [2]. This theory gave us, for example, an understanding of why copper is a metal while diamonds are insulators (not to mention explaining semiconductors and resulting in the transistor). This leads to another fascinating observation: although the emergent metal bears little resemblance to the individual atoms, vastly different atoms can give rise to similar behavior. For example, all metals — be they aluminum, copper, silver, or gold atoms, or a combination — share most of gold’s characteristics listed above. This is not a coincidence: understanding this universality culminated in the development of the renormalization group in the 1970’s (see Refs. [3, 4, 5, 6, 7, 8]. for good overviews). These ideas and tools of emergence, universality, and the renormalization group have since permeated well outside of physics, for example to biology (flocking, swarming, and bacterial motion [9], population dynamics [10], and the theory of disease propagation [11, 12, 13]), chemistry (reaction/diffusion equations [14] or *ab initio* quantum simulations of molecules [15]), mathematics (bifurcations and period doubling [16], and extreme value distributions [17, 18]), civil engineering (traffic flow [19]), sociology (refinements and elaborations of sociology’s “balance theory” [20]), and economics and finance (a wide variety of concepts, ideas, and models in Refs. [21, 22, 23]). There are also some entertain-

ing, popular overviews touching on this area: “Sync,” by Steven Strogatz [24], “The Collapse of Chaos,” by Ian Stewart and Jack Cohen [25], and “Chaos” by James Gleick are particularly relevant [26]. The examples are illustrative — other examples abound.

Applications.—Finally, a little more practically, the fruits of studying emergent phenomena in physics have frequently led to technological advances: the transistor, hard drive, laser, and MRI’s (magnetic resonance images) are just a few examples which owe their existence to fundamental discoveries in condensed matter physics over the last century. As we are presently confronting many phases of matter which cannot be understood within our current framework of how properties emerge from their constituent particles [2], one imagines that these will have equally dramatic applications. One that is often talked about is the application of so-called topological states to quantum computing [27].

Cold atomic systems offer great promise for precision measurement — spectroscopy, accelerometry, magnetometry, tests of fundamental physics such as time-variations of fundamental constants or violations of the standard model, and much more [28, 29]. At the intersection of these two fields, cold atoms can emulate real materials and models of materials, for example high temperature superconductors [30]. It is in the latter role as analog systems to explore many body systems on which this thesis concentrates.

Quantum emulation.—At a first glance, one might suspect that using cold atomic experiments to emulate condensed matter models is simply creating a glorified, and highly special purpose, computer. However, because we are interested in quantum mechanical systems, this conclusion is incorrect: classical computers are unable to efficiently simulate general quantum systems. To be precise, the resources required to simulate a general quantum system on a classical computer

grows exponentially with the simulated system's size. In contrast, the resources required to emulate a system using cold atoms grow linearly with the system's size: to emulate twice as large of a system, one requires twice as large of an emulator.

A simple argument allows us to understand the difficulty in simulating quantum mechanics in classical systems. Consider a spin-1/2 lattice system for concreteness. If there are L sites, then there are 2^L basis states in the Hilbert space, requiring 2^L complex numbers to specify the amplitudes of a single wavefunction in this space – this leads to an exponential growth in computational resources just to *store* the wavefunction of the quantum system at a given instance of time. To give a feeling for the size of this, for $L = 30$, this requires a several gigabytes of storage, even with modest precision for each of the amplitudes; for $L = 400$, one would require storing more amplitudes than there are particles in the observable universe. Meanwhile, a few grams of material will have $L \sim 10^{23}$ lattice sites, each of which may possess many more degrees of freedom than a spin-1/2 system. Clearly, simulating quantum mechanics with any classical in this manner is infeasible. Recent, thorough analysis from quantum information indicates that for the relevant observables of physical systems, this estimate is somewhat too pessimistic: the cost scales as the exponential of the surface area rather than volume of a system. This has led to the development of much improved classical simulation algorithms [31, 32], but the exponential cost almost certainly persists for general quantum systems.

A universal quantum computer would allow one to efficiently simulate quantum systems (efficiently here meaning, roughly, resources scaling polynomially in the size of the simulated system). An enormous effort is underway to realize such systems, but scalable quantum computers of power even remotely comparable to classical quantum computers seem far off. Cold atoms realizations of condensed matter models is well underway, with many novel results found in these experiments

— Sec. 1.3 gives a brief historical overview. Additionally, they provide realizations of the physics that a quantum computer generally does not (e.g. mass flow), possibly useful in unforeseen applications.

Understood foundations and open frontiers in many-body physics. Although I argued that exactly calculating a general quantum system’s properties is impossible, there are many cases that are tractable: using a combination of approximations (e.g., perturbation theory), simple models (e.g., weakly interacting systems), and/or focusing on special observables (e.g., local static properties), one may make progress towards understanding broad classes of these systems. Increasing this understanding is a primary goal of efforts in many-body theory.

Physicists made tremendous progress in understanding a broad class of experimentally relevant materials that culminated in what I term “traditional many body theory.” Early results were found shortly after the advent of quantum mechanics and were heavily developed in the 1940’s-70’s. “Fermi liquids,” “quasiparticles,” and “symmetry breaking” are key concepts at the core of these results, which very briefly may be summarized as saying that frequently, at low energies strongly interacting systems may be described in terms of a set of fictitious, weakly interacting “quasiparticles.” Moreover, many of the systems we care about in nature possess such a description [2].

Naturally, then, modern many-body theory has a large focus on finding descriptions of systems where this picture breaks down. Perhaps the most studied examples in condensed matter are exotic phases of matter (e.g., spin liquids, topological phases, glasses) and other systems with exotic, non-quasiparticle behavior (e.g., non-Fermi liquids, quantum criticality). Examples of both classes will appear in this thesis, and impacting these subjects using cold atoms will be my main focus herein. The effects of disorder, finite size (“mesoscopics”), and far from equilibrium

physics are additional, somewhat conceptually different frontiers that offer exciting opportunities for study in condensed matter and cold atoms [33]. Although condensed matter emulations are the focus of this thesis, cold atoms can realize conditions similar to neutron matter (BEC/BCS crossover at unitarity [34]), and realize qualitative analogs of high energy nuclear phenomena (color superconductivity), which also impacts astrophysical phenomena (vortices in multicomponent superfluids, as argued to be found in neutron stars) [35, 36, 37].

1.2 Motivation: general atomic physics

Advances in atomic physics have led to an ability to measure the internal structure of isolated atoms with high precision. To give an example of the extraordinary precision that has been possible, the electron g factor has been determined to thirteen significant digits and with theoretical input from quantum electrodynamics provides a ten-digit accurate measurement of the fine structure constant α [38]. Additionally, this ability to address the internal structure has led to unrivaled control of quantum systems.

Atoms possess several internal degrees of freedom: electronic charge, electronic spin, and nuclear spin excitations. Molecules additionally possess vibrational and rotational degrees of freedom. Electromagnetic radiation is frequently used to excite and probe these degrees of freedom, and lasers are one of the most powerful tools available for coupling with monochromatic, coherent, and high intensity radiation. The field studying atomic properties with these tools is termed “atomic and molecular optics.”

These tools provide information about fundamental physics — precision measurement of fundamental constants — and also provide stringent tests of quantum mechanics and the standard model by being able to test for small deviations of

physics from expectations and to directly work with single photons of light coupled to matter [39]. They provide the most accurate clocks, with frequencies having relative systematic uncertainties of only 10^{-15} (See Ref. [40] and references within). In astrophysics, precision knowledge of spectra allow us to characterize composition of extraterrestrial objects: planets, interstellar gas, and stars. Indeed, many fields of astronomical observation are characterized by the region of the electromagnetic spectrum probed: e.g., “radio astronomy,” “infrared astronomy,” “optical astronomy,” etc. Such methods even offer the prospect for detecting extraterrestrial life by looking for life’s characteristic building blocks [41]!

The tools also offer a number of applications in other fields. In chemistry, spectroscopy has improved our knowledge of chemical compounds and their reactions; specific examples are numerous, but one timely example is environmentally important pollutants and greenhouse gases [42, 43]. This has led to a new type of chemistry, with reactions catalyzed and otherwise controlled of these reactions with external tools, such as lasers [44, 45] (one might even consider the laser light as a “reactant”). Extending these methods to more complex molecules has allowed study of biological molecules and processes: photosynthesis, signal transport in nerves and neurons, and energy production in cells, to name a few [46]. Perhaps the most publicly visible applications are to technology and entertainment. To give just a small subset of examples, lasers are used to read and write high density optical storage for computers; for high bandwidth data transmission; to mark, weld, and cut metals and other materials; and for eye surgery and clean scalpels [47].

A new frontier in atomic physics is to focus on what happens when atoms are not completely isolated from each other, and even when they strongly influence each other. In particular, in cold atoms, this leads to a highly unique place to study many-body physics, discussed in the rest of this thesis.

1.3 History and introduction to many-body physics in cold atomic systems

1.3.1 Background and achievements.

To improve control and measurement of atomic systems, two important components are reducing fluctuations by decreasing the temperature and reducing the complex-to-analyze effects of interactions with other atoms by decreasing the atomic density. A typical modern cold atoms experiment may achieve temperatures as low as a few nanokelvin and densities of $n \sim 10\mu\text{m}^{-3}$. Together with the simplicity of the constituents, one can ensure that the system is a closed quantum system — with essentially no unaccounted for external degrees of freedom on the timescales of interest — and allow the application of external potentials, for example lattices. The cold, dilute regime has enabled the study of quantum many-body systems with highly desirable features. The low temperatures enable quantum effects to manifest at the incredibly low densities in these experiments; the diluteness of the gas compared to the effective range of the interaction ensures that the interactions have a simple description, frequently in terms of a delta function contact interaction. Despite diluteness in this sense, the interaction *energy* may be made extremely large compared to the other energy scales, opening the way many-body physics [48, 33].

Historically, the first step into many-body physics in these systems was the achievement of Bose-Einstein condensation in dilute Bose gases in 1995, the culmination of decades of development of laser cooling, trapping, and other techniques. The initial focus in the late 1990's was on the study of dilute gases for which $na^3 \ll 1$, with n the density and a the s-wave scattering length (see Chapter 2 for

a definition of this quantity, a measure of the interaction strength). This is the realization of a model system introduced in the 1950's to understand superfluidity in a setting that was much more tractable than in ^4He . Cold atoms physicists explored numerous phenomena in these gases: the equation of state, collective modes, vortices, and dynamics [48]. Quantum turbulence [49, 50] and reduced dimensionality [51] remain exciting examples of physics studied in these systems.

The field has continued realizing model systems of interest in condensed matter, but since roughly 2001, a large component focuses on models which are *strongly interacting* and possess open questions for modern condensed matter research: the Mott insulator/superfluid phase transition for bosons in optical lattices, the BEC/BCS crossover in strongly interacting fermions, disordered systems, and reduced dimensional systems [33]. To give examples of the relevance of these systems, the BEC/BCS crossover probes the simplest model of superconductivity/superfluidity going beyond the Bardeen-Cooper-Schrieffer (BCS) theory that describes conventional superconductors. Going away from the BCS limit, the pairs become more tightly bound. Eventually, even in the absence of a Fermi sea they are bound, and for strong enough binding are described as a BEC of pairs. The system in between these limits is similar to systems in nuclear physics [34], and it is worth noting that, similar to the unitarity limit of the BEC/BCS crossover, the pair size in the cuprate high-temperature superconductors is also comparable to the interparticle spacing [52, 53]. Cold atoms experiments have contributed to quantitative studies of the thermodynamics [34], dynamics [54], and effects of reduced dimensionality and polarization in these systems, which can lead to exotic states such as FFLO [55].

The frontier of research goals for the next few years is attempting to realize still more exotic, more relevant to condensed matter, and less understood phenomena:

nematics in dipolar gases [56], the phase diagram of the Fermi Hubbard model, in particular the question of whether it displays d -wave superconductivity [30], rotation or other techniques to realize topologically ordered states such as fractional quantum Hall states and topological insulators (See Chapter 8), and exotic “spin liquid” states in frustrated antiferromagnets. Thanks to the ideas presented in **Chapters 13, 14, and 15**, I am hopeful that we may add a major category to areas impacted by cold atoms in the near future: quantum criticality.

Chapter 2 will provide a more complete introduction to the experimental and theoretical tools used in optical lattice experiments. Optical lattices are probably the most common experimental tool with which to explore exotic physics with the most direct connection to condensed matter models.

1.3.2 Challenges.

I briefly outlined a subset of the most important achievements of cold atoms towards the study of many-body physics. The community is also facing major challenges in moving forward to more exotic states. The most important few are probably:

1. **Cooling:** Although cold atoms systems are the coldest systems in the universe (with a record low temperature of 500 pK), there is a constant effort to further decrease temperatures. In the context of many-body physics, the most important impetus is to push to temperatures well below the bandwidth of particles in deep optical lattices (\sim nK in typical setups) and to temperatures where superexchange and magnetism in optical lattices becomes important (\lesssim 100 pK) [57]. New cooling methods are needed, and many are being pursued.
2. **Equilibration:** Much of what we hope to learn from cold atoms exper-

iments concerns many-body systems near equilibrium (although there are exciting far-from-equilibrium processes, as well). However, the dynamics of cold atomic systems slows down at low temperatures, and optical lattices further slow the motional degrees of freedom. Indeed, the time to quantum mechanically tunnel between lattice sites can be tens of milliseconds. A typical cloud lifetime is at most a few seconds, so this limits the time for the system to equilibrate. Indeed, the experimental consequences of this have recently become quite ubiquitous, and as temperatures of interest are lowered — and correspondingly timescales of interest get longer — even more work will need to be done on this separation of timescales. Loss-induced correlations may offer one route to move forward (Ref. [58] is one example).

3. **Hamiltonian engineering and state control:** In order to quantitatively emulate model systems of interest, one needs to be able to reliably and accurately create the relevant Hamiltonians. While experimentalists are presently able to do this for many cases of interest — including the Bose and Fermi Hubbard models — the accuracy is modest (errors on the order of a percent in the best cases) and frequently require very low energy scales. Finding ways of characterizing the discrepancies from simple models, improving the accuracy of the Hamiltonians, and extending this to allow higher energy scales (to alleviate the preceding two challenges) are important goals for the field. Related to this, better state control may allow creation of novel and interesting many-body correlated states without them being equilibrium states of a Hamiltonian, or faster more accurate preparation of equilibrium (or metastable) states of a Hamiltonian (effectively a cooling procedure).
4. **Probes and methods to characterize behavior:** Even once novel states and behavior are achieved in a cold atoms system, we require new tools

to extract an understanding of the physics of these systems. A standard technique is absorption imaging, which gives the column integrated density of the cloud, but we are still using only a fraction of the information in these images. Moreover, we would like to understand response functions, correlations, and dynamics, which are inaccessible by straightforward density images.

The work in this thesis will largely concentrate on the last two challenges.

Chapter 2

Theoretical and experimental techniques used to explore many-body physics in cold atoms, especially optical lattices

2.1 Experimental techniques

2.1.1 Common experimental techniques for all cold atoms experiments: trapping and cooling

The first stage of producing an ultracold atomic gas is to vaporize a solid (with an “oven” or other source) to create a hot gas, whose center of mass is then slowed sufficiently to be trapped. The slowing is frequently accomplished by a “Zeeman slower”¹: a series of current carrying coils that generate magnetic fields, and which decrease in intensity over the length of the slower, to create a magnetic field gradient. Atoms used in this technique possess an electron spin degree of freedom so that the internal energy of the atom depends on the applied magnetic field and thus the magnetic field gradient introduces a potential energy gradient for the atoms, resulting in their slowing [48, 59].

Magnetic trapping works similarly, by magnetic forces, but with some subtleties because the naive setup of a quadrupolar magnetic field leads to a magnetic field zero at the trap center with highest atomic density, and magnetic field zeroes cause spin states to become degenerate. Then atoms can transition between spin states as they move through magnetic field variations near the magnetic field zero, and — since the states transitioned to may be either untrapped or even repelled — the

¹Stark decelerators — very roughly speaking replacing magnetic fields with electric fields — are another option, often used with molecules

atoms will be lost. Moving the trap around to create a time-averaged potential or by using asymmetric traps [48, 59]. Optical traps are also possible (using techniques analogous to those used to create periodic lattice potentials discussed in Section 2.1.2) which have advantages, including the ability to generate degenerate spin mixtures [48, 59].

After atoms are trapped, they are cooled in multiple stages [59]. The first stage is generally Doppler laser cooling: a laser is red-detuned to an optical transition and the relativistic Doppler effect brings atoms moving towards the laser closer to resonance, therefore causing them to absorb more photons from the laser and slow down. The last cooling is evaporation, in which the cloud cools itself by losing the most rapidly moving atoms. These may be supplemented with other cooling schemes [48], leading to temperatures that have reached 500 picoKelvin.

Most commonly, experimentalists work with alkali atoms. These are convenient: their simple internal structure and single unpaired electron allow for straightforward optical and magnetic manipulation. Nevertheless, extensions of the techniques developed for alkalis have enabled BEC's of metastable He [60, 61] and several isotopes of Cr [62], Yb [63], Ca [64], and Sr [65, 66], as well as nearly degenerate Feshbach or ground state KRb molecules [67]. Refs. [48, 59] contain more details and references.

It is worth noting that at these temperatures, the true equilibrium state is not a Bose-Einstein condensate, but a solid. However, on the timescales of interest, the system may frequently be described as an equilibrium state of some Hamiltonian. The BEC is the simplest example: the loss rates to form molecules and small solid clusters are negligibly small (on the order of seconds) compared to the time to equilibrate to a BEC (on the order of tens of milliseconds).

To understand what drives the pursuit of such extraordinarily cold tempera-

tures, let's consider the transition temperature of a dilute gas, neglecting interactions. This result will also be useful later. Dimensional analysis get us most of the way: when the characteristic length scale of quantum mechanical motion grows to become on the order of the interparticle spacing, particles will lose their distinguishability and a normal gas will Bose condense. The length scale of quantum mechanical motion is the thermal de Broglie wavelength $\lambda_T = \sqrt{\frac{\hbar^2}{2mk_B T}}$ for particles with mass m , temperature T , and \hbar and k_B Planck's and Boltzmann's constant respectively. For density n , the interparticle spacing is $r_s = n^{-1/3}$, so this gives a transition temperature

$$T_c \sim \frac{\hbar^2 n^{2/3}}{k_B m}. \quad (2.1)$$

To understand this microscopically and obtain the prefactor, consider a gas with density of states $\nu(\epsilon) = C\epsilon^\alpha\Theta(\epsilon)$ for some constants C and α , and with Θ the Heaviside step function (the energy zero is set to be that of the lowest energy state). At sufficiently low temperatures this will generically describe the density of states. For free particles of mass m in three dimensions, one has $\alpha = 1/2$, but for other α this also describes trapped gases and other dimensions. For bosons, the occupation of a state with energy ϵ in a grand canonical system with chemical potential μ is ²

$$n(\mu, \epsilon) = \frac{1}{e^{(\epsilon-\mu)/T} - 1}. \quad (2.2)$$

The chemical potential must be less than the lowest energy state, or one obtains unphysical occupations. Then the maximum occupations and thus maximum number of particles occurs for $\mu = 0$. Thus, for these Bose statistics, there is a maximum

²I will go between setting \hbar and k_B to one and showing them explicitly throughout this thesis.

number of particles

$$\begin{aligned} N_{\max} &= \int_0^\infty d\epsilon \frac{C\epsilon^\alpha}{e^{\epsilon/T} - 1} \\ &= C\Gamma(\alpha + 1)\zeta(\alpha + 1)T^{\alpha+1} \end{aligned} \quad (2.3)$$

where $\zeta(\eta) \equiv \sum_{n=1}^\infty \frac{1}{n^\eta}$ is the Riemann zeta-function and $\Gamma(\eta)$ is the Euler gamma function. The last equality follows by Taylor expanding $(e^{\beta\epsilon} - 1)^{-1}$. If we put in more particles than N_{\max} , the occupation formula Eq. (2.2) fails and the lowest energy mode becomes macroscopically occupied with the excess particles, signifying a phase transition to the Bose-condensed state. Thus, for a given number of particles N , the transition occurs at

$$T_c = \left(\frac{N}{C\Gamma(\alpha + 1)\zeta(\alpha + 1)} \right)^{1/(\alpha+1)}. \quad (2.4)$$

Note that C is an extensive constant, so that the transition temperature depends on the number of particles only through the density, as expected for the homogeneous system. For free particles in three dimensions, we have $C = \frac{Vm^{3/2}}{\sqrt{2\pi^2\hbar^3}}$ and $\alpha = 1/2$, so $T_c = \left(\frac{n\sqrt{2\pi^2\hbar^3}}{m^{3/2}\Gamma(3/2)\zeta(3/2)} \right)^{2/3} = \frac{2\pi\hbar^2}{m} \left(\frac{n^2/3}{\zeta(3/2)} \right)^{2/3} \approx 3.3 \frac{\hbar^2 n^{2/3}}{m}$.

Finally, contrast the temperature scale of BEC in these dilute gases with that of ^4He , in which superfluidity onsets at 2.2K. The difference of several millions in transition temperatures is associated with the much lower density of the dilute gases.

The cooling enables one to access not only bosonic superfluidity, but also fermionic degeneracy for Fermi gases. The characteristic temperature at which a Fermi surface develops is set by the same condition as the boson degeneracy — the thermal de Broglie wavelength is on the order of the interatomic spacing. In this case, however, there is no phase transition, just a crossover between two qualitatively distinct behaviors.

With interactions, these ultracold temperatures open up numerous opportunities to explore many-body physics in both fermionic and bosonic gases. A broad

class of these involves lattices, the creation of which is the focus of the following section.

2.1.2 Optical lattice experimental techniques

Here I discuss how lattice structures are realized experimentally in cold atoms. Optical lattices play a major role in exploring many-body physics in cold atoms. At the broadest level, they slow the atomic motion, increasing the importance of the interaction energy relative to the kinetic energy. They play a special role in emulating condensed matter models, since at the microscopic level solid state systems usually have some lattice structure.

Experimentally, one creates optical potentials using the AC stark effect of de-tuned laser light in which the cloud sits. For strong lasers (many photons in the lasing mode) it is appropriate to treat the atom-light interaction by treating the light as a classical oscillating electrical field

$$\mathbf{E}(\mathbf{r}, t) = \mathbf{E}_0 e^{i\mathbf{k}\cdot\mathbf{r}} \cos(\omega t) \quad (2.5)$$

There is also an oscillating magnetic field, but this has a much smaller effect on the atoms. We assume the atom has only one optical transition near resonant with the laser frequency, and thus we can treat it as a two-level atom with ground and excited state energy levels $|g\rangle$ and $|e\rangle$ described by the Hamiltonian

$$H_a = E_g^{(0)} |g\rangle \langle g| + E_e^{(0)} |e\rangle \langle e|. \quad (2.6)$$

The transition frequency ω' is given by $\hbar\omega' = E_e^{(0)} - E_g^{(0)}$. The relationship $\delta = \omega - \omega'$ defines the detuning frequency δ of the laser beam from the optical transition. The atom-light interaction Hamiltonian is

$$H_{a-l} = \gamma E(\mathbf{r}, t) |e\rangle \langle g| + \text{H.c.} \quad (2.7)$$

where γ is a constant and H.c. denoting Hermitian conjugate. The dipole approximation is justified here because the wavelength of light is much larger than the atomic dimensions, and so γ is proportional to the dipole matrix element $\langle e|\mathbf{r}|g\rangle$. To simplify the time-dependence, we make the transformation to a new time-dependent basis with a new excited state, $|\tilde{e}\rangle$, defined by

$$|\tilde{e}\rangle = e^{i\omega t} |e\rangle. \quad (2.8)$$

In terms of the new states, the total Hamiltonian $H = H_a + H_{a-l}$ is ³

$$H = E_g^{(0)} |g\rangle \langle g| + (E_e^{(0)} - \hbar\omega) |\tilde{e}\rangle \langle \tilde{e}| + \frac{E_0}{2} (e^{2i\omega t} + 1) |\tilde{e}\rangle \langle g| + \text{H.c.} \quad (2.12)$$

Within the rotating wave approximation, we can neglect the $e^{2i\omega t}$ term since it oscillates rapidly compared to the energy splitting of the $|\tilde{e}\rangle$ and $|g\rangle$ states: $E_e^{(0)} - \hbar\omega - E_g^{(0)}$, which is just $\hbar(\omega' - \omega) = \hbar\delta$. So as long as the detuning δ is small relative to the energy splitting, the physics is well described by the approximate Hamiltonian

$$H = E_g^{(0)} |g\rangle \langle g| + (E_e^{(0)} - \hbar\omega) |\tilde{e}\rangle \langle \tilde{e}| + \frac{E_0}{2} |\tilde{e}\rangle \langle g| + \text{H.c.} \quad (2.13)$$

This is a static two-level system, and the Hamiltonian is easily diagonalized. However, the important regime has detunings much less than $(\gamma E_0)^2$, and we may treat

³Note that to get the new Hamiltonian governing the system in the transformed basis, we need to ensure that its solution give the same equations of motion (EOM) in the original basis as the original Hamiltonian (this is inequivalent to simply substituting the definition of the new basis states in the old Hamiltonian). The EOM of $|g\rangle$ is unchanged. The EOM for $|e\rangle$ is, from the original Hamiltonian,

$$i\partial_t |e\rangle = H |e\rangle = E_e^{(0)} |e\rangle + E_0 \cos(\omega t) |g\rangle. \quad (2.9)$$

Substituting the definition of $|\tilde{e}\rangle$, we have

$$\begin{aligned} i\partial_t e^{-i\omega t} |\tilde{e}\rangle &= H |\tilde{e}\rangle = E_e^{(0)} e^{-i\omega t} |\tilde{e}\rangle + E_0 \cos(\omega t) |g\rangle \\ \Rightarrow i [e^{-i\omega t} \partial_t |\tilde{e}\rangle - i\omega e^{-i\omega t} |\tilde{e}\rangle] + \frac{E_0}{2} (e^{i\omega t} + e^{-i\omega t}) |g\rangle &= E_e^{(0)} e^{-i\omega t} |\tilde{e}\rangle. \end{aligned} \quad (2.10)$$

Thus

$$i\partial |\tilde{e}\rangle + \frac{E_0}{2} (e^{2i\omega t} + 1) |g\rangle = (E_e^{(0)} - \omega) |\tilde{e}\rangle, \quad (2.11)$$

exactly the EOM obtained from the new Hamiltonian given in Eq. (2.12).

the atom-light interaction via second order perturbation theory to give the energy level shift for the internal ground state ⁴

$$E_g - E_g^{(0)} = \frac{2\gamma^2 I}{c\epsilon_0\delta} \quad (2.14)$$

with $I = c\epsilon_0 E_0^2/2$ the laser intensity. The key result is that potential energy is proportional to E_0^2 and hence the laser intensity. Thus, by shaping intensity profiles, one can shape potential surfaces. In addition to the applications here, this is the same idea behind optical tweezers applied to small systems, an experimental technique used extensively in chemical and biological systems [68].

Note that in deriving Eq. (2.14) I neglected any finite lifetime of the states, but this arises due to spontaneous and stimulated photon emission and photon absorption. One can model the decay as adding an imaginary part $i\Gamma/2$, with Γ the decay rate, to the energy of the E_e state, in which case the above analysis yields

$$E_g - E_g^{(0)} = \frac{2\gamma^2\delta I}{c\epsilon_0(\delta^2 + \Gamma^2)}. \quad (2.15)$$

Then the simple picture above is valid only when the detuning is large compared to Γ (proportional to the linewidth), in which case we were justified in neglecting the real absorption and emission.

Using the observation that spatial variations of light intensity give spatial potential energy variations for the atoms, one can create various potential energy surfaces. The most common optical potential is made by interfering two coherent, counterpropagating lasers. The standing wave interference pattern yields a sinusoidal lattice potential

$$V(\mathbf{r}) = \sum_{\alpha=x,y,z} V_{0,\alpha} \sin(\mathbf{k}_\alpha \cdot \mathbf{r}) \quad (2.16)$$

⁴Had we directly done an appropriate time-dependent perturbation theory, we could have done this directly and bypassed the rotating wave approximation — it would have emerged automatically.

for a set of lattice intensities $V_{0,\alpha}$ and wavevectors \mathbf{k}_α . Doing this in three orthogonal directions, one forms a cubic sinusoidal lattice. The many-body physics of bosons and fermions in such a lattice is quite rich and related to important models of solid state physics. This will be introduced in Section 2.2.3 and discussed throughout this thesis.

This technique can be employed to create other optical external potentials. For example, if the counterpropagating lasers are incoherent, no interference pattern forms and the light intensity is just the beam profile, creating a trapping potential. Such optical potentials are increasingly used, and are sometimes necessary. For example, to create spinor gases, one must eliminate magnetic fields that break the spin degeneracy [69]. Another example is the patterning of arbitrary potential landscapes — using masks and high quality, high numerical aperture optics — that is possible in some experimental setups [70].

2.1.3 Detection

The main tool used to probe cold atomic gases is absorption imaging. In this technique, one shines a laser on the cloud, and a CCD camera on the other side of the cloud measures the light transmitted. In other words, one measures the cloud's shadow. In the limit where multiple scattering can be neglected (valid for many experiments), the transmitted intensity I_t at position (x, y) is

$$I_t(x, y) = I_i e^{-\tau} \quad (2.17)$$

with I_i the incident intensity, and τ the optical depth is given by

$$\tau = N(x, y)\sigma \quad (2.18)$$

where $N(x, y)$ is the cross sectional density of atoms in the path of the beam captured at the pixel with location (x, y) , and σ is the scattering cross section for

the light scattering off of an individual atom. Thus, we see that measuring I_t/I_i gives the column integrated density of the cloud.

By applying various protocols before imaging, one can obtain much more general information than the density profile. Instead, one can perform various manipulations before imaging the cloud. Spectroscopy is one example — one can create excitations of the cloud and then imagine the system after this procedure. Chapters 3, 4, 5, 6, and 7 discuss this in the context of radio-frequency spectroscopy. Another, very common protocol, is *time of flight* imaging. Here, one instantaneously turns off all external potentials and interactions and let the cloud expand for a long time. In this limit, the density at a position \mathbf{r} is proportional to the momentum distribution at a velocity $\mathbf{k} \propto \mathbf{r}$: thus for a condensate, the real space image is just the momentum space structure factor. To see this, note that the sudden turn-off of the trap, lattice, interactions, etc. projects the quantum state onto momentum-space eigenstates $|\mathbf{k}_1, \mathbf{k}_2, \dots, \mathbf{k}_N\rangle$ (for N -particles). The dynamic evolution then displaces a state with momentum \mathbf{k} by $\hbar\mathbf{k}t/m$ in time t . For long times, the initial position is irrelevant and the final position is proportional to \mathbf{k} , as claimed.

The resolution of these imaging techniques varies, but in the past the imaging resolution has been much coarser than the atomic spacing⁵ However, very recent developments enable imaging of single atoms with high resolution. At least six such experimental setups have been demonstrated. In 2007 David Weiss's group gave an early demonstration of imaging atoms in an optical lattice with single-site accuracy [71] by employing a large lattice spacing (several microns). Due to the large lattice spacing, the tunneling energy was negligible, so that there was no quantum mechanical coupling between the sites — all observed motion was thermal

⁵This is another reason for the prominence of time-of-flight imaging, since it expands the imaged cloud's size.

activation. In 2008, using an scanning electron microscope, Herwig Ott’s group measured individual atoms in optical lattices with lattice spacings useful for doing many body physics, with resolution a fraction of the lattice spacing [72]. While this technique provides spectacular resolution for these gases, the detection fidelity is rather low: only $\sim 10\%$ of the atoms are detected, somewhat limiting the utility for, say, measuring density fluctuations or spatial correlations. In 2009, through the use of a two-dimensional system near the imaging optics and extremely high quality, high numerical aperture optics, Cheng Chin’s group has measured [73] the density profiles and fluctuations of bosons in an optical lattice in the Bose-Hubbard regime with linear spatial resolution of 2-3 sites ⁶. At the end of 2009, Markus Greiner’s group demonstrated single site resolution imaging (with near unity fidelity) of a BEC in an optical lattice [70], approaching the Mott insulator regime by using a two-dimensional gas near the imaging optics, high quality optics, and a large numerical aperture. The main drawback of the approach is that the imaging light induces atomic to pair into molecules when they are on the same site, and thus only measures the parity of the occupation — $n \bmod 2$ — not the occupation n .

2.2 Theoretical techniques

2.2.1 Interactions in cold atom systems

Interactions are the key ingredient in many-body physics — without them, the behavior is reducible to single particle physics! In this section, I introduce the appropriate description of interactions in cold atoms experiments. Good (broader) discussions can also be found in the books [48, 74].

⁶The pixel size is slightly smaller. At the moment, other imaging elements limit the resolution, but may be removed if one can properly account for the point-spread function of the optics.

The first point to be emphasized is that the word “dilute” is used with (at least) two very distinct meanings. Both involving the interactions. The first is that the interaction energy is small — in three dimensions this requires that the scattering length a (defined shortly) satisfies $na^3 \ll 1$ with n the density ⁷. Although many early cold atoms experiments were in this regime, the most interesting many-body physics requires strong interactions. Consequently many modern cold atom experiments explore regimes that are not dilute in this sense ⁸

Although experiments on many-body physics are not dilute in this first sense, there is a second sense in which virtually all cold atoms experiments are dilute: the *range* of the interaction, r_{eff} satisfies nr_{eff}^3 . Note that r_{eff} is in principle independent of the scattering length. This second sense of diluteness allows one to describe the interactions with an appropriately regularized delta function, with second quantized Hamiltonian

$$H_{\text{int}} = \frac{g}{2} \int d\mathbf{r} \psi^\dagger(\mathbf{r})\psi^\dagger(\mathbf{r})\psi(\mathbf{r})\psi(\mathbf{r}) \quad (2.19)$$

where $\psi^\dagger(\mathbf{r})$ and $\psi(\mathbf{r})$ are creation and annihilation operators for particles at position \mathbf{r} , respectively. Some care is required in having the interactions occur only at a single point in space, and I will return to this momentarily.

Our goal is to determine the coupling constant g in Eq. (2.19). One can imagine different philosophies to approach this question. One can imagine computing the

⁷This criterion follows from a simple argument: basically by dimensional analysis (assuming that the interaction energy is proportional to a , motivated later), the kinetic energy per particle is $E_k \sim n^{2/3}$ and the interaction energy per particle is $E_i \sim an$. Requiring $E_i \ll E_k$ gives $na^3 \ll 1$.

⁸A warning about notation is in order. Ostensibly, this argument would preclude experiments from studying many-body physics in the Bose-Hubbard model, since these experiments are in a regime $na^3 \ll 1$ — in fact, this is a necessary criterion for the applicability of the Bose-Hubbard model to describe optical lattice experiments (see Section 2.2.3). However, the “ a ” appearing in the text’s criterion is the scattering length for two particle problem *in whatever external potential is applied*, including any optical lattice. The effective scattering length in a lattice — call it a_L — is much larger than the free space a . Indeed, for strong lattices is on the order of the lattice spacing d . Thus, the scattering length a_L describing two low energy particles in a lattice is comparable to the density in the Bose-Hubbard regime as one approaches the Mott insulator, and one is indeed in a strongly correlated regime.

interaction energy for two particles in some configuration to determine g from an *ab initio* description of the atoms in terms of the nuclei and electrons comprising them. However, this is very challenging, and despite the fact that g is just a measure of two particles' interactions, it is still impossible to compute g with significant accuracy for many-electron atoms even with sophisticated numerical techniques and computational power. A more general philosophy is to try to relate g to independently accessible experimental measurements. Here, we will see that measuring two particle scattering properties allows one to determine g .

Our approach is to formally calculate the large distance scattering properties of the true interatomic potential and do the same for the contact interaction. We will see these can be matched with a proper choice of g , justifying our description of the system's physics in terms of a delta function, since the atoms are always separated by large distances. Define $V(r)$ to be the true two-particle interatomic interaction potential at interparticle separation r . The two-particle problem reduces to a single particle problem by working in relative coordinates where the wavefunction satisfies the Schrödinger equation [75]

$$-\frac{\hbar^2}{m}\nabla^2\psi(\mathbf{r}) + V(r)\psi(\mathbf{r}) = E\psi(\mathbf{r}) \quad (2.20)$$

for the three dimensional wavefunction ψ . Moreover, at the low energies of interest, s -wave scattering is the only relevant scattering channel, so we use the Schrödinger equation for the s -wave channel in radial coordinates [75]:

$$-\frac{\hbar^2}{mr}\frac{d^2}{dr^2}[rR(r)] + V(r)R(r) = \frac{\hbar^2k^2}{m}R(r) \quad (2.21)$$

where R is the s -wave radial wavefunction and k is the asymptotic momentum.

One can characterize the large distance scattering with the scattering length a . This is defined to be the radius of a hard sphere (yet another potential) that would give the same long distance scattering properties. Since we want to match

long-distance wavefunction, I start by calculating the large distance, low energy wavefunction for the hard sphere potential. Equation (2.21) for a hard sphere of radius a is

$$-\frac{1}{r} \frac{d^2}{dr^2} [rR(r)] = k^2 R(r) \quad \text{for } r > a \quad (2.22)$$

supplemented with a boundary condition $\psi(a) = 0$. (As a second order differential equation, one needs a second boundary condition, but this is equivalent to choosing a normalization for the wavefunction.) This equation is just $f''(r) = k^2 f$ for $f \equiv rR$, so the solution with $R(a) = 0$ is, for $r > a$ (up to normalization factor)

$$\begin{aligned} R(r) &\sim \frac{1}{r} \sin [k(r - a)] \\ &\sim 1 - \frac{a}{r} \end{aligned} \quad (2.23)$$

expanding for low energies — $kr, ka \ll 1$ — in the second line.

Now let's examine the form of the large distance scattering problem. Choose the incident wave to come along the z axis; angular momentum channels decouple at large distances, so for potential decaying sufficiently rapidly (faster than some power) we can write the large distance wavefunction as

$$\psi(r, \theta) = e^{ikz} + f(\theta) \frac{e^{ikr}}{r} \quad (2.24)$$

with θ the angle of from the z axis and $f(\theta)$ called the scattering amplitude. At low energies and large distances, the s -wave channel dominates, the scattering wavefunction simplifies to $\psi \rightarrow 1 + f/r$. Comparing with Eq. (2.23) shows that scattering in *any* potential gives a large distance scattering wavefunction of the same form as that of the hard sphere's. Moreover, it shows how to relate the scattering length a describing an arbitrary potential to the experimentally observable two-particle scattering cross section σ , since ⁹ $\sigma = 8\pi a^2$.

⁹This depends somewhat on particle statistics and conventions; the result is given for bosons. For single particle scattering from a potential or distinguishable particles, one obtains $\sigma = 4\pi a^2$.

There is one final step: we compute the scattering length corresponding to a contact interaction with strength g ; this will tell us how to choose g to reproduce the scattering properties of an arbitrary potential with some measured scattering length. Some subtlety arises in describing contact interactions, so it is beneficial to work with the Lippmann-Schwinger reformulation of the Schrödinger equation and break the problem into two steps: we calculate the T -matrix (defined below) in terms of g , and then we relate the T -matrix to a ; together this relates a to g .

First, we re-write the Schrödinger equation in integral form as ¹⁰

$$|\psi\rangle = |\psi_0\rangle + \hat{G}_0 \hat{V} |\psi\rangle \quad (2.25)$$

with $|\psi_0\rangle$ the solution for H_0 , the Hamiltonian in the absence of the potential operator \hat{V} , and the bare Green's function defined as $\hat{G}_0 \equiv (E - \hat{H}_0 + i\delta)^{-1}$ (where the infinitesimal $\delta \rightarrow 0^+$ will be chosen to give outgoing scattered waves later). We define the T -matrix via ¹¹

$$\hat{V} |\psi\rangle \equiv \hat{T} |\psi_0\rangle, \quad (2.26)$$

Eq. (2.25) implies $V |\psi\rangle = V(1 - \hat{V}\hat{G}_0)^{-1} |\psi_0\rangle$, so the T -matrix is

$$\hat{T} = V(1 - \hat{V}\hat{G}_0)^{-1}. \quad (2.27)$$

In Fourier space this is

$$T(\mathbf{k}, \mathbf{k}', E) = V(\mathbf{k} - \mathbf{k}') + \frac{1}{\Omega} \sum_{\mathbf{k}''} V(\mathbf{k}' - \mathbf{k}'') (E - k''^2/m + i\delta)^{-1} T(\mathbf{k}, \mathbf{k}', E) \quad (2.28)$$

¹⁰To see this, rewrite the Schrödinger equation as $(E - H_0) |\psi\rangle = V |\psi\rangle$. Then an equation of the form $\hat{L} |\psi\rangle = |\phi\rangle$ with \hat{L} a linear operator has the general solution $|\psi\rangle = |\psi_0\rangle + \hat{G}_0 |\phi\rangle$ where $\hat{G}_0 \equiv \hat{L}^{-1}$ is the Green's function associated with \hat{L} and $|\psi_0\rangle$ is the general solution of $\hat{L} |\psi_0\rangle = 0$. [[This is a generalization of the usual statement for differential equations, that (1) the general solution is the general solution of the homogeneous equation plus any particular solution of the inhomogeneous equation and (2) an inhomogeneous solution is given by summing over the Green's functions times the source function.]]

¹¹There are other, equivalent, definitions of the T -matrix, but this has relevant physical content: it allows one to obtain exact quantities by using the T -matrix acting on the unperturbed wavefunction.

with Ω the volume of space. For a contact interaction, $V(\mathbf{k}) = g$, and thus Eq. (2.28) becomes

$$T(\mathbf{k}, \mathbf{k}', E) = g + \frac{g}{\Omega} \sum_{\mathbf{k}''} (E - k''^2/m + i\delta)^{-1} T(\mathbf{k}, \mathbf{k}', E). \quad (2.29)$$

One may verify that the solution to this equation is

$$T(\mathbf{k}, \mathbf{k}', E) = \frac{g}{1 - (g/\Omega) \sum_{\mathbf{k}''} (k''^2/m + i\delta)^{-1}}. \quad (2.30)$$

Appendix A shows that $a = \frac{mT(0,0,0)}{4\pi}$ so Eq. (2.30) gives

$$a = \frac{m}{4\pi} \frac{g}{1 - (g/\Omega) \sum_{\mathbf{k}''} (k''^2/m + i\delta)^{-1}}. \quad (2.31)$$

For a given physically measured a and cutoff Λ , this tells us which g we should use in the Hamiltonian.

Note that the relationship between the scattering length a and g depends on cutoff Λ , even in the limit with $\Lambda \rightarrow \infty$. Moreover, the equation indicates $g(\Lambda)$ diverges for large Λ (for example, expanding in g , the $O(g^2)$ term diverges). This however is no problem: g is an unmeasurable quantity (independently of the cutoff Λ), and in any physical quantity, Λ and g will drop out so that only a appears in the final expressions (this is a statement of the renormalizability of our theory). Consequently, as we will see later, if we are interested in capturing dilute limit physics, we can do first order perturbation theory or mean field theory, use $g(\Lambda = 0) = 4\pi\hbar^2 a/m$ in place of the bare g and get the *exact* answer in this limit.

Tuning the interactions in cold atoms systems. To explore many-body physics in cold atoms, one needs to move away from the dilute limit where the interaction energy dominates over the kinetic energy. In cold atoms, there are two main experimental techniques to reach the strongly interacting regime: (1) In the first method, one boosts the interaction energy using a Feshbach resonance. With this technique, one can tune the scattering length from $a = -\infty$ to $a = +\infty$. In this

technique, experimentalists use an external magnetic field to move a closed channel bound state near resonance with the open scattering channel, and the scattering length diverges at the resonance [48]. (2) In the second method, one diminishes the kinetic energy by placing the particles in an optical lattice, in which case tunneling is required to move between lattice sites, and the kinetic energy may be suppressed essentially to zero by increasing the lattice depth. Chapter 2.2.3 introduces this technique.

A final avenue of manipulating interactions is to use atoms with long range interactions¹² that are indescribable with a contact interaction. In experiments, this may be accomplished using ground state ultracold molecules [67], Rydberg atoms, or, on a very weak energy scale, using the magnetic dipole moment of atoms [56]. These interactions go as $1/r^3$ at long distances, and are being intensively studied right now. This is due at least partially to their ability to stabilize intermediately ordered liquids (quantum nematics) [56].

¹²The definition of “long ranged” is dependent on context: whether a given potential counts as long ranged depends on the physics one is interested in. For example, specifying to three dimensions, there are at least two senses in which a $1/r^3$ potential is long ranged: (1) in the thermodynamic limit, the interaction energy grows faster than extensively for a uniform system and (2) it is indescribable by a contact interaction at low energies (note it is the *fastest* decaying interaction indescribable by a contact interaction at low energies, since all $1/r^\alpha$ with $\alpha > 3$ may be described as contact interactions at low energies). However, it is *not* long ranged in the sense that it decays faster than the $1/(\text{length})^2$ characteristic of kinetic energy. Consequently, the high (low) density limit is still strongly (weakly) interacting, in contrast to say the Coulombic interaction, where this is switched (e.g., one forms a Wigner crystal at low density and a Fermi liquid at high density). A final subtlety is that although some other interactions decay slower, for example the Coulomb interaction, they can still have extensive interaction energy in the thermodynamic limit because they are compensated systems: positive and negative charges screen each other at long distance.

2.2.2 Weak interactions: Mean field theory and fluctuations

Section 2.1.1 discussed the Bose-Einstein condensation of the non-interacting Bose gas. Here I discuss how weak interactions alter this picture. In particular, I will consider the effect of the interaction on the ground state energy and on the ground state's structure. The Hamiltonian describing the dilute Bose gas is

$$H = \int d\mathbf{r} \left[-\psi^\dagger(\mathbf{r}) \frac{\nabla^2}{2m} \psi^\dagger(\mathbf{r}) \right] + \frac{g}{2} \int d\mathbf{r} \psi^\dagger(\mathbf{r}) \psi^\dagger(\mathbf{r}) \psi(\mathbf{r}) \psi(\mathbf{r}), \quad (2.32)$$

with an implicit momentum cutoff and the contact interaction g appropriately renormalized, as discussed in Section 2.2.1. In Fourier space, this is

$$H = \sum_{\mathbf{k}} \frac{k^2}{2m} b_{\mathbf{k}}^\dagger b_{\mathbf{k}} + \frac{g}{2V} \sum_{\mathbf{k}, \mathbf{k}', \mathbf{q}} b_{\mathbf{k}+\mathbf{q}}^\dagger b_{\mathbf{k}'-\mathbf{q}}^\dagger b_{\mathbf{k}'} b_{\mathbf{k}}. \quad (2.33)$$

Since we are interested in weak interactions, we perturb in g . We know the ground state $|N\rangle$ is that of N particles in the $k = 0$ ground state: $|N\rangle = \mathcal{N}(\psi_k^\dagger)^N |\text{vac}\rangle$ for some normalization factor \mathcal{N} with $|\text{vac}\rangle$ the vacuum state. The first order correction to the ground state energy is then read off from Eq. (2.33) to be

$$\langle N|H|N\rangle = \frac{gN(N-1)}{2V} \quad (2.34)$$

In the thermodynamic limit, this is

$$\langle E\rangle = N \frac{gn}{2}, \quad (2.35)$$

with $n \equiv N/V$. which gives the energy shift due to weak interactions.

Section 2.2.1 showed that g was a function of the cutoff used. However, we never specified a cutoff, and our naive perturbative calculation yields an energy

$g(\Lambda)n/2$ as the energy density, independent of Λ . Since g depends on Λ , this looks like a problem: our answer depends on the cutoff. Deciding on the proper Λ requires a little work.

First, I give an intuitive picture of why we should take $g(\Lambda = 0)$, then describe a more formal route (for more discussion, see Refs. [74] and [48]). Intuitively, we want to use zero cutoff, so that already at the first order level, we have included the effects of all two-body scattering. More formally, we keep a finite cutoff in the calculation, and expand perturbatively in g . The cutoff dependence drops out and we are led to the same conclusion: we should use the g corresponding to zero cutoff ¹³.

This perturbative result is also obtained by treating the interaction with mean field theory, and assuming that the system macroscopically occupies some mode. Such a picture also allows one to treat the spatially varying case, in which case the mean field picture leads to a nonlinear eigenvalue equation — the *Gross-Pitaevskii equation*,

$$E\psi(\mathbf{r}) = \psi^*(\mathbf{r}) \left(-\frac{1}{2m}\nabla^2 + V(\mathbf{r}) \right) \psi(\mathbf{r}) + g|\psi(\mathbf{r})|^2\psi(\mathbf{r}), \quad (2.36)$$

where $\psi(\mathbf{r})$ is the condensate wavefunction and $V(\mathbf{r})$ is a possible external potential.

In addition to the energy, it is also instructive to consider the interactions' effect on the ground state itself. One consequence is a depletion of the condensate. At zero temperature all of the particles were in the ground state wavefunction, the $\mathbf{k} = 0$ wavefunction for homogeneous systems. Interactions cause some fraction of these atoms to scatter into higher momenta states. The lowest order depletion is calculated by replacing the zero momentum field operator with a c-number: $b_{\mathbf{k}=0} \approx N_0$ for some number N_0 (not necessarily the total particle number), and expanding the Hamiltonian to second order in the $b_{\mathbf{k}}$ for $\mathbf{k} \neq 0$. In this “Boguliobov

¹³If we tried the same trick expanding perturbatively in g_0 , the second order correction would diverge.

approximation,” one finds [48]

$$\frac{N - N_0}{N} = \frac{8}{3\sqrt{\pi}} (na^3)^{1/2} \quad (2.37)$$

and we see that the condensate fraction, $\langle b_{\mathbf{k}=0}^\dagger b_{\mathbf{k}=0} \rangle / \sum_{\mathbf{k}} \langle b_{\mathbf{k}}^\dagger b_{\mathbf{k}} \rangle = N_0/N$, is less than unity.

Thus, increasing interaction strength depletes the condensate. It is natural to ask if it is possible to completely deplete the condensate, and if so what happens. The following section discusses this question for interactions in a deep lattice.

2.2.3 Bosons in an optical lattice and the Bose-Hubbard model

I will argue that bosonic atoms in the sinusoidal optical lattice potential given by Equation (2.16) are frequently well-described by the Bose-Hubbard model [76], whose Hamiltonian is

$$H = -t \sum_{\langle i,j \rangle} b_i^\dagger b_j + \frac{U}{2} \sum_i b_i^\dagger b_i^\dagger b_i b_i \quad (2.38)$$

where the $\sum_{\langle i,j \rangle}$ runs over nearest neighbor pairs i, j , and b_i and b_i^\dagger are bosonic annihilation and creation operators, satisfying $[b_i, b_j] = 0$ and $[b_i, b_j^\dagger] = \delta_{ij}$. The Bose-Hubbard model is a canonical model of solid state physics introduced in the context of granular superconductors, and give the conditions under which this is accurate. This argument was first given by Jaksch *et al.* in 1998 [77]. Although the Bose-Hubbard model is arguably the simplest lattice model showing phase transitions¹⁴, the physics is quite rich and there are even quite large open questions in the quantum critical regime (see **Chapter 13**). A basic introduction is given in Section 2.2.4 and more is discussed throughout the thesis.

¹⁴Beyond the fairly trivial transitions from finite density to the vacuum that occur even in non-interacting continuum systems.

The same concept — that ultracold atoms in optical lattices emulate important models of solid state physics — are being used to realize the Fermi-Hubbard model ¹⁵, a central model in strongly correlated electron systems and which contains much of the physics of the high temperature superconducting compounds, in these systems. The community is exploring many other possibilities, as discussed in the introduction, and the prospects are exciting.

A simple physical picture to understand the applicability of the Bose-Hubbard model comes from thinking about deep lattices, where sites decouple. In this limit, each site may be solved individually, and one obtains a tightly localized spatial wavefunction at each site. In the absence of interactions, we obtain a series of discrete energy levels, roughly harmonic oscillator like. For weak interactions, adding particles to the site just multiply occupies the lowest energy on-site eigenstate, and this determines an on-site interaction energy. The most important perturbation from this limit is the ability for particles to tunnel to neighboring sites, and this is captured by the tunneling term in the Hamiltonian.

To capture this idea more precisely and formally, one constructs a set of Wannier functions [78]. One can define the Wannier functions $w(\mathbf{r})$ by

$$w_\alpha(\mathbf{r}) \equiv \frac{1}{\sqrt{N}} \sum_{\mathbf{k} \in \text{BZ}} \phi_{\alpha, \mathbf{k}}(\mathbf{r}) \quad (2.39)$$

where $\phi_{\alpha, \mathbf{k}}$ is the quasi-momentum \mathbf{k} Bloch function ¹⁶ for the α 'th band and the sum runs over first Brillouin zone, N is the total number of lattice sites, and the sum runs over first Brillouin zone. Using the properties of the Bloch functions, one can show that they may be written in terms of the Wannier function as

$$\phi_{\alpha, \mathbf{k}}(\mathbf{r}) = \frac{1}{\sqrt{N}} \sum_{\mathbf{R}} e^{i\mathbf{k} \cdot \mathbf{R}} w_\alpha(\mathbf{r} - \mathbf{R}) \quad (2.40)$$

¹⁵Just called “The Hubbard model” in virtually all other areas of physics.

¹⁶Bloch functions are just the eigenstates of a non-interacting periodic system. Symmetry dictates that they are periodic under translations by lattice vectors \mathbf{R} up to a phase, from which the rest of the properties follow.

where the sum runs over all lattice vectors \mathbf{R} . Thus we see that the Wannier states $w_\alpha(\mathbf{r} - \mathbf{R})$ for all lattice vectors \mathbf{R} form a complete basis for the α 'th band. We can thus write our lattice Hamiltonian in the basis of Wannier functions and we are justified in describing the system using only the lowest band Wannier functions when the band gap to the first excited band is sufficiently large that few excitations to this band are relevant — we will examine the condition under which this applies below. We associate the creation and annihilation operators with the Wannier states as

$$c_j = \int d\mathbf{r} w(\mathbf{r} - \mathbf{R}_j) \psi(\mathbf{r}) \quad (2.41)$$

with $\psi(\mathbf{r})$ the annihilation operator at a position \mathbf{r} . Because the Wannier functions turn out to be short ranged under quite general conditions — certainly for deep lattices — and this justifies keeping only the short ranged terms in the resulting Hamiltonian for the lowest band Wannier functions, yielding the Bose-Hubbard Hamiltonian with parameters [77]

$$\begin{aligned} t &= \int d\mathbf{r} w^*(\mathbf{r}) \left[\frac{-\hbar^2}{2m} \nabla^2 + \sum_{\alpha=x,y,z} V_\alpha \sin(\mathbf{k}_\alpha \cdot \mathbf{r}) \right] w(\mathbf{r}) \\ U &= \frac{4\pi\hbar^2 a}{m} \int d\mathbf{r} |w(\mathbf{r})|^4. \end{aligned} \quad (2.42)$$

The first requirements for the Bose-Hubbard description to be valid — that the band gap is large compared to interactions (and temperature) — requires that the interaction energy density, $\propto a\rho^1/3$, with ρ the maximum three dimensional density, is small compared to the kinetic energy density $\propto \rho^{2/3}$, or $a\rho^{-1/3} \ll 1$. For deep lattices, particles are put in the lowest harmonic oscillator state associated with oscillations of frequency Ω around the potential minimum at each site, and the density is thus n/ℓ^3 where $\ell = \sqrt{\hbar/(m\Omega)}$ is the harmonic oscillator length and n is the site occupation. Then the requirement that the interaction effects are describable with a single band is that $a \ll \ell$. The criterion that Wannier

functions are short range requires that $\ell \ll d$, where d is the lattice spacing. So, to summarize, the Bose-Hubbard description is valid for

$$a \ll \ell \ll d. \tag{2.43}$$

For typical numbers, $a = 5\text{nm}$ for ^{87}Rb and $d = 500\text{nm}$, so that we can find lattice depths satisfying these criteria.

2.2.4 Gutzwiller mean field

In this section, I will discuss the qualitative physics of the Bose-Hubbard model, Eq. (2.38). Here and in Section 2.2.5 I will also introduce some theoretical approaches to describing the many-body physics of this system and discuss how the required formalism is somewhat different than that introduced in typical many-body (e.g., diagrammatic) formalisms.

To obtain a global picture of the system's behavior, I will first consider two limits: very weak and very deep lattices. Note that there are only two energy scales in the Hamiltonian, t and U , and thus up to an overall scale, the physics depends only on the ratio t/U . The weak and deep lattice limits correspond to $t/U = \infty$ and $t/U = 0$ respectively. In the weak limit, interactions play no role. As long as the temperature is much less than the bandwidth ($\sim t$) the system occupies only low momentum states, and the dispersion may be approximated as quadratic. Then the physics reduces to the superfluidity of nearly free particles. In the deep lattice limit limit, the absence of tunneling implies that can treat sites independently, and the eigenstates are Fock states with fixed particle occupation n at each site. For small t/U , if the average occupation is an integer, then there is a large energy cost ($\sim U$) to moving a particle from one lattice site to another, which the kinetic energy cannot overcome: the system is a Mott insulator. In between

there is a phase transition. The phase diagram and physics of the phases at zero and finite temperature are explored throughout the rest of the thesis.

A typical approach to the many-body problem is to try to use perturbation theory from either the weak or strong coupling limits, where the behavior is known. However, perturbing from one limit is guaranteed to fail to describe the other phase because the perturbation theory guarantees analytic behavior in the expansion parameter, while the phase transition is signified by non-analyticities of observables¹⁷. However, there is a simple mean field theory capable of qualitatively capturing both limits. This “Gutzwiller mean field theory” [77, 76] is described in this section. Although it is simple, its formal structure is quite different than traditional mean field theories, such as Hartree-Fock, BCS, etc., and going beyond the mean field theory is non-trivial, discussed in Section 2.2.5. Although sophisticated numerical algorithms such as the worm algorithm [79] can obtain high accuracy numerical results for static behavior, no method exists to quantitatively calculate dynamics across the full phase diagram (especially in the quantum critical regime).

There are several ways to formulate the Gutzwiller mean field method given here, as with other mean fields methods. One may approximate some operator in the Hamiltonian by its average value (mean field approach), construct a variational wavefunction, resum some infinite set of diagrams, or make some approximation to the path integral. Here, I will give very the variational formulation, and then briefly interpret it as a mean field. **Chapters 13, 14, and 15** introduce and make use of the path integral formulation.

The variational ansatz is to take each site to be uncorrelated with the other sites. That is, the variational wavefunction $|\Psi\rangle$ is a tensor product over all lattice

¹⁷An exciting alternative perspective to understand both regimes is to do perturbation theory around the phase transition point, and this (much more difficult) perturbation theory is essentially the basis of describing quantum critical systems.

sites of wavefunctions on each site:

$$|\Psi\rangle = \otimes_i \left(\sum_{n=0}^{\infty} f_{n,i} |n\rangle_i \right) \quad (2.44)$$

where $|n\rangle_i$ is the number eigenstate for site i with occupation n . We will deal with translationally invariant system and assume that translational invariance is not spontaneously broken, so that $f_{n,i}$ is independent of the site index i . Minimizing the Bose-Hubbard model, Eq. (2.38)'s, energy expectation value in this state gives equations for the f_n 's:

$$\epsilon f_n = -tz \left(\sqrt{n} \alpha^* f_{n-1} + \sqrt{n+1} \alpha f_{n+1} \right) + \left(\frac{U}{2} n(n-1) - \mu n \right) f_n \quad (2.45)$$

with ϵ the eigenvalue of this problem, z the lattice coordination number, and

$$\alpha = \sum_n \sqrt{n} f_n^* f_{n-1}. \quad (2.46)$$

These are coupled non-linear equations in a few variables. To solve them, we take a guess for α , solve the first equation for the f_n 's by truncating to a reasonable number of occupations. Even deep in the superfluid, the number of states kept need only be $\sim \sqrt{\langle n \rangle}$ where, and for the low filling states usually of interest, with $\langle n \rangle \lesssim 3$, truncating to occupations $n = 0, 1, 2, 3, 4, 5$ is generally sufficient to get many decimal places of accuracy. Next, we determine a new α from the second equation. We then repeat this procedure until it converges. Even keeping a large range of occupations, this can be done virtually instantaneously with any modern computer. In the limit where one has small t/U , one can generically truncate to two occupations, $|n\rangle$ and $|n+1\rangle$, and solve the equations analytically. Note that these equations are identical to those obtained for the eigenvalue problem obtained by approximating the Hamiltonian Eq. (2.38) by writing $\sum_{\langle i,j \rangle} a_i^\dagger a_j \approx z \langle a_j \rangle \sum_i a_i^\dagger$.

The main feature of the solutions to these equations are that they capture the Mott insulator to superfluid phase transition. The system displays a non-analytic

behavior, and thus a phase transition: below a critical t/U for any given μ , the solutions are just the number eigenstates: $f_n = \delta_{nm}$ for some m . For larger t/U , small number fluctuations start upon increasing t/U (entering the superfluid) and get larger as one goes deeper into the superfluid (larger t/U).

The Gutzwiller approximation is exact when $t = 0$ — it can represent number eigenstates. It is also exact in infinite dimension¹⁸, since in this case one site feels the influence of infinitely many neighbors, and any fluctuations of the mean field average out. Remarkably, it is also exact deep in the superfluid (in the non-interacting limit): if one takes the f_n 's to describe coherent states at each site, and project the resulting Gutzwiller wavefunction onto a state of fixed *total* particle number N , one obtains exactly the non-interacting ground state, with N particles in the $k = 0$ single particle ground state. The fact that the ansatz exactly captures both limits' behavior is remarkable, but it is worth noting that it captures physics away from these limits only qualitatively — even for arbitrarily small deviations from the limits. Numerically, it has been confirmed to give qualitatively quite accurate phase diagrams in $d = 1, 2, 3$. For example, the unity site filling Mott insulator/superfluid transition on a three-dimensional cubic lattice occurs at $(t/U)_c = 0.03408(2)$ while GMFT yields $(t/U)_c = 0.029$ [1].

2.2.5 Fluctuations in strong lattice potentials: beyond Gutzwiller

The Gutzwiller approximation captures on-site number fluctuations and infinite range condensate order, but fails to capture intermediate range correlations. Thus,

¹⁸Although this holds in classical mechanics, the issue in quantum mechanics is somewhat trickier. Thinking of a path integral description, one needs to worry about the time dimension. The proper description of the infinite spatial dimension (but still one real or imaginary time dimension) requires *dynamical mean field theory*, which for bosonic systems is presented in Ref. [80].

although it is exact in the deep Mott limit and superfluid limit, it fails to capture even infinitesimal deviations from these limits exactly. For example, in the dilute superfluid limit the Gutzwiller approximation captures the condensate depletion only approximately, failing to quantitatively reproduce the Bogoliubov result above.

There are several approaches to incorporating intermediate range fluctuations around the Gutzwiller ansatz. One is to abandon Gutzwiller in favor of a strong coupling perturbation theory in t/U . Remarkably, when resummed with a Padé determinant — approximating the observables as

$$f(\tilde{t}) = \frac{\sum_{i=0}^{i_{\max}} \tilde{t}^i}{\sum_{j=0}^{j_{\max}} \tilde{t}^j}, \quad (2.47)$$

with the definition $\tilde{t} \equiv t/U$, and truncating sums in both the numerator (i_{\max}) and denominator (j_{\max}) beyond lowest order. Then low order perturbation theory can reproduce numerically exact quantum Monte Carlo simulations for systems not too deep in the superfluid [81, 82].

A more global approach is to include fluctuations around the Gutzwiller approximation. This is an appealing approach because it can extend the strength of the Gutzwiller approach — its exactness in both the small and large t/U and high dimensions — so that it captures the intermediate range correlations and momentum space structure of the dispersion. However, it is a technically difficult calculation. The broad idea is that the Gutzwiller ansatz forms the vacuum around which one wants to include fluctuations, and this vacuum’s structure is non-trivial. Specifically, fields operators in this state do *not* satisfy Wick’s theorem; in contrast to equilibrium states of quadratic Hamiltonians, the more complicated structure of the Gutzwiller ansatz prevents Wick’s theorem from applying.

Although the ansatz provides some simplifications of its own — for example, expectations of products of operators factor if the operators are on different sites

— this non-triviality means that the standard techniques of many body theory fail, since these all rely on the applicability of Wick’s theorem to the vacuum ¹⁹. For similar reasons, even linear response dynamics are non-trivial, and Chapter 5 gives an approximate solution to one linear response problem — radio-frequency spectroscopy.

2.2.6 Extracting information about homogeneous systems from trapped systems

In condensed matter physics we usually wish to understand macroscopically homogeneous samples. Cold atomic systems are invariably trapped, and are at most hundreds of lattice sites across in this varying potential. Here I discuss the conditions under which it is possible to extract information about a homogeneous system from a cold atoms system, and how one may do this.

In the limit where the potential varies infinitely slowly, it is clear that we can break the system up into macroscopic regions, in each of which the potential varies sufficiently little to be treated as homogeneous. Thus, measurements in each region give properties of the appropriate homogeneous system. We can write absorb the spatially varying potential $V(\mathbf{r})$ into the free energy to define a spatially varying chemical potential $\mu(\mathbf{r}) \equiv \mu_c - V(\mathbf{r})$. Then in the limit where the trap varies sufficiently slowly, the system at point \mathbf{r} must share all the local properties of that of a homogeneous with chemical potential $\mu(\mathbf{r})$. This approximation is called the Thomas-Fermi or local density approximation (LDA) ²⁰, and was originally

¹⁹Even symmetry breaking causes some difficulties, since the vacuum is altered, but these can generally be alleviated by perturbing around the quadratic theory applicable near the new symmetry broken solution.

²⁰Not to be confused with the much more sophisticated local density approximation used in the electronic structure community. Only the *corrections* to the non-interacting quantum mechanics problem are treated with a local approximation there.

introduced to approximate the properties of atoms by treating the electrons around nuclei in this manner.

Define

$$L \equiv \mu(r)/\mu'(r), \quad (2.48)$$

which is a measure of the characteristic length scale on which the chemical potential varies by an amount comparable to its value ²¹ If the effective chemical potential varies negligibly over a correlation length, then different regions with this small chemical potential difference are independent when separated by scales much more than that. That is, the Thomas-Fermi approximation is valid if

$$\xi \ll L \quad (2.49)$$

where ξ is the longest correlation length of the system. In typical systems, $L \sim 10$ - 20 , and can be made larger in some regions by engineering the shape of $V(r)$. Deep in phases of matter (far from transitions), ξ is typically a few lattice spacings. When ξ is much larger than the lattice spacing, as happens near critical points, universal behavior manifests. This phenomena has the largest correlation lengths of interest ²², and since one can explore ξ up to $\sim L$, there is even a window into even this regime. To summarize, we expect that we can obtain rather accurate information of homogenous system over whole phase diagram, even where the physics has reached its long wavelength critical behavior.

From another vantage point, we can ask how obtaining information about systems that are only homogeneous on scales $\sim L$ compares with numerically calculating the properties on a computer. Although L may seem small, recall that even

²¹For many cases of interest, the value of the chemical potential is also on the order of all the interesting scales in the problem, e.g. the tunneling rate t and interaction energy U . Other circumstances may be treated analogously.

²² Once one understands the physics of this regime, one can extrapolate to infinitely large ξ to obtain a complete picture of behavior throughout a system's phase diagram.

for the simplest systems, e.g., simple spin-1/2 lattice models, our arguments in the introduction indicated that calculating general properties of a $10 \times 10 \times 10$ system, even with sophisticated numerical algorithms, supercomputers, and years of patience, is impossible. Thus, measurements of trapped systems can give otherwise intractable information about a homogeneous system's behaviors.

There is (at least) one important caveat to this conclusion, however. In systems with spontaneously formed inhomogeneities (such as charge density waves or vortex lattices), there is an ordering length scale which may be much larger than the lattice spacing. Even if this order is fluctuating — that is, has no long range, as may happen when multiple phases compete, one needs to worry about this. In this case, the Thomas-Fermi approximation is inapplicable under typical trapping conditions.

Chapter 3

Radio-frequency spectroscopy: background and motivation

3.1 Motivation and background

Radio-frequency (RF) spectroscopy has emerged as a powerful probe of cold atoms. It provided the first evidence of BEC in dilute hydrogen gases [83], probed the pair structure and breaking across the BEC/BCS crossover [84], and was used to study the quantum phase transition between Mott and superfluid states of lattice boson [85].

Generally speaking, spectra are useful because they probe excitation structure, which is hidden in density profiles and time-of-flight measurements common in cold atoms. That is, they tell happens when particles and energy are added to or removed from a system in various manners. This is moreover connected to the correlations present in the initial state.

In cold atoms, RF spectra are particularly feasible, compared to other spectroscopic probes, since in a typical cold atoms setup, the only extra necessary equipment is an RF coil, and this often is already present, for evaporative cooling or other purposes. In RF spectroscopy, an RF photon is absorbed to alter the internal state of an atom. Usually, this is a transition between the atom's hyperfine energy levels. In practice, experimentalists may utilize other transitions such as microwave or optical transitions, but I will refer to these as “RF spectra” as long as the recoil momentum is negligible ¹.

As argued above, RF spectra are relatively experimentally feasible and provide

¹This can be accomplished by using two counter-propagating lasers to drive an optical transition, for example. Because this eliminates momentum recoil, there is no Doppler broadening of the line and is referred to as Doppler-free spectroscopy.

significant information about correlations and excitations. Also, because of their low momentum transfer, they can be used to probe spectral lines in a momentum-insensitive, “Doppler free” manner. However, the flip side of this is that measuring momentum dependence of excitations is impossible. For this reason, the probe is less powerful than Bragg or Raman spectroscopy, although these are significantly more difficult experimentally. It is worth pointing out that if one can do momentum resolved Bragg spectra, then one can just as easily do Raman spectroscopy, for which RF spectroscopy is the zero-momentum limit. Thus RF spectra also offer a first step to understanding these spectra. An alternative to obtain momentum resolution using rf spectra is to do time-of-flight imaging after applying the RF pulse. Debbie Jin’s group has demonstrated this on strongly interacting Fermi gases in the BEC/BCS crossover [54], but any significant spatial resolution is impossible to achieve in this context.

3.2 Two differing pictures of RF spectroscopy

RF spectra probe cold atoms’ correlations and excitation structure. However, two pictures, both commonly used in the literature, suggest very different results for how these correlations and excitations manifest themselves. The first picture is based on sum rules, while the second is based on the single particle Green’s function.

Sum rule picture.—In a standard application of sum rules to understand spectra, one usually derives an expression for the average spectral line shift $\langle\delta\omega\rangle$ due to interactions with other atoms, and then assumes the spectrum is a single δ -function line with the associated spectral location. This gives an accurate assessment of many situations such as dilute gases [86] and density inhomogeneity-limited accuracy of atomic clocks [87, 88]. Chapter 4 fleshes out this picture in relation to

experiments at MIT for lattice bosons near the Mott insulator/superfluid quantum phase transition.

Single particle Green's functions.—Another common approach to calculate RF spectra is to relate them to single particle spectra. In the limit where there are no final state interactions — that is, the final internal state of the atom does not interact with atoms in the initial internal state — the RF spectrum is a convolution of the zero-momentum part of the hole single particle Green's function (and in special cases is simply the the single particle Green's function). This leads to quite a different picture for the RF spectra in the superfluid: inserting a hole into the system can excite phonons, but can also excite gapped amplitude modes.

Remarkably, Chapter 5 demonstrates that each of these pictures emerges in separate limits of a more complete calculation. We give a simple physical picture of this, and believe that the basic point will persist to other many-body systems.

After this, Chapter 6 considers the finite temperature spectra in the deep Mott and superfluid phases. The finite temperature quantum critical region is discussed later, in Chapter 15.

Chapter 4

RF spectra: a sum rule approach to trapped bosons in an optical lattice

*This chapter was adapted from “Hyperfine spectra of trapped bosons in optical lattices” by Kaden R. A. Hazzard and Erich J. Mueller, published in Physical Review A **76**, 063612 (2007).*

4.1 Abstract

We calculate the interaction induced inhomogeneous broadening of spectral lines in a trapped Bose gas as a function of the depth of a three-dimensional cubic optical lattice. As observed in recent experiments, we find that the terraced “wedding-cake” structure of Mott plateaus splits the spectrum into a series of discrete peaks. The spectra are extremely sensitive to density corrugations and trap anharmonicities. For example, even when the majority of the cloud is superfluid the spectrum displays discrete peaks.

4.2 Introduction

The study of quantum degenerate atoms confined to periodic potentials forms an important subfield of modern atomic physics. Research in this area is driven by its connection to condensed matter physics and quantum information processing [89, 90]. A rich set of probes, including optical spectroscopy, noise spectroscopy, interference, and density profile measurements [91, 92, 93, 94, 33, 85], have been used to characterize these systems, with a focus on understanding the interaction driven superfluid-insulator transition. Here we analyze in detail what information

one gains from inhomogeneous pressure shifts of spectral lines in a gas of bosons confined to an optical lattice.

Atomic interactions lead to pressure and density dependent shifts of atomic lines. These “clock shifts” limit the accuracy of atomic clocks. In an inhomogeneous system they are spatially dependent, yielding a broadened spectrum whose structure reveals details about the local atomic correlations. In many situations the clock shift is proportional to the atomic density, and the spectral line directly gives a histogram of the atomic density. As an example of this technique, Bose-Einstein condensation in spin polarized atomic hydrogen was detected through the line shape of a two-photon 1s-2s transition [83]. More recently, Campbell *et al.* [85] utilized atomic clock shifts to experimentally probe bosons trapped in an optical lattice, finding evidence for Mott insulating shells. Motivated by these latter experiments, we present a theoretical analysis of the lineshapes which should be found when bosonic atoms in a periodic potential are confined by a nominally harmonic potential.

In Sec. 4.3 we use a local density approximation to calculate the spectrum of a harmonically trapped gas as a function of the depth of an optical lattice (Fig. 4.1). In the deep lattice limit, the spectral line splits into several distinct peaks, associated with the formation of density plateaus. Due to the sensitivity of these spectra to small density corrugations, this splitting occurs even when large sections of the cloud are superfluid. Despite qualitative agreement with experiments, our calculation severely underestimates the small detuning spectral weight. In Sec. 4.4 we show that these discrepancies are consistent with trap anharmonicities. We also explore other mechanisms for enhancing the low detuning spectral weight.

Experimental Details. Since we are largely concerned with the experiment

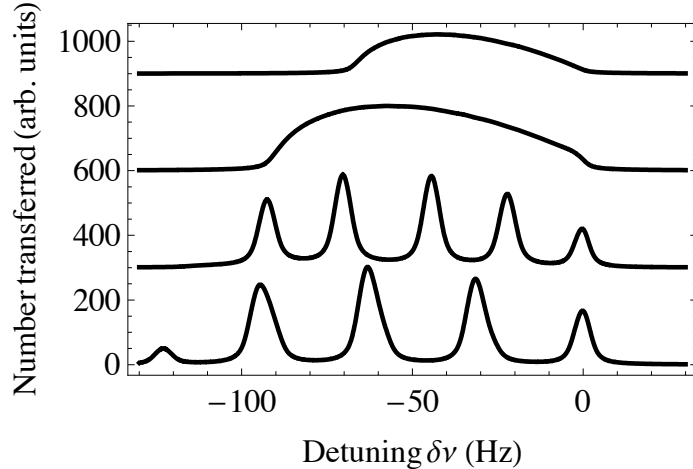


Figure 4.1: Theoretical spectra showing the number of ^{87}Rb atoms transferred from hyperfine state $|a\rangle = |F = 1, m_F = -1\rangle$ to state $|b\rangle = |F = 2, m_F = 1\rangle$ when excited by light detuned from resonance by the frequency $\delta\nu$. The $N = 9 \times 10^4$ atoms are confined by a harmonic potential with $\bar{\omega} = (\omega_x\omega_y\omega_z)^{1/3} = 2\pi \times 100\text{Hz}$ and a three-dimensional periodic potential with lattice depth $V_0 = 5, 10, 25, 35E_{\text{rec}}$ (from top to bottom).

in Ref. [85], we give a brief review of the important experimental details. In these experiments, a gas of ^{87}Rb atoms in the $|a\rangle = |F = 1, m_F = -1\rangle$ hyperfine state (F the total spin and m_F its z component) was cooled well below the condensation temperature [95]. By combining optical and magnetic fields, a three-dimensional periodic potential $V_{\text{per}} = -V_0 [\cos(2\pi x/d) + \cos(2\pi y/d) + \cos(2\pi z/d)]$ was superimposed on a trapping potential. The spacing between lattice sites, $d = \lambda/2 = 532\text{nm}$, is half of the lattice lasers' wavelength. The lattice depth V_0 was tuned from zero to $40E_{\text{rec}}$ where $E_{\text{rec}} = \frac{\hbar^2}{2m} \left(\frac{2\pi}{\lambda}\right)^2$ is the photon recoil energy. A microwave and RF field were tuned near resonance for a two photon transition from the $|a\rangle$ state to an excited hyperfine state $|b\rangle = |F = 2, m_F = 1\rangle$ [96]. The number of atoms transferred during a fixed time interval was studied as a function of the RF frequency.

4.3 Spectrum of harmonically trapped gas

4.3.1 Hamiltonian and approximations

Hamiltonian. Bosons in a sufficiently deep optical lattice are described by the Bose-Hubbard model [77], found by projecting the full Hamiltonian onto the lowest Bloch band. We will work with a two-internal state Bose-Hubbard Hamiltonian, where a_i and b_i annihilate bosons at site i in states $|a\rangle$ and $|b\rangle$, respectively. Including an external trapping potential the Hamiltonian is

$$\begin{aligned}
 H = & -t_a \sum_{\langle i,j \rangle} a_i^\dagger a_j + \sum_i \left[\frac{U_a}{2} n_{i,a} (n_{i,a} - 1) + V_{i,a} n_{i,a} \right] \\
 & - t_b \sum_{\langle i,j \rangle} b_i^\dagger b_j + \sum_i \left[\frac{U_b}{2} n_{i,b} (n_{i,b} - 1) + V_{i,b} n_{i,b} \right] \\
 & + U_{ab} \sum_i n_{i,a} n_{i,b} + \text{H.c.}
 \end{aligned} \tag{4.1}$$

where $n_{i,\alpha} \stackrel{\text{def.}}{=} \alpha_i^\dagger \alpha_i$. The t_α 's describe hopping rates and $U_{\alpha\beta}$ the interaction where α and β label the species ($|a\rangle$ or $|b\rangle$). We abbreviate $U_\alpha = U_{\alpha\alpha}$. We have absorbed the chemical potentials and hyperfine splittings into the trapping potential, writing $V_{i,\alpha} = \mathcal{V}_{i,\alpha} + \epsilon_\alpha^{\text{HF}} - \mu_\alpha$ where $\mathcal{V}_{i,\alpha}$ is the external potential at site i for species α , and $\epsilon_b^{\text{HF}} - \epsilon_a^{\text{HF}} = \Delta_0$ is the vacuum hyperfine splitting. In terms of microscopic quantities, the Hubbard parameters are $t_\alpha = \int d\mathbf{r} w_\alpha^*(\mathbf{r}) [-\hbar^2/(2m_\alpha)\nabla^2 + V_{\text{per}}(\mathbf{r})] w_\alpha(\mathbf{r})$, $\mathcal{V}_{i,\alpha} \approx V_{\text{trap}}(\mathbf{R}_i)$, and $U_{\alpha\beta} = (4\pi\hbar^2 a_{\alpha\beta}/m) \int d\mathbf{r} |w_\alpha(\mathbf{r})|^2 |w_\beta(\mathbf{r})|^2$ where m_α is the mass and w_α the normalized Wannier function for state α , while $a_{\alpha\beta}$ denotes the α - β scattering length. For ^{87}Rb , the relevant scattering lengths are $a_{aa} = 5.32\text{nm}$ and $a_{ab} = 5.19\text{nm}$ [97]. The $|b\rangle$ atoms will be sufficiently dilute that a_{bb} will not enter our calculation. The competition between the kinetic and interaction terms drives the Mott insulator to superfluid phase transition.

In the experiments of interest, the atoms all begin in the $|a\rangle$ state, and one

measures the rate at which atoms are transferred to the $|b\rangle$ state under the influence of a weak probe of the form $H_{\text{probe}} \propto \sum_j b_j^\dagger a_j e^{-i(\omega + \mu_b - \mu_a)t} + \text{H.c.}$, within the rotating wave approximation, where ω is the frequency of the photons. [The factors of μ_b and μ_a arise from the canonical transformation which introduces the chemical potential into the Hamiltonian.] To calculate this response, it is sufficient to understand the properties of the single-component Bose-Hubbard model (the terms in Eq. (4.1) containing only a 's).

Formally the lack of $|b\rangle$ atoms in the initial state implies that $\mu_b < \epsilon(0)$ where $\epsilon(0)$ is the energy of the $k = 0$ single particle state. All (zero-temperature) observables will be independent of μ_b .

Mean-field theory. The ground state of the single component Bose-Hubbard model is well approximated by the Gutzwiller mean-field theory (GMF) of Ref [76]. This approach is exact in infinite dimensions and in the deep Mott insulator and superfluid limits. Sophisticated numerical calculations, some with a trapping potential, have shown that this mean field theory yields qualitatively accurate phase diagrams, energies, and spatial density profiles [98, 99, 100, 101, 102]. As a point of reference, Monte-Carlo calculations predict that for unity filling the 3D Bose-Hubbard model on a cubic lattice has an insulator-superfluid transition at $t/U = 0.03408(2)$, while mean field theory gives $t/U = 0.029$ [1]. We will work within this approximation. As will be apparent, one could extend our results to include fluctuation effects by numerically calculating the density and compressibility of the homogeneous system. Within the local density approximation discussed below these homogeneous quantities are the only theoretical input needed to determine the spectrum.

The Gutzwiller mean field approximation to the Bose-Hubbard model can be developed either from a mean-field or variational standpoint. As a variational

ansatz, GMF corresponds to taking the wavefunction to be a tensor product of states at each site: $|\Psi\rangle = \otimes_i \left(\sum_n f_n^{(i)} |i, n\rangle \right)$ where $|i, n\rangle$ is the state with n particles at the i 'th site; the $f_n^{(i)}$ are varied. In the corresponding mean-field language, fluctuations of the annihilation operators from their expectations are assumed not to affect neighboring sites. Then, assuming translation symmetry remains unbroken and letting q be the number of nearest neighbors, one has

$$H_{\text{MF}} = \sum_i \left[-qta_i^\dagger \langle a \rangle + U \frac{n_i^2}{2} + V_i n_i + \text{H.c.} \right] \quad (4.2)$$

from which one can find a self-consistent ground state with $\langle a \rangle = \sum_n \sqrt{n+1} f_n^* f_{n+1}$.

As a mean-field theory, this approach cannot accurately determine some of the properties of the system near the critical point at the tip of the Mott lobe. Furthermore, it treats the Mott state as inert, neglecting small, but finite, density fluctuations. Given the smallness of these fluctuations in three dimensions [103], we do not believe that they play an important role in the experiments. Furthermore, whatever role they do play will likely be obscured by the trap.

Local density approximation. We use a local density (or Thomas-Fermi) approximation (LDA) to calculate the spatial dependence of thermodynamic quantities: all physical quantities at location \mathbf{r} are taken to be those of a homogeneous system at a chemical potential $\mu - \mathcal{V}(\mathbf{r})$. This is expected to be valid when the spatial correlation length of the homogeneous system is much smaller than the length scale of the trapping potential [48]. The validity of the GMF+LDA is discussed in Ref.'s [98, 99, 100, 101, 102].

4.3.2 Homogeneous clock shifts

The clock shift is a density-dependent shift in the energy splitting Δ for driving a transition from internal atomic states $|a\rangle$ to states $|b\rangle$ due to the inter-particle

interactions. In this section we review the known results for the clock shift of a homogeneous system in terms of local correlations, and specialize to the case of atoms in a periodic potential.

We will assume that $t_a = t_b$ and $\mathcal{V}_{i,b} = \mathcal{V}_{i,a}$. These assumptions are justified in the recent experiments, where the polarizabilities of the two internal states are nearly indistinguishable. In linear response, the average clock shift energy of the homogeneous system, is then

$$\delta E_2 = (U_{ab} - U_a) \frac{\langle \sum_i a_i^\dagger a_i^\dagger a_i a_i \rangle}{\langle \sum_i a_i^\dagger a_i \rangle} \quad (4.3)$$

where the expectation is in the initial, all- $|a\rangle$ state [104, 86]. This expression can be rewritten in a somewhat more familiar form by defining the local second order correlation function $g_2 \stackrel{\text{def.}}{\equiv} \langle a_i^\dagger a_i^\dagger a_i a_i \rangle / \langle a_i^\dagger a_i \rangle^2$ so

$$\delta E_2 = (U_{ab} - U_a) g_2 \langle n \rangle. \quad (4.4)$$

Special cases of the clock-shift formula: dilute superfluid, Mott insulator, and normal fluid. For a dilute superfluid, the initial state is a coherent state, and Eq. (4.3) gives a shift proportional to the occupation of each site,

$$\delta E_{\text{SF}} = (U_{ab} - U_a) n. \quad (4.5)$$

Deep within the Mott insulating phase, the initial state is a number eigenstate and

$$\delta E_{\text{MI}} = (U_{ab} - U_a)(n - 1).$$

This latter formula has an intuitive explanation. In a Mott insulator with filling of one particle per site, the atoms are isolated so there is no interaction between particles. Hence δE_{MI} must vanish when $n = 1$. Fig. 4.2 illustrates how the clock shift energy evolves from being proportional to n to $n - 1$ by juxtaposing the contours of fixed δE_2 and those of fixed density.

If one raises the temperature the system becomes a normal fluid, even at weak interactions. In the absence of interactions, the normal fluid statistical factor g_2 appearing in Eq. (4.4) is $g_2 = 2$, [105] so that the clock shift energy is twice as large as in the superfluid:

$$\delta E_{\text{NF}} = 2(U_{ab} - U_a)n. \quad (4.6)$$

Given that there is no phase transition between the zero temperature Mott insulator and the normal gas, it is interesting that the clock shift energy changes from $2(U_{ab} - U_a)n$ in the normal fluid to $(U_{ab} - U_a)(n - 1)$ in the Mott insulator. A quantitative understanding of this crossover would require calculating the temperature dependence of the pair correlations in the strongly interacting limit.

4.3.3 Calculation of spectrum in a trap

To calculate the spectrum we assume that the gas can be treated as locally homogeneous, and we can independently sum the spectrum from each region in the cloud. The number of atoms of atoms transferred to the $|b\rangle$ state will be

$$\begin{aligned} N_b(\omega) &\propto \int d^3r n(r) I_{\mathbf{r}}(\omega) \\ &\approx \int d^3r n(r) \delta_{1/\tau}(\Delta(\mathbf{r}) - \omega), \end{aligned} \quad (4.7)$$

where $I_{\mathbf{r}}(\omega)$ is the spectrum of a homogeneous system with chemical potential $\mu(\mathbf{r}) = \mu_0 - V_{\text{trap}}(\mathbf{r})$ appropriate to position \mathbf{r} in the trap. Averaging over the trap will wash-out all of the structure in $I_{\mathbf{r}}(\omega)$, so we make the simplifying approximation of replacing it with a broadened delta function $\delta_{1/\tau}(\omega - \Delta(\mathbf{r}))$, where the peak location, $\Delta(\mathbf{r})$, is given by the mean clock-shift of a homogeneous system with chemical potential $\mu(\mathbf{r}) = \mu_0 - V_{\text{trap}}(\mathbf{r})$. We will model $\delta_{\gamma}(\nu) = (1/\pi)\gamma/(\nu^2 + \gamma^2)$ as a Lorentzian of width γ , and use $\tau = 1/\gamma = 100\text{ms}$, corresponding to the finite probe duration in the experiments.

Note that the replacement of $I_{\mathbf{r}}(\omega)$ by $\delta_{1/\tau}(\omega - \Delta(\mathbf{r}))$ is a severe approximation. The homogeneous spectrum can have important structure, even displaying bimodality in a narrow parameter range. However, inhomogeneous broadening obscures this structure, and we believe that one can adequately model the experiment via Eq. (4.7).

We calculate the integral in Eq. (4.7) within the Gutzwiller mean field approximation to the Bose-Hubbard model. As illustrated in Fig. 4.2, both the density n and the clock shift Δ can be expressed as functions of the parameters μ/U and t/U . Within the local density approximation, t is constant throughout the trap, and μ varies in space, taking its maximal value μ_0 at the center of the trap.

For extreme values of t/U (either large or small) we can analytically calculate the contours in Fig. 4.2(a). Generically, however we must rely on numerical methods.

Our results are shown in Fig. 4.1 for a harmonic trap $V_{\text{trap}}(\mathbf{r}) = m\omega_x^2 x^2/2 + m\omega_y^2 y^2/2 + m\omega_z^2 z^2/2$. One sees that in the deep Mott limit, the spectrum displays sharp peaks, while in the deep superfluid limit, the lineshape is smooth. The peaks are due to the stepwise variation of $\Delta(\mu)$ (illustrated in Fig. 4.2(a)) which lead to large regions of the trap where $\Delta(r)$ takes on discrete values. Compared with the experiments in Ref. [85], our spectral lines have severely reduced small detuning spectral weight. In Sec. 4.4 we show that trap anharmonicities can account for this difference.

Note that within the local density approximation, the spectrum is independent of trap anisotropies, as long as the trap is harmonic. This generic feature of the LDA is seen by examining an integral of the form $I = \int d^3r f(\mu) = \int d^3r f(\mu_0 - m\omega_x^2 x^2/2 - m\omega_y^2 y^2/2 - m\omega_z^2 z^2/2)$. Rescaling the coordinates so that $m\omega_x^2 x^2/2 = \mu_0 \bar{x}^2$ (and similarly for y and z), this integral becomes

$I = \sqrt{8\mu_0^3/m^3\omega_x^2\omega_y^2\omega_z^2}4\pi \int d\bar{r} \bar{r}^2 f(\mu_0 - \mu_0\bar{r}^2)$, where $\bar{r} = \sqrt{\bar{x}^2 + \bar{y}^2 + \bar{z}^2}$. From this analysis it is clear that apart from an overall scale factor, the spectral lineshape is only a function of the central chemical potential μ_0 .

Experimental Parameters. The experimental control parameters are the optical lattice depth V_0 , the number of particles N , and the trap frequencies ω_ν . The natural theoretical parameters are t, U , and μ_0 . To compare our results to experiment, we use a non-interacting band structure calculation to relate t and U to V_0 [77]. To relate μ_0 to experimental parameters we note that within the LDA the number of trapped atoms N is only a function of t/U , and $\mu_0/\hbar\bar{\omega}$ where $\bar{\omega}^3 = \omega_x\omega_y\omega_z$. For each value of t/U we compute $N(\mu_0/\hbar\bar{\omega})$, for several values of μ_0 , then invert the function to get μ_0 as a function of N . We then have the ability to select the value of μ_0 corresponding to the number of particles used in the experiment.

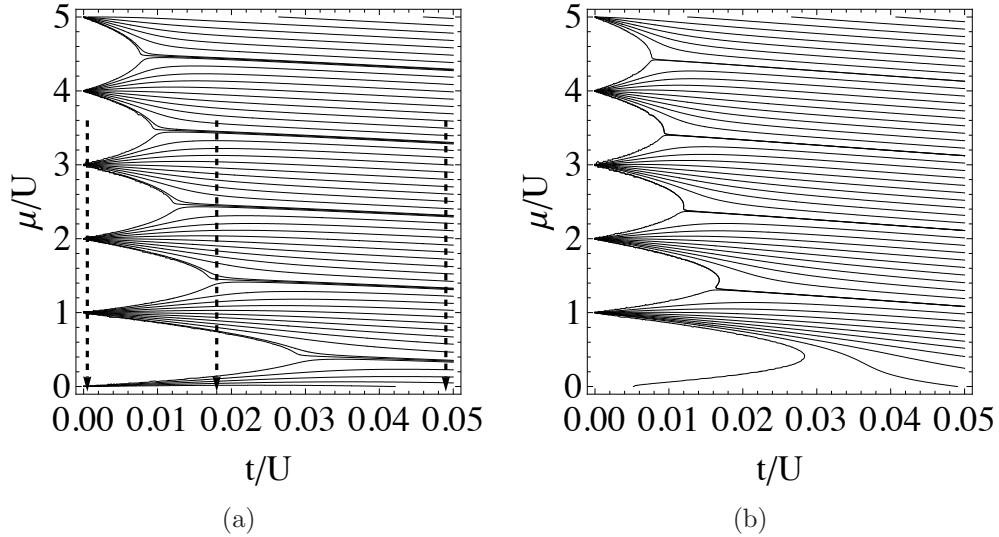


Figure 4.2: (a) Gutzwiller Mean Field phase diagram with constant density contours. The vertical dashed lines show the spatial dependence of the chemical potential for a trapped gas in the LDA: from left-to-right these correspond to the deep Mott limit, the “corrugated superfluid” situation appropriate to Fig. 4.4(b), and the dilute superfluid. (b) Phase diagram with contours of constant $\langle n \rangle g_2 = \langle n(n-1) \rangle / \langle n \rangle$. Contours are spaced by 0.1, with additional lines at $m \pm 0.01$, for integer m , to emphasize the Mott regions.

Campbell *et al.* [85] do not report the number of particles in the experiment. For Fig. 4.1, we choose $N = 9 \times 10^4$ so that the maximum site filling for $V_0 = 35E_{\text{rec}}$ and $V_0 = 25E_{\text{rec}}$ is $n = 5$, as is observed in the experiment.

4.3.4 Analytic Results

Dilute superfluid

Having numerically calculated the spectra, we now specialize to the dilute superfluid limit where the line shape can be calculated analytically. The clock shift energy in this limit is $\Delta = (U_{ab} - U_a) \langle n \rangle$, and within the local density approximation the site filling at position \mathbf{r} is the greater of zero and

$$n(\mathbf{r}) = (\mu_0 - \epsilon(0) - V_{\text{trap}}(\mathbf{r})) / U_a \quad (4.8)$$

where as previously stated, $V_{\text{trap}}(\mathbf{r}) = m\omega_x x^2/2 + m\omega_y^2/2 + m\omega_z z^2/2$ is the trapping potential, μ_0 is the central chemical potential. In the tight binding limit, the energy of the single-particle $k = 0$ state is $\epsilon(0) = -qt$ where q is the number of nearest neighbors. Substituting this result into Eq. (4.7), and neglecting the broadening one finds

$$N_b(\delta\omega) \propto \delta\omega \sqrt{(U_{ab} - U_a)n(0) - \delta\omega}, \quad (4.9)$$

where $n(0) = (\mu_0 - \epsilon(0))/U_a$ is the central density. Similar expressions were obtained in Ref. [106].

At fixed central chemical potential (equivalently, fixed central density) the width of the spectrum is proportional to $U_{ab} - U_a$, and hence U . Given a fixed number of particles, the central density varies as $n(0) \sim 1/U^{3/5}$, so the width of the spectral line instead varies as $Un(0) \sim U^{2/5}$.

Deep Mott limit

Now we analytically calculate the spectrum in the deep Mott insulator limit, where the density of the homogeneous system with chemical potential μ equals the smallest integer exceeding μ/U , denoted $\lceil \mu/U \rceil$ [102, 77]. In the local density approximation the density jumps from density $n-1$ to n as one moves through the location in space where local chemical potential is given by $\tilde{\mu} = U_a(n-1)$. Each plateau of fixed n gives a (broadened) delta-function contribution to the line shape at detuning $\delta\omega_n = (n-1)(U_{ab} - U_a)$. The magnitude of the delta function is proportional to the number of particles in the plateau, leading to a spectrum

$$\begin{aligned}
 N_b(\delta\omega) &\propto \sum_{n=1}^{\bar{n}} A_n \delta_{1/\tau}(\delta\omega - \delta\omega_n) \\
 A_{\bar{n}} &= [\mu_0 - U_a(\bar{n} - 1)]^{3/2} \bar{n} \\
 A_{n \neq \bar{n}} &= \left[(\mu_0 - U_a(n-1))^{3/2} - (\mu_0 - U_a n)^{3/2} \right] n,
 \end{aligned} \tag{4.10}$$

where $\bar{n} = \lceil \mu_0/U_a \rceil$ is the central density.

The deep superfluid and deep Mott insulator spectra are plotted in Fig. 4.3 using Eq.'s (4.9) and (4.10). Note the envelope of the spikes seen in the insulating state has the same shape as the superfluid spectrum. This can be understood from noting that in both cases the density is proportional to μ or $\lceil \mu/U \rceil$, resulting in similar coarse-grained Δ .

4.3.5 Intermediate Coupling

Finally, let's consider how the spectrum evolves as one increases t/U from zero. For non-zero t/U , superfluid shells form between Mott plateaus. These regions make the density continuous. Consequently, in the spectra, the areas of zero signal between peaks begin to fill in. Using our numerics, we find that the peaks remain visible until the system is well into the superfluid regime. An example is shown

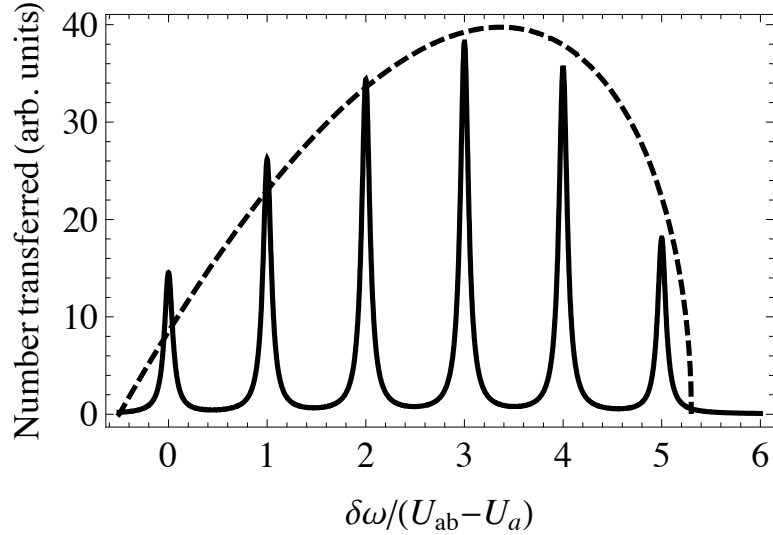


Figure 4.3: Analytically calculated spectra for the harmonically trapped system in the deep Mott limit (solid line), plotted as a function of $\delta\omega/(U_{ab} - U_a)$. Superimposed is the spectrum of the superfluid (dashed line) with the same parameters, but horizontally shifted to the left by $-(\delta\omega/2)(U_{ab} - U_a)$. The central density is $n_s(0) = [\mu_0 - \epsilon(0)]/U_a = 5.8$. This illustrates that the envelope of the spectral line in the Mott insulating state has the same shape as the superfluid spectrum, shifted horizontally.

in Fig. 4.4(b), corresponding to the chemical potential trajectory at $t/U_a = 0.018$ shown in Fig. 4.2(a). Note that although the only Mott lobe crossed is at $n = 1$, six peaks are clearly visible. Clearly one must be cautious about using such spectra to distinguish superfluid and Mott insulating states.

The source of the peaks for $t/U_a = 0.018$ is weak density corrugations which arise in the *superfluid* state near the Mott boundaries. These corrugations can be inferred from the unequal spacing of the isodensity contours in Fig. 4.2. The spectrum is a powerful amplifier of these corrugations, as they are hardly prominent in the real-space density shown in Fig. 4.4(a).

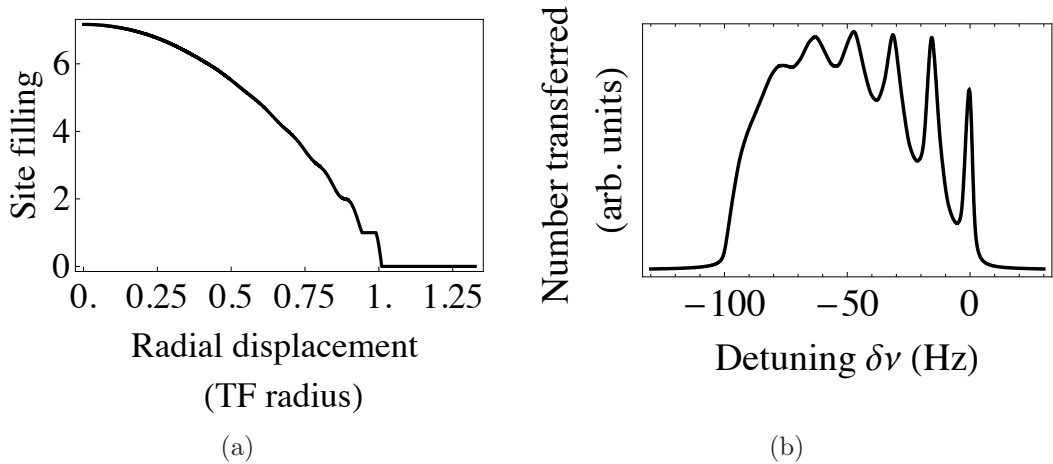


Figure 4.4: (a) The density as a function of distance from the trap center for a harmonic trap in units of the Thomas-Fermi radius ℓ_{TF} , defined as $\ell_{\text{TF}} \equiv \sqrt{(\mu_0 - \epsilon_0) / (m \omega^2 / 2)}$. The density profile corresponds to the LDA contour at $t/U_a = 0.018$ of Fig. 4.2(a). The corrugation of the density is observable, but not dramatic; it would be particularly difficult to image in experiments looking at columnar integrated densities. (b) The hyperfine spectra arising from the density plotted in (a).

4.4 Refinements

As seen previously, GMF+LDA captures the main features of the experimental spectra: sharp peaks occur in the Mott insulator limit, a smooth distribution in the deep superfluid limit. Furthermore, the overall energy scales of our spectra are consistent with those found experimentally. We caution however that we have treated the harmonic trapping frequency as independent of the lattice depth, while experimentally the harmonic confinement varies in an uncharacterized manner when the optical lattice intensity is changed. With this systematic variation makes quantitative comparison difficult.

Despite the qualitative similarities between theory and experiment, serious discrepancies remain. In particular, the experiment finds much more spectral weight at small detunings than theory predicts. Here we explore possible sources of this

discrepancy. Our primary result is that the discrepancies are consistent with trap anharmonicities.

In Sec. 4.4.1 we give an analysis of trap anharmonicities. In the following sections we briefly discuss several other possible explanations of the discrepancies: non-equilibrium effects and nonlinearities in the transfer rate. Although these latter two effects could distort the spectrum in a manner qualitatively consistent with experiment, we find that neither of them plays a significant role in these particular experiments.

4.4.1 Anharmonicity

The trap used in the experiments of Ref. [85] is a combination of an Ioffe-Pritchard magnetic trap, which is roughly harmonic, and an optical trap, which provide highly anisotropic Gaussian confinement. This results in a trap with “soft” anharmonicities, increasing the number of particles in the low density tails of the cloud. This will accentuate the small $\delta\omega$ peaks in the spectrum. The presence of anharmonicities is clear in Fig. 4 of Ref. [85], where the spatial distribution of the Mott insulator shells is far from elliptical.

We model the trapping potential as

$$V_{\text{trap}}(x, y, z) = \frac{m\omega_a^2}{2}x^2 + \frac{m\omega_r^2}{2}(y^2 + z^2) + I_a \left(1 - e^{-x^2/(2\sigma^2)}\right) + I_r \left(1 - e^{-(y^2+z^2)/(2\sigma^2)}\right) \quad (4.11)$$

where x lies in the soft “axial” direction while y and z constitute the “radial” directions. The $1/e^2$ beam waist is quoted as $70\mu\text{m}$, corresponding to $\sigma = 35\mu\text{m}$, however we find spatial profiles closer to experiment from the slightly smaller $\sigma = 28\mu\text{m}$ and use this value throughout. The explicit harmonic terms come from the magnetic trap. The anharmonic Gaussian part has two contributions, $I_{o,j}$

from the optical trap and $\alpha_j V_0$ from the optical lattice inducing a further trapping potential, for some constants α_j , with $I_j = I_{o,j} + \alpha_j V_0$. The parameters ω_a , ω_r , α_a , and α_r are determined from $I_{o,a}$, $I_{o,r}$ and the quadratic trap frequencies Ω_{j,V_0} at $V_0 = 0$ and $V_0 = 40E_{\text{rec}}$ by matching the quadratic terms of Eq. (4.11), giving

$$\begin{aligned}\alpha_j &= \frac{m\sigma^2}{40E_{\text{rec}}} (\Omega_{j,40}^2 - \Omega_{j,0}^2), \\ \omega_j^2 &= \Omega_{j,0}^2 - \frac{I_{o,j}}{m\sigma^2}.\end{aligned}$$

The quadratic trap frequencies Ω_{j,V_0} are given in Ref. [85] as $\Omega_{r,0} = 2\pi \times 70\text{Hz}$, $\Omega_{r,40} = 2\pi \times 110\text{Hz}$, $\Omega_{a,0} = 2\pi \times 20\text{Hz}$, and $\Omega_{a,40} = 2\pi \times 30\text{Hz}$. The remaining unknown parameter I_o is chosen to be $I_{o,a} = 1.17E_{\text{rec}}$ so that the spatial density profile appears similar to that in the experiment. We take $I_{o,r} = I_{o,a}$ though $I_{o,r}$ has little effect on the spatial density profiles. This yields $\omega_a = 4.8\text{Hz}$, $\omega_r = 67\text{Hz}$, $\alpha_a = 0.039E_{\text{rec}}^{-1}$, and $\alpha_r = 0.56E_{\text{rec}}^{-1}$ to completely characterize the trapping potential of Eq. (4.11). Note, that while we have chosen values to mimic the experimental observations, we have not attempted to produce a quantitative ‘‘fit’’ to the experimental data. Fig 4.5(b) shows the isopotential lines of our model trap.

For numerical efficiency, we produce spectra from a spherically symmetric model with parameters equal to those of the axial direction, which somewhat exaggerates the anharmonic effects. As shown in Fig. 4.5(c) the small detuning spectral weight is greatly enhanced by the anharmonicity, producing spectra which are consistent with experiments.

4.4.2 Alternative explanations of enhanced low-density spectral weight

Here we examine alternative sources of the enhancement of the small detuning spectral weight observed in experiments. We make no claim that this is com-

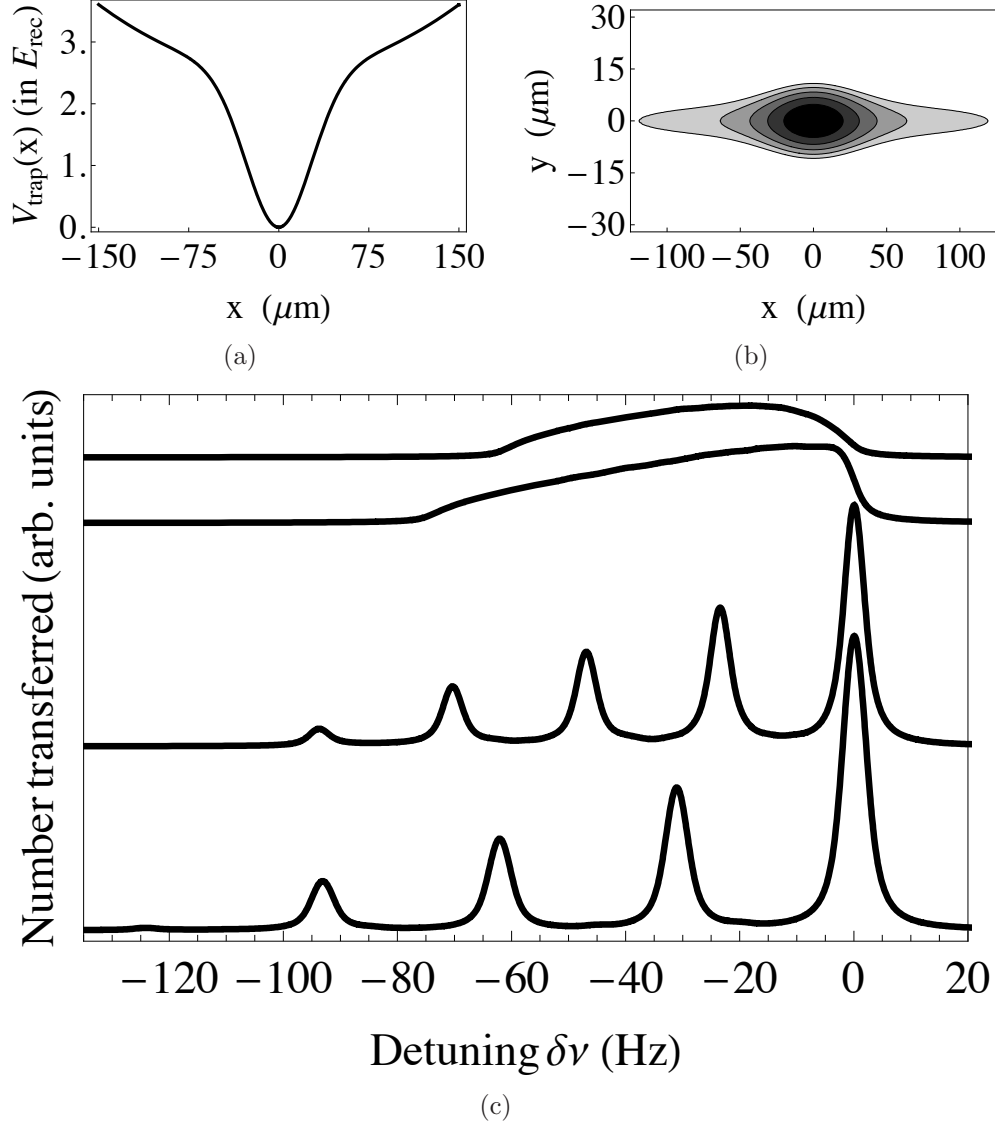


Figure 4.5: (a) A slice of the anharmonic potential $V_{\text{trap}}(\mathbf{r})$ similar to the one found in experiments. (b) Contour lines of constant density in the x-y plane for $n = 1, 2, \dots, 5$ in the anharmonic trap at $V_0 = 35E_{\text{rec}}$. (c) Corresponding spectra (using the “spherical trap model” discussed in text) for $V_0 = 5, 10, 25, 35E_{\text{rec}}$ with $N = 1.4 \times 10^7$ particles.

prehensive. Rather, this is an examination of the most plausible factors possibly present in the experiments of Ref. [85].

Losses. First, we explore the possibility that three-body collisions drive the cloud out of equilibrium. Atoms are removed preferentially from high density sites, ostensibly enhancing the small-detuning spectral weight. The timescale for decay from the $n = 5$ Mott insulator state is 200ms [85]. A characteristic equilibration time is the trap period, ~ 10 ms. Given the separation of timescales it is extremely unlikely that the system is far out of equilibrium. Furthermore, the loss rate is effectively zero for one- and two-particle site fillings and hence losses are unable to explain the experimentally observed enhancement of the $n = 1$ peak relative to the $n = 2$ peak.

Nonlinearities in transfer rate. The probes used to measure the spectrum may possibly drive the system out of the linear regime where the transfer rate is proportional to the density. For example, if the transition becomes saturated in the high density regions of the cloud, then the observed spectral weight will be reduced at large detunings. However, the density dependence of these saturation effects is slow, making it unlikely that they could not be responsible for the dramatic suppression of the ratio of the spectral weight in the $n = 2$ and $n = 1$ peaks. A model calculation in the deep Mott regime, where the sites decouple, confirms this result.

Non-equilibrium effects. Another possible mechanism for distorting the spectrum would be that the relatively short lattice ramp time might drive the system out of thermal equilibrium. Modelling these nonequilibrium effects is non-trivial, however we can put an upper bound on the size of the distortion by considering the “sudden limit,” where the lattice intensity is quickly increased, quenching the superfluid into the Mott state. After the quench, each decoupled

site will be in a quantum superposition of different particle numbers, with a Poisson probability distribution. The spectrum will then consist of a series of discrete peaks with the intensity of the peak at detuning $\nu_m = (m - 1)(U_{ab} - U_a)$ given by $I_m = \int d^3r n(\mathbf{r})^m e^{-n(\mathbf{r})} / (m - 1)!$, where $m = 1, 2, \dots$ and $n(r) = \max\{(\mu_0 - \epsilon(0) - V_{\text{trap}}(\mathbf{r}) / U_a, 0\}$ is the density in the superfluid in the Thomas-Fermi approximation. While this non-equilibrium spectrum is significantly different from the equilibrium spectrum, no strong peak at $m = 1$ appears when the central density is much larger than one.

Moreover, since the characteristic equilibration time is of order of the trap period, $\sim 10\text{ms}$, while the lattice is changed with a characteristic timescale of 40ms , we expect the system to be very near equilibrium [85], and any nonequilibrium effects should be much reduced compared to those predicted by the sudden approximation.

4.5 Summary

We calculate the hyperfine spectra of trapped bosonic atoms in an optical lattice. We consider the cases of harmonic and model anharmonic traps. We show that a harmonic trap produces a spectrum which shares qualitative features with the experimental spectra measured by Campbell *et al.* [85]: in the deep superfluid limit one has a smooth peak, while in the deep Mott limit, one sees several discrete peaks. To reproduce the small-detuning spectral weights, however, trap anharmonicities are necessary.

We find the spectra are extremely sensitive to density corrugation. As an example, the mild density corrugations which are found in the superfluid near the Mott insulator boundary are sufficient to produce a pronounced splitting of the spectral line. Consequently, the spectra are continuous across the superfluid

to Mott insulator transition. Such continuity is characteristic of a second-order phase transition, and makes identifying the superfluid transition difficult.

We acknowledge an illuminating discussion with Jim Sethna regarding the Mott insulating state's clock shift energy. We thank Wolfgang Ketterle and Gretchen Campbell for information regarding their experiment, and Smitha Vishveshwara for critical comments. This work was supported by NSF grant No. PHY-0456261 and GAANN Award No. P200A030111 from the US Department of Education.

Chapter 5

RF spectra: multiple peaked spectrum in a homogeneous system

*This chapter was adapted from “Many-body physics in the radio-frequency spectrum of lattice bosons” by Kaden R. A. Hazzard and Erich J. Mueller, published in Physical Review A **81**, 033404 (2010).*

This chapter will discuss RF spectroscopy of lattice bosons from a point of view complementary to that of Chapter 5. That chapter looked at things from the vantage of sum rules assuming a single, narrow spectral line, one common approach in the literature. This chapter is more closely related to another common approach in the literature: taking the rf spectra to be (convolutions of) the single particle spectrum, perhaps with shifts of lines due to final state interactions. This naturally leads to a two-peaked structure in the superfluid: there are gapless Goldstone modes (superfluid phonons) and gapped order parameter amplitude modes (Higgs modes). After constructing an approximation sufficient to capture the global physics, we will reconcile the two points of view. In addition to giving a global calculation for the spectrum of bosons in an optical lattice, the reconciliation provides a new general lesson for interpreting RF spectra of many-body systems, showing how standard viewpoints emerge in special limits of the proper calculation.

5.1 abstract

We calculate the radio-frequency spectrum of a trapped cloud of cold bosonic atoms in an optical lattice. Using random phase and local density approximations we produce both trap averaged and spatially resolved spectra, identifying simple

features in the spectra that reveal information about both superfluidity and correlations. Our approach is exact in the deep Mott limit and in the dilute superfluid when the hopping rates for the two internal spin states are equal. It contains final state interactions, obeys the Ward identities (and the associated conservation laws), and satisfies the f -sum rule. Motivated by earlier work by Sun, Lannert, and Vishveshwara [Phys. Rev. A **79**, 043422 (2009)], we also discuss the features which arise in a spin-dependent optical lattice.

5.2 Introduction

Bosonic atoms in optical lattices, described by the Bose-Hubbard model [77, 76], display a non-trivial quantum phase transition between a superfluid and Mott insulator. The latter is an incompressible state with an integer number of atoms per site. In a trap the phase diagram is revealed by the spatial structure of the gas: one has concentric superfluid and insulating shells. This structure has been elegantly explored by radio frequency (RF) spectroscopy [85], a technique which has also given insight into strongly interacting Fermi gases across the BEC-BCS crossover [84]. Here we use a Random Phase Approximation (RPA) that treats fluctuations around the strong coupling Gutzwiller mean field theory to explore the radio-frequency spectrum of lattice bosons.

We find two key results: (1) Our previous sum-rule based analysis [107] of experiments at MIT [85] stands up to more rigorous analysis: in the limit of small spectral shifts, the RPA calculation reduces to that simpler theory. (2) In a gas with more disparate initial and final state interactions (such as Cesium), the spectrum becomes more complex, with a bimodal spectrum appearing even in a homogeneous gas. The bimodality reveals key features of the many-body state. For example, in the limit considered by Sun, Lannert, and Vishveshwara [108],

the spectral features are related to the nearest-neighbor phase coherence. In the Gutzwiller approximation, the phase coherence directly maps onto the condensate density. In this paper we provide a physical picture of this result and explain how this bimodality can be observed in a spatially resolved experiment.

5.2.1 RF Spectroscopy

In RF spectroscopy, a radio wave is used to flip the hyperfine spin of an atom from $|a\rangle$ to $|b\rangle$. The rate of excitation reveals details about the many-body state because the $|a\rangle$ and $|b\rangle$ atoms have slightly different interactions. Generically the interaction Hamiltonian is $H_{\text{int}} = \sum_j U_{aa}n_a(n_a - 1)/2 + U_{bb}n_b(n_b - 1)/2 + U_{ab}n_a n_b$, with $U_{aa} \neq U_{ab} \neq U_{bb}$, where n_σ is the number of σ -state atoms on site j . In the simplest mean-field picture, the energy needed to flip an atom on site j from state a to state b is shifted by an energy $\delta\omega = U_{bb}n_b + (U_{ab} - U_{aa})n_a$. Applying this picture to an inhomogeneous gas suggests that the absorption spectrum reveals a histogram of the atomic density. Such a density probe is quite valuable: in addition to the aforementioned examples, it was the primary means of identifying Bose-Einstein condensation in atomic hydrogen [83].

Recently Sun, Lannert, and Vishveshwara [108] found a bimodal spectrum in a special limit of this problem, as did Ohashi, Kitaura, and Matsumoto [109] in a separate limit, calling into question this simple picture. We give a simple physical interpretation of the bimodality. As illustrated in Fig. 5.1, the superfluid state near the Mott insulator can be caricatured as a dilute gas of atoms/holes moving in a Mott background. An RF photon can either flip the spin of one of the core atoms, or flip the spin of one of the mobile atoms. The energy of these two excitations will be very different, implying that the RF spectrum should be bimodal. Through our RPA calculation, we verify this feature, calculating the frequencies of the two

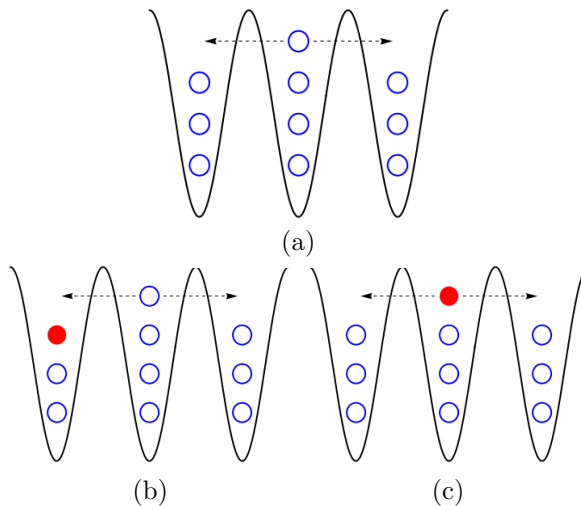


Figure 5.1: (Color online) Illustration of two types of RF-active excitations of the lattice superfluid near the Mott transition. Open (blue) circles are atoms in the $|a\rangle$ state, filled (red) circles are atoms in the $|b\rangle$ state, and the arrows indicate a delocalized particle while other particles are localized. (a) Illustrates the initial superfluid state, consisting of a dilute gas of atoms moving in a Mott background. Final states in (b) and (c), show the excitation of a core or delocalized atom.

peaks and their spectral weights. Interestingly, this calculation reveals that the two excitations in our cartoon are strongly hybridized.

We find that for parameters relevant to previous ^{87}Rb experiments, the degree of bimodality is vanishingly small and our previous sum rule arguments [107] accurately describe such experiments. On the other hand, there are opportunities to study other atoms (for example, Na, Cs, Yb) for which the bimodality may be more pronounced. Moreover, if the interactions or tunneling rates can be tuned via a spin-dependent lattice or a Feshbach resonance then this spectral feature will appear in a dramatic fashion.

This bimodal spectrum, with one peak produced by the “Mott” component and another by the “superfluid” component, is reminiscent of the spectrum of a finite temperature Bose gas in the absence of a lattice. As described by Oktel and Levitov [110], in that situation one sees one peak from the condensate, and one

from the incoherent thermal atoms. We would expect that at finite temperature our “Mott” peak continuously evolves into their “thermal” peak.

5.3 Bose-Hubbard Model

5.3.1 Model and RF spectra

In the RF spectra experiments we consider, initially all atoms are in the a -internal state and the RF pulse drives them to the b -state. Consequently, we consider two-component bosons trapped in the periodic potential formed by interfering laser beams, described by a Bose-Hubbard model [77],

$$\begin{aligned}
 H = & - \sum_{\langle i,j \rangle} t_{\sigma} c_{i,\sigma}^{\dagger} c_{j,\sigma} + \sum_{\sigma,j} (V_{j,\sigma} - \mu_{\sigma}) c_{j,\sigma}^{\dagger} c_{j,\sigma} \\
 & \sigma=\{a,b\} \\
 & + \sum_j \left(\sum_{\alpha,\beta} \frac{U_{\alpha\beta}}{2} c_{j,\alpha}^{\dagger} c_{j,\beta}^{\dagger} c_{j,\beta} c_{j,\alpha} \right), \tag{5.1}
 \end{aligned}$$

where c_{σ} and c_{σ}^{\dagger} are the annihilation and creation operators for states in the internal state σ , μ_{σ} is the chemical potential, $V_{j,\sigma}$ is the external potential with δ , the vacuum a - b splitting, absorbed into it, $U_{\alpha\beta}$ is the α state- β state on-site interaction strength, and t_{σ} is the hopping matrix element. The interactions are tunable via Feshbach resonances and spin-dependent lattices are also available [111]. For this latter setup, the hopping matrix elements may be tuned by the intensity of the lattices, and introducing small displacements of the lattice will reduce the overlap between the Wannier states of a and b atoms, and therefore may also be an efficient way to control the relative size of U_{aa} and U_{ab} . The interaction U_{bb} will be irrelevant: we will only consider the case where there is a vanishingly small concentration of b -state particles. In calculating the response to RF photons we

will take $V_j = \text{constant}$. Trap effects will later be included through a local density approximation [107] which is valid for slowly varying traps [98, 99, 100, 101, 102, 112, 113, 114, 115, 109].

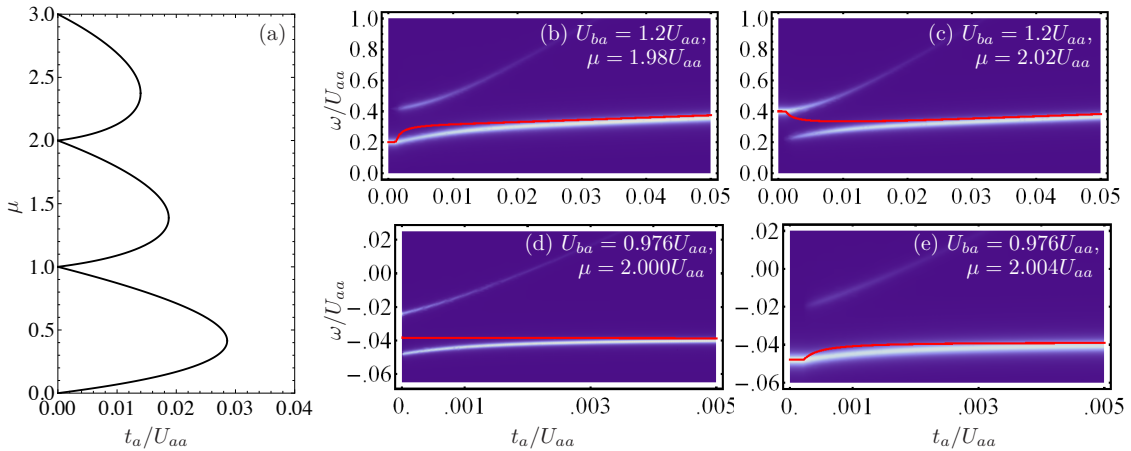


Figure 5.2: (Color online) Homogeneous system's spectral density as a function of ω/U_{aa} and t_a/U_{aa} (whiter indicates larger spectral density) compared with sum rule prediction (red, single line). Delta functions are broadened to Lorentzians for visualization purposes. (a) Ground state phase diagram within the Gutzwiller approximation, for reference. (b,c) We take $U_{ba} = 1.2U_{aa}$ and $t_b = t_a$, with (b) $\mu = 1.98U_{aa}$ and (c) $\mu = 2.02U_{aa}$. (d,e) We take parameters corresponding to typical ^{87}Rb experiments: $U_{ba} = 0.976U_{aa}$ and $t_b = t_a$, and take (d) $\mu = 2.000U_{aa}$ and (e) $\mu = 2.004U_{aa}$. In both cases, a double peak structure is visible, but the region of the phase diagram in which it is important is much smaller for ^{87}Rb parameters than for Fig. (b,c)'s parameters.

Experimentally the RF spectrum is measured by counting the number of atoms transferred from state a to b when the system is illuminated by a RF pulse. These dynamics are driven by a perturbation

$$H_{\text{rf}} = \sum_j \gamma(t) c_{j,b}^\dagger c_{j,a} + \text{H.c.} \quad (5.2)$$

where $\gamma(t)$ is proportional to the time-dependent amplitude of the applied RF field multiplied by the dipole matrix element between states a and b : typically γ is a sinusoidal pulse with frequency ω with a slowly varying envelope ensuring a small bandwidth. Due to the small wave-number of RF photons, recoil can be neglected.

For a purely sinusoidal drive, Fermi's Golden Rule gives the number of atoms transferred per unit time for short times to be

$$\Gamma(\omega) = \frac{2\pi}{\hbar} \sum_{i,f} p_i \delta(\omega - (E_f - E_i)) |\langle f | H_{\text{rf}} | i \rangle|^2 \quad (5.3)$$

where the sum is over the initial states (occupied with probability $p_i = e^{-\beta E_i}$) and the final states, all of which are eigenstates of H with energies E_i and E_f . We will restrict ourselves to $T = 0$ and the physically relevant case where the initial states contain no b -atoms.

5.3.2 Sum Rules

Taking moments of Eq. (5.3) [110, 104], the mean absorbed photon frequency is

$$\langle \omega \rangle = \frac{\int d\omega \omega \Gamma(\omega)}{\int d\omega \Gamma(\omega)} = \frac{\langle [H_{\text{rf}}, H] H_{\text{rf}} \rangle}{\langle H_{\text{rf}}^2 \rangle} \quad (5.4)$$

$$= \delta - z(t_b - t_a) f_c + (U_{ab} - U_{aa}) g_2 \langle n \rangle. \quad (5.5)$$

We defined δ to be the vacuum a - b splitting, the local phase coherence factor is

$$f_c = \frac{\langle c_{i,a}^\dagger c_{j,a} \rangle}{\langle n \rangle}, \quad (5.6)$$

with i and j nearest neighbors, the site filling is $n \equiv c_a^\dagger c_a$, and the lattice coordination is z . The zero-distance density-density correlation function is

$$g_2 = \frac{\langle c_a^\dagger c_a^\dagger c_a c_a \rangle}{\langle n \rangle^2}. \quad (5.7)$$

The second term in Eq. (5.5) may be interpreted as the mean shift in the kinetic energy when the spin of an atom is flipped. In particular, within a strong-coupling mean-field picture $\langle c_{i,a}^\dagger c_{j,a} \rangle = \langle c_{i,a}^\dagger \rangle \langle c_{j,a} \rangle$ is the condensate density, which can therefore be measured with this technique. The second term in Eq. (5.5) is the shift in the interaction energy.

Our subsequent approximations will satisfy this sum rule. This is non-trivial: for example, even in simultaneous limits of $t_b = 0$, $U_{ab} = U_{aa}$, and $t_a \rightarrow 0$ considered in Ref. [108], their results violate this sum rule by a factor of ~ 3 .

Since it plays no role in the remainder of the discussion, we will set to zero the vacuum level splitting: $\delta = 0$. This amounts to working in a “rotating frame”.

5.4 Random phase approximation

5.4.1 General setup and solution

To calculate the RF spectrum we employ a time-dependent strong-coupling mean-field theory which includes $k = 0$ fluctuations around the static strong-coupling Gutzwiller mean field theory [76]. This mean field theory is exact in the deep Mott limit and in the dilute superfluid when $t_a = t_b$, and it yields fairly accurate ground states in the intermediate regime [98, 99, 100, 101, 102]. Refs. [115, 109] previously used analogous RPA’s to calculate the Bose-Hubbard model’s quasiparticle spectra and RF spectra with $U_{ab} = 0$, which reduce to the $k = 0$ single particle spectra.

We use the homogeneous time-dependent Gutzwiller variational ansatz

$$|\psi(t)\rangle = \bigotimes_i \left[\sum_n (f_n(t) |n, 0\rangle_i + g_n(t) |n-1, 1\rangle_i) \right] \quad (5.8)$$

where $|n_a, n_b\rangle_i$ is the state at site i with n_a particles in the a state and n_b in the b state. The equation of motion for $f_n(t)$ and $g_n(t)$ are derived by minimizing the action $S = \int dt \mathcal{L}$, with Lagrangian

$$\mathcal{L} = \langle \psi | i\partial_t | \psi \rangle - \langle \psi | H | \psi \rangle - \lambda \langle \psi | \psi \rangle, \quad (5.9)$$

where λ is a Lagrange multiplier which enforces conservation of probability. At

time $t = -\infty$, where $\gamma(t) = 0$, we take $g_n = 0$, and choose f_n to minimize $\langle \psi | H | \psi \rangle$,

$$\begin{aligned} \lambda f_n &= -t_a z \left(\sqrt{n} \alpha^* f_{n-1} + \sqrt{n+1} \alpha f_{n+1} \right) \\ &\quad + \left(\frac{U_{aa}}{2} n(n-1) - \mu n \right) f_n, \end{aligned} \quad (5.10)$$

where

$$\alpha = \sum_n \sqrt{n} f_n^* f_{n-1}. \quad (5.11)$$

Solving the subsequent dynamics to quadratic order in γ , one finds

$$\Gamma(t) = N_s \int dt' \gamma(t) \gamma(t') \chi^{(R)}(t-t'), \quad (5.12)$$

where the retarded response function is

$$\chi^{(R)}(t) = \frac{1}{i} \sum_n \sqrt{n} (G_n^*(t) f_n - G_n(t) f_n^*). \quad (5.13)$$

The Green's functions $G_n(t)$ satisfy the equations of motion for the g_n 's in the absence of an RF field, but in the presence of a delta function source, and boundary condition $G_n(t) = 0$ for $t < 0$. The relevant equations are simplest in Fourier space, where $G_n(\omega) = \int dt e^{i\omega t} G_n(t)$ obeys

$$\sqrt{n} f_n = -\omega G_n + \sum_m \Lambda_{nm} G_m \quad (5.14)$$

where $\Lambda = \bar{\Lambda} + \Theta$ is a Hermitian matrix. The tridagonal part $\bar{\Lambda}$ is

$$\bar{\Lambda}_{n,n+1} = -z t_a \alpha \sqrt{n} \quad (5.15)$$

$$\bar{\Lambda}_{n,n-1} = -z t_a \alpha^* \sqrt{n-1} \quad (5.16)$$

$$\begin{aligned} \bar{\Lambda}_{nn} &= -\mu n - \lambda + \frac{U_{aa}}{2} (n-1)(n-2) \\ &\quad + U_{ab} (n-1). \end{aligned} \quad (5.17)$$

The remaining contribution, Θ , is

$$\Theta_{nm} = -z t_b f_{n-1} f_{m-1}^*. \quad (5.18)$$

Specializing to the case where $\gamma(t) = \gamma e^{i\omega t}$, the response is given in terms of normalized eigenvectors v_m , with $\sum_m \Lambda_{nm} v_m^{(j)} = \epsilon_j v_n^{(j)}$. It takes the form of a sum of delta-functions,

$$I(\omega) = \sum_j \left(\sum_m \sqrt{m} f_m v_m^{(j)} \right)^2 \delta(\omega - \epsilon_j). \quad (5.19)$$

The f_n 's are found at each point in the phase diagram by starting with a trial α , solving Eq. (5.10), then updating α via Eq. (5.11) and iterating. We find that almost all spectral weight typically lies in only one or two peaks. Fig. 5.2 shows sample spectra, whose general behavior is discussed in more detail in Sec. 5.4.2. The superfluid near the Mott state displays a multi-modal spectrum, but in the weakly interacting limit only a single peak is seen. An avoided crossing is clearly visible in these plots. Taking moments of $\chi^R(\omega)$, we see that Eq. (5.5) is satisfied.

5.4.2 Limiting Cases and Dependence on Final State Interactions

Bimodality's evolution over the phaes diagram

Although finding the spectrum in Eq. (5.19) is a trivial numerical task, one can gain further insight by considering limiting cases. First, when $U_{ab} = U_{aa}$ and $t_a = t_b$ the system possesses an $SU(2)$ symmetry. In this limit we find that $G_n(t) = -i\sqrt{n}f_n\theta(t)$ is constant for $t > 0$. Thus our approximation gives a spectrum $I(\omega)$ which is proportional to $\delta(\omega)$. This result coincides with the exact behavior of the system: the operator $X = \sum_j b_j^\dagger a_j$ is a ladder operator, $[H, X] = \delta X$, and can only generate excitations with energy δ (set equal to zero in our calculation). The fact that our approximations correctly capture this behavior is nontrivial: in a field theoretic language one would say that our equation of motion

approach includes the vertex corrections necessary for satisfying the relevant “Ward identities” [86, 116, 7].

The current ^{87}Rb experiments are slightly perturbed from this limit, with $(U_{ab} - U_{aa})/U_{aa} \approx -0.024$ and $t_b = t_a$. We find that the δ -function is shifted by a frequency proportional to $U_{ab} - U_{aa}$, but that the total spectral weight remains concentrated on that one frequency: the sum of the spectral weights at all other frequencies scale as $\eta \equiv (U_{ab} - U_{aa})/(zt_a)$. Consequently it is an excellent approximation to treat the spectrum as a delta-function, and our RPA calculation reduces to the results in Ref. [107]. We emphasize however that other atoms, such as Cesium, can be in a regime where η is large.

When $\eta \ll 1$ (that is, rapid tunneling rates $t_a \gg (U_{ab} - U_{aa})/z$) the spectral weight is concentrated in a single, shifted peak. Conversely, when $\eta \gg 1$ (that is, slow tunneling rates $t_a \ll (U_{ab} - U_{aa})/z$) the spectral weight is generically multimodal. This behavior can be understood as an analog of “motional narrowing” [117]. Our cartoon Fig. 5.1 gives two excitation processes, and the two states can convert between themselves at a rate $\sim zt_a$. one will only be to separately resolve the two states if the splitting between them is large compared to the rate of the interconversion.

Analytic solution in deep lattice limit

We gain further insight by considering the superfluid near the Mott phase with $t_a/U_a \ll 1$. Here one can truncate the basis to two states with total particle number n and $n + 1$ on each site. In this truncation, our calculation is the mean field implementation of the picture in Fig. 5.1. Then the f_n 's and G_n 's can be found analytically: one only needs to solve 2×2 linear algebra problems. In the $t_b = 0$, $U_{ab} = U_{aa}$ limit, this is similar to Ref. [108]'s approach, but includes the hopping self consistently, allowing us to satisfy the sum rule Eq. (5.5). This truncation is

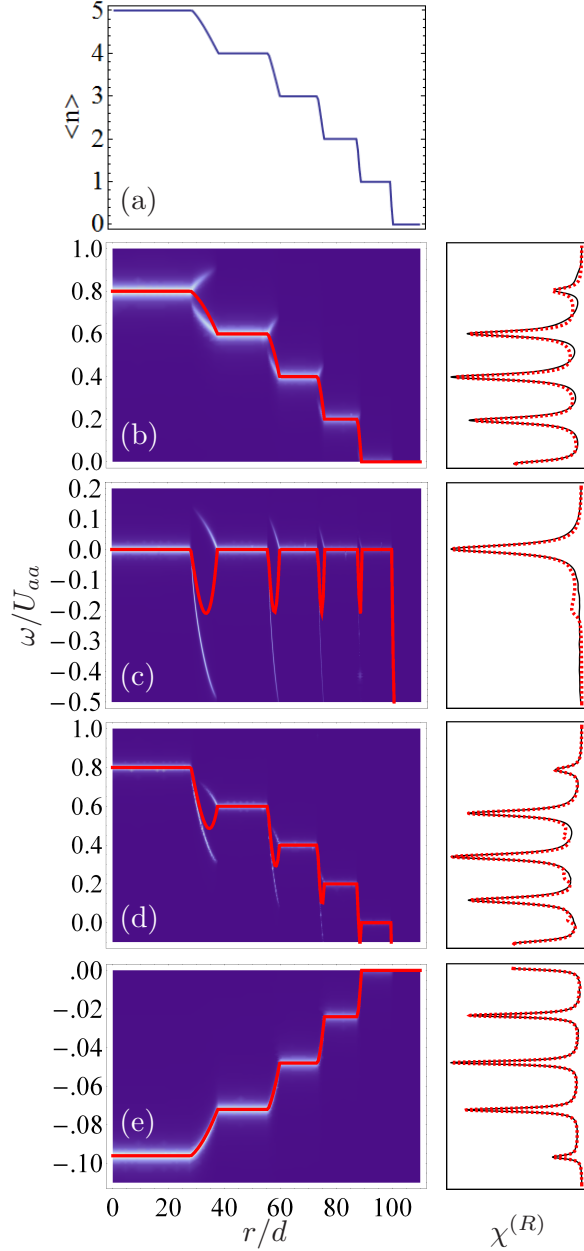


Figure 5.3: (Color online) (a) Density n as a function of distance to trap center rescaled by the lattice spacing, r/d , in a local density approximation. For all subfigures, we take $t_a/U_{aa} = 0.004$, which is moderately smaller than the tip of the first Mott lobe. (b-e) Left: spectrum of a homogeneous gas with density $n(r)$, representing the spatially resolved spectrum observed in an experiment on a trapped gas. Horizontal axis is position, vertical is frequency, color from dark to light represents increasing spectral density. Continuous (red) curve denotes sum rule result for $\langle \omega \rangle$. We round the δ -functions to Lorentzians for visualization. Right: trap-averaged spectrum for a 3D trap within our RPA (black, solid line) compared with sum rule (red, dashed line). (b) $U_{ab} = 1.2U_{aa}, t_b = t_a$ (c) $U_{ab} = U_{aa}, t_b = t_a + 0.1U_{aa}$ (d) $U_{ab} = 1.2U_{aa}, t_b = t_a + 0.1U_{aa}$ (e) ^{87}Rb parameters: $U_{ab} = 0.976U_{aa}, t_b = t_a$.

exact in the small t_a limit, and yields

$$\chi^{(R)}(\omega) = A_+ \delta(\omega - \omega_+) + A_- \delta(\omega - \omega_-) \quad (5.20)$$

with

$$\omega_{\pm} = \frac{\epsilon_1 + \epsilon_2}{2} \pm \sqrt{\Delta^2 + \left(\frac{\epsilon_1 - \epsilon_2}{2}\right)^2} \quad (5.21)$$

where

$$\begin{aligned} \epsilon_1 &\equiv (U_{ab} - U_{aa})(n-1) + z t_a f_{n+1}^2 (n+1) \\ \epsilon_2 &\equiv (U_{ab} - U_{aa})n + z [t_a(n+1) - t_b] f_n^2 \\ \Delta &\equiv -\sqrt{n(n+1)} t_a z f_n f_{n+1}. \end{aligned} \quad (5.22)$$

if $n \geq 1$ and

$$\begin{aligned} \epsilon_1 &\equiv z t_a f_1^2 \\ \epsilon_2 &\equiv z (t_a - t_b) f_0^2 \\ \Delta &\equiv 0. \end{aligned} \quad (5.23)$$

if $n = 0$ (here, only the ϵ_2 peak has non-zero spectral weight). We omit the cumbersome analytic expressions for the spectral weights A_{\pm} . The spectrum consist of two peaks – hybridized versions of the excitations caricatured in Fig. 5.1. One can identify ϵ_1 and ϵ_2 as the energies of those caricature processes, recognizing that the hybridization term, Δ , grows with t_a . The avoided crossing between these modes is evident in Fig. 5.2.

5.4.3 Inhomogeneous spectrum

We model the trapped spectrum through a local density approximation. We assume that a given point in the trap has the properties of a homogeneous gas with

chemical potential $\mu(r) = \mu_0 - V(r)$. In Fig. 5.3 we show the density profile and the spectrum corresponding to each point in space. Also shown is the trap averaged spectrum.

When U_{ab} is slightly smaller than U_{aa} , corresponding to ^{87}Rb and illustrated in Fig. 3(e), the spectrum is unimodal at each point in space. The shift, given by the sum rule in (5), maps out the density seen in Fig. 3(a). For larger $|U_{ab} - U_{aa}|$, illustrated in Fig. 3(b), the spectrum in the superfluid regions is distinctly bimodal. If, as in Fig. 3(c), one makes $U_{ab} = U_{aa}$, but sets $t_b \neq t_a$, the spectrum reflects the condensate density rather than the particle density. One only sees spectral shifts in the superfluid regions – finding spectral weight gradually shift from one peak to another as one moves in space. In Fig 3(d) we illustrate what happens when both $U_{ab} \neq U_{aa}$ and $t_b \neq t_a$. One sees a pattern which is roughly a superposition of Figs. 3(b) and 3(c).

In all cases, the bimodality of the homogeneous spectrum is quite effectively washed out by the inhomogeneous broadening of the trap. On the other hand, if one spatially images the atoms flipped into the b state as in Ref. [85], there is a clear qualitative signature of the bimodality. If one excites the system with an RF pulse whose frequency lies between the resonant frequencies of two Mott plateaus, one will excite two “shells” of atoms. These shells should be clearly visible, even in column integrated data.

5.5 Conclusions and discussion

In this paper we have shown that the RF spectra of a homogeneous Bose gas in an optical lattice will have two (or more) peaks in the superfluid state when the parameters are tuned close to the superfluid-Mott insulator phase transition. Physically, this bimodality is a result of the strong correlations in the system.

These correlations result in two distinct forms of excitations (which are strongly hybridized): those involving “core” atoms, and those involving delocalized atoms. When $\eta = (U_{ab} - U_{aa})/(zt_{aa})$ is small, such as in typical ^{87}Rb experiments, this bimodality is absent.

Our approach, based upon applying linear response to a time dependent Gutzwiller mean field theory, is both simple and quite general. It allows arbitrary interactions between both spin states, and it allows arbitrary spin-dependent hopping rates. The major weakness of the theory is that it fails to fully account for short range-correlations: the atoms are in a quantum superposition of being completely delocalized, and being confined to a single site. The physical significance of this approximation is most clearly seen when one considers the case where the final-state atoms have no interactions, $U_{ab} = 0$, and see no trap or lattice. Imaging the b -atoms after a time-of-flight is analogous to momentum resolved photoemission [118], and would reveal the dispersion relationship of the single-particle excitations. The fact that the spectrum consists of two sharp peaks means that all of the non-condensed atoms are approximated to have the same energy. One will also see that their momentum is uniformly distributed throughout the first Brillouin zone. In the strong lattice limit, where the bandwidth is small, this approximation is not severe.

5.6 Acknowledgements

We thank Sourish Basu, Stefan Baur, Stefan Natu, Eliot Kapit, Wolfgang Ketterle, Kuei Sun, Smitha Vishveshwara, Henk Stoof, Ian Spielman, and Mukund Vengalattore for useful discussions. This material is based upon work supported by the National Science Foundation through grant No. PHY-0758104, and partially performed at the Aspen Center for Physics.

Chapter 6

Radio-frequency spectra at finite temperature and other applications and theoretical developments of rf spectra

6.1 Abstract

We develop the theory necessary to apply rf spectra (here referred to as “clock shift measurement”) techniques to overcoming experimental challenges in ultracold atomic systems. Specifically, we address the most salient features of the finite temperature theory of bosons in optical lattices through the Mott insulator-superfluid phase transition. Here I focus on the Mott insulator and superfluid regimes; the quantum critical regime is addressed in Chapter 13. This suggests applications, including thermometry and perhaps cooling.

I develop ideas to relate clock RF spectra in a trap to local susceptibilities, density profiles, and spatial correlations of the bosonic lattice system.

Finally, I show how using longer range interactions, one can probe arbitrary n -point density correlations of multiple sites. Although the experimental difficulty to resolve these decreases with increasing n and distance spanned in the correlation function, realistic experimental parameters indicate that it may be usefully probe $n \lesssim 5$ correlators up to a 3 – 4 sites apart.

6.2 Introduction

To experimentally examine any ultracold atomic system presents two challenges: creating it and measuring its properties. For one, achieving sufficiently low enough temperatures is difficult [57]. To know the system temperature is also difficult, and

single-digit accuracy is state-of-the art. Finally, to probe a system is to measure its correlation functions, and while the cold atom systems lend themselves to measuring real- and k -space density distributions, many other correlation functions necessary to diagnose phase transitions and properties of phases are presently inaccessible. As notable examples, consider the momentum dependence of the anomalous 1-particle Green’s function in the fermion Hubbard model (i.e., is there d -wave superconductivity?), and n -particle Green’s functions with $n > 2$ for general liquids (interesting because many approximations amount assuming the $n > 2$ Green’s functions have a certain structure even though this structure is not well understood due to the lack of experimental accessibility.)

We suggest and develop the theory for multiple applications towards overcoming present experimental limitations in ultracold atoms. Specifically, we show how through clock-shift (CS) measurements one may obtain local compressibilities and various spatial correlations, and to performing thermometry and selective cooling.

We provide a theoretical toolbox to enable future experiments: Section 4.3 outlines calculation of “CS diagrams.” Section 6.4 treats the finite temperature superfluid, and Section 6.5 suggests applications.

6.3 Clock shift diagrams.

Hamiltonian. The Bose-Hubbard (BH) model describing lattice bosons with two internal states is [77]

$$\begin{aligned}
H = & -t_a \sum_{\langle i,j \rangle} a_i^\dagger a_j + \sum_i \left[\frac{U_a}{2} n_{i,a} (n_{i,a} - 1) + V_{i,a} n_{i,a} \right] \\
& - t_b \sum_{\langle i,j \rangle} b_i^\dagger b_j + \sum_i \left[\frac{U_b}{2} n_{i,b} (n_{i,b} - 1) + V_{i,b} n_{i,b} \right] \\
& + U_{ab} \sum_i n_{i,a} n_{i,b} + \text{H.c.}
\end{aligned} \tag{6.1}$$

where $n_{i,\alpha} \stackrel{\text{def.}}{=} \alpha_i^\dagger \alpha_i$, and the a 's and b 's are boson operators. The t_α 's describe hopping rates of species α , and $U_{\alpha\beta}$ the interaction of species α and β . Define $V_{i,\alpha} = \mathcal{V}_{i,\alpha} - \mu_\alpha$ where $\mathcal{V}_{i,\alpha}$ is the external potential at site i for species α , so H becomes the grand canonical free energy. The Hamiltonian's parameters are $t_\alpha = \int d\mathbf{r} w_\alpha^*(\mathbf{r}) [-1/(2m_\alpha)\nabla^2 + V_p(\mathbf{r})] w_\alpha(\mathbf{r})$, $\mathcal{V}_{i,\alpha} \approx V_{\text{trap}}(\mathbf{R}_i)$, and $U_{\alpha\beta} = (4\pi a_{\alpha\beta}/m) \int d\mathbf{r} |w_\alpha(\mathbf{r})|^2 |w_\beta(\mathbf{r})|^2$ (with $\hbar = 1$) where m_α is the mass of species α , $a_{\alpha\beta}$ is the species α -species β scattering length, and where w_α indicates the normalized Wannier function for atoms in state α . V_p is the lattice potential. The competition of the kinetic and interaction terms drive the well-known Mott insulator (MI)-superfluid (SF) phase transition.

Approximations. The CS diagrams only depend on the state of the all- a system and parameters appearing explicitly in Equation 4.1 (that is, no b operators need be included). We use the Gutzwiller mean-field (GMF) theory and local density approximation (LDA); though this theory is simple, it is sufficient for the purpose of calculating rather accurate CS diagram, as we have argued elsewhere [119, 107]. We briefly review these approximations. The mean-field formulation of GMF assumes the fluctuations of the operators from their expectation values affect neighboring sites negligibly. Then one can write $a_i^\dagger = \langle a_i^\dagger \rangle + (a_i^\dagger - \langle a_i^\dagger \rangle) \approx \langle a_i^\dagger \rangle$ for the operators “at other sites,” so that the mean-field Hamiltonian is, assuming unbroken translational symmetry,

$$H_{\text{MF}} = \sum_i \left[-q t a_i^\dagger \langle a \rangle + U \frac{n_i^2}{2} + V_i n_i + \text{H.c.} \right] \quad (6.2)$$

where q is the number of nearest neighbors.

The LDA is used to calculate the spatial dependence of thermodynamic quantities, especially the density. That is, we write properties P (local density, energy, etc.) at a spatial location \mathbf{r} , as $P(\mathbf{r}) = P(\mu - V(\mathbf{r}))$ where $P(\mu)$ is the observable as a function of the chemical potential in the homogeneous system with no external

potential and $V(\mathbf{r})$ is the external potential.

Clock shift basics. The *collisional frequency shift* or *clock shift* (CS) Δ is a shift in the energy between a and b states due to the inter-particle interactions, so named because it limits the accuracy of atomic clocks.

The general formula for Δ in a homogeneous system is [104, 86]

$$\Delta = (U_{ab} - U_a) \frac{\langle n(n-1) \rangle}{\langle n \rangle}.$$

where n is the site occupation. In the SF, MI, and normal fluid (NF) states, it is [119, 107]

$$\Delta_{\text{SF}} = (U_{ab} - U_a) \langle n \rangle \tag{6.3}$$

$$\Delta_{\text{MI}} = (U_{ab} - U_a) (\langle n \rangle - 1) \tag{6.4}$$

$$\Delta_{\text{NF}} = 2(U_{ab} - U_a) \langle n \rangle. \tag{6.5}$$

Calculation of clock-shift diagrams. So far, we have explored the CS energies of a single state. In a trap, the system will take on a variety of CS energies, corresponding to different points in space. Shining a laser with frequency near the a to b transition energy and counting the number of b states yields the number of atoms with CS energy $\Delta = \omega$. We christen this function $N_b(\omega)$ the “clock-shift diagram.”

We have outlined our method for calculating the CS diagrams elsewhere. [119, 107] To summarize, we discretize in r and calculate $\Delta(r)$ and $n(r)$ numerically within GMF+LDA. Then for each CS energy range $\Delta(r)$ we find the corresponding radial shells (of width δr) and sum up $n(r)4\pi r^2 \delta r$ over these shells.

6.4 Finite temperature superfluid

We consider the finite-temperature modification of the CS diagram in the SF limit. The MI state will be treated in Section 6.5. Finite temperature yields an additional

layer of complexity to the physics of the system, which CS diagrams may be useful in analyzing.

Neglecting the “hybridization” of the states that occur after transfer of atoms, the NF and the condensate give independent contributions to the CS diagram. Oktel and Levitov have treated the hybridization in Ref. [110]. In general, one needs Oktel and Levitov’s full theory, but in many regimes or for a qualitative understanding, neglecting this hybridization is a good approximation.

Finite temperature leads to an thermal excitation gas coexisting with a condensate with modified density. We calculate these densities using a semiclassical version of Hartree-Fock (HF) mean-field theory.¹ In this limit, the condensate and excitation densities determine CS diagrams since Equations 4.5 and 6.5 relate the condensate density and the excitation density to CS energies in the system. As an example, a *homogeneous* SF has two CS peaks: one due to the condensate and one (at twice of the SF CS energy) due to the NF.

The semiclassical HF excitation density is is [48, 120]

$$n_{\text{ex}}(\mathbf{r}) = \int \frac{d\mathbf{p}}{(2\pi\hbar)^3} \frac{1}{e^{(\epsilon_{\mathbf{p}}(\mathbf{r})-\mu)/k_B T} - 1} \quad (6.6)$$

where the integral is over all momenta and the excitation energy is (more on this in a moment) $\epsilon_{\mathbf{p}}(\mathbf{r}) = p^2/2m + 2n(\mathbf{r})U_a + V(\mathbf{r})$. Finally, the condensate density is

$$n_0(\mathbf{r}) = \frac{\mu - V(\mathbf{r})}{U_a} - 2n_{\text{ex}}(\mathbf{r}).$$

The chemical potential is determined from the number of total atoms integrated over the entire trap in the Thomas-Fermi semiclassical approximation. Then all of these equations are solved self-consistently. In words, this calculation is easily summarized: the condensate density is given by the Thomas-Fermi approximation,

¹Technically, since the scattering length is renormalized, it is something more akin to Brueckner-Hartree-Fock.

as is the density of the thermal excitations; in each case, interactions are treated within the HF approximation.

We return our approximations. The kinetic part of the single particle energy $\epsilon_{\mathbf{p}}$ is taken to have the “free” particle form, $p^2/(2m)$, which is justified if (1) the temperatures are small compared to the bandwidth so that the dispersion may be expanded to quadratic order (the square lattice assures that the dispersions is isotropic to quadratic order) and (2) the temperatures are large enough that the interactions are in the single-particle rather than Bogoliubov regime – the criterion for this is that $T \gg ms^2 \simeq nU_\alpha$ where s is the sound speed. The interaction term with the total density takes the form $2n(\mathbf{r})U_a$ in the HF approximation, which is also qualitatively accurate over a wide temperature range. [120] As long as the thermal de Broglie wavelength and coherence length are small compared to the trap’s characteristic length scales, the Thomas-Fermi approximation is valid for large enough particle number. [48]

Figure 6.1 shows a characteristic example of a finite temperature SF CS diagrams, as well as the condensate and excitation density profiles. The most salient feature that emerges is the presence of a peak near zero density on the CS diagram – this occurs due to the tail of thermally populated NF at the edge of the trap.

We conclude our analysis of the finite temperature SF with two provocative observations: (1) the NF peak may enable thermometry; by measuring the peak height relative to the SF CS diagram background may enable accurate measurement of the temperature, a key challenge in ultracold atomic systems. (2) Going beyond the HF theory, one finds a finite thermal excitation density at the center of the trap at low enough temperatures that then peaks at the edge of the condensate cloud, and then decreases beyond the condensate (see, e.g., Ref. [120]). Thus, a temperature-dependent *kink* appears in the CS diagram at an energy correspond-

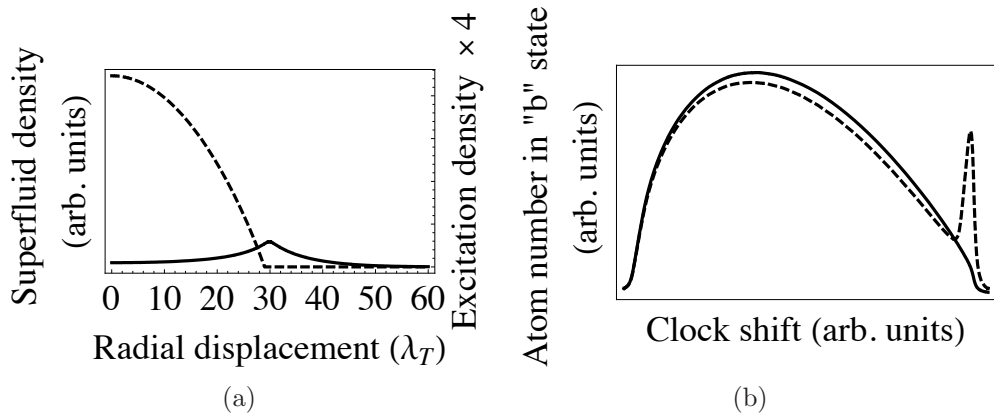


Figure 6.1: (a) Condensate and excitation densities of a finite temperature superfluid at a temperature of 30 in units of the coupling constant U_α , the radial displacement is in units of the thermal de Broglie wavelength λ_T , and the trapping potential is αr^2 with $\alpha = 10^{-2}U_\alpha/\lambda_T^2$. The excitation density is rescaled to make it more visible. (b) Corresponding clock shift diagram at temperatures $T = 1, 30$ for the solid and dashed curves respectively. (b) The peak at low densities comes from the normal fluid tail.

ing to the excitation density at the center of the trap. Since this kink persists, and its magnitude changes, all the way to zero temperature, this may enable very-low temperature thermometry. Furthermore, it provides experimental access to the beyond-HF complexities of the finite-temperature Bose-liquid that control the density at the center.

6.5 Applications

6.5.1 Thermometry with the Mott insulator

Finite temperature Mott insulator clock shift theory

Accurate thermometry is a crucial area for development in ultracold atoms: their use as quantum simulators for many-body physics requires an accurate knowledge and control of the temperature. We propose a thermometry method based on the

MI state's CS diagrams.

We first review the elementary theory of the finite-temperature MI as $t/U \rightarrow 0$. Each lattice site becomes uncorrelated with the others, and we can solve the single site problem to obtain the excitation spectrum. The eigenstates $|\psi\rangle$ are then Fock states, $|n\rangle = (1/\sqrt{n!})(a^\dagger)^n |0\rangle$ where $|0\rangle$ is the vacuum, with energies

$$E_n = \frac{U_a}{2}n(n-1). \quad (6.7)$$

Now, one might expect that since $t/U \ll 1$, the system is “deep in the Mott state” and the CS frequency is just $(U_a - U_{ab})(\langle n \rangle - 1)$ – the formula argued previously, but with the expectation including a thermal as well as quantum expectation. Indeed, this is implied by the sum rule approach to locate the “center” of the CS diagram. [104, 86] But it is not only the center of the CS diagram we are interested in – we will see that the diagram develops extra structure in the form of peaks at the various integer densities, even in a homogeneous system.

The proper calculation is provided in Ref. [104, 86] for a state initially in a superposition of eigenstates $|n\rangle$ with probabilities P_n . The result is that one can associate a CS Δ_n with each initial eigenstate $|n\rangle$, with only a quantum average – no thermal average. Then the resulting CS diagram consists of the sum of pieces for each eigenstate at energy Δ_n with height weighted by P_n .

In other words, we need to calculate P_n ; then the number of states transferred by the laser is just the number calculated transferred from the quantum state $|n\rangle$ (that is, the rate $\Gamma(n) \propto n$) times P_n . P_n is

$$P_n = \frac{e^{-\beta(E_n - \mu n)}}{\sum_{n=0}^{\infty} e^{-\beta(E_n - \mu n)}}.$$

Rewriting $\beta(E_n - \mu n) = \frac{\beta U_a}{2} [(n - n_0)^2 - n_0^2]$ with $n_0 = \mu/U_a - 1/2$. Hence the homogeneous CS diagram is a set of peaks at integer density enveloped by a linear function times a Gaussian with mean n_0 and standard deviation $\sigma \stackrel{\text{def.}}{=} (\beta U_a)^{-1/2}$

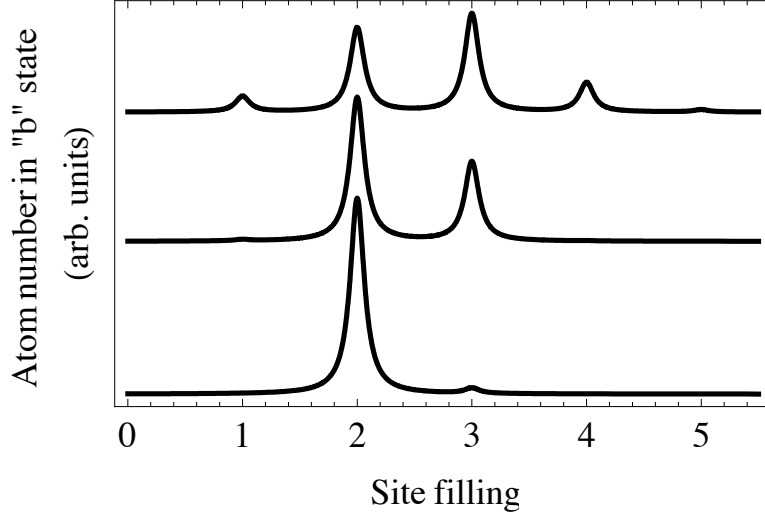


Figure 6.2: Finite temperature clock shift diagrams in the deep Mott limit for a *homogeneous system*, at temperatures $T = 0.05, 0.2, 0.8$ in units of U_a , from bottom to top. The appearance of multiple peaks signals the occupation of states with different site fillings. The chemical potential is $\mu = 1.8$ (corresponding to a $n = 2$ site filling at zero temperature).

(the normalization is unimportant):

$$\mathcal{I}_{\text{hom}}(\mu) = \mathcal{Z}(\mu) n e^{-(n-n_0(\mu))^2/2\sigma^2} \quad (6.8)$$

where $\mathcal{Z}(\mu) = \sum_{n=0}^{\infty} e^{-(n-n_0)^2/2\sigma^2}$ is for normalization.

Figure 6.2 shows a finite temperature CS diagram for a homogeneous system with a site filling $n = 2$ at the trap center (the delta function peaks are convolved with Lorentzians to simulate line broadening due).

This should serve as a warning towards use of this technique to diagnose the Mott insulating state: even a homogeneous normal lattice gas can give peaks in the Mott diagram. A defense might be that the Mott insulator is adiabatically connected to the NF, and therefore the experimental technique does not really mis-diagnose the NF. However, this is missing the point: the point is that a *homogeneous* system with no shell structure at all yields the peaks; this emphasizes the point in Ref. [119, 107] that all the peaks prove is a number squeezing of the eigenstates of the system, and they say little about the state of matter or structure

of the system in the trap.

Finite temperature Mott clock-shift diagrams in a trap

To calculate CS diagrams in a harmonic trapping potential, we use an LDA approximation: calculate the homogeneous CS diagram for local chemical potential $\mu_{\text{eff}}(\mathbf{r}) = \mu - \alpha r^2$ for each position and add these. Hence, the CS diagram in the trapped system is

$$\mathcal{I}_{\text{trap}} \propto \int_0^\infty 4\pi r^2 dr \mathcal{I}_{\text{hom}}(\mu_{\text{eff}}(r)).$$

We numerically integrate \mathcal{I}_{hom} from Equation 6.8.

To apply this to typical experiments, we must fix particle number N rather than μ as the temperature is changed. This is easily accomplished by computing N as a function of the μ and numerically inverting. Moreover, in the temperature and particle number ranges of interest (say $T < 3U_a$, $N > 10^5$), μ is nearly temperature-independent, so it is unnecessary account for this variation to produce quite accurate CS diagrams.

Figure 6.3 shows the CS diagrams for the inhomogeneous MI for various temperatures, at fixed particle number. Figure 6.3(a) gives another warning: although the system is everywhere in the singly- and doubly-occupied MI states, fillings as high as $n = 5$ can appear at temperatures on the order of U_a due to thermal excitations. Hence, the CS diagrams appear as if there were $n = 3, 4, 5$ MI shells even though no such shells exist, further questioning the interpretation of the experiments of Ref. [85].

Thermometry

As detailed in the introduction, thermometry of ultracold atomic systems is a key goal for the field. Because the MI CS diagram depends strongly on temperature

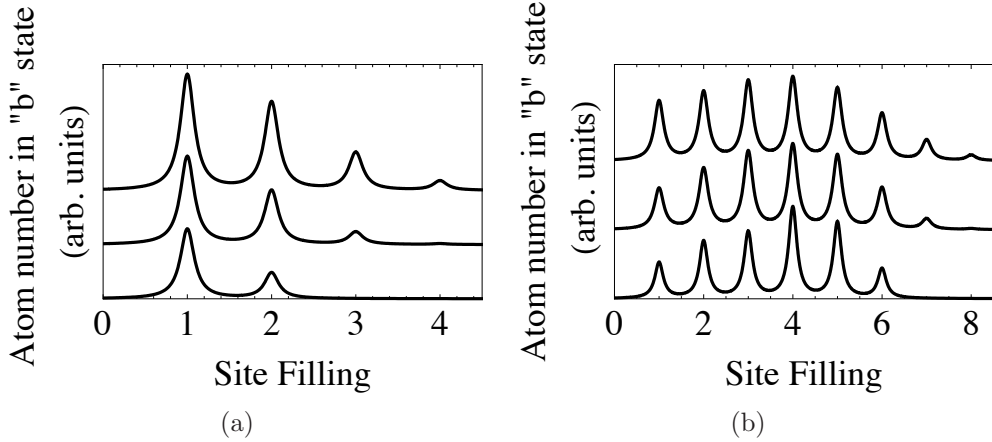


Figure 6.3: Finite temperature clock shift diagrams in the deep Mott limit for a harmonically trapped system. The temperatures are $T = 0.01, 0.7, 1.5$ in units of U_a from bottom to top. Vertical offsets are for clarity only. The chemical potential is $\mu = 1.4, 5.7$ (corresponding to $n = 2, 6$ zero-temperature site fillings at the trap center) in (a) and (b) respectively.

(e.g., new peaks appear rapidly at some temperature on the order of U_a), it suggests looking into this system as a thermometer. We argue that it has many other desirable features for thermometry.

Review and drawbacks of existing methods. Before describing the proposed thermometry method, we first review the typical method for doing thermometry – measuring density in the tails of the cloud – and highlight its drawbacks. The system becomes dilute in this region, and hence the density just decays, in the LDA approximation, as an exponential of the local chemical potential; this leads to Gaussian decay as a function of position in a harmonic trap. By fitting the Gaussian’s length scale ℓ , one obtains the temperature.

There are several drawbacks to this method, however:

1. Only a small fraction of atoms at the surface of the cloud are imaged, leading to small signal-to-noise.
2. One must inverse Abel transform columnar integrated densities to obtain the true density profile. This leads not only to additional analysis, but more

importantly to further propagation of error, and sensitivity to systematic errors from anisotropy – the Abel transform assumes isotropy about at least one axis.

3. The trap is most anharmonic in the tails; only densities inside some radius r_o are harmonic. Let r_i be the distance beyond which the density is dilute enough to be Gaussian. To accurately measure temperature, one must have $\ell/(r_o - r_i) \ll 1$.
4. If ℓ is smaller than the laser's spatial resolution ($\sim 10\mu\text{m}$), the length scale/temperature is unresolvable. Since $\ell \sim 1/T$, this imposes a fundamental limit on the lowest measurable temperatures. For a trap with frequency $\omega_0 \sim 100 \text{ s}^{-1}$ and Rubidium atoms, one find that the lowest resolvable temperatures are about 10 nK. *Much* lower temperatures are desired for simulating strongly correlated and exotic spin systems.
5. Measuring states at the edge of the cloud drives the system out of equilibrium. Although the equilibration rate may be fast, locally creating a density depletion requires that far away parts of the system adjust to account for this so that equilibration may take a prohibitively long time.
6. The measurement is not robust: (a) One needs to know the ω_0 ; large errors in ω_0 propagate to equally large errors in temperature. (b) One needs a globally harmonic trap, and anharmonicities are not automatically detected if the trap is harmonic in the tail region (as any sufficiently small region is); if the system looks harmonic locally but is anharmonic globally then the density locally looks Gaussian, but frequency is the *local frequency* of the anharmonic trap, and the temperature will be correspondingly wrong. (c) There is no way to tell from the data whether the trap is isotropic over the two directions assumed to be identical.

An ostensible solution to point (1) is to measure the complete profile of the gas rather than just the tails, but then one must fit to obtain both the chemical potential and temperature from an essentially one-dimensional function. In addition to the lack of data for this fit, there is another problem (taking a fermi gas for concreteness, though the essential problems apply to a Bose gas as well): it is an inherently nonlinear fit with multiple parameters, a notoriously hard problem in general. In this case, the fitting itself does not run into severe problems, but only a small portion of the function depends strongly on temperature, namely the tails, so that point (1) applies to this case as well and it difficult to get a much better fit by using the entire cloud.

Thermometry proposal. CS diagrams of the MI provide a thermometer free of each difficulty above. First equilibrate the MI with the measured system; by tuning the interaction strength through a Feshbach resonance or other means, the thermometer can be temporarily in equilibrium with the measured system, but turned off the dynamics are not affected after the temperature measurement. Then calculate CS diagrams as in the previous section to fit the experiment's particle number and temperature. Because of the strong qualitative change in the CS diagram with these parameters, one can fit reliably.

Perhaps the optimal situation for fitting is where the interaction energy is large enough so that at zero temperature there are no doubly-occupied states, but plenty of singly-occupied states. Then by increasing the temperature, a qualitative feature appears: a new peak at $|n = 2\rangle$, which grows with increasing temperature. The relative peak heights allows one to infer the temperature.

We enumerate ways in which this technique circumvents the problems of the density tail-measurements:

1. In CS measurements, all atoms participate and consequently one achieves

better signal-to-noise.

2. There is no columnar density integration, keeping features from washing out. Moreover, anisotropy presents no problems so long as the trap is harmonic. The calculations already given still give correct CS diagrams, because the surface area of an ellipsoid is still proportional to r^2 (with r the distance to the center of the trap); it's just the irrelevant numerical prefactor that's modified.
3. There are important contributions from the entire trap, so anharmonic tails are less important.
4. There is no intrinsic low-temperature limit. The goal is to achieve the minimum U_a , since the temperature signature is only significant when T is comparable or larger than U_a , while remaining in the MI limit ($t \ll U_a$). Hence, one needs t very small compared to U_a even when U_a is small. This can be effected by increasing the lattice spacing – this suppresses U_a as well as t/U .
5. CS measurement changes the system over the entire trap, so locally everything is still near-equilibrium, unlike the density-tail measurement where the tails are drastically out-of-equilibrium. Hence faster equilibration is expected in the CS technique, bolstered by evidence for fast equilibration in the MI system. [100]
6. The method is robust: problems are easily diagnosed. By changing the optical lattice depth U_a changes in a predictable way and hence one can calculate the expected changes in the clock shift diagram, assuming a harmonic trap. If the diagrams don't change in the expected manner, then it signals that one has an anisotropic trap, a wrong fit to the theory, or some other problem.

Because of these numerous advantages, particularly the first and the last, we expect this method to provide a substantially more robust and accurate thermom-

etry than measuring the tails of density distributions. Or, by measuring the same number of atoms as one would in the tail-measurement, one may have the same accuracy, but with less disturbance to the system.²

6.5.2 Number correlations and local compressibility.

Considering response functions provides an alternative, intuitive picture of CS diagrams, leading naturally to the direct measurement of previously inaccessible *local* compressibilities. First, define the compressibility

$$\kappa \stackrel{\text{def.}}{\equiv} \frac{\partial n}{\partial \mu}.$$

Since $\mu = \partial \epsilon / \partial n$, this can be related to a perhaps more common definition $\kappa^{-1} \propto \partial^2 \epsilon / \partial n^2$ with ϵ the energy. Systems (at zero temperature) with a gap are incompressible ($\kappa = 0$). Consequently, the MI is incompressible.

CS diagram-compressibility relation (approximate)

To establish the compressibility-CS diagram connection requires an approximation: CS diagrams are histograms of the number of particles with a local particle density n . Both the deep MI and SF limits satisfy this exactly, and everywhere else satisfies this approximately. [119, 107]

To facilitate rewriting the CS diagram $\mathcal{I}(n)$, it helps to introduce the cumulative distribution

$$C(\rho) = - \int_{\mathcal{V}_\rho} d\mathbf{r} n(\mathbf{r}) \tag{6.9}$$

where \mathcal{V}_ρ is the volume of atoms with density ρ or higher. Thus, the CS signal for densities in $(\rho, \rho + \delta\rho)$, given by $\mathcal{I}(\rho)\delta\rho$, is equal to $-C'(\rho)\delta\rho$ (the minus sign

²To be precise, the “disturbance” went from a localized drastic change to a small, faster healing, global change.

occurs because $C(\rho)$ decreases as ρ increases) and

$$\mathcal{I}(\rho) = -\frac{dC}{d\rho}.$$

Actually, $I(\rho)$ more properly is $\mathcal{I}(\rho + f)$, since we only assume that CS energies are proportional to the filling up to a constant offset, but we will ignore f ; in order to relate CS diagram as a function of ρ to CS diagrams as a function of density, we need another means of determining the offset, perhaps from theoretical considerations.

Thus the CS diagram is

$$\begin{aligned} \mathcal{I}(\rho) &= -\frac{d}{d\rho} \left[\int_0^{r(\rho)} 4\pi r^2 dr n(r) \right] \\ &= -4\pi \frac{dr}{d\rho} [r(\rho)]^2 \rho \\ &= -4\pi \frac{dr}{d\mu_{\text{eff}}} \frac{d\mu_{\text{eff}}}{d\rho} [r(\rho)]^2 \rho \\ &= -4\pi \frac{dr}{d\mu_{\text{eff}}} [\kappa(\rho)]^{-1} [r(\rho)]^2 \rho. \end{aligned} \tag{6.10}$$

The derivative is $\left. \frac{dr}{d\mu_{\text{eff}}} \right|_{\mu_{\text{eff}}(\rho)} = -\frac{1}{m\omega^2 r(\rho)}$ so

$$\mathcal{I}(\rho) = \frac{4\pi}{m\omega^2} \frac{\rho r(\rho)}{\kappa(\rho)}. \tag{6.11}$$

This relates CS diagrams at a density ρ and the compressibility of the density- ρ *homogeneous* system, providing an intuitive way of thinking about CS diagrams: large CS signal comes from relatively incompressible regions, in which the density varies slowly. As usual, it also holds in an anisotropic trap because the surface area of a constant-density shell still scales as r^2 .

Local compressibilities (approximate)

Equation 6.11 relates the CS diagram and κ :

$$\kappa(\rho) = \gamma \frac{\rho r(\rho)}{\mathcal{I}(\rho)}$$

where γ is independent of ρ . One can determine $r(\rho)$ by spatially measuring where the CS diagram absorption at energy corresponding to ρ occurs. Hence CS diagrams measure κ of the *homogeneous* phase with density ρ .

This yields a significant novel measurement tool. Although one can presently measure the *global* compressibility of the trapped system by changing the trap frequency and seeing how the filling distribution changes, the *local* compressibilities are elusive. The deep MI system provides a particularly striking example of the limitations of measuring only global compressibility. Even though the MI is everywhere incompressible, with $\kappa(\rho) = 0$, the global compressibility is finite. [101] This is due to the regions at the edges of MI shells where the gap closes; here the system is compressible. Although these regions strictly occupy zero volume, they provide a mechanism for density adjustment by particles moving across these regions, leading to a globally compressible system.

Finally, it is worth relating the compressibility to number fluctuations, so that one has another tool for measuring these as well (or, conversely, another tool for calculating CS diagrams). The site- i compressibility is

$$\kappa_i = \frac{\partial \langle n_i \rangle}{\partial \mu_i} = \beta (\langle n_i^2 \rangle - \langle n_i \rangle^2)$$

via usual correlation-response relations.

CS diagram-compressibility relation in the general case

While Equation 6.11 is useful for interpreting and calculating CS diagrams, as well as for a novel measurement, it is true only insofar as the CS energy is proportional to the density, up to an additive constant. Though this is exact in both the deep MI and SF limits, and to a good approximation true in between, it need not be accurate for general systems. Consequently, it is valuable to pursue an exact, general relation for those cases.

The CS diagram is in general functions of $\mathcal{S} \stackrel{\text{def.}}{=} \langle n(n-1) \rangle / \langle n \rangle$. So introduce the analog of Equation 6.9:

$$C(\mathcal{S}) = - \int_{\mathcal{V}_s} d\mathbf{r} n(\mathbf{r}).$$

The CS diagram $\mathcal{I}(\rho)$ is

$$\mathcal{I}(\mathcal{S}) = - \frac{d}{d\mathcal{S}} \left[\int_{\mathcal{V}_s} d\mathbf{r} n(\mathbf{r}) \right]$$

since $\mathcal{I}(\mathcal{S})\delta\mathcal{S} = C(\mathcal{S}) - C(\mathcal{S} + \delta\mathcal{S})$ from the definition of \mathcal{I} and C . Differentiating, essentially repeating the steps to Equation 6.10 while assuming the CS observable is monotonic in displacement from the trap center,

$$\mathcal{I}(\mathcal{S}) = -\gamma \frac{d\mu_{\text{eff}}}{d\mathcal{S}} r(\mathcal{S}) n(r(\mathcal{S})). \quad (6.12)$$

This is the generalization of the CS diagram-compressibility relation: $\frac{d\mathcal{S}}{d\mu_{\text{eff}}}$ takes the role of the compressibility, and $n(r(\mathcal{S}))$ – that is, the density corresponding to CS observable \mathcal{S} – takes the role of the density ρ .

Finally, as in the approximate case previously treated, the response $\frac{d\mathcal{S}}{d\mu_{\text{eff}}}$ can be related to number fluctuations through a usual “correlation-response” derivation:

$$\begin{aligned} \frac{d\mathcal{S}}{d\mu_{\text{eff}}} &= \beta \left[\frac{\langle n^3 \rangle - \langle n^2 \rangle \langle n \rangle}{\langle n \rangle} - \frac{\langle n^2 \rangle}{\langle n \rangle^2} (\langle n^2 \rangle - \langle n \rangle^2) \right] \\ &= \beta \left(\frac{\langle n^3 \rangle}{\langle n \rangle} - \frac{\langle n^2 \rangle^2}{\langle n \rangle^2} \right). \end{aligned}$$

Summary

In summary, we previously thought of the CS peaks as coming from corrugated density profiles, and the height of a CS diagram getting larger as the density changes more slowly with μ or r ; here, we made this precise, and showed (in an approximation) that additionally (1) the CS diagram’s height at a density n is related in a precise way – Equation 6.11– to the *local* compressibility and

n ; and (2) this is directly related to the number squeezing and fluctuations of the state. We then derive the general versions of this statement, Equation 6.12. Finally, we pointed out that the local compressibility previously was experimentally inaccessible, and this opens up a new window into the local thermodynamic and quantum phases that appear in an inhomogeneous, trapped system.

The relations readily generalize to arbitrary dimension.

6.6 “Inverse clock diagram” calculation

Here we show that the CS diagram can be uniquely inverted to yield the density profile up to an overall spatial scale, under the assumptions of a monotonically changing density in a harmonic trap.

6.6.1 Inverse diagram when clock shift energy is proportional to the density plus a constant

First, we use the development of Section 6.5.2, and work in the same approximation as there: that the CS energy is proportional to the density up to some constant-in-the-trap offset. Later we will examine how this approximation can be eliminated.

Equation 6.10 shows that the CS diagram is given by

$$\mathcal{I}(\rho) = -\gamma\rho r^2 \frac{dr}{d\rho}$$

where γ is a constant independent of x and ρ . This is a differential equation for ρ , written in the usual form as

$$\frac{d\rho}{dr} = -\frac{\gamma}{\mathcal{I}(\rho)} r^2 \rho.$$

Re-arranging, and always considering equality up to a constant,

$$\begin{aligned} \frac{1}{r^2 \rho} \frac{d\rho}{dr} &= -\frac{1}{\mathcal{I}(\rho)} \\ \Leftrightarrow \frac{d(\log \rho)}{d(r^3)} &= -\frac{1}{\mathcal{I}(\rho)}. \end{aligned}$$

In this form, it is clear that any constants can be absorbed into r , so that constants only change the overall spatial scale. Since this is one-dimensional differential equation, we can integrate to obtain

$$\begin{aligned} -r^3 &= \int_{-\infty}^{\log \rho} d(\log \rho) \mathcal{I}(\rho) \\ -r^3 &= \int_{-\infty}^{\log \rho} d\zeta \mathcal{I}(e^\zeta). \end{aligned}$$

The right-hand side of this equation defines a new function

$$F(\rho) \stackrel{\text{def.}}{=} \int_{-\infty}^{\log \rho} d\zeta \mathcal{I}(e^\zeta) \tag{6.13}$$

which can be calculated and inverted numerically to obtain ρ as a function of r .

Thus

$$\rho = F^{-1}(-r^3) \tag{6.14}$$

and the full inverse CS transform is given by Equations 6.13 and 6.14. In regions where the CS diagram is essentially flat, the spatial variation is correspondingly e^{-r^3} .

Actually, as discussed in Section 6.5.2, the expressions above only holds for $\mathcal{I}(\rho + f)$ where f is an offset, and not for $\mathcal{I}(\rho)$ itself, so our density profiles may be shifted by a constant value by the values we will determine below; however, we should be able to obtain the correct constant by ensuring that the density goes to zero at infinity.

6.6.2 Inverse clock shift diagram in the general case

The general case, where CS energies are not proportional to the site filling plus a constant, was considered in Section 6.5.2, as well. We can try to invert this relation in a similar manner as in the previous subsection by noting that the CS diagram is given by (equation is up to a rescaling of r again)

$$\mathcal{I}(\mathcal{S}) = -n(\mathcal{S})r^2 \frac{dr}{d\mathcal{S}}$$

which is re-arranged to give

$$\frac{d\mathcal{S}}{dx} = -r^2 \frac{n(\mathcal{S})}{\mathcal{I}(\mathcal{S})} \quad (6.15)$$

which is not solvable without knowledge of $n(\mathcal{S})$. This is the general formula for the “inverse clock shift diagram.” In practice, if one knows *something* about the relation between \mathcal{S} and n , one can hope to solve this equation and obtain the \mathcal{S} profile in the trap. As an example, assume that one knows $\mathcal{S} = n + Dn^2$ for some constant D , so one knows that $n(\mathcal{S}) = (1/2D)(-1 \pm \sqrt{1 + 4D\mathcal{S}})$. Then one can solve Equation 6.15 if one knows D ; even if D is unknown, the differential equation can be solved for all possible values of D and all possible density profiles examined that could correspond to the given CS diagram.

These equations can be readily generalized to (possibly anisotropic) harmonic traps in arbitrary dimension.

6.6.3 Cooling and quantum register initialization

A key requirement for all quantum algorithms is the production of a well-characterized initial (“fiducial”) state; a popular choice for neutral ultracold atomic gas proposals is the $n = 1$ MI. However, forming the MI invariably forms defects. Spectroscopically addressing and removing atoms from sites having too many or

few atoms, the system moves towards an ideal MI state, as suggested in Ref. [85]. We point out that such manipulation towards a single quantum state constitutes cooling. This should then enable temperatures even lower than present. The MI can then sympathetically cool others.

6.6.4 Measuring spatial correlations; quantum computer readout

As a final – and arguably the most potent – application of the CS diagram measurements, we show how it can be used to measure details of spatial correlations. Actually, we present two techniques: first, an idea with limited scope, and then a more interesting idea that enables substantially informative imaging of spatial correlations. Specifically, it provides the ability to measure all m -point density correlation functions $\langle n_i n_j \cdots n_m \rangle$ or equivalent, the probability distribution $P(n_i, n_j, n_k, \dots)$ for having n_i atoms at site i , n_j at site j , etc. We mention in passing that this might function as a state readout for a quantum computer, since it can provide the probability of two qubits i and j being in states s_i and s_j respectively. We will show elsewhere that this enables partial measurement of the n -body Green's functions of *arbitrary* systems for n not too large.³

The simplest spatial correlation probe with CS diagrams is perhaps to measure very accurately the CS lineshapes. Since the system is trapped, the external potential will manifest the correlation functions of the homogeneous phase in the trapped system's density profile; this follows immediately from the correlation-response relation. This method is fraught with numerous difficulties, however: the trap must vary significantly in a correlation length to produce a measurable signal, it is necessary to know the LDA lineshapes extremely accurately, since one is

³Forthcoming.

measuring the corrections to these, and because the density is not monotonically decreasing from the center of the trap, one cannot uniquely reconstruct in any straightforward way the density profile. (For the monotonic case, we treat the “inverse transformation” in Appendix 6.6.) Because of these problems, the method will not be of broad utility.

Background for proposed experimental probe: clock-shifts in the presence of long-range interactions

A significantly better proposal enables measuring spatial correlation functions – including the density-density correlation function, but going well beyond this. Moreover, it is applicable to a broad set of systems.

The method is implemented by augmenting the on-site interaction with a small, off-site potential, different for a - a and a - b interactions. The system is tuned deep into the MI state, and the long range interaction needs to be small enough so as not to disturb the state of the system. Henceforth, we refer to the off-site potential as “long-range.” Possible candidates for the long-range interaction then are dipolar condensates and nearest-neighbor interactions. Condensates with significant dipole moments have been realized with chromium, [62] with stronger dipolar interactions via diatomic molecular condensates or Rydberg atoms appearing in the near future [56].

Because our proposed spatial correlation measurement will not depend in any crucial way on the details of the potential used, we consider a general 2-body potential

$$V_l \stackrel{\text{def.}}{\equiv} \sum_{i \neq j} \sum_{\alpha, \beta} V_{\alpha\beta}^{(l)}(i, j) n_{i,\alpha} n_{j,\beta}$$

where $V_{\alpha\beta}^{(l)}(i, j)$ give the interaction of an atom of type α at site i with an atom of type β at site j , the first sum runs over all pairs (i, j) such that $i \neq j$, and the

second runs over $\alpha, \beta \in \{a, b\}$. We can assume $V_{\alpha\beta}^{(l)} = V_{\beta\alpha}^{(l)}$.

For simplicity of analysis, we consider the probe system to be confined to one-dimension; this is not a necessity for the measurement technique, but simplifies the exposition of the idea behind the technique.

Clock shift diagrams with long-range interactions

The clock shift diagram observed in a system with a long range interaction is interesting and the basis for our measurement proposal.

In the deep MI, since the sites decouple, the complete set of eigenstates is $|\{n_i\}\rangle \stackrel{\text{def.}}{\equiv} \bigotimes_i |n_i\rangle_i$ where $|n\rangle_i$ is the state with n particles at site i . Thus n_i represents the number of particles at site i ; the set n_i 's can take any integer value, independently for each i .

As discussed previously, a system in a superposition of initial eigenstates $|\psi\rangle$ with probability P_ψ responds to a transfer laser with probability P_ψ if the laser is on resonance with the CS energy for state ψ . In other words, as discussed in the sections on finite temperature, the expectation values occurring in the formulas for the CS energy are not taken over a thermal ensemble of quantum states – this gives the “center” of the entire CS diagram; instead, the contribution from each eigenstate is calculated using the quantum expectation in that eigenstate.

The CS energy for the state $|\{n_i\}\rangle$ is, using the method of calculating commutators from Ref. [104],

$$\begin{aligned} \Delta_j &= \delta E_{1,j} + (U_{ab} - U_a)(n_{j,a} - 1) \\ &\quad + 2 \sum_{i \neq j} \delta V_{i,j} n_{i,a} \end{aligned} \tag{6.16}$$

with $\delta V_{i,j} \stackrel{\text{def.}}{\equiv} V_{ab}^{(l)}(i, j) - V_{aa}^{(l)}(i, j)$.

Notice the crucial feature of the resulting CS energies: Equation 6.16 shows that each spatial variation leads to a different Δ_j : **each CS diagram peak is**

uniquely associated with a spatial correlation, and allows us to determine the probability of that correlation occurring in the initial state. That is, the number of particles at site j times $U_{ab} - U_a$ gives the on-site CS energy contribution, while the number of particles at the neighboring site times δV_{ij} (which should be somewhat smaller than $U_{ab} - U_a$ to unambiguously associate peaks with spatial variations – see Section 6.6.4) for i and j being nearest neighbors gives the nearest neighbor contribution, and so on. The weight of the peak is proportional to the number of sites in the transfer laser’s path satisfying the criterion that the correlations in its nearest neighbors, next-nearest neighbors, and so on are appropriate to the energy of the transfer laser.

Figure 6.4 shows an example CS diagram and how to read off the spatial correlations. It is generated, just for illustration, with a three-(relevant)-site MI with all possible states such that each site is unoccupied or singly-occupied having equal probability. We have labeled some of the peaks to visually illustrate how the probabilities corresponding to various number fluctuations/correlations are manifested in the CS diagram.

As a final note, if one can focus the laser beam to a single lattice site, one can measure the correlations specifically involving that site; otherwise one measures the average over the transfer laser beam’s volume.

Constraints on experimental parameters

Let’s thoroughly examine the restrictions on the interaction due to competing requirements of not disturbing the MI and having a large enough to be resolvable energy shift. Moreover, the interaction needs to be small enough that the peaks can easily be associated with spatial variations – for too large interactions, the peaks of Figure 6.4 get mixed up and are difficult to assign to their given spatial variation.

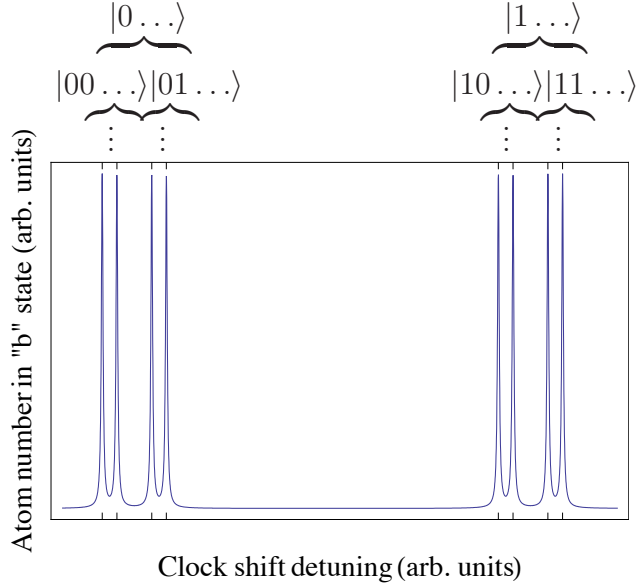


Figure 6.4: Deep Mott clock shift diagram with dipolar interactions for the state given in the text. The correspondence between peak and spatial variation is indicated, where a string “ $n_1 n_2 n_3$ ” indicates n_1 particles in the first neighbor site, n_2 in the second neighbor, and n_3 in the third neighbor. The labels instruct how to read-off the probabilities for each state.

The condition that the MI not be disturbed by the long-range interaction is

$$V_{\alpha\beta}^{(l)}(i, j) \ll U_a \quad (6.17)$$

for all i, j ; this is due to the fact that U_a sets the energy scale for the Mott physics. This condition is not terribly difficult to satisfy; if nothing else, one can increase the lattice depth and hence U_a .

A helpful condition for associating particular peaks with particular states is the condition that

$$\left[V_{ab}^{(l)}(i, j) - V_{aa}^{(l)}(i, j) \right] (n - 1) < U_{ab} - U_a \quad (6.18)$$

is the difference in CS energies between states with n and $n + 1$ atoms, for n the maximum filling of interest to which the system fluctuates (more attention to the i, j dependence is required and will be given in a moment); this ensures that the correlation-probing shifts due to interactions with neighboring sites is less than

that due to the on-site CS, so that all the side-peaks to a given filling n (due to offsite correlations) are less than those of filling $n + 1$.

In competition with the previous conditions, however, is the condition that the correlations between i and j be resolvable; this requires that

$$V_{ab}^{(l)}(i, j) - V_{aa}^{(l)}(i, j) > W \quad (6.19)$$

where W is the linewidth of the MI peaks. It is not too difficult to meet these requirements since W and $(U_{ab} - U_a)/n$ can be separated by orders of magnitude: they differ already factor of 2-3 in Campbell *et al.*'s experiments, while using, say, sodium would increase $U_{ab} - U_a$ by a factor of 30. [85] The linewidth of Ref. [85] looks pulse limited, so longer pulses could presumably decreasing W further. Conservatively, a factor of roughly 200 between $U_{ab} - U_a$ and W seems achievable. If one can find or design an interaction such that $V_{ab}^{(l)} - V_{aa}^{(l)}$ is close to the minimum allowed value of W , one can measure fluctuations in particle number up to 200 – likely a far larger number than will be of interest in the near future.

Actually, so far we have failed to treat the interaction's i, j dependence carefully, and doing so imposes further constraints. Because the dipole-dipole interaction, which decays as $1/r^3$, is the most favorable to measuring correlations between far-away sites in neutral atomic systems, we will give it special consideration in the analysis. The constraint given by Equation 6.17 is easily satisfied.

Turning to the constraint of Equation 6.18 with a proper consideration of i, j dependence, it should more properly state that, picking a site j , the sum over all $i \neq j$ of the interaction with that site gives an energy that is smaller than the CS energy between filling n and $n + 1$ at site j ; the sum was ignored in this formula. However, even for the longest range potential of interest, the dipole-dipole-interaction, this sum is of the form $V \sum_{l=1}^{\infty} n_l/l^3$ for some constant V with l the displacement away from j . We can get an upper bound on this energy by

considering the maximum filling to which the system might fluctuate, say n_{\max} and replace n_l by this filling, yielding for the sum $V n_{\max} \zeta(3) \approx 1.2 V n_{\max}$ where ζ is the Riemann zeta function. Thus, we need only replace $U_{ab} - U_a$ with $(U_{ab} - U_a)/1.2$ in Equation 6.18.

Equation 6.18 needs further augmentation for sideband resolvability: all of the $|n_1, n_2, \dots\rangle$ states must be lower in energy from $|n_1, n_2 + 1, \dots\rangle$ states, and so on for states with the first m -sites with equal filling. This limits one to $1.2 n_{\max} \lesssim n_{\max} + 1$ or $n_{\max} \lesssim 5$. Faster decaying potentials enable larger n_{\max} , although that comes with another tradeoff (see next paragraph).

Finally, we include i, j dependence in Equation 6.19's constraint. This equation is easily corrected: it just says that for any pair of sites i and j 's whose correlations are to be measured, one must have $V_{ab}^{(l)}(i, j) - V_{aa}^{(l)}(i, j) > W$. The correlations between sites i and j will be resolved for sites (and only for sites) such that Equation 6.19 is satisfied. For the dipole-dipole potential, we see that this constraint simultaneous with the constraint in Equation 6.18 seriously limits the distance between sites whose correlations can be measured, if one wants also to resolve the nearest-neighbor correlations: we want to maximize $V_{ab}^{(l)}(i, j) - V_{aa}^{(l)}(i, j)$ while satisfying Equation 6.18. Call the resulting optimal nearest neighbor interaction V . Then for sites 2, 3, 4, ... sites apart, the energies are $V/8, V/27, V/64, \dots$. Hence, even if $V/W \sim 100$, only sites a few lattice spacings apart are measurable, and at that distance, rather than being able to measure particle fluctuations ~ 100 as in the nearest-neighbor correlations, one is limited to fluctuations that are on the order of unity (indeed, this signals in general that one measures the furthest possible correlations). By increasing $U_{ab} - U_a$ and V correspondingly, one can do better, but the growth in distance between sites measurable is slow, going as $(U_{ab} - U_a)^{1/3}$.

We have just seen that the constraints in Equations 6.17, 6.18, and 6.19 strongly

constrain measuring correlations between distant sites simultaneously with the nearest sites, but they provide ample opportunity to measure at least the nearest-neighbor correlations. Moreover, even if we use only the nearest neighbors, arbitrary distances can be created between the two sites simply by adjusting the lattice spacing of the optical lattice. The only feature and constraint uncovered by proper treatment of the i,j dependence, then, is the inability to easily measure correlators involving more than two sites. Still, through careful choice of interactions to fully exploit the range of energies allowed by Equations 6.17, 6.18, and 6.19, by straightforward development of present apparatuses three- or four-site correlators of n -body correlations are measurable!

Measuring away from the deep Mott state

Let's consider the system *away from the deep Mott limit*: it may be at finite temperature in the MI, at finite t/U in the MI, or in the SF. More generally, other interactions/Hamiltonian terms could be turned on to study new phases (for example, one could engineer dipolar interactions, spin-dependent interactions, more complex lattices, whatever...); we show here that all these systems can be measured by straightforward application of the method suggested in Section 6.6.4.

In Section 6.6.4 we showed that CS diagrams with perturbing state-dependent off-site interactions measure probabilities of spatial variations, assuming the system was in the deep MI. However, for a general boson lattice system, it is in principle easy to imprint the correlations of the system into an out-of-equilibrium deep MI, simply by ramping up the lattice instantaneously.

Recall from elementary quantum mechanics the so-called “instantaneous” or “sudden” approximation. The Hamiltonian of the system is switched from H_- to H_+ instantaneously at a time $t = 0$. Let's call the state for $t < 0$, $|-, t\rangle$, and call $|S\rangle$ the eigenstates of H_+ . The key observation is that the wavefunction is

continuous in time, so that enforcing continuity and expanding the final state in terms of the eigenstates of H_+ gives

$$\lim_{t \rightarrow 0^-} |-, t\rangle = \sum_S A_S |S\rangle,$$

with $A_S = \langle S|-, 0\rangle$. For $t > 0$, $|A_S|^2$ is the S -state probability.

This is usefully combined with Section 6.6.4's measurement. We work with a general system (most commonly, but not necessarily) in equilibrium for a Hamiltonian H_m of interest, which may be arbitrarily complicated; then the Hamiltonian is suddenly switched to that of the deep MI limit of the BH Hamiltonian. Via the sudden approximation, this creates the equilibrium state of H_m , in a system with a Hamiltonian for the deep MI limit of the BH model. The method of Section 6.6.4 can then be utilized to measure the correlations of this state.

An illuminating, simple, and very important example is provided by the SF in the BH model. Initially the system is in equilibrium in a SF region of the phase diagram. Then the lattice is ramped up quickly; the site-to-site hopping is suppressed (exponentially) with the increasing lattice height, and hence one very quickly is in the MI. As in the general case, the correlations are measurable via the procedure of Section 6.6.4.

In short, we have proposed an extremely informative experimental protocol for measuring spatial correlations. The requisite technology is mostly developed: the components of the measurement technique – CS measurements, “long range” interactions, and dynamic control of experimental parameters – have all been demonstrated.

6.7 Conclusions

General finite temperature effects in the superfluid and Mott insulator were considered. Both the superfluid and Mott insulator were shown to develop qualitatively new features at sufficiently high temperatures: in the superfluid, a peak near zero clock-shift energy coming from the tail of excitations, and in the Mott insulator a set of peaks corresponding to fillings that are not the ground state filling.

Furthermore, we show that finite temperature *homogeneous* Mott states or non-equilibrium states can lead to multiple Mott peaks, since different filling eigenstates are occupied: this gives an illusion of inhomogeneity if interpreted using the naïve zero-temperature theory. In a trap, we saw that a $n = 1$ zero temperature Mott insulator can appear like a series of Mott shells from the perspective of the clock-shift diagram. Hence, on its own, the technique is not sufficient to conclusively identify the Mott state and its properties.

Finally, we propose and analyze a number of experimental applications: performing thermometry and selective cooling; measuring density profiles via an inverse clock-shift transform, measuring the number-squeezing correlations of the superfluid, and measuring spatial correlations of the system, each of which addresses significant challenges and has significant potential in the field.

To overview the applications, the proposed *thermometry* allows measurements temperatures down to the smallest Mott gaps one can create, which are in turn limited only by how small one can make the hopping; since wider lattice depths decrease this exponentially, this appears to offer considerable opportunity. We have argued that the thermometry possesses many additional desirable features of accuracy, robustness, and self-diagnosis lacking in current methods. The *cooling* offers prospects to reach lower temperatures. The *inversion of clock-shift diagrams* to

give density profiles gives complementary information to Abel-transforming columnar integrated density profiles. A similar argument shows that the magnitude of the clock shift signal is related in a simple fashion to the *local compressibility*, which is otherwise inaccessible to experiments (these generally measure only the global compressibility). Finally, the most ambitious proposal, as well as the most experimentally difficult, is *an experimental technique to measure general n-point density correlation functions*.

Chapter 7

RF spectra: summary, conclusions, and the future

To summarize our studies of RF spectroscopy, we have showed that two common but qualitatively distinct pictures of RF spectroscopy — one based on sum rules, and one based on single particle Green’s functions — emerge as special limits of a more complete calculation, depending on the final state interactions through the quantity $(U_{ab} - U_{aa})/t_a$. In the deep Mott and superfluid limits, we have extended our calculations to finite temperature. We have also discussed how RF spectra with interactions beyond on-site may be used to probe full joint number distributions between sites, for example using Rydberg excitations or molecular gases.

Experimentally, an exciting future goal for the field would be the observation of the bimodal spectrum identified in Chapter 5. The main impediment to immediate observation by the MIT group is that they use ^{87}Rb , which in typical optical lattices displays a significant bimodal feature in only a small part of the phase diagram. Two routes may circumvent this: (i) one may use spin dependent optical lattices to displace the two spin components’ lattices, in which case U_{ab} can be significantly smaller than U_{aa} (this setup is being pursued by the MIT group [95]) or (ii) one may use a different species, such as Na, Yb, or Cs, which possess larger η ’s or Feshbach resonances (Cheng Chin’s group is ideally poised to study this using Cs and high resolution *in situ* imaging techniques for the 2D Bose-Hubbard model). This could lead naturally to observation of non-quasiparticle behavior in the quantum critical regime using the tools developed in Chapter 14.

Theoretically, it is desirable to better understand the structure beyond the flat-band approximation inherent in the Gutzwiller approximation (that is, to incorporate intermediate range correlations). There exists a formalism to go be-

yond Gutzwiller in a way that correctly reproduces the Bogoliobov low energy excitations in the deep superfluid [115, 113]. Konabe *et al.* and Ohashi has computed the RF spectra for vanishing final state interactions ($U_{ab} = 0$) using this method [114, 109]. This approach captures the finite bandwidth in the Mott insulator as well as the different dispersion for the a and b type atoms in the deep superfluid limit. Finally, the latter limit could be treated simply and directly via Bogoliobov theory.

As another theoretical avenue, the prospect of a more complete understanding of the finite temperature phase diagram is highly exciting. As one example, discussed in Chapter 15, the RF spectra can display non-quasiparticle behavior. To capture the quantum dynamics in the critical region, we will require a different approach. The large- N and ϵ expansions offer possibilities to qualitatively capture the physics [121]. Cold atom experiments have potential to dramatically improve our understanding of the validity of these expansions.

Finally, an understanding of how the state created in RF spectroscopy evolves at long times to equilibrium would be interesting from the point of view of far from equilibrium physics, for understanding rf spectra in practice (which are only moderately in the linear response regime), and could shed light on accuracy of atomic clocks [87, 88]. Numerically solving our time-dependent mean field theory beyond the linear response regime would be a natural building block for a theory of this equilibration, but the extent to which this provides an accurate treatment of the physics is unclear.

Another interesting idea to calculate quantum critical properties (more generally than RF spectra) is inspired by our work: we can try to develop a perturbation theory in $\eta = (U_{ab} - U_{aa})/t_a$. This may be feasible since for $\eta = 0$, one obtains a simple spectrum of an unshifted delta function, and for small η in our calculation

this always leads simply to a shift. It would be interesting to see if this approach allows a seemingly quite novel alternative to other types of expansions, with the additional advantage that the $\eta = 0$ limit is physical, in contrast to large- N and ϵ expansions.

Chapter 8

Rotation, inducing gauge fields, and exotic states of matter in cold atoms

Rotating quantum systems leads to dramatic and exotic phenomena. The first rotational phenomena to be experimentally explored in cold atoms is the appearance of vortices and vortex lattices in a rotating superfluid. Because a superfluid is irrotational, all rotation is contained in topological defects with circulation quantized in units of \hbar . This is a phenomena that occurs in superfluid ^4He and ^3He , as well as in type-2 superconductors (superconductors only show vortices in a certain limit, corresponding to type-2 superconductors, because the electromagnetic field's energy also has to be considered [122, 123, 124]). Images of vortices in cold gas experiments directly showed this spectacular manifestations of superfluidity.

Faster rotation is predicted to manifest more exotic behavior. A specific case is discussed in Section 8.1, but we can understand this very generally from a few qualitative perspectives. One way of looking at the physics is that a gauge field introduces a quantum mechanical phase for a particle to traverse a loop (introducing or increasing the severity of the “sign problem” into the physics, making it difficult to simulate). Another perspective is that the wavefunction must be single-valued, yet minimizing the energy cost of phase twists upon traversing a loop fails to satisfy this condition; this “frustration” leads to any loop drawn in the system to have competing kinetic energies which can be resolved by interactions. Perhaps the most general viewpoint is the observation that rotation causes the appearance of a degeneracy. This is particularly striking for fast rotation when rotation leads to macroscopically degenerate Landau levels [33].

More generally than just rotation, we are interested in inducing “effective gauge fields.” I will discuss methods of stabilizing exotic states in cold atom systems,

especially those induced by “effective” gauge fields. Most often, one engineers the system so that the neutral particles behave as if they were atoms in a homogeneous magnetic field. Rotation is the most common approach [125, 126], but there has been recent success with light-induced gauge potentials — Refs. [127, 128, 129] give some prominent proposals and Ref. [130] gives an experimental realization. These techniques also enable non-Abelian gauge fields [131] and may allow creation of the stronger gauge fields necessary to induce exotic behavior (more on this below). I will discuss some of these approaches. I will also introduce a novel approach, which utilizes time-dependent laser configurations, and discuss some of the possibilities this could open up. The most interesting — and long-term — possibility is the study of topological phases of matter (e.g., the fractional quantum hall effect) on non-trivial topologies (e.g., a torus).

It is worth noting that the gauge fields discussed here are static, external gauge fields. Emulating dynamic gauge fields with their own degrees of freedom is another, further off, experimental possibility for which theoretical proposals exist (for one example, see Ref. [132]).

This chapter provides the background to understand methods to induce gauge fields, as well as the properties of the resulting physical states.

8.1 Physics of rotating particles/particles in gauge fields

Much fascinating physics occurs when particles are subjected to gauge fields. I briefly review some of the most intriguing and experimentally relevant examples: vortices, the integer quantum Hall effect and interplay with lattices (Hofstadter butterfly), and the fractional quantum Hall effect. Table 8.1 gives an overview of classes of physics formed by the interplay of rotation, lattices, and the trap for bosonic atoms in limits where one or two of these dominate the physics, demon-

strating the richness of the general case, even for purely scalar bosonic systems.

8.1.1 Vortices

Assuming interactions and rotation are weak enough so as to not destroy the Bose-Einstein condensate, we may describe it via a condensate wavefunction $\psi(\mathbf{r}, t) = A(\mathbf{r}, t)e^{i\phi(\mathbf{r}, t)}$, writing ψ in terms of an amplitude $A(\mathbf{r}, t)$ and a phase $\phi(\mathbf{r}, t)$. Define the current operator $\mathbf{j}(\mathbf{r}, t)$ via $\partial_t \rho = -\nabla \cdot \mathbf{j}(\mathbf{r}, t)$ with $\rho(\mathbf{r}, t) = |\psi(\mathbf{r}, t)|^2$ the density at point \mathbf{r} and time t . Then using that ψ solves the Schrödinger equation, we find that

$$\mathbf{j} = \frac{\hbar}{m} \nabla \phi. \quad (8.1)$$

Thus the rotational circulation is

$$\begin{aligned} \oint d\mathbf{r} \cdot \mathbf{j}(\mathbf{r}) &= \frac{\hbar}{m} \oint d\mathbf{r} \cdot \nabla \phi \\ &= \frac{\hbar}{m} (\phi_f - \phi_i) \end{aligned} \quad (8.2)$$

with ϕ_i the phase at \mathbf{r} before traversing the loop and ϕ_f the phase at \mathbf{r} after. If ϕ were a single valued function, these would be identical, but we require only that the wavefunction ψ is single valued, requiring ϕ to be quantized to $\phi = 2\pi n$ for integer n , and consequently

$$m \oint d\mathbf{r} \cdot \mathbf{j}(\mathbf{r}) = 2\pi \hbar n. \quad (8.3)$$

Thus the momentum circulation of a condensate is quantized in multiples of $h = 2\pi\hbar$. That is, it appears in discrete jumps, by vortex formation. Associated with the circulation, by contracting the loop, there must be a singularity in the wavefunction, at which point ρ vanishes, and this shows up as zero density points in the spatial absorption images, leading to spectacular images of vortices and vortex lattices in cold atoms [138].

Table 8.1: Behavior of rotating lattice bosons in the simplest limits for *homogeneous* systems. The various length scales characterize interactions (scattering length a), the trap (oscillator length ℓ), the lattice spacing (d), and rotation (rotational length ℓ_R). Here \wedge represents logical “AND” and \vee the logical “OR.” One sees that even for the homogeneous system there are a remarkable variety of limits: the ordinary Bose-Hubbard model is arguably the simplest of all the limits, and it already displays the highly non-trivial physics of the superfluid physics. Each of the limits is an areas of study in its own right. The references are representative, not comprehensive.

Limit	Behavior
$(a = 0) \wedge (\ell_R \gg \ell) \wedge (\ell \ll d)$	Hofstadter butterfly [133]
$(a = 0) \wedge (\ell \gg d)$	Thouless butterfly (dual of Hofstadter butterfly) [134]
$(a \ll r_s) \wedge (\ell_R \gg \{d, r_s\})$	Vortex lattices [135, 136, 137, 138, 139]
$(a \gg \ell_R - \ell) \wedge (\ell_R \lesssim r_s) \wedge [(r_s \gg d) \vee (\ell \gg d)]$	Bulk fractional quantum hall [140, 141, 142]
$(a \gg \ell_R - \ell) \wedge (\ell_R \lesssim r_s \lesssim \ell \ll d)$	FQH puddle arrays [143, 144, 145, 146, 147, 148, 149, 150]
$(\ell_R = \infty) \wedge (\ell \ll d)$	Non-rotating strongly interacting bosons: atomic SF/molecular SF QPT [151, 152, 153]
$(\ell_R = \infty) \wedge (0 < a \ll \ell \ll d)$	Non-rotating ordinary Bose-Hubbard model [91, 77]

8.1.2 Vortices in lattices: Hofstadter butterfly

Vortices can have intriguing interplay with external potentials, including static disorder, the trapping potential, and lattices. The first is responsible for pinning of flux lines in type-2 superconductors [124]; the second, in the case of a very thin toroidal potential (or an annular cell for, say, helium experiments), vortex tunneling across the annulus is expected to be the dominant decay mechanism for destruction of the superfluid flow [154, 155].

External lattice potentials also display rich rotational physics. In a simple picture, one might expect pinning of low density cores at the maxima of potential energy in between sites. Some understanding exists for low vortex densities (compared to the lattice spacing). The picture is essentially true for fairly deep lattices and low vortex density, but for weak lattices the pinning may be destroyed because the vortex-vortex interaction favors a triangular lattice. This leads to a set of structural phase transitions, and the competition between phases may be selected by interactions; this has been studied, along with the effects of the trap, by Goldbaum and Mueller [156, 157].

For high vortex densities, approaching one vortex per site, less is known. The non-interacting case is understood for very deep (tight-binding) and for very shallow (perturbative) lattices, and the energy spectrum shows a remarkable fractal structure as a function of vortex filling, called the “Hofstadter butterfly [133].”

There is similar structure for weak lattices [134]. As an aside, at some point I collaborated with an excellent undergraduate (Tim Yang) to numerically solve the equations for intermediate lattice depths, enabling us to study the crossover between these limits.

8.1.3 Quantum Hall effect

When rotation rates are increased above those considered previously, so that the effect of rotation destroys the condensate, more exotic physics are stabilized. In particular, various quantum Hall states can appear. It is impossible to characterize these states with a local order parameter, possess topological order, undergo phase transitions without symmetry breaking, and display fractionalized excitations (See Chapter 9 and references therein). These highly intriguing states will be the main cases of rotational physics considered in this thesis, discussed in Chapters 9 and 10.

The simplest case occurs for non-interacting particles in the absence of a lattice (which is a continuum limit of the Hofstadter problem). The physics can be understood from a simple semiclassical picture of particles in a magnetic field (which Section 8.2.2 shows is equivalent to a rotating system). The quantum mechanical system in a strong magnetic field forms spin-polarized Landau levels, and when the chemical potential is between Landau levels in the bulk, the bulk is insulating. At the edge of the sample, the external confining potential increases which decreases the effective chemical potential to cross the Landau level, so at the edge one obtains low energy excitations — from the velocity formula $\mathbf{v}_k = \partial\epsilon_k/\partial\mathbf{k}$, these are seen to be “chiral edge states.”

Even more interesting physics manifests for fractionally filled Landau levels. With a filling fraction ν we have a massive degeneracy corresponding to the many ways of distributing N particles among N/ν single particle states (Landau level states), and the ground state is then selected by the interactions. The contact interaction is most relevant for cold atoms, and in this case, in contrast to Coulombic interactions, the problem is exactly soluble. The solution yields the Laughlin states, which were the variational states introduced by Laughlin for the Coulombic system [158], as the exact ground state.

Solution for a contact interaction.—To construct the exact solution for a contact interaction, we use the solution for the non-interacting 2D homogeneous system’s lowest energy eigenstates in a strong magnetic field (the first Landau level). These are all degenerate, with the symmetric gauge wavefunctions indexed by angular momentum k

$$\psi_k(x, y) = (\pi k!)^{-1/2} z^k e^{-z^* z/2}, \quad (8.4)$$

where $z = (x + iy)/d$ and $d = \sqrt{\hbar/(M\Omega)}$ with M the atomic mass [75].

The N -body wavefunction is then a function of N complex numbers: $\psi(z_1, z_2, \dots, z_N)$. Since it can be written as a sum of products of the single-particle wavefunctions in Eq. (8.4), it is an analytic function of z_1, z_2, \dots, z_N times $e^{-\sum_j z_j^* z_j/2}$, ultimately a consequence of restricting the single particle Hilbert space to the lowest Landau level. It must satisfy the exchange symmetry $\psi \rightarrow \pm\psi$ upon exchanging any two of its arguments, with “+” for bosons and “-” for fermions. Since the Landau levels are degenerate, the interaction energy is the only energy in the problem, and thus the ground state must minimize the interaction energy. The minimum interaction energy possible is zero, and this is achievable when there is no overlap between pairs of particles. Thus wavefunctions of the form $\psi(z_1, z_2, \dots, z_N) = \left[\prod_{i<j} (z_i - z_j)^{m_{ij}} \right] e^{-\sum_j |z_j|^2/2}$ with $m_{ij} > 0$ are all zero energy ground states. If a small energy penalty is added for angular momentum, slightly breaking the degeneracy of the Landau levels as is appropriate for a finite or a trapped system, one seeks to minimize the angular momentum, which is accomplished by $m_{ij} = 2$ for bosons and $m_{ij} = 1$ for fermions. This gives $\nu = 1/2$ and $\nu = 1/3$ Laughlin wavefunctions Ψ as the ground states, with

$$\Psi(\{z_j\}) = \left[\prod_{i<j} (z_i - z_j)^{1/\nu} \right] e^{-\sum_j |z_j|^2/2} \quad (8.5)$$

up to normalization. There is a nice physical interpretation: each particle binds a vortex. Excitations of this system may be constructed similarly.

There are several very interesting physical consequences of the ground and excited states: (1) the bulk has an energy gap, (2) there are gapless edge states, and (3) the gapped bulk excitations have fractional charge and statistics. One can also see that if Laughlin states of different fillings are stabilized (as occurs for non-contact interactions in semiconductor heterostructures) that transitions between them are indescribable via symmetry breaking and the phases must be characterized by some “topological order.”[155]

8.2 Rotation

8.2.1 Rotation and angular momentum boosts — principles and experimental techniques

Consider a system described by a Hamiltonian H in some reference frame A . A system in a frame B rotating with frequency $\boldsymbol{\Omega}$ — the vector accounts for the rotation axis — relative to reference frame A is described by the Hamiltonian

$$H' = H - \boldsymbol{\Omega} \cdot \mathbf{L} \quad (8.6)$$

where \mathbf{L} is the total angular momentum operator of the system [75]. A consequence is that adding a fixed amount of angular momentum \mathbf{L} to an angular momentum conserving system is equivalent to this, since the same description applies with $\boldsymbol{\Omega}$ a Lagrange multiplier to fix the total angular momentum.

Experimentally, one may rotate a whole system: one can rotate the entire trap, and lattice if one is there. Stably rotating lenses or lasers in unison is difficult, so a common technique is to shine light through a metal mask with holes cut in it, with the resulting diffraction pattern forming the lattice. Other techniques are also used (e.g., Ref. [159]). From the equivalence discussed above, another possibility

is to impart angular momentum to the system by “stirring it.” In such techniques, a focused laser beam generally provides the required localized spatial potential.

8.2.2 Rotation leads to effective magnetic field (gauge field) and limitations for exotic states

I will derive how rotation leads to an effective magnetic field, considering the case of a single free particle. The derivation extends straightforwardly to multiple particles in an external potential.

A free particle is described by Hamiltonian $H = p^2/(2m)$. Equation (8.6) and the definition of angular momentum gives the rotating frame Hamiltonian to be

$$H' = \frac{p^2}{2m} - \boldsymbol{\Omega} \cdot (\mathbf{r} \times \mathbf{p}). \quad (8.7)$$

Cyclic invariance of the triple product yields

$$H' = \frac{p^2}{2m} - \mathbf{p} \cdot (\boldsymbol{\Omega} \times \mathbf{r}). \quad (8.8)$$

In principle one needs to worry about the non-commutation of the operators in the triple product, but here this is easily seen to be valid. We complete the square to give

$$H' = \frac{(p - m\boldsymbol{\Omega} \times \mathbf{r})^2}{2m} - m\Omega^2 r^2/2. \quad (8.9)$$

Thus, there is an added centrifugal force, and an effective gauge potential

$$\mathbf{A} = \frac{c\boldsymbol{\Omega} \times \mathbf{r}}{e} \quad (8.10)$$

which is precisely the gauge potential of a homogeneous magnetic field $B = mc\boldsymbol{\Omega}/e$ in the symmetric gauge [75]. Thus, neutral particles in a rotating frame will act exactly as charged particles in an effective magnetic field (plus a harmonic centrifugal potential which may be absorbed into the harmonic trapping potential).

While rotation is can potentially lead to exotic states such as fractional quantum Hall states, it has severe limitations that have led cold atom physicists to propose new methods. In particular, to achieve fractional quantum Hall ground states the system must be rotated near the centrifugal limit where Ω matches the trap frequency ω . To be precise, by considering the competing ground states at nearby rotation frequencies, one finds that the maximum allowable frequency deviation to achieve fractional quantum Hall states scales as $|\Omega - \omega| \sim 1/N$ with N the number of particles. Thus, one requires high rotation frequency control and stability, severely limiting the size of fractional quantum Hall states that can be stabilized.

There are two main methods to circumvent this difficulty. (1) One method is to work with few-particle states so that $1/N$ is sufficiently large. These clusters remarkably show much of the physics of their thermodynamic brethren, even for $N \lesssim 10$, including gapped excitations that are well described by fractional charge and statistics, gapless edge modes, and a roughly quantized density [160, 161, 141, 140, 136, 162, 142, 126, 143, 144, 145, 146, 149, 147, 148]. This is the approach we take in Chapter 9.

8.3 Other methods of inducing gauge fields

A number of alternative methods to create gauge fields have been proposed. These frequently rely on an atom receiving a momentum kick transverse to its motion from a laser when the atom hops [127, 128]). These ideas may also be extended to non-Abelian gauge potentials [131]. Erich and I have proposed and studied a particular class of these schemes, not discussed in this thesis.

Recently, these ideas have been generalized to spin-dependent gauge potentials, giving an effective spin orbit coupling (Ref. [163] gives one example). This has

generated considerable excitement of the prospect of creating topological insulators in cold atoms. These are intriguing generalizations of the quantum Hall effect to systems without time-reversal symmetry breaking that have recently been observed in solid state systems (Ref. [164] gives a fairly up-to-date review). Perhaps most intriguingly, these system allow topological behavior to persist to three-dimensional systems, and generate two-dimensional conducting surfaces that are robust to weak disorder (in contrast to non-topological two-dimensional metals).

8.4 On-site correlations

Chapter 9’s proposal to create fractional quantum Hall states leads to the creation of many few particle “puddles” of fractional quantum Hall states at each node of a two-dimensional optical lattice. This is a particular case of the more general problem of what happens in lattice systems when atoms within a site are allowed to correlate. Describing this requires going beyond the simple Bose-Hubbard description of Chapter 2, and Chapter 10 describes a novel, efficient way of describing arbitrarily strong on-site correlations and estimates the magnitude of effects. Chapter 11 develops the theoretical tools to quantitatively calculate the model’s parameters using path integral Monte Carlo simulations of moderate sized systems (the model can then be used to describe large systems).

Chapter 9

Stirring up fractional quantum Hall puddles

*This chapter was adapted from “Stirring trapped atoms into fractional quantum Hall puddles” by Stefan K. Baur, Kaden R. A. Hazzard, and Erich J. Mueller, published in Physical Review A **78**, 061608(R) (2008).*

9.1 Abstract

We theoretically explore the generation of few-body analogs of fractional quantum Hall states. We consider an array of identical few-atom clusters ($n = 2, 3, 4$), each cluster trapped at the node of an optical lattice. By temporally varying the amplitude and phase of the trapping lasers, one can introduce a rotating deformation at each site. We analyze protocols for coherently transferring ground state clusters into highly correlated states, producing theoretical fidelities (probability of reaching the target state) in excess of 99%.

9.2 Introduction

Cold atom experiments promise to produce unique states of matter, allowing controllable exploration of exotic physics. For example, since rotation couples to neutral atoms in the same way that a uniform magnetic field couples to charged particles, many groups are excited about the possibility of producing analogs of fractional quantum hall states [160, 161, 141, 140, 136, 162, 142, 126, 143, 144, 145, 146, 149, 147, 148]. In particular, if a two dimensional harmonically trapped gas of bosons is rotated at a frequency Ω sufficiently close to the trapping frequency

ω , then the ground state will have vortices bound to the atoms – an analog of the binding of flux tubes to electrons in the fractional quantum hall effect. The ground state will be topologically ordered and possess fractional excitations. Technically, the difficulty with realizing this goal experimentally has been that it requires Ω to be tuned to a precision which scales as $1/n$, where n is the number of particles. Responding to this impediment, several authors [143, 144, 145, 146, 149, 147, 148] have proposed studying clusters with $n \lesssim 10$. Such clusters possess many of the features of a bulk quantum hall liquid, and producing them would be a great achievement. Here we propose and study protocols for producing strongly correlated clusters of rotating atoms.

The issue prompting this investigation is that in such clusters there are very few mechanisms for dissipating energy, and hence experimentally producing the ground state of a rotating cluster is nontrivial. First, the small number of particles results in a discrete spectrum, and leaves few kinetic paths. Second, in the strongly correlated states of interest the atoms largely avoid each other, further blocking the kinetics. On these grounds, one should not expect to be able to cool into the ground state. Instead we advocate a dynamical process where one coherently *drives* the system into the strongly correlated state through a well-planned sequence of rotating trap deformations. This approach is based upon an analogy between the states of these atomic clusters, and the energy levels of a molecule. By deforming the harmonic trap, and rotating the deformation, one couples the many-body states in much the same way that an oscillating electric field from a laser couples molecular states. We consider a number of pulse sequences, finding that one can rapidly transfer atoms to a strongly correlated state with nearly unit efficiency. Following a proposal by Popp *et al.* [149], experimentalists at Stanford have achieved considerable success with a related procedure, where one

slowly increases the rate of rotation, adiabatically transferring bosonic atoms from an initially non-rotating state, to an analog of the Laughlin state [165]. One could also imagine implementing more sophisticated protocols such as rapid adiabatic passage [166].

To achieve sufficient signal to noise, any experimental attempt to study small clusters of atoms must employ an ensemble of identical systems: for example by trapping small numbers of atoms at the nodes of an optical lattice. When formed by sufficiently intense lasers, this lattice will isolate the individual clusters, preventing any “hopping” from one node to another. We will not address the very interesting question of what would happen if the barriers separating the clusters were lowered. By using filtering techniques, one can ensure that the same number of atoms sit at each node [165]. A rotating deformation of each *microtrap* can be engineered through a number of techniques. For example, if the intensity of the lattice beams forming a triangular lattice are modulated in sequence, then a rotating quadrupolar deformation is produced. A more versatile technique is to modulate the phases between counterpropagating lattice beams. Changing these phases uniformly translates the lattice sites. If one moves the lattice sites around faster than the characteristic times of atomic motion ($10^{-5}s$) but slow compared to the times for electronic excitations ($10^{-15}s$) then the atoms see a time averaged potential. This technique, which is closely related to the time orbital potential traps pioneered at JILA [167], can produce almost arbitrary time dependent deformations of the individual traps which each of the clusters experiences [165]. Each cluster feels the same potential.

Once created, the ensemble of clusters can be experimentally studied by a number of means. *In situ* probes such as photoassociation [168] and RF spectroscopy [110] reveal details about the interparticle correlations. In the regime of

interest, time-of-flight expansion, followed by imaging, spatially resolves the ensemble averaged *pre-expansion* density. This result follows from the scaling form of the dynamics of lowest Landau level wavefunctions [147].

We model a single cluster as a small number of two-dimensional harmonically trapped bosonic atoms. The two dimensionality can be ensured by increasing the intensity of the lattice beams in the perpendicular direction. Neglecting the zero-point energy, one finds that in the frame rotating with frequency Ω , the single particle harmonic oscillator eigenstates have the form $E_{jk} = \hbar(\omega - \Omega)k + \hbar(\omega + \Omega)j$; ($j, k = 0, 1, \dots$). In typical lattices, the interaction energy $U/\hbar \sim 10$ kHz is small compared to the small oscillation frequency $\omega \sim 100$ kHz [77]. Therefore the many-body state will be made up of single particle states with $j = 0$: the lowest Landau level, with wavefunctions of the form

$$\psi_k(x, y) = (\pi k!)^{-1/2} z^k e^{-z^* z/2}, \quad (9.1)$$

where $z = (x + iy)/d$ with $d = \sqrt{\hbar/M\omega}$ is the complex representation of the coordinate in the plane measured in units of the oscillator length, where M is the atomic mass. Including interactions, the many-body Hamiltonian for a single cluster is then

$$H_{LLL} = \sum_j j\hbar(\omega - \Omega)a_j^\dagger a_j + \sum_{jklm} V_{jklm} a_j^\dagger a_k^\dagger a_l a_m \quad (9.2)$$

where a_m is the annihilation operator for the single particle state ψ_m . For point interactions the interaction kernel is

$$V_{jklm} = \frac{U}{2} \delta_{j+k-l-m} 2^{-(j+k)} \frac{(j+k)!}{\sqrt{j!k!l!m!}}, \quad (9.3)$$

where $U = \sqrt{2/\pi} \hbar^2 a / (M d_z d^2)$ is the on-site interaction between two particles in the same well, a is the three dimensional s-wave scattering length and d_z is the oscillator length in the transverse direction. As has been explored in depth by

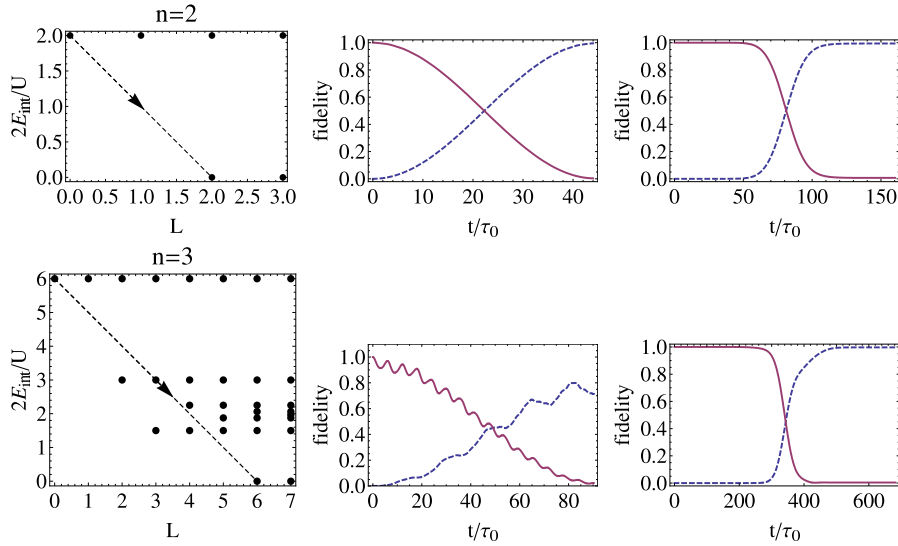


Figure 9.1: (Color Online) Transferring small clusters from non-rotating ground state to $\nu = 1/2$ Laughlin state using rotating quadrupolar ($m = 2$) deformations. Left: Interaction energy (in units of $U/2$) of quantum states of harmonically trapped two dimensional clusters as a function of total angular momentum projection L in units of \hbar . Excitation paths are shown by arrows. Central: squared overlap (fidelity) of $|\psi(t)\rangle$ with the initial (solid) and final (dashed) states as a function of the duration of a square pulse. Right: Fidelities as a function of time for an optimized Gaussian pulse of the form $e^{-(t-t_0)^2/\tau^2}$. Time is measured in units of $\tau_0 = \hbar/U \sim 10^{-4}$ s. For $n = 2$, the peak perturbation amplitude is $V_p = 0.05(U/2)$, $\omega - \Omega_p = 2.0(U/2)$, and a Gaussian pulse time of $\tau = 24\tau_0$. For $n = 3$, $\tau = 102\tau_0$ and $\omega - \Omega_p = 2.046(U/2)$ and $2.055(U/2)$ for the Gaussian and square cases, respectively. For $n = 3$, nonlinear effects (coupling with near-resonant levels) shifted the optimal frequency away from the linear response expectation, $\omega - \Omega_p = 2(U/2)$.

previous authors [160, 161, 141, 140, 136, 162, 142, 126, 143, 144, 145, 146, 149, 147, 148], for a given total number of particles n , and angular momentum projection L , the Hamiltonian (9.2) is a finite matrix which is readily diagonalized. Example spectra are shown in Figures 9.1 through 9.3. We plot the spectra as energy versus angular momentum, with $\Omega = \omega$. Spectra at other rotation speeds are readily found by “tilting” the graphs – the energy of a state with angular momentum projection L is simply shifted up by $\hbar(\omega - \Omega)L$.

We imagine applying to each cluster a rotating single particle potential (in the

lab frame) of the form

$$H_S(r, t) = V_p(t) [z^m e^{im\Omega_p t} + (z^*)^m e^{-im\Omega_p t}], \quad (9.4)$$

where m determines the symmetry of the deformation (e.g. $m = 2$ is a quadrupolar deformation), the envelope function $V_p(t)$ is the time-dependent amplitude of the deformation, and Ω_p is the frequency at which the perturbation rotates. We will mainly focus on the case $m = 2$. When restricted to the lowest Landau level, this potential generates a coupling between the many-body states which in the rotating frame is expressed as

$$H_S = V_p(t) \sum_l v_{lm} \left(e^{im(\Omega_p - \Omega)t} a_{l+m}^\dagger a_l + \text{H.C.} \right) \quad (9.5)$$

with $v_{lm} = 2^{-m/2} (l+m)! / \sqrt{l!(l+m)!}$. As such it only couples states whose total angular momentum projection differs by m . For our calculation will work in the co-rotating frame with $\Omega = \Omega_p$, where the only time dependence is given by $V_p(t)$.

We wish to implement a π -pulse, where the amplitude $V_p(t)$ is engineered so that after the pulse, a cluster is transferred from its initial state to a target state of our choosing. If the perturbation coupled only two states, this would be a straightforward procedure. The frequency Ω_p is selected so that the initial and target state are degenerate in the rotating frame. For any finite V_p , the system Rabi flops between the two coupled states, and by turning off the perturbation at the right time one ends up in the target state with unit probability. The present example is more complicated, as there are many states coupled by the perturbation. The basic idea however remains sound: one still chooses Ω_p to make the initial and final state degenerate. The time dependence of $V_p(t)$ should be tailored to minimize the coupling to unwanted states. These stray couplings could be particularly disastrous, because the coupling between the initial and target state are generically quite high order in V_p . As a particularly relevant example,

we consider transferring clusters from the ground state (with $L = 0$) to the the $\nu = 1/2$ Laughlin state $\psi_L(z_1, \dots, z_n) = \prod_{i < j} (z_i - z_j)^2 \exp(-\sum_j |z_j|^2/4l_B^2)$, which has angular momentum $n(n-1)$. Using a perturbation with $m = 2$, this requires a $n(n-1)/2$ -order process. A picturesque way of thinking about the dynamics in the presence of the perturbation is to map the problem onto the motion of a particle on a complicated “lattice”. The states of the unperturbed system are analogous to “lattice sites”, while the perturbation produces a “hopping” between sites. The goal is to engineer a time-dependent hopping which efficiently moves the “particle” from a known starting position to a desired ending position. The transfer efficiency is measured by the probability that the system is in the target state ψ_T at the end of the time evolution: we plot this probability – known as the fidelity – as a function of time, given by $f(t) = |\langle \psi_T | \psi(t) \rangle|^2$.

As this analogy emphasizes, the problem of transferring a quantum system from one state to another is generic. Müller, Chiow, and Chu [169] recently considered how one can optimize pulse shapes to produce high order Bragg diffraction, while avoiding transferring atoms into unwanted momentum states. These authors developed a formalism for calculating the fidelity by adiabatically eliminating the off-resonant states. They found that Gaussian pulse shapes greatly outperformed simple square pulses. This result is natural, as the smoother pulses have a much smaller bandwidth.

We numerically solve the time dependent Schrödinger equation, truncating our Hilbert space at finite total angular momentum $L = n(n-1) + 4$ for $n = 2, 3$ and $L = n(n-1) + 8$ for $n = 4$. We have numerically verified that changing this cutoff to higher values has negligible effects. Figure 9.1 shows f in the case of $n = 2$ and $n = 3$ for square and Gaussian pulses. For the square pulse the fidelity is shown as a function of pulse length. For the Gaussian pulse, a fixed pulse duration

is used, and the fidelity is shown as a function of time. For $n = 2$, where only two states are involved, the pulse shape is irrelevant. For $n = 3$, where there is a near-resonant state with $L = 4$, the Gaussian pulse shape greatly outperforms the square pulse, producing nearly 100% transfer efficiency in 10's of ms, even for a very weak perturbation.

For $n > 3$ we find that these high order processes become inefficient. For $m = 2$ the coupling between the initial and final state scale as $(V_p/U)^{n(n-1)/2}$, making transfer times unrealistical long unless one drives the system into a highly nonlinear regime. As illustrated in figure 9.2, this difficulty can be mitigated by using perturbations with higher m . There, for illustration, we consider exciting a 3-particle cluster from the lowest energy $L = 2$ state to the $L = 6$ Laughlin state. The second order $m = 2$ pulse requires much longer than the first order $m = 4$ pulse. An interesting aside is that one would naively have expected that the resonant $l = 4$ state would make the second-order process extremely inefficient. It turns out that the coupling to that state is fortuitously zero.

Further improved scaling can be arranged by using a sequence of π pulses. One transfers the cluster from one long-lived state to another. Since the number of pulses scales as the angular momentum, the transfer time is then quadratic in the angular momentum, rather than exponential. One can also tailor the path to maximize the fidelity of each step. Some two-pulse sequences are shown in figure 9.3. The guiding principle in designing the pulse sequences is that in each step one wants as few as possible near-resonant intermediate states.

9.3 Summary

We have shown it is possible to use time dependent trap perturbations to coherently transfer boson clusters from nonrotating ground states to analogs of fractional

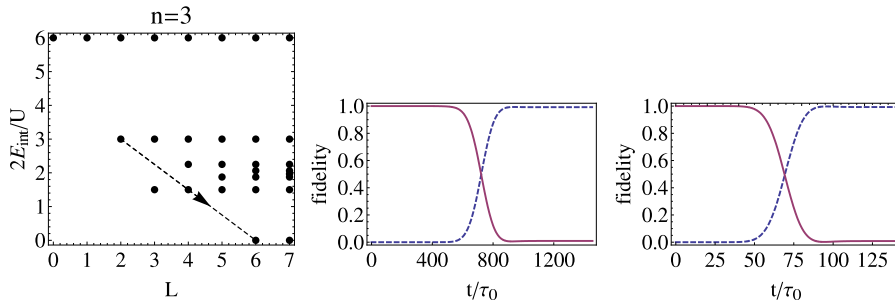


Figure 9.2: (Color Online) Using a rotating m -fold symmetric perturbation to drive $n = 3$ particle clusters from $L = 2$ to the $\nu = 1/2$ Laughlin state. Left: path on the energy level diagram. Center: second-order process coming from a deformation with $m = 2$. Right: direct transition produced with $m = 4$. Solid (dashed) lines are fidelities with the initial (Laughlin) state. In both cases the peak deformation is $V_p = 0.05(U/2)$. Both use a Gaussian pulse. The frequencies and pulse times τ we used for $m = 2, 4$ were $\omega - \Omega_p = (3.00/2)(U/2), 3.035(U/2)$ and $\tau/\tau_0 = 218, 21$. Note how much more rapid the direct process is.

quantum hall states. We achieve fidelity $f > 99\%$ for $n = 2, 3$ using very weak rotating $m = 2$ deformations, whose duration is of order tens of ms. Using a two-pulse sequence, we achieve similar results for $n = 4$. We find that smooth Gaussian pulses are much more effective than square pulses, and that further efficiency can be gained by using higher order perturbations of the form z^m with $m > 2$.

We briefly compare our technique with Ref. [149]’s proposal. While our approaches share the use of a rotating time-averaged optical lattice potential, our proposal offers significant differences and advantages. While Ref. [149] suggests an adiabatic evolution, we propose a coherent evolution – analogous to a Rabi oscillation – to the Laughlin state. This has the advantage of being faster, easier to implement, and more robust. For a slightly smaller perturbation relative to the adiabatic method, we achieve fidelity ~ 1 in contrast to the adiabatic method’s 0.97 fidelity. Moreover, our method requires half the time. More importantly, the adiabatic method requires carefully navigating a path through possible rotating potential strengths and frequencies as a function of time. In contrast, our method requires only setting the pulse duration and strength, and is thus more

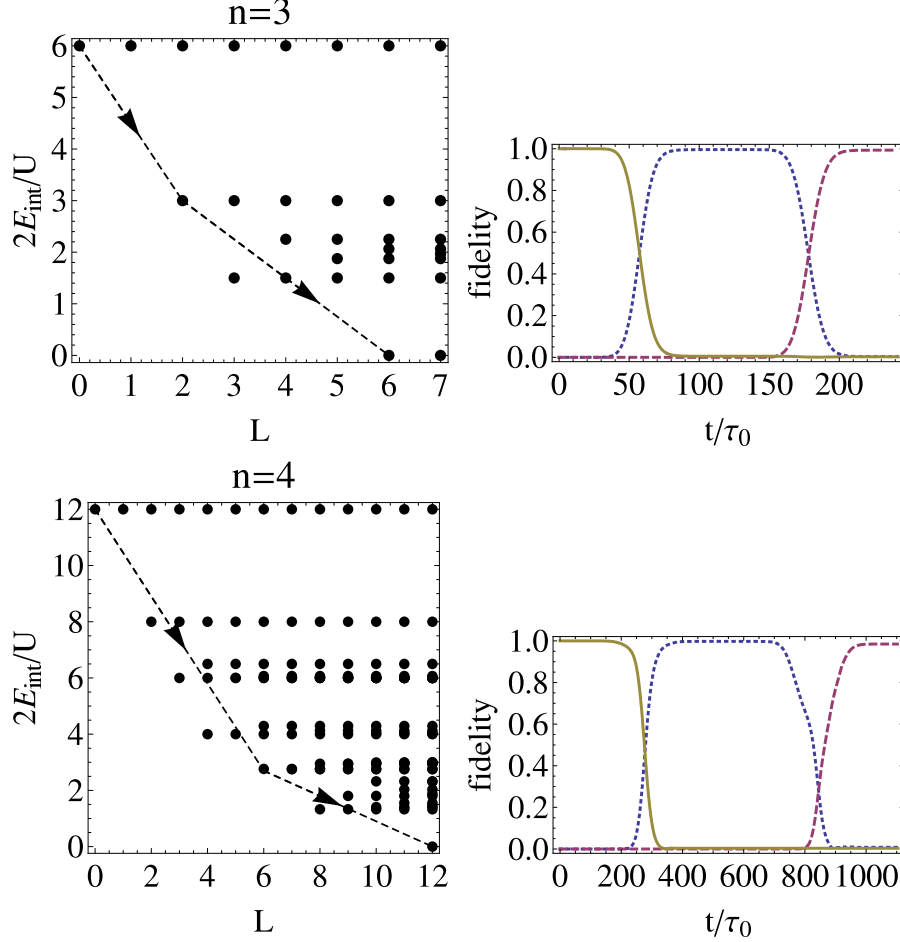


Figure 9.3: (Color Online) Transferring atoms using multiple pulses. Left: paths from initial to Laughlin states for $n = 3, 4$. Right: Solid line is the fidelity with the initial state, dotted with the intermediate $(L, E) = (2\hbar, 3(U/2))$ state, and the dashed line with the Laughlin state. All pulses are Gaussians. Despite using multiple pulses, this technique is faster than using a higher order $m = 2$ pulse. The frequencies (Ω_p) , shape (m) , and pulse times (τ) for the $N = 3$ sequence were $\hbar(\omega - \Omega_p)/(U/2) = 3.00, 3.035$, $m = 2, 4$, and $\tau/\tau_0 = 16.95, 19.2$. For both, $V_p = 0.05(U/2)$. For $N = 4$, using two pulses with $m = 2$ and $V_p = 0.2(U/2)$, we achieve $> 98\%$ fidelity after a total two-pulse sequences with $\hbar(\omega - \Omega_p)/(U/2) = 3.130, 1.0376$ and $\tau/\tau_0 = 82.5, 87.0$.

easily implementable and less susceptible to small experimental errors.

This technique will allow the efficient creation of bosonic quantum Hall puddles – a state of matter which has not yet been observed. The clusters produced will be orbitally entangled, have strong interparticle correlations, have fractional excitations, and possess topological orders [160, 161, 141, 140, 136, 162, 142, 126, 143, 144, 145, 146, 149, 147, 148]. Although current experiments, and the present theory, is focussed on the small-atom limit, it would be exciting to apply these techniques to larger collections of atoms, producing true analogs of fractional quantum Hall states. The main difficulty is that the spectra become dense as n increases, requiring one to set Ω_p to extremely high precision. By carefully choosing the trajectory, taking advantage of gaps in the spectrum, one might be able to overcome such difficulties.

Finally, we mention that our approach allows one to drive the system into almost arbitrary excited states. This may, for example, be important for using quantum hall puddles in a topological quantum computing scheme [170].

Acknowledgements and Author Credits: Stefan K. Baur and Kaden R. A. Hazard contributed equally to this work. We would like to thank Steven Chu and Nathan Gemelke for discussions about experiments and protocols. This material is based upon work supported by the National Science Foundation through grant No. PHY-0758104.

Chapter 10

Incorporating arbitrarily strong on-site correlations into lattice models

*This chapter was adapted from “On-site correlations in optical lattices: Band mixing to coupled quantum Hall puddles” by Kaden R. A. Hazzard and Erich J. Mueller, published in Physical Review A **81**, 031602(R) (2010).*

In Chapter 9 I described a protocol to efficiently small clusters of fractional quantum Hall states at sites of a deep optical lattice, in the limit where particles were unable to tunnel between sites on experimentally relevant timescales. One motivation for this chapter is to construct a theory of deep lattices that are nevertheless weak enough to allow particle tunneling between sites (analogous to the Bose-Hubbard limit of bosons in an optical lattice introduced in Chapter 2.). I construct a theory — specifically an effective lattice model — that captures the dominant behavior for bosons, and essentially identical techniques lead to a description of fermions. In the bosonic case, I construct an analog of the Gutzwiller mean field theory (introduced in Chapter 2) for this generalized model. I show that the resulting model has a phase diagram topologically the same as the Bose-Hubbard model: there are globally insulating phases with fractional quantum Hall puddles at each site and no coherence between them occupying “Mott lobes” in the chemical potential-lattice depth phase diagram, and a superfluid phase with coherence between the fractional quantum Halls states at each site.

This state is intriguing: for example, the superfluid order parameter $\langle a_j \rangle$ is exactly the nonlocal topological order parameter for the FQH state defined by Girvin and MacDonald [171, 172]. By including higher order corrections to our effective description, the problem is similar to those studied in the community interested in networks of quantum Hall systems (e.g., Refs. [173]).

However, the ideas resulting from these considerations apply more generally than arrays of fractional quantum Hall puddles. Most importantly, our model is able to capture the on-site correlations that occur in many varieties of optical lattice experiments, for example in strongly interacting gases with scattering lengths comparable to the lattice spacing, or for site fillings much greater than unity. When more than one particle is put on a site, instead of multiply occupying the lowest band (lowest oscillator state) as assumed in the derivation of **Chapter 2**, particles partially occupy higher bands due to interactions. Our model captures arbitrary on-site correlations even in the mean field approximation.

We also estimate model parameters for various situations, and surprisingly find that even for common ^{87}Rb experiments, with $a/d \approx 0.01$, quantitative renormalizations of $\sim 10\%$ manifest for site fillings as low as $n \sim 3$. Since the publication of our paper, some of these have been measured, for example in Ref. [174]

10.1 Abstract

We extend the standard Bose-Hubbard model to capture arbitrarily strong on-site correlations. In addition to being important for quantitatively modeling experiments, for example, with Rubidium atoms, these correlations must be included to describe more exotic situations. Two such examples are when the interactions are made large via a Feshbach resonance, or when each site rotates rapidly, making a coupled array of quantum Hall puddles. Remarkably, even the mean field approximation to our model includes all on-site correlations. We describe how these on-site correlations manifest themselves in the system's global properties: modifying the phase diagram and depleting the condensate.

10.2 Body

Optical lattice systems, where a dilute atomic gas is trapped in a periodic potential formed by interfering laser beams, provide a close connection between solid state systems and atomic physics [33]. The models used to describe these systems generally assume that each lattice site’s wavefunction is easily built up from single particle states [77]. Here we argue that this approximation is inappropriate to quantitatively model current experiments, and sometimes fails more drastically, e.g., for resonant bosons. We show how to include arbitrary on-site correlations via a generalized Hubbard model, which can be approached by standard methods. By construction, the mean field approximation to our model captures all on-site correlations, contrasting with prior approaches [175, 176, 177, 178, 179, 180].

Our method’s key idea is to first consider deep lattices, where lattice sites are isolated and then solve the few-body problem on each site. Next, truncating to this few-body problem’s low energy manifold, we calculate how tunneling couples the few-body states on neighboring sites. The resulting theory resembles a Hubbard model, but with number-dependent hopping and interaction parameters. We show that the corrections to the ordinary Bose-Hubbard model captured by this theory are crucial to quantitatively describe current Rubidium experiments. They become even more important when the 3D scattering length a becomes a significant fraction of the size of the Wannier states ℓ , such as in recent experiments on Cesium atoms near a Feshbach resonance [181]. This approach is also essential to describe more exotic on-site correlations; as one example, one can rotate each lattice site, creating a lattice of coupled “quantum Hall puddles” [149, 150]. Related ideas can be applied to double well lattices and coupled “plaquettes” of four sites [182, 183]. We explore the impact of the on-site physics on the extended system’s phase diagram.

Our approach is most simply illustrated by a single-component Bose gas in a cubic sinusoidal lattice potential $V_p(x, y, z) = V_0 \sum_{\eta=x,y,z} \sin^2(\pi\eta/d)$ with Hamiltonian

$$H_f = \int d^3r \left[\psi^\dagger(\mathbf{r}) \left(-\frac{\hbar^2}{2m} \nabla^2 - \mu + V_p(\mathbf{r}) \right) \psi(\mathbf{r}) + \frac{2\pi\hbar^2 a}{m} \psi^\dagger(\mathbf{r}) \psi^\dagger(\mathbf{r}) \psi(\mathbf{r}) \psi(\mathbf{r}) \right], \quad (10.1)$$

where m is the particle mass, μ is the chemical potential, and ψ and ψ^\dagger are bosonic annihilation and creation operators. Adding an additional trapping potential presents no additional difficulties.

Constructing the effective Hamiltonian.—For each isolated site, we proceed to build up the many-body states from the solution of the n -body problem at site j : $\langle \mathbf{r}_1, \dots, \mathbf{r}_n | \overline{|n\rangle}_j = \psi_n(\mathbf{r}_1 - \mathbf{R}_j, \dots, \mathbf{r}_n - \mathbf{R}_j)$, which obeys $H_j \overline{|n\rangle}_j = \epsilon_n \overline{|n\rangle}_j$ where H_j is the same as Eq. (10.1)'s H_f , except replacing the periodic potential V_p there with an on-site potential V_j . A convenient approximation is to take $V_j(\mathbf{r}) = (m\omega^2/2)(\mathbf{r} - \mathbf{R}_j)^2$ with $\omega = 2\sqrt{V_0 E_R}/\hbar$, the harmonic approximation to the site located at \mathbf{R}_j . For each site filling n , we restrict our on-site basis to the lowest energy n -body state; however, including a finite number of excited states is straightforward. Note that even in the non-interacting case these states are *not* Wannier states. The principle difference is that states defined in this way are non-orthogonal. From these, however, one can construct a new set of orthogonal states $|n\rangle_j$, which hold similar physical meaning. In the noninteracting limit, the $|n\rangle_j$ approximate the Wannier states.

Because the single-site wavefunctions decay like Gaussians, it typically suffices to build up the effective Hamiltonian from neighboring sites. In particular, consider two sites L and R , and the space spanned by $\overline{|n_L, n_R\rangle} = \overline{|n_L\rangle}_L \otimes \overline{|n_R\rangle}_R$, with overlaps $S^{(mn)} = \overline{\langle m, n | m+1, n-1 \rangle}$. To lowest order in the overlaps, we can define orthogonal $|n_L, n_R\rangle$ by taking $|n_L, n_R\rangle = \overline{|n_L, n_R\rangle} - (1/2)[S^{(n_R, n_L)} \overline{|n_R+1, n_L-1\rangle} +$

$$S^{(n_L, n_R)} \overline{|n_R - 1, n_L + 1\rangle}].$$

Within this restricted basis, the effective Hamiltonian for these two sites is $H_{\text{eff}} = \sum_{n, m, n', m'} |n', m'\rangle \langle n', m'| H_f |n, m\rangle \langle n, m|$. Evaluation to lowest order in $S^{(mn)}$ yields on-site energy terms $\sum_{n, m} (E_n + E_m) |n, m\rangle \langle n, m|$ and a ‘‘hopping’’ term $-\sum_{nm} t^{(mn)} |m + 1, n - 1\rangle \langle m, n| + \text{H.c.}$ with

$$\begin{aligned} E_n &= \overline{\langle n| H_f |n\rangle}, \\ t^{(mn)} &= -\overline{\langle m + 1, n - 1| H_f |m, n\rangle} + \frac{S^{(mn)}}{2} (E_m + E_n). \end{aligned} \quad (10.2)$$

Additionally there is an interaction term $U = \sum_{nm} [U_{LL}^{(n)} + U_{RR}^{(m)} + U_{LR}^{(n, m)}] |m, n\rangle \langle m, n|$ with $U_{LL}^{(m)} = U_{RR}^{(m)} = E_m$ and

$$U_{LR}^{(n, m)} = \overline{\langle m, n| H_f |m, n\rangle} - E_m - E_n \quad (10.3)$$

to $O(S^2)$, consistent with the rest of our calculations. In the remainder of this paper we will neglect the off-site interaction, Eq. (10.3), and the last term in Eq. (10.2). The former is rigorously justified as it falls off exponentially faster than the other interaction terms. Formally, the non-orthogonality contribution to Eq. (10.2) is suppressed only by a factor of $(V_0/E_R)^{1/4}$ with $E_R = \hbar^2 \pi^2 / (2md^2)$, but as shown in Fig. 10.1, it is typically small.

The simplest many-site Hamiltonian which reduces to this one in the limit of two sites is

$$\begin{aligned} H &= - \sum_{\langle i, j \rangle; m, n} t_{ij}^{(mn)} |m + 1\rangle_i |n - 1\rangle_j \langle m|_i \langle n|_j \\ &\quad + \sum_{i, n} E_n |n\rangle_i \langle n|_i, \end{aligned} \quad (10.4)$$

where $\sum_{\langle i, j \rangle}$ indicates a sum over nearest neighbors i and j . At higher order, one generates more terms such as next nearest neighbor hoppings, pair hoppings, and longer range interactions.

Calculating the Hamiltonian parameters.—Here we consider the cases of weak interactions, resonant interactions, and coupled quantum Hall puddles.

In the limit of weak interactions, one can estimate the parameters in Eq. (10.4) by taking the on-site wavefunction to be $\psi_n \propto \exp(-\sum_{j=1}^n r_j^2/2\sigma_n^2)$, with variational width σ_n . To leading order in a/d we find $E_n = E_R[(3\sqrt{V_0/E_R} - \mu/E_R)n + (U/2)n(n-1)(1 - \frac{3\pi}{4\sqrt{2\pi}}(a/d)(n-1)(V_0/E_R)^{1/4})]$ with $U = (a/d)\sqrt{2\pi}(V_0/E_R)^{3/4}$ and $t^{(mn)} = t\sqrt{n(m+1)}[1 + \frac{\sqrt{2}a\pi^{5/2}}{4d}(m+n-1)(V_0/E_R)^{3/4}]$ with $t = V_0(\pi^2/4 - 1)e^{-(\pi^2/4)\sqrt{V_0/E_R}}$. Note that as expected, interaction spreads out the Wannier functions, increasing the $t^{(mn)}$'s and decreasing the E_n 's. Fig. 10.1 shows several of the resulting $t^{(mn)}$ as a function of V_0 for parameters in typical optical lattice experiments with ^{87}Rb . Also shown are $t^{(01)}$ and the next-nearest-neighbor hopping, t_{nnn} , calculated from the exact Wannier states. Our estimates are consistent with previous work regarding t 's n -dependence [177, 175, 176], validating our approach. As can be seen in Fig. 10.1(c), the relative size of the next nearest neighbor hopping t_{nnn}/t is 10% (1%) for $V_0 = 3E_R$ ($V_0 = 10E_R$), justifying our approximation of including only nearest neighbor overlaps to describe the system near the Mott state. Fig. 10.1 also illustrates that the Gaussian approximation only qualitatively captures the behavior even for non-interacting particles. *We also see that even for this weakly interacting case the number dependence of t is crucial for a quantitative description of the experiments.* Similarly, the number dependence of the on-site interaction is quantitatively significant. This latter deficiency of the standard Hubbard model has been noted in the past, for example by the MIT experimental group [85].

For more general experimental systems, one needs to include still more on-site correlations. As our first example, we consider lattice bosons near a Feshbach resonance [58, 184], describing, for example, ongoing Cesium atom experiments [181].

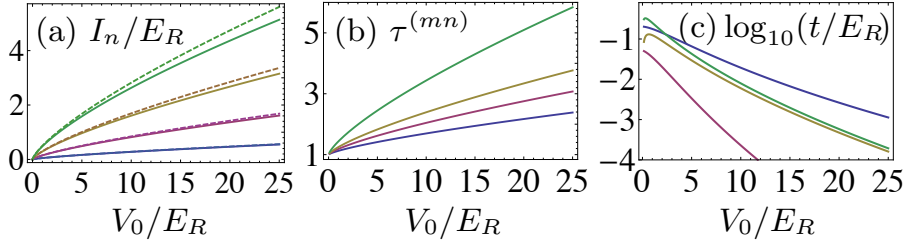


Figure 10.1: (color online) (a) On-site energy with non-interacting energies subtracted off, $I_n = E_n - (3\hbar\omega/2 - \mu)n$, and energies scaled by $E_R = \hbar^2\pi^2/(2md^2)$, using typical ^{87}Rb parameters: lattice spacing $d = 532\text{nm}$, scattering length $a = 5.32\text{nm}$. Dashed: neglecting on-site correlations, solid: including correlations. Bottom to top curve: $n=2,3,4,5$. (b) Representative hopping matrix elements with on-site correlations, relative to those neglecting on-site correlations, $\tau^{(mn)} \equiv t^{(mn)}/(t\sqrt{(m+1)n})$, as a function of lattice depth V_0 on a scale. Bottom to top line: $t^{(03)}, t^{(31)}, t^{(05)}, t^{(35)}$. (c) For comparison, $t^{(01)}/E_R$ calculated from the exact Wannier states (upper curve) along with our Gaussian approximation to it with and without non-orthogonality corrections (second and third highest, respectively); also shown is the next-nearest neighbor hopping matrix element (bottom curve). The effective Hamiltonian parameters are calculated perturbatively in a/d for a Gaussian ansatz.

We restrict ourselves to site occupations $n = 0, 1, 2$, for which we have exact analytic solutions to the on-site problem for arbitrary a in terms of confluent hypergeometric functions [185]. Fig. 10.2 shows graphs of E_n and $t^{(mn)}$ rescaled by $\hbar\omega$ as a function of a in the deep lattice limit.

As Fig. 10.2(b) illustrates dramatically, the hopping from and to doubly-occupied sites is strongly suppressed near the Feshbach resonance when atoms occupy the lowest branch, and is enhanced for the next-lowest branch. The former has implications for studies of boson pairing on a lattice [58, 184], showing that one must dramatically modify previous models near resonance, and, as will be discussed more below, the latter implies a substantial reduction of the $n = 2$ Mott lobe's size for repulsive bosons.

We give one further example, namely the case, similar to the one discussed in [149, 150], where the individual sites of the optical lattice are elliptically deformed and rotated about their center. This is accomplished by rapidly mod-

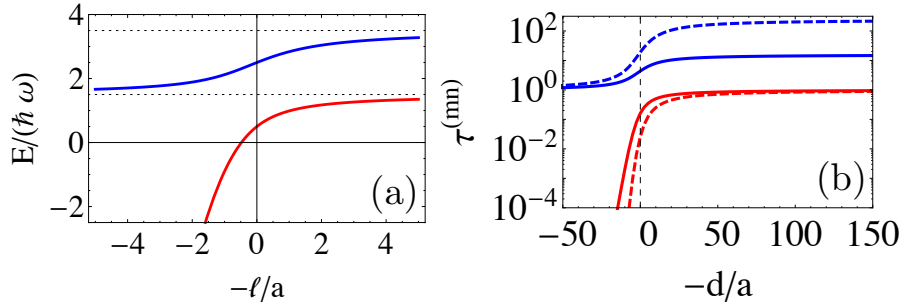


Figure 10.2: (color online) Left: On-site two-particle energy as a function of scattering length a rescaled by the on-site harmonic oscillator energy $\hbar\omega = 2\sqrt{V_0 E_R}$, for the two lowest energy branches. The corresponding characteristic length is $\ell = \sqrt{\hbar/m\omega}$. Right: Log plot of rescaled hopping matrix elements $\tau^{(mn)} \equiv t^{(mn)}/(t\sqrt{(m+1)n})$. Solid and dashed curves are $t^{(11)}/(\sqrt{2}t)$ and $t^{(12)}/(2t)$, respectively. We have chosen the lattice depth $V_0 = 15E_R$; this affects only the horizontal scale. In the ordinary Bose-Hubbard model, $t^{(mn)}/(\sqrt{(m+1)n}t) = 1$ for all m, n , as confirmed by this figure's $a = 0^-$ lowest (red) branch and $a = 0^+$ second (blue) branch limits. The resonance at $-d/a = 0$ separates the molecular side (left), from the atomic side (right). Note that $t^{(10)}/t$ (not shown) is universally equal to unity regardless of interaction strength, since interatomic correlations are absent when there is a single particle per site.

ulating the phase of the optical lattice lasers to generate an appropriate time-averaged optical potential. At an appropriate rotation speed Ω the lowest energy n -particle state on each site is a $\nu = 2$ Laughlin state $\psi_n(\mathbf{r}_1, \dots, \mathbf{r}_n) = \mathcal{N}_n \left[\prod_{i < j=1}^n (w_i - w_j)^2 \right] e^{-\sum_j |w_j|^2 / (4\ell^2)}$, where we define $w_j \equiv x_j + iy_j$, and \mathcal{N}_n is a normalization factor with phase chosen to gauge away phase factors appearing in $t^{(mn)}$. Truncating to this set of states for $n = 0, 1, 2$, we produce an effective Hubbard model of the same form as Eq. (10.4). The hopping parameters for asymptotically deep lattices $V_0/E_R \gg 1$ are $t^{(01)} = t$, $t^{(02)} = t(\pi^2/32)(V_0/E_R)^{1/2}$, and $t^{(12)} = t(\pi^4/1024)(V_0/E_R)$ where $E_R = \hbar^2\pi^2/(2md^2)$ is the recoil energy, and t is the same as in the weakly interacting case treated above; the interaction parameters are $E_m = \frac{\omega - \Omega}{2}m(m-1) - \mu m$. One particularly interesting aspect of this model of coupled quantum Hall puddles is that when the system is superfluid, the order

parameter is exactly the quantity defined by Girvin and MacDonald [171, 172] to describe the nonlocal order of a fractional quantum Hall state. Thus when one probes the superfluid phase stiffness, one directly couples to this quantity.

Mean-field theory.—The true strength of our approach is that the resulting generalized Hubbard model is amenable to all of the analysis used to study the standard Bose-Hubbard model. In particular, we can gain insight from a Gutzwiller mean-field theory (GMFT) [77, 76]. This approximation to the ordinary Bose-Hubbard model gives moderate quantitative agreement with more sophisticated methods: for example, the unity site filling MI/SF transition on a 3D cubic lattice occurs at $(t/U)_c = 0.03408(2)$ while GMFT yields $(t/U)_c = 0.029$ [1].

In the ground state $|\Psi\rangle$, we introduce mean fields $\xi_m \equiv \langle \Psi | m+1 \rangle \langle m | \Psi \rangle$. Neglecting terms which are quadratic in $\delta L_m^i = |i, m+1\rangle \langle i, m| - \xi_m$, the Hamiltonian is $H_{MF} = \sum_i H_{MF,i}$ with

$$H_{MF,i} = E_{n_i} |n\rangle_i \langle n|_i - z \sum_m \left[\zeta_m |m-1\rangle_i \langle m|_i - \zeta_m \xi_{m-1} + \text{H.c.} \right], \quad (10.5)$$

where H.c. denotes Hermitian conjugate, z is the lattice coordination number, and $\zeta_n = \sum_m \xi_m t^{(mn)}$.

Truncating the number of atoms on a site to $n \leq n_{\max}$, we self-consistently solve Eq. (10.5) by an iterative method. We start with trial mean-fields, calculate the lowest energy eigenvector of the $(n_{\max} + 1) \times (n_{\max} + 1)$ mean field Hamiltonian matrix, then update the mean-fields. We find that it typically suffices to take n_{\max} roughly three times the mean occupation of the sites. Fig. 10.3 illustrates how the density dependence of the parameters introduced by the on-site correlations modify the GMFT phase diagram — particularly the phase boundary's shape, and the density and order parameter in the superfluid phase.

As one would expect, the topology of the MI/SF phase boundaries are similar

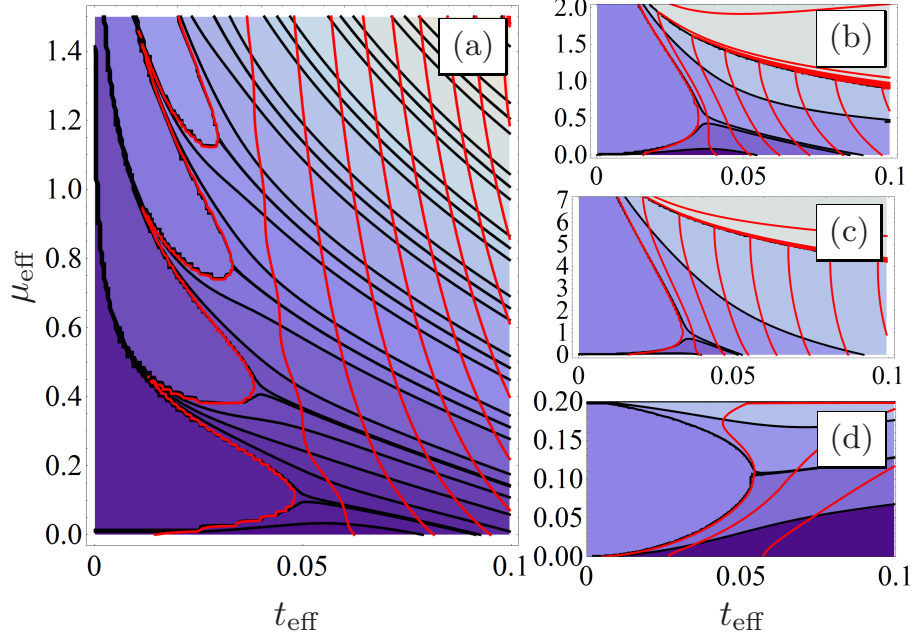


Figure 10.3: (color online) Representative Gutzwiller mean-field theory phase diagrams, showing constant density (black, roughly horizontal) and constant $\xi \equiv \zeta_1 + \zeta_2 + \zeta_3$ (red, roughly vertical) contours: ξ , similar to the condensate density, is a combination of the mean fields ζ_m , defined after Eq. (10.5). Density contours are $n = \{0.01, 0.2, 0.5, 0.8, 0.99, 1.01, 1.2, \dots\}$ and order parameter contours are $\xi = \{0.2, 0.4, \dots\}$, except (d) where we take contours $\xi = \{0.02, 0.04, \dots\}$. The phase diagrams are functions of $\mu_{\text{eff}} \equiv \mu/E_R$ and $t_{\text{eff}} \equiv \exp(-\sqrt{V_0/E_R})$, where the lattice depth V_0 is the natural experimental control parameter. We plot versus t_{eff} , instead of V_0 , as this is closer to the Hamiltonian matrix elements and more analogous to traditional visualizations of the Bose-Hubbard phase diagram. (a) Ordinary Bose-Hubbard model for $a = 0.01d$, (b) lattice bosons restricted to fillings $n = 0, 1, 2$ with $a = 0.01d$, on the next to lowest energy branch on the $a > 0$ side of resonance, (c) lattice boson model with $a = d$, and (d) FQH puddle array model taking $\omega - \Omega = 0.1E_R$ (see text for details). Parts (b,c) use the Hamiltonian parameters from the exact two-particle harmonic well solution.

to that of the standard Bose-Hubbard model, but the Mott lobes' shapes can be significantly distorted. Within mean-field theory the boundary's shape can be determined analytically by taking $|\Psi\rangle = \epsilon'|n-1\rangle + \sqrt{1-\epsilon'^2-\epsilon^2}f_{n-1}|n\rangle + \epsilon|n+1\rangle$, and expanding $\langle\Psi|H_{MF}|\Psi\rangle$ to quadratic order in ϵ and ϵ' . The Mott boundary corresponds to when the energy expectation value's Hessian changes

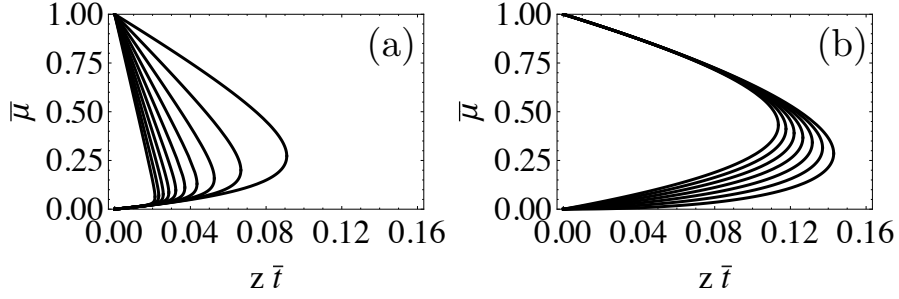


Figure 10.4: Single lobe of the Mott insulator/superfluid boundary. Complete characterization of the mean-field lobe shape in the $z\bar{t}$ - $\bar{\mu}$ plane for all possible t^\pm 's (see Eq. (10.7) for definitions). (a) Fix $t^- = 0.5$, vary t^+ from 1 (outer curve) to 21 (inner curve) in steps of 2. (b) Fix $t^+ = 1.5$, vary t^- from 0 (outer curve) to 1 (inner curve) in steps of 0.15.

sign; this boundary occurs when

$$(E_{n+1} - E_n + 2zt^{(n,n+1)}) \times (E_{n-1} - E_n + 2zt^{(n-1,n)}) = (2zt^{(n,n)})^2. \quad (10.6)$$

The five scaled parameters

$$\begin{aligned} \bar{\mu} &\equiv \frac{E_n - E_{n-1}}{E_n}, & x_U &\equiv \frac{E_{n+1} + E_{n-1} - 2E_n}{E_n}, \\ \bar{t} &\equiv \frac{t^{(n,n)}}{E_n}, & t^+ &\equiv \frac{t^{(n,n+1)}}{t^{(n,n)}}, & t^- &\equiv \frac{t^{(n-1,n)}}{t^{(n,n)}}, \end{aligned} \quad (10.7)$$

completely characterize the shape of a filling- n Mott phase boundary. Varying \bar{t} and $\bar{\mu}$ while fixing the other parameters then maps out a Mott-lobe like feature in the \bar{t} and $\bar{\mu}$ plane, is illustrated in Fig. 10.4.

Summary and discussion.—We have demonstrated a novel approach to strongly correlated lattice boson problems. One constructs a model by truncating the on-site Hilbert space to a single state for each site filling n and includes only nearest-site, single particle hoppings. While this approximation captures many multi-band effects, it is not a multi-band Hubbard model and in particular retains the ordinary Bose-Hubbard model's simplicity. In this method, arbitrary on-site correlations

may be treated, even in the mean field theory, and consequently it captures the condensate depletion, modified excitation spectra, altered condensate wavefunction, and altered equation of state characteristic of strongly interacting bosons. We have calculated the mean field Mott insulator/superfluid phase boundary analytically and observables across the phase diagram numerically.

Finally, although we have truncated to a single many-body state for each filling n , no difficulty arises from including on-site many-body excitations in the Hamiltonian. These are especially important, for example, for double well lattices and spinor bosons. The ideas also extend straightforwardly to fermions; see Refs. [186, 187, 188, 189, 190] for related considerations.

Acknowledgments.—This material is based upon work supported by the National Science Foundation through grant No. PHY-0758104. We thank Stefan Baur, John Shumway, and Mukund Vengalattore for useful conversations.

Chapter 11

Quantitative calculation of parameters for a model sufficiently general to capture all on-site correlations

11.1 Background

Chapter 10 introduced a generalized Bose-Hubbard model that is, under appropriate circumstances, capable of describing experimentally important situations, and which is much more general than the ordinary Bose-Hubbard model. However, while we could deduce the *form* of the Hamiltonian, quantitative calculation of the model's parameters is a non-trivial problem.

This chapter develops a method to calculate these model parameters for bosons with scattering length much less than the interparticle spacing (as is relevant to ^{87}Rb) and which is extensible to somewhat stronger interacting systems. It proceeds by numerical path integral Monte Carlo solution of the two (or few) site continuum problem, from which one can extract the relevant lattice description parameters for the many-site problem. This much simpler problem may then be examined with analytic techniques, or by numerical simulation much more efficiently than direct simulation of the many-site continuum problem.

11.2 Introduction, notation, and set up

The Hamiltonian of the Bose-Hubbard model extended to capture on-site correlations is (recalling Eq. (10.4))

$$\begin{aligned}
 H = & - \sum_{\langle i,j \rangle; m,n} t_{ij}^{(mn)} |m+1\rangle_i |n-1\rangle_j \langle m|_i \langle n|_j \\
 & + \sum_{i,n} \epsilon_n |n\rangle_i \langle n|_i.
 \end{aligned} \tag{11.1}$$

There are additional pair (and more) hopping terms and an off-site interaction that we argued are irrelevant in the asymptotically deep lattice. Although I neglect these here, our approach is straightforwardly extended to calculate these parameters. Here $|m\rangle_i$ is the m -particle ground state for a harmonic potential centered at site i with frequency set to match the on-site lattice oscillation frequency.

The Hamiltonian parameters are found by requiring $\langle \psi' | H | \psi \rangle = \langle \psi' | H_f | \psi \rangle$ for all $|\psi\rangle$ and $|\psi'\rangle$ for which $\langle \psi' | H_f | \psi \rangle$ is non-negligible, where H_f is the true Hamiltonian. This yields

$$E_n = \langle n | H_f | n \rangle \tag{11.2}$$

$$t^{(mn)} = -\langle m+1, n-1 | H_f | m, n \rangle. \tag{11.3}$$

We work with cold atomic systems with short range potentials, which are described by

$$\begin{aligned}
 H_f = & \int d^3r \left[\psi^\dagger(\mathbf{r}) \left(-\frac{\hbar^2}{2m} \nabla^2 - \mu + V_p(\mathbf{r}) \right) \psi(\mathbf{r}) \right. \\
 & \left. + \frac{2\pi\hbar^2 a}{m} \psi^\dagger(\mathbf{r}) \psi^\dagger(\mathbf{r}) \psi(\mathbf{r}) \psi(\mathbf{r}) \right],
 \end{aligned} \tag{11.4}$$

in the limit of interest, with m is the particle mass, μ is the chemical potential, and ψ and ψ^\dagger are bosonic annihilation and creation operators.

11.3 Quantitative estimates of the Hamiltonian parameters with quantum Monte Carlo

11.3.1 General idea

Although Eq. (10.2) gives the Hamiltonian parameters, there are two fundamental deficiencies of **Chapter 10**'s approach to calculating the model parameters (there, only estimates were attempted). The first deficiency is a technical one: since the few-body problem is generically intractable, we were unable even to evaluate the wavefunctions $|m\rangle$ except in very special circumstances; and evaluating the matrix elements is still more difficult. The second deficiency is more fundamental: even if we could evaluate the $|m\rangle$ — the solutions in a harmonic trap — these fail to give exact solutions for the energy dispersion, even in the deep lattice limit, and even for non-interacting particles. Put another way, even if one could in principle calculate the matrix elements exactly, these would not yield the correct energy dispersion. The reason for this is our solutions' incorrect behavior in the “tails” between sites, our Hilbert space does not fully include states with low energy. Formally, we may still truncate to the basis we have (and this is what will enable our description with this model, but a more sophisticated estimate of parameters), but the zero'th order condition of equating matrix elements of our generalized Bose-Hubbard Hamiltonian with the full Hamiltonian's matrix elements would need to be supplemented with higher order terms in perturbation theory.

Thus, although our earlier paper established that it is necessary to go beyond the ordinary Bose-Hubbard model by including on-site correlations with our model, we were unable to quantitatively calculate the correct Hamiltonian parameters. To overcome these difficulties we suggest the use of a quantum Monte Carlo procedure

for two sites.

The central idea is that we need the GBHM's parameters only for a two-site system, from which we can construct the model for an arbitrary lattice. To determine these, we should choose our GBHM's parameters to give rise to the same observables as the actual physical system. A first thought would be to match the moments $\langle n_L \rangle, \langle n_L^2 \rangle, \langle n_L^3 \rangle, \dots$ where n_L is the number operator on the left site (L). However, this provides only a few numbers, each of which is largely redundant with the others, to determine the parameters. It seems that a better way is to match $\langle P_m(\tau)P_n(0) \rangle$ with the operator P_m defined by $P_m \equiv |m, N - m\rangle \langle m, N - m|$; we are working within an N total particle basis and $|m, n\rangle \equiv |m\rangle_L |n\rangle_R$. This approach gives us considerably more information to match — an entire matrix of variables, each of which is a function of imaginary time — yet the problem is still tractable both for the full Hamiltonian and the GBHM (with essentially no more difficulty than calculating the moments). (This procedure is reserved for determining the $t^{(mn)}$'s. The E_m 's are determined from the still-simpler one-site problem.)

11.3.2 Relating response to correlation functions

To make our idea in the previous section precise, we note that in directly sampling the imaginary time worldlines, path integral Monte Carlo (PIMC) [191] already samples the necessary information to obtain the imaginary time-ordered Green's function

$$\mathcal{G}_{mp}(\tau) = \langle \mathcal{T} P_m(\tau) P_p(0) \rangle \quad (11.5)$$

with the expectation value in the thermal state of the full Hamiltonian, where \mathcal{T} indicates time-ordering. We will concern ourselves with the temperature $T = 0$ limit for the rest of these notes, in which case the average is carried out in the

ground state, but this condition can be relaxed if it is helpful to compare with PIMC results.

11.3.3 Implementation of correlation function in PIMC

Path integral Monte Carlo naturally measures time-ordered correlation functions. However, we want $\mathcal{G}_{mp}(\tau) = \langle \mathcal{T} P_m(\tau) P_p(0) \rangle$, which would require implementing the many-body wavefunctions $|m\rangle$ and obtaining their evolution and correlations. An approximation allows a much simpler calculation with little loss of accuracy.

The idea is to partition space into two regions; we create an imaginary dividing plane between the left and right wells. We define S_m as the operator that is one if m particles are to the left of the dividing plane. We can then calculate $\langle \mathcal{T} S_m(\tau) S_p(0) \rangle$ by counting at each time slice in the PIMC simulation if p atoms are in the left well at time $\tau = 0$ and m are in the left well at time τ .

We argue that, in the limit where the GBHM is expected to be a good approximation, it is equally accurate to take

$$\langle \mathcal{T} P_m(\tau) P_p(0) \rangle \approx \langle \mathcal{T} S_m(\tau) S_p(0) \rangle. \quad (11.6)$$

This is most concrete in the case of a single particle: the criterion is that of the single band limit, in which case the difference between projection onto the right plane and the right side comes only in the tails of the right site's Wannier function. Thus, the error in our approximation is of relative order S where S is the overlap between sites, and is on the order of one percent for our systems.

11.4 Solutions for various values of $t^{(mn)}$ and E_m

To anchor our intuition, will we do simple limits — non-interacting and non-hopping. Then we turn to numerically solving the general case.

11.4.1 Non-interacting case

Eigenstates and eigenvalues

By the non-interacting case here, I mean the non-interacting case of the original Hamiltonian, so that one obtains an ordinary Bose-Hubbard model (this is a stronger requirement than just having E_m linear in the GBHM, which could also be called non-interacting).

In the non-interacting case, we can reduce the physics to the single particle physics. For a single particle, there are two energy eigenstates, the symmetric (bonding) and antisymmetric (anti-bonding) orbitals; this is required already by symmetry since the potential is reflection symmetric.

Then, the normalized single particle states are $|\Psi_1^{(\pm)}\rangle' = (1/\sqrt{2})(|0\rangle \pm |1\rangle)$. We again use our earlier notation $|m\rangle \equiv |m, N - m\rangle$. This is rewritten in terms of annihilation operators for the left and right sites, L and R , respectively, and the associated creation operators as

$$|\Psi_1^{(\pm)}\rangle' = S_{\pm}^{\dagger} |\text{vac}\rangle = \frac{L^{\dagger} \pm R^{\dagger}}{\sqrt{2}} |\text{vac}\rangle, \quad (11.7)$$

defining $S_{\pm} \equiv (1/\sqrt{2})(L \pm R)$. As an aside: (1) we should not confuse this S with the spin operator in the spin picture that Erich has suggested for the problem; (2) the $|\rangle'$ notation indicates that we are dealing here with the one particle energy eigenstates rather than number eigenstates.

The advantage of writing things this way is the ease with which we build up the many body states; for example, the normalized ground state is simply

$$|\Psi_N\rangle' = \frac{(S^{\dagger})^N}{\sqrt{N!}} |\text{vac}\rangle. \quad (11.8)$$

More generally, the normalized s 'th excited state of the N body system, which we

denote $\overline{|s\rangle}$ is

$$\overline{|s\rangle} = \frac{1}{\sqrt{s!(N-s)!}} \left(S_+^\dagger\right)^{N-s} \left(S_-^\dagger\right)^s |\text{vac}\rangle \quad (11.9)$$

which puts s particles in the single particle excited state and $N - s$ in the single particle ground state. It immediately follows that the energies defined by $H\overline{|s\rangle} = E_s\overline{|s\rangle}$ are

$$\begin{aligned} E_s &= s\frac{\Delta}{2} - (N-s)\frac{\Delta}{2} \\ &= (s - N/2)\Delta \end{aligned} \quad (11.10)$$

where I defined Δ as the energy splitting between the single particle energy eigenstates, and put the zero of energy halfway between them. In reference to the usual two site non-interacting Bose-Hubbard Hamiltonian, $H_{\text{ni}} = -t(L^\dagger R + R^\dagger L)$, we obtain $\Delta = t$, and ignore the irrelevant constant energy shift. I shall work in terms of Δ in what remains.

Expectations of $P_m = |m\rangle\langle m|$

One of the most basic things in which we are interested is the thermal expectation value $\langle P_m \rangle$ with $P_m \equiv |m\rangle\langle m|$. Combinatoric arguments for placing distinguishable particles should give this to be a normalized binomial distribution in the ground state. In a general thermal state we obtain

$$\langle P_m \rangle = \frac{\sum_s e^{-\beta E_s} \overline{\langle s|P_m|s\rangle}}{\sum_s e^{-\beta E_s}}. \quad (11.11)$$

We know E_s so to calculate this, we just need to calculate $\overline{\langle s|P_m|s\rangle}$. Start by writing $\overline{|s\rangle}$ in the number basis, starting from Eq. (11.9):

$$\begin{aligned}
\overline{|s\rangle} &= \frac{1}{\sqrt{2^N s!(N-s)!}} (L+R)^{N-s} (L-R)^s |\text{vac}\rangle \\
&= \frac{1}{\sqrt{2^N s!(N-s)!}} \sum_{m_1=0}^s \sum_{m_2=0}^{N-s} (-1)^{m_1} \binom{s}{m_1} \binom{N-s}{m_2} \\
&\quad \times (L^\dagger)^{m_1+m_2} (R^\dagger)^{N-(m_1+m_2)} |\text{vac}\rangle \\
&= \frac{1}{\sqrt{2^N s!(N-s)!}} \sum_{m_1=0}^s \sum_{m_2=0}^{N-s} (-1)^{m_1} \binom{s}{m_1} \binom{N-s}{m_2} \\
&\quad \times \sqrt{(m_1+m_2)!(N-(m_1+m_2))!} |m_1+m_2\rangle \quad (11.12)
\end{aligned}$$

Consequently, $\overline{\langle s|P_m|s\rangle}$ is

$$\overline{\langle s|P_m|s\rangle} = \frac{m!(N-m)!}{2^N s!(N-s)!} \left(\sum_{m_1=\max\{m-N+s,0\}}^{\min\{m,s\}} (-1)^{m_1} \binom{s}{m_1} \binom{N-s}{m-m_1} \right)^2.$$

This sum is tractable according to Mathematica, if one counts hypergeometric functions as tractable. Note that

$$\overline{\langle s|P_m|s\rangle} = |f_{ms}|^2 \quad (11.13)$$

with $f_{ms} = \langle m|\overline{|s\rangle}$. Then we find

$$\begin{aligned}
f_{ms} &= \sqrt{\frac{m!(N-m)!}{2^N s!(N-s)!}} \left[\binom{N-s}{m} {}_2F_1(-m, -s, N-s-m, -1) \right. \\
&\quad \times \theta[N-(m+s)-1/2] \\
&\quad + (-1)^{N+s+m} \binom{s}{m-N+s} {}_2F_1(m-N, -N+s, 1+m-N+s, -1) \\
&\quad \left. \times \theta[-(N-(m+s)-1/2)] \right] \quad (11.14)
\end{aligned}$$

where $\theta(x)$ is the unit step function. A check is in order: for $s = 0$, the expectation becomes $\overline{\langle 0|P_m|0\rangle} = \binom{N}{m}/2^N$, as expected for the zero temperature ground state.

Now the thermal expectation is

$$\langle P_m \rangle = \frac{1}{\sum_s e^{-\beta E_s}} \left(\sum_s e^{-\beta E_s} |f_{ms}|^2 \right) \quad (11.15)$$

with f_{ms} given by Eq. (11.14). These are plotted in Fig. 11.1.

Operator correlations of $P_m = |m\rangle\langle m|$

Here we would like to calculate the imaginary time Green's function $\mathcal{G}_{mp}(\tau) = \langle \mathcal{T} P_m(\tau) P_p(0) \rangle$ defined by Eq. (11.5). We will use spectral representation of the imaginary time Green's function, which allows us to obtain $\mathcal{G}_{mp}(\omega_n)$ given the eigenstates and eigenvalues. Note that in this section, rather than denoting many-body states with an overline — as $\overline{|s\rangle}$ — I will denote them implicitly by using Greek letters — e.g, $|\alpha\rangle$.

The spectral representation for the thermal imaginary time Green's functions is

$$\mathcal{G}_{mp}(\omega_n) = \frac{1}{\mathcal{Z}} \sum_{\alpha\beta} \left\{ \langle \alpha | P_m | \beta \rangle \langle \beta | P_p | \alpha \rangle \frac{e^{-\beta E_\alpha} - e^{-\beta E_\beta}}{i\omega_n - (E_\beta - E_\alpha)} \right\} \quad (11.16)$$

defining

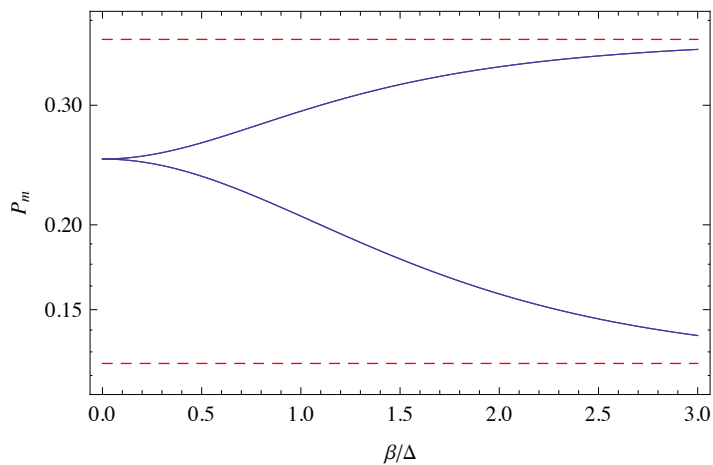
$$\mathcal{Z} \equiv \sum_{\alpha} e^{-\beta E_\alpha}. \quad (11.17)$$

I haven't included a derivation because it is the same for all operators, but have checked it if anyone cares (see OneNote). Using our results in the previous section for $\langle \beta | P_p | \alpha \rangle$ and E_α , this is

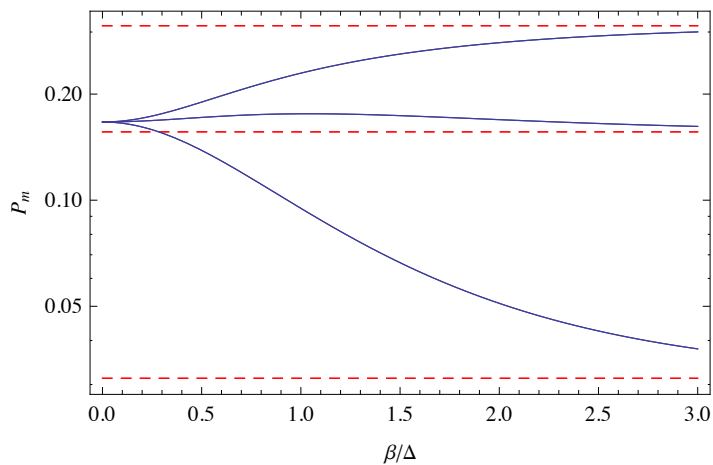
$$\mathcal{G}_{mp}(\omega_n) = \frac{1}{\mathcal{Z}} \sum_{\alpha\beta} \left\{ f_{\alpha m} f_{\beta m} f_{\alpha p} f_{\beta p} \frac{e^{-\beta E_\alpha} - e^{-\beta E_\beta}}{i\omega_n - (E_\beta - E_\alpha)} \right\} \quad (11.18)$$

where the $f_{\alpha m}$'s are given by Eq. (11.14) and the E_α 's are given by Eq. (11.10).

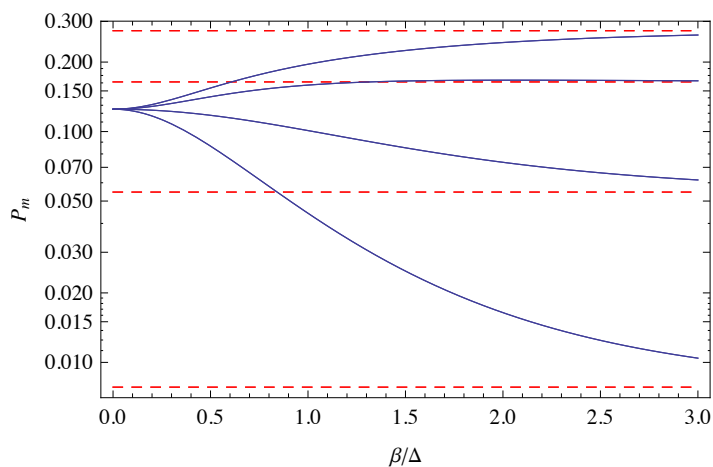
We may further drop the constant in this equation to obtain $E_s = s\Delta$.



(a)



(b)



(c)

Figure 11.1: Thermal expectation values $\overline{\langle s | P_m | s \rangle}$ versus inverse temperature $\beta\Delta$. At high temperature, all states are equally likely, while at high temperature they tend to a binomial distribution, indicated by the dashed red lines. Top to bottom: $N = 3, 5, 7$. It should be clear from the graphs which curves correspond to which m .

11.4.2 Strong coupling $t/U \rightarrow 0$ limit

In this section, I calculate the correlation function $\mathcal{G}_{mn}(\omega_n)$ in the limit of small tunnelings. This will turn out to be quite useful because the expressions obtained are analytically simple and fairly intuitive because the correlations are in a basis of almost-eigenstates. The approximations I'm making are defined more precisely in what follows.

I have carried out the calculation with two separate techniques, each with their own virtues. In the first method, I have utilized a “slave-boson” technique (this is described below, but is the same basic idea as “Schwinger bosons” in magnetic systems, mentioned just in case one is more familiar with that). This technique enables one to easily pick out and calculate the terms of interest out of the many terms present (e.g., the off-diagonal, non-zero modes of the correlation function). Moreover, it has the familiarity of many-body perturbation theory, and one can easily go to more sites and higher orders in “ t/U ” — a very challenging (or at least tedious) task with the more traditional second method. However, while I initially thought this would be a panacea, there are a few difficulties with the technique: (1) the theory contains Bose functions where Boltzmann functions could be obtained, (2) there is a free parameter in the theory — the slave boson chemical potential — which seems difficult or impossible to solve for analytically, and (3) some results in the literature seem to indicate that the slave boson approach is inexact at non-zero temperature, even in the strong-coupling limit.

Here, to complete the slave boson calculation, I overcome its failures by replacing, by hand, the Bose functions with Boltzmann functions, in which case the constant factor may be obtained analytically. Doing this yields the exact solution obtained via our second technique, however given the somewhat *ad hoc* nature of the last steps in this calculation, it is unclear whether the method will work to

higher order and for more sites.

In the second method, which suffers none of the stumbling blocks of the slave boson theory, I work directly with the spectral representation for the response function, Eq. (11.16), solving for the many-body eigenstates and eigenvalues perturbatively to obtain the response function to second order in “ t/U ”. Although this has the virtue of having no handwaving steps in the calculation, it is quite tedious already at second order with two sites, and the i^2 site, more than second order calculation would be painful.

Before giving the calculations, I will set up the general formalism. I compute the response to first order in the hoppings by splitting Eq. (10.4) into

$$H = H_0 + \lambda H_{\text{pert}} \quad (11.19)$$

with

$$H_0 = \sum_{i,n} \epsilon_n |n\rangle_i \langle n|_i. \quad (11.20)$$

and

$$H_{\text{pert}} = - \sum_{\langle i,j \rangle; m,n} t_{ij}^{(mn)} |m+1\rangle_i |n-1\rangle_j \langle m|_i \langle n|_j \quad (11.21)$$

and computing properties to first order in the control parameter λ (which is unity, physically). This should be accurate when the $t^{(mn)}$'s are smaller than the energy *differences* between the ϵ_m — that is, for deep lattices.

Small hopping, calculation with slave bosons

The first response function calculation uses slave bosons. The idea is to first note that the Hilbert space on each site j is spanned by the kets $|n\rangle_j$ enumerated by site fillings $n = 0, 1, 2, \dots$. Then we may introduce a set of creation operators ϕ_n^\dagger which act on the vacuum to give these. In an equation, we have:

$$\phi_{j,n}^\dagger |\text{vac}\rangle = |n\rangle_j \quad (11.22)$$

where the $\phi_{j,n}$'s ($\phi_{j,n}^\dagger$'s) are usual bosonic annihilation (creation) operators. Note that the vacuum is *not* the $n = 0$ state. We may then construct our theory in terms of the ϕ operators in the usual manner, obtaining a relatively simple bosonic theory in the Hilbert space formed by allowing spanned by the $(\phi_n^\dagger)^\alpha$'s acting on the vacuum. However, this theory has one unusual aspect: in this prescription we have expanded our Hilbert space enormously — for each ket $|n\rangle$ there are now many kets $\phi_n^\dagger |\text{vac}\rangle, (\phi_n^\dagger)^2 |\text{vac}\rangle, (\phi_n^\dagger)^3 |\text{vac}\rangle, \dots$. Consequently, in order to reproduce the original Hilbert space we need to enforce the constraint for the particles to remain in the original Hilbert space. This is most easily accomplished in a coherent state path integral formalism giving a generating function \mathcal{Z} for imaginary time correlation functions as

$$\mathcal{Z} = \int \left(\prod_{n=0}^{\infty} \mathcal{D}\phi_n \right) \left[\prod_{\tau,j} \delta \left(\sum_{n=0}^{\infty} \phi_{j,n}^*(\tau) \phi_{j,n}(\tau) - 1 \right) \right] \times \exp [-S_{\text{sb}}[\phi^*, \phi]] \quad (11.23)$$

the integral runs over all functions periodic with period β , and the delta function constraint limits our particles to the original Hilbert space — that is, it ensures the system has total probability of unity for occupying some state in the on-site Hilbert space; where the action is

$$S_{\text{sb}} = \int_0^\beta d\tau \left\{ \sum_j \phi_{j,n}^*(\tau) \partial_\tau \phi_{j,n}(\tau) + H_{\text{sb}}[\phi_{j,n}] \right\}, \quad (11.24)$$

with slave-boson Hamiltonian

$$H_{\text{sb}}[\phi_{j,n}] = \sum_{i,m} E_{i,m} \phi_{i,m}^* \phi_{i,m} - \sum_{\langle i,j \rangle, mn} t^{(m,n)} \phi_{i,m+1}^* \phi_{j,n-1}^* \phi_{i,m} \phi_{j,n}. \quad (11.25)$$

Equation (11.25) reveals a major strength of the slave boson formalism: it treats the on-site term exactly so is exact in the $t/U = 0$ limit, while the hopping

term now takes the form of a (somewhat unfamiliar) two-body interaction, which may be treated using usual diagrammatic perturbation theory. The sole caveat is that one must enforce the constraint at the end of the calculation; this caveat may be removed by an approximation: we (exactly) rewrite the delta function as

$$\begin{aligned} & \left[\prod_{\tau,j} \delta \left(\sum_n \phi_{j,n}^*(\tau) \phi_{j,n}(\tau) - 1 \right) \right] \\ & = \int \mathcal{D}\xi e^{i \int d\tau \sum_j \xi_j(\tau) (\sum_n \phi_{j,n}^*(\tau) \phi_{j,n}(\tau) - 1)} \end{aligned} \quad (11.26)$$

(dropping constant factors from the integration measure as usual) and follow this by approximating the $\xi_j(\tau)$ as a constant (only enforcing the constraint on average over the system):

$$\begin{aligned} & \int \mathcal{D}\xi e^{i \int d\tau \sum_j \xi_j(\tau) (\sum_n \phi_{j,n}^*(\tau) \phi_{j,n}(\tau) - 1)} \\ & \doteq \int d\xi e^{i\xi \int d\tau \sum_j (\sum_n \phi_{j,n}^*(\tau) \phi_{j,n}(\tau) - 1)} \end{aligned} \quad (11.27)$$

so that ξ appears only as an effective chemical potential for the slave bosons. I believe this exact at zero temperature and strong couplings.

At this point, one may do various sophisticated things; I do the simplest, a straightforward perturbation theory in the hopping terms. Because our system is now described by an ordinary bosonic theory once we approximate the constraint with an effective chemical potential, we may use ordinary diagrammatic perturbation theory to calculate the finite temperature correlation functions. We are interested in $\mathcal{G}_{mp}(\nu_n) = \langle T P_m(\tau) P_p(0) \rangle$. For future use, I would like to generalize this to multi site systems. Recall that we defined P_m for the two site, N total particle system as $P_m \equiv |m\rangle_L |N-m\rangle_R \langle m|_L \langle N-m|_R$. For multiple sites, probably the most useful generalization of \mathcal{G} to measure with PIMC is

$$\mathcal{Q}_{mn;ij}(\tau) \equiv \langle T S_{mi}(\tau) S_{nj}(0) \rangle \quad (11.28)$$

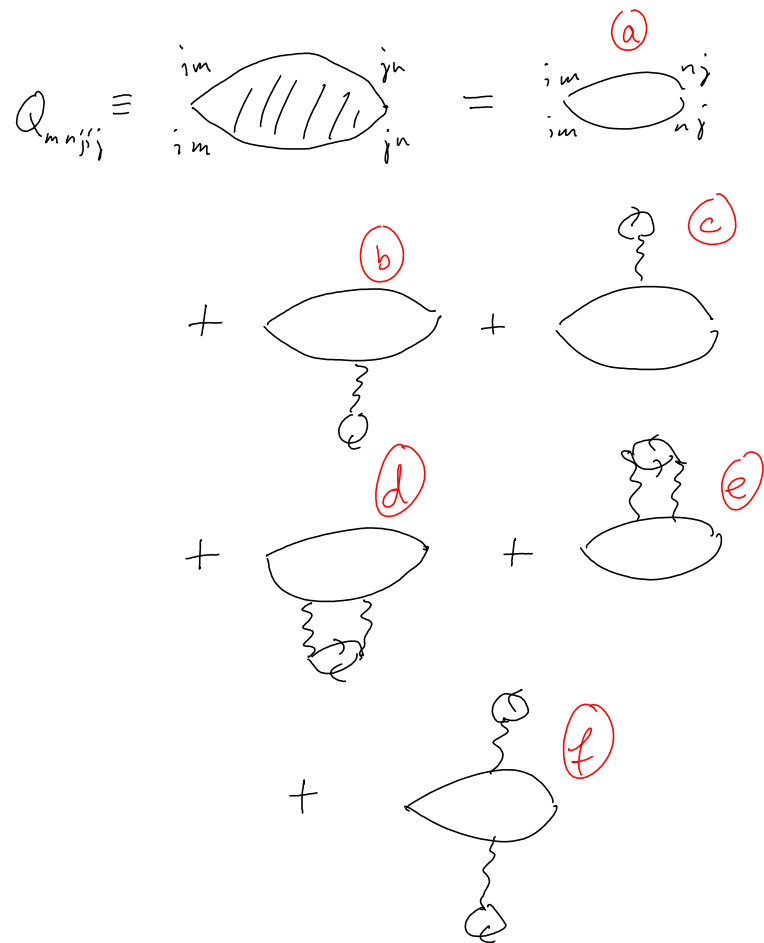


Figure 11.2: Representative diagrams for the slave boson perturbation theory at low order in “ t/U ”.

with

$$S_{mi} \equiv |m\rangle_i \langle m|_i. \quad (11.29)$$

Note that this generalization to \mathcal{Q} is different than the generalization I introduced to close the equations of motion, where I took $P_m \rightarrow P_{mn} \equiv |m\rangle \langle n|$. Written in terms of the slave boson operators, the generalized \mathcal{Q} is

$$\mathcal{Q}_{mp;ij}(\tau) = \langle T \phi_{mi}^*(\tau) \phi_{mi}(\tau) \phi_{nj}^*(0) \phi_{nj}(0) \rangle. \quad (11.30)$$

Some generic diagrams for this are shown in Fig. 11.2: the hoppings now appear as a more or less ordinary two particle interaction. For example, in words diagram (c) has a particle hopping from site m to a site s and then to site j . One strength of this approach is immediate: since the “bare” propagator is diagonal in the on-site Hilbert space, we immediately see that only diagram “(f)” contributes to the off-diagonal response to second order in “ t/U .”

In general we can evaluate the perturbation series with these diagrams. However, for two sites the problem is even simpler. We return to \mathcal{G} rather than the \mathcal{Q} . In this case, rather than introducing slave bosons for each occupation at each site, we take advantage of the fact that once the occupation of the left site is known, the right site’s occupation is also known. So we introduce slave boson operators ϕ_m and ϕ_m^* for each state $|m\rangle$, for $m = 0, 1, \dots, N$. Then the functional integral is similar to before, but the slave boson Hamiltonian is even simpler:

$$H_{sb} = \epsilon_m \phi_m^* \phi_m - t^{(m-1)} \phi_m^* \phi_{m-1} - t^{(m)} \phi_m^* \phi_{m+1} \quad (11.31)$$

with $\epsilon \equiv E_m + E_{N-m}$. The diagrammatic theory for this problem is then simply that of a particle in an external potential. From this, we can easily calculate $\mathcal{G}_{mn}(\tau) = \langle T \phi_m(\tau) \phi_m(\tau) \phi_n(0) \phi_n(0) \rangle$, writing the Green’s function in terms of the slave boson operators, as illustrated in Fig. 11.3.

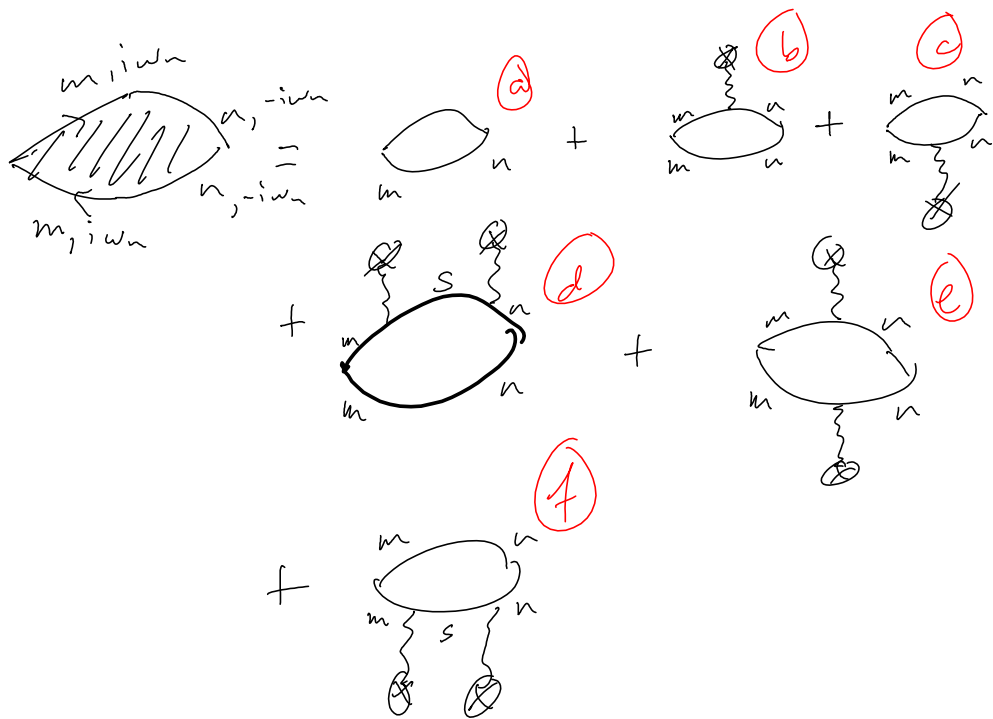


Figure 11.3: Representative diagrams for the two-site slave boson perturbation theory at low order in “ t/U ”.

Out of all the figures in Fig. 11.3 only (e) contributes to the off-diagonal response. Using standard diagrammatic rules, it gives the second order correction to the off-diagonal piece $\delta\mathcal{G}_{mp}^{(2)}$ to be

$$\begin{aligned} \delta\mathcal{G}_{mp}^{(2)}(\nu_n) &= \frac{1}{\beta^2} \sum_{\omega_1, \omega_3} \frac{1}{(-i(\nu_n + \omega_1) - \epsilon_m)(-i(\nu_n + \omega_3) - \epsilon_n)} \\ &\times \frac{\delta_{\omega_1, \omega_3} (-t^{(m-1)}\delta_{m-1, n} - t^{(m)}\delta_{m+1, n})^2}{(-i\omega_1 - \epsilon_m)(-i\omega_3 - \epsilon_n)} \end{aligned} \quad (11.32)$$

where I have absorbed the chemical potential ξ into the ϵ_m 's for the moment. I won't write out the calculation (if you're dying to see it, I can send pdfs of my illegible handwritten notes), but one may evaluate the Matsubara sums in the usual fashion, giving

$$\begin{aligned} \delta\mathcal{G}_{mn}^{(2)}(\nu_n) &= \frac{2(t^{(m)})^2 \delta_{m+1, n}}{(\epsilon_m - \epsilon_{m+1})\beta} \frac{n(\epsilon_{m+1}) - n(\epsilon_m)}{\nu_n^2 + (\epsilon_{m+1} - \epsilon_m)^2} \\ &+ \frac{2(t^{(m-1)})^2 \delta_{m-1, n}}{(\epsilon_m - \epsilon_{m-1})\beta} \frac{n(\epsilon_{m-1}) - n(\epsilon_m)}{\nu_n^2 + (\epsilon_{m-1} - \epsilon_m)^2} \end{aligned} \quad (11.33)$$

where $n(\epsilon) \equiv (e^{\beta(\epsilon - \xi)} - 1)^{-1}$ is the usual Bose function (no longer absorbing the chemical potential into the energies ϵ).

We have yet to determine the slave bosons' chemical potential ξ . This requires solving

$$\sum_m n(\epsilon_m) = 1 \quad (11.34)$$

which it wasn't obvious to me how to do, even for $t^{(n)} = 0$. However, an *ad hoc* guess reproduced the exact answer (calculated below): we replace the Bose functions with Boltzmann functions, in which case the chemical potential is simply a normalization, which is $1/\sum_m e^{-\beta\epsilon_m}$. This exact answer compares favorably with the exact diagonalization and is confirmed doing direct perturbation theory below. Various visualizations can be found in my Mathematica notebook.

There is one point that must be kept in working with Eq. (11.33) in practice: when energies m and $m + 1$ or m and $m - 1$ approach each other, one must take

the limit of the summand where the energies approach each other to avoid the indeterminate $0/0$.

Small hopping, calculation with ordinary perturbation theory in spectral representation

In this section I calculate the correlation function $\mathcal{G}_{mn}(\omega_n)$ in the limit of small tunnelings directly from the spectral representation, which is more tedious and less intuitive than the slave bosons, but doesn't require any "handwavey" steps.

We start with the spectral representation given in Eq. (11.16) and expand the eigenstates and eigenvalues to second order in t/U . Careful examination reveals that one only needs to expand the eigenstates to first order in t/U and can neglect the expansion of the eigenenergies. In a little detail: (1) the energy corrections occur to lowest order at t^2 , so for second order terms, the many-body states in the matrix elements $\langle\alpha|P_m|\beta\rangle\langle\beta|P_p|\alpha\rangle$ may be taken to be the unperturbed states. In this case, the response function gets only a diagonal contribution, which we is uninteresting for us. (2) The second order corrections to the many-body eigenstates also give only diagonal contributions. So we simply calculate the matrix elements in the spectral representation by computing the many-body eigenstates' corrections to lowest order. Naively, this gives 24 terms which I don't write down here (again, I can pdf illegible notes with the structure); of these, only four terms survive giving in the spectral representation

$$\delta\mathcal{G}_{mp}^{(2)}(\nu_n) = \frac{1}{\sum_m e^{-\beta\epsilon_m}} \left[\frac{|t^{(m)}|^2 \delta_{m,n-1}}{(\epsilon_m - \epsilon_{m+1})^2} \left(\frac{e^{-\beta\epsilon_{m+1}} - e^{-\beta\epsilon_m}}{i\nu_n - (\epsilon_m - \epsilon_{m+1})} + \frac{e^{-\beta\epsilon_m} - e^{-\beta\epsilon_{m+1}}}{i\nu_n - (\epsilon_{m+1} - \epsilon_m)} \right) + \frac{|t^{(m-1)}|^2 \delta_{m,n+1}}{(\epsilon_m - \epsilon_{m-1})^2} \left(\frac{e^{-\beta\epsilon_{m-1}} - e^{-\beta\epsilon_m}}{i\nu_n - (\epsilon_m - \epsilon_{m-1})} + \frac{e^{-\beta\epsilon_m} - e^{-\beta\epsilon_{m-1}}}{i\nu_n - (\epsilon_{m-1} - \epsilon_m)} \right) \right] \quad (11.35)$$

which simplifies to

$$\delta\mathcal{G}_{mp}^{(2)}(\nu_n) = \frac{2}{\sum_m e^{-\beta\epsilon_m}} \left[\delta_{m,n-1} (e^{-\beta\epsilon_{m+1}} - e^{-\beta\epsilon_m}) \frac{(t^{(m)})^2}{(\epsilon_{m+1} - \epsilon_m)(\nu_n^2 + (\epsilon_m - \epsilon_{m+1})^2)} \right. \\ \left. + \delta_{m,n+1} (e^{-\beta\epsilon_{m-1}} - e^{-\beta\epsilon_m}) \frac{(t^{(m-1)})^2}{(\epsilon_{m-1} - \epsilon_m)(\nu_n^2 + (\epsilon_m - \epsilon_{m-1})^2)} \right] \quad (11.36)$$

This agrees very well with the exact result and agrees exactly with the slave boson calculation supplemented with the Bose→Boltzmann replacement.

11.4.3 General — correlation functions from exact diagonalization

We want to find the correlation functions $\mathcal{G}_{mp}(\omega_n)$ for our 2-site generalized Bose-Hubbard model, described by the Hamiltonian of Eq. (10.4). Rewriting this for two sites, using our now-familiar notation $|m\rangle \equiv |m\rangle_L |N-m\rangle_R$, we obtain

$$\langle m|H|n\rangle \\ = -t^{(m-1, N-m+1)} \delta_{m-1, n} - t^{(N-m-1, m+1)} \delta_{m+1, n} + (\epsilon_m + \epsilon_{N-m}) \delta_{mn} \quad (11.37)$$

We may now find the $\mathcal{G}_{mn}(\omega_n)$'s by finding this matrix's eigenvalues and eigenvectors, and then using \mathcal{G}_{mn} 's spectral representation Eq. (11.16). I have written a Mathematica code to do this.

Note that because of the symmetry under interchanging α and β , the expressions for \mathcal{G} may look nice by rewriting the $(i\omega - E_\alpha + E_\beta)^{-1}$ in terms of a Lorentzian in both this and previous sections.

11.5 Note on temperature dependence of response functions.

At high temperature, temperature gives only a scale: the exponential difference in spectral expansion expands so that one gets only a constant factor of $1/T$ (and the scale of my spectral functions does change, consistent w/ this; there is also a change in scale, but no ω -dependence, from the partition function). At low temperature, the temperature dependence again gives only an overall scale: the ground state should remain in the sum, others disappear, by which I mean one sum disappears (either $\alpha = \text{GS}$ and β sums or $\beta = \text{GS}$ and α sums) — so $e^{-\beta E_{GS}}$ factors. Similarly, non-interacting Green's functions will be temperature independent except for a possible scale. So it is unsurprising if the shape of our imaginary time correlation functions are roughly independent of temperature. This is a completely general property of Green's functions, not just the ones we have considered here.

Chapter 12

Summary, conclusions, and the future of induced gauge fields and lattices with on-site correlations

Although rotation and effective magnetic fields have been around essentially since the first observations of Bose-Einstein condensates, they have only more recently become capable of approaching exotic states.

The (former) Chu group have created fractional quantum Hall puddles in a lattice, using methods similar to those discussed in Chapter 9 (in preparation[192]). The NIST group have recently demonstrated creation of vortices via light-induced gauge fields, and these are estimated to be capable of reaching the ~ 100 particle quantum Hall regime in elongated geometries [130].

Theoretically, it would be interesting to better understand the connection between these arrays of quantum Hall puddles in lattices where tunneling is important (as discussed in Chapter 10) and networks of FQH states in semiconductors [173]. Experimentally, this physics can be explored in the immediate future by continuing the Chu group's experiments mentioned above at lower lattice depths.

The importance of on-site correlations in other situations has been experimentally demonstrated, even in seemingly weakly interacting ^{87}Rb optical lattice experiments. It will be interesting to quantitatively examine these and other experiments' inferred model parameters with those calculated using the techniques of Chapter 11. There are further interesting opportunities for using lattices far outside the Hubbard regime to maximize the transition temperature of desired ordered states (such as antiferromagnetism) [193] or to explore universal phenomena that are insensitive to these microscopic details (such as quantum criticality, see Chapter 13).

Chapter 13

Quantum criticality: introduction

This Chapter and Chapters 14 and 15 are in preparation for submission for publication.

Cold atom experiments have realized exciting models and phases of matter relevant to condensed matter physics [33]: bosons in optical lattices realize the Bose-Hubbard model, and in reduced dimension create a Tonks-Girardeau gas; fermions near a Feshbach resonance explore the BCS-BEC crossover and with increasing polarization the Clogston limit and novel phases of matter (e.g. FFLO), and spinor gases show possible “supersolid” order. Ongoing experiments attempt to realize spin models, FFLO in quasi-1d, and the Fermi Hubbard model’s anti-ferromagnetic Mott insulating phase; somewhat further off is the study of d -wave superconductivity.

At present we have a very incomplete understanding of strongly correlated phases of matter, and the prospects of studying this zoo of phases with the control of cold atoms has generated tremendous excitement in the community. In the condensed matter community, behavior near zero-temperature phase transitions between these phases — especially in the finite temperature “quantum critical region” — is an equally important theme with crucial open questions. In this regard, it is somewhat surprising that the quantum critical region associated with the cold atomic systems’ phase transitions has been largely ignored. This is especially true since many ongoing cold atoms experiments are already at temperatures and parameters corresponding to the quantum critical region! This is partially due to concerns that finite particle number and finite size/harmonic confinement render these properties unobservable.

In Section 14.1 we point out that, despite these concerns, quantum critical

behavior survives even in present cold atom experiments. Then in Section 14.2 we show that although the universal behavior is masked in present measurements — for example, density profiles — *it is possible to construct novel analysis methods to observe this physics, even from density profiles*. We also briefly discuss how quantum critical dynamics may be extracted using feasible cold atoms probes, particularly spectroscopic tools.

After establishing these general principles, we explicitly demonstrate our arguments on fairly well-understood QCP's: the quantum phase transition between the vacuum and a spinless Fermi liquid, the vacuum to dilute Bose gas transition, and the Bose-Hubbard model's Mott insulator to superfluid transitions (although even here, some major questions remain and are topics of vigorous theoretical investigation which we will discuss in the text). We highlight the requisite analysis to extract quantum critical properties from cold atoms experiments, and compute the relevant quantities for these experiments. Since present cold atoms experiments are actively exploring each of these transitions, in addition to demonstrating our claim that quantum criticality manifests in cold atoms systems these calculations also provide theory for comparison to these experiments.

Even for these conventional quantum phase transitions, and even at the simplest level of *static* observables near the $O(2)$ rotor quantum critical point — which is essentially solved, via large scale numerics — calculations of the universal coefficients of the power laws near this point have yet to be verified experimentally [194, 195]. We will show that existing experiments on the Bose-Hubbard model are able to probe measure these numbers.

Turning to dynamics, again restricting to these conventional phase transitions, only some basic universal features are known. For example, consider arguably the simplest interacting quantum phase transition in $d > 1$ (that is simultaneously

below the upper critical dimension where mean field theory applies): the 2D dilute Bose gas. The most quantitative theory we possess of this transition has only modest accuracy: comparing in a special limit to an exact calculation shows a 20% disagreement in the experimentally relevant regime [196]. Moreover, its quantum critical dynamics show significant (factor of 2-6) discrepancies when compared to experiments on antiferromagnets in this universality class [196].

The mysteries are even greater for other models relevant to cold atoms. One example is the $O(2)$ rotor model, which is relevant to describing the “tip of the Mott lobe” in the Bose-Hubbard model. When put in a finite chemical potential, even the qualitative dynamical features are still the subject of research; this has been tackled recently with advanced applications of hydrodynamics and the AdS/CFT correspondence [197, 198, 199].

Tunable physical realizations of these models this would allow investigation of these fundamental questions. They would also provide access to non-universal features, e.g. (1) the region of validity of the universality at high temperature and to non-low energy probes, (2) the leading corrections to the universal behavior, and (3) the numerical parameters appearing in the low energy effective theories of these systems. Moreover, due to the higher temperatures and clear scaling signatures, it may be possible to observe the quantum critical characteristics associated with novel phases more easily than the phases themselves!

We re-emphasize that although we demonstrate our general arguments on specific models, these arguments apply to generic quantum critical points. The ability to access more general quantum critical points in cold atoms is quite enticing, especially for fermionic quantum critical points. Here, even quite simple systems apparently give rise to qualitatively ill-understood transitions, where even the range of universality classes is unclear; indeed, it is contentious whether the standard

types of scaling relations need apply at these transitions. The most immediate example occurring in present experiments is the finite-temperature Mott-metal crossover — for which it is unclear whether it is governed by a hidden quantum critical point, and if so, which universality class applies. Realizations of many still more fascinating systems are well underway.

Chapter 14

Quantum criticality in cold atoms

14.1 General criteria to observe cold atomic quantum criticality

Cold atom experiments have observed phase transitions associated with quantum critical points. Perhaps the most prominent example is the Mott insulator to superfluid phase transition for bosons in an optical lattice, which has been thoroughly studied in various dimensions, utilizing various probes: density profiles, noise spectroscopy, modulation spectroscopies, Bragg spectroscopy, and rf spectroscopy are notable methods [91, 85, 92, 200, 201, 73]. We will briefly discuss the physics of this phase transition, which is taken up in more detail in Section 14.5, as many of its generic features recur through all quantum critical regions.

For this phase transition, the lattice site filling is quantized to integer values over finite ranges of chemical potential (finite regions of the trap within the LDA approximation). Spatially, in between these quantized densities are shells with intermediate fillings, which at zero temperature are associated with the superfluid. At finite temperature, these shells are in general a mixture of superfluid (SF) and normal fluid (NF). The normal fluid exists in two regimes with distinct qualitative behavior and scaling: NF above the superfluid, NF quantum critical. (Strictly, the MI exists only at zero temperature, so the MI plateaus seen in experiment is a third type of NF; it is the NF above the MI state.) Resultantly, this system's shells are good candidates to display quantum critical behavior. The richness of the finite temperature phase diagram is illustrated in Fig. 14.1.

Before we calculate expected behavior for any particular phase transitions, we take a step back: is the picture of the behavior of a low energy effective theory of a

thermodynamic, homogeneous critical system even relevant here — does it apply and possess experimental consequences? This is a central question for this chapter, which we answer for quite general systems. We find that quantum critical behavior *is* observable in cold atoms. Although it is washed out in typical observables, we construct robust techniques to extract the universal quantum critical behavior from typical cold atoms experimental measurements. In this section we start with qualitative scaling arguments.

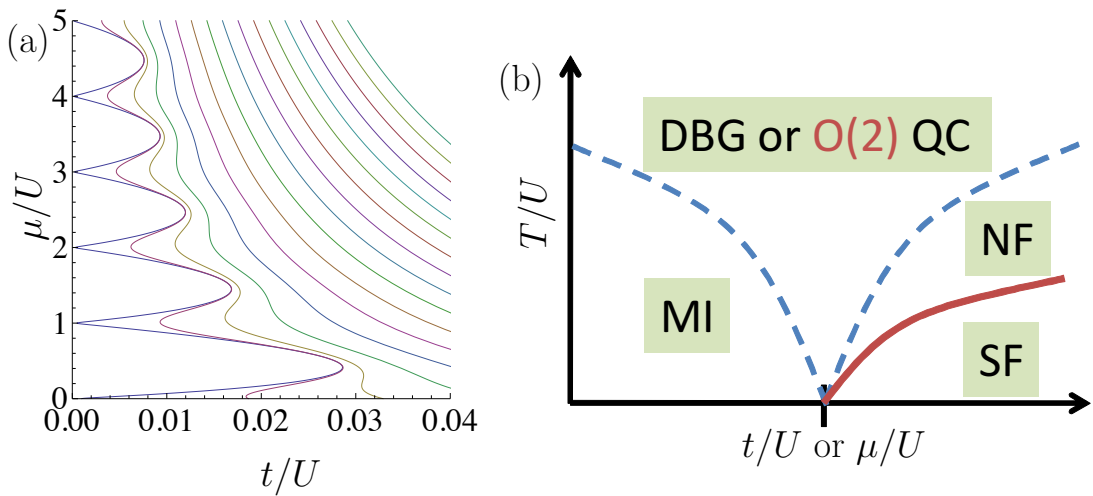


Figure 14.1: (a) Zero-temperature phase diagram illustrating Mott and superfluid phases computed within a finite-temperature extension of Gutzwiller mean field theory; constant density contours are phase transitions at temperature $T/U = (0, 0.06, 0.12, \dots, 0.96)$, from smallest to largest “lobes.” (b) Finite-temperature slice of phase diagram demonstrating the normal fluid and quantum critical regimes, the classical critical regime (a region near the SF/NF transition line), and the superfluid and Mott regimes. Note that all of the energy scales — the quantum critical crossover, the width of the classical critical region, and the superfluid transition temperature all scale in the same universal manner, as $\left| \frac{t-t_c}{t_c} \right|^{z\nu}$ where $z = 2$ generically and $z = 1$ for the transition at fixed density at the tip of the Mott lobe and ν is the critical exponent associated with the most relevant scaling variable (although this last property isn’t preserved in the Gutzwiller approximation to the finite temperature phase diagram).

First let us enumerate the most fundamental ostensible hurdles to observing QC behavior: experiments need

1. to be sufficiently cold to be in universal region,
2. enough particles in the trap in the QC region for a measurable signal,
3. suitable probes,
4. sufficiently slowly varying potential that homogeneous thermodynamics applies locally
5. reconstruction of local properties, from column integrated, possibly low-resolution data.

We argue that none these problems are a significant obstacle.

Points (1-2).—The first two requirements compete: the first requires sufficiently low temperatures for the system to be universal while the second requires sufficiently large temperatures for the quantum critical region to be observably large. We show that there exists a window of temperatures well-satisfying both criteria, and that current experiments already obtain these temperatures for important phase transitions.

Point (1) requires that the system is cold enough that the temperature is much less than the UV cutoff energy. For dilute gas transitions the UV cutoff scale is associated with the shape of the interaction potential beyond what is characterized by the s -wave scattering length (this may be estimated by the effective range) and current experiments often possess temperatures several orders of magnitude smaller than this energy scale. For lattice transitions, generically the high energy cutoff is set by the tunneling energy t ; here the coldest experiments have achieved perhaps $T/t \sim 0.3-0.5$. Later we shall show for several examples that this is cold enough to be quite well into the universal regime, which may persist semi-quantitatively to temperatures as high as $T/t \sim 2-3$.

Point (2) requires the system to be warm enough that the quantum critical regime occupies a wide enough region of chemical potentials to be observable, which

is accomplished by warming the system, as shown in Fig. 14.1. Thus, individually points (1-2) are readily satisfied, but together they are in tension. Nevertheless, even at temperatures well into the universal regime — say $T/t \sim 1$, the quantum critical region occupies a sufficient width in the trap. We will give estimates for the Bose-Hubbard model, but the qualitative considerations should pertain to any lattice model and include continuum cases (e.g., the vacuum-to-superfluid transition in the dilute Bose gas) as special cases.

We divide the possibilities into two cases, progressively more challenging. First, let's consider the transition from the site filling $n < 1$ superfluid to the $n = 1$ Mott insulator illustrated in Fig. 14.1. Rather than directly thinking about width in the trap, we initially consider the range of relevant energies (chemical potentials) in the trap. Then we consider the fraction of those that lie in the quantum critical regime. Within the Thomas-Fermi approximation (the validity of which is discussed later), this straightforwardly yields the spatial fraction of the system in the quantum critical regime. With parameters so the phase transition happens near the trap center, the total energy range spanned by the cloud is $\Delta_C \sim \mu_c$ where μ_c is the critical μ . For the transition presently considered at small t the critical μ_c satisfies $\mu_c \propto t$. Consequently, $\Delta_C \sim t$. The width of the quantum critical regime¹ is $\Delta_{QC} \sim T$, while the criteria of point (1) requires that the temperature T is low compared to the particle bandwidth to be in the universal regime: $\Delta_{QC} \ll t$. Point (2) requires that the number of particles in the QC region is measurable: high spatial resolution experiments can measure regions occupying 2% or more of the cloud radius. Let's temporarily assume this means that observability requires $> 2\%$ of the energy range to be quantum critical. Then we have the energy window

¹Here, I mean the region where $T \ll g - g_c$ with g the variable tuning the system through the $T = 0$ quantum critical point. The universal scaling regime includes this but is even more general.

for simultaneous observability and universality of

$$0.02\Delta_C \lesssim \Delta_{QC} \lesssim t \quad (14.1)$$

or

$$0.02t \lesssim T \lesssim t, \quad (14.2)$$

which allows each criteria to be satisfied by an order of magnitude. Since, as we claimed above and will see later, universality persists even to $T \sim 2$ -3, this in principle allows exploration into the universal quantum critical regime.

Secondly, let's consider the somewhat harder to observe transition from the $n = 1$ MI to the $n > 1$ SF illustrated in Fig. 14.1 (the same scales actually also apply to the $n > 1$ SF to $n = 2$ MI transition). Now, $\Delta_C \sim U$ and the temperature window for simultaneous universality and observability of Eq. 14.1 becomes

$$0.02U \lesssim T \lesssim t. \quad (14.3)$$

Relevant U/t 's range in 2D from $U/t = 15$ at the tip of the Mott lobe to $U/t = 40$ quite deep in the Mott lobe, so the temperature window is

$$\{0.3, 0.8\}t \lesssim T \lesssim t. \quad (14.4)$$

This indicates that quantum criticality may persist, even for deep lattices with tunnelings much smaller than required to enter the Mott state.

Even though this already indicates that observing universal quantum criticality is feasible in present experiments, even for deep lattices with $U/t > 40$ and for the most demanding of the two cases of phase transitions considered, *there are four reasons that its observation is considerably more feasible than this estimate indicates:* (A) As previously mentioned, we shall show that universality survives up to temperatures a few times t . (B) For the most stringent case, there are actually

four quantum critical regions occurring in a single cloud, each of which meets the observability criteria given above, which all may be studied simultaneously: the vacuum-SF, SF ($n < 1$)-MI ($n = 1$), MI ($n = 1$)-SF ($n > 1$), and the SF ($n > 1$)-MI ($n = 1$) phase transitions. (C) Turning to length scales, rather than energy scales above, because the trap varies more rapidly as one moves from the trap center, the regions that occur toward the center of the trap actually occupy more relative space than relative energy range (and those occurring near the edge of the cloud occupy less space than relative energy range). Because the most difficult to achieve transitions first occur at the center, this boosts the relative portion of the cloud size relative to the relative energy size. (D) Finally, over the longer term, continued progress in cooling and trap engineering will improve the achievable temperatures as well as the capability to increase the size of the interesting regions of the trap.

Point (3).—We more fully address point (3) in the next section, but the conclusion is that the density profiles already show distinguishing characteristics of quantum critical scaling sufficient to differentiate this behavior from that on either side of the quantum critical point, from non-universal physics, and to distinguish between universality classes. More sophisticated probes, such as spectroscopy or nonequilibrium measurement, would allow even more informative measurement of the behavior.

Point (4).—The diverging correlation length ξ associated with second order phase transitions is an ostensible obstacle to studying criticality with cold atoms, and indeed will give the most stringent requirement on observing universal physics. However, this characteristic deserves a more careful examination: the universal behavior manifests whenever ξ is much smaller than the system size L , but much larger than all other characteristic lengths. For the simple model lattice systems

realized in cold atoms, near the zero temperature phase transition this amounts to requiring $d \ll \xi \ll L$ where d is the lattice spacing. This is equivalent to requiring temperatures sufficiently below the UV cutoff, $E_L \ll T \ll t$ where E_L is the energy scale associated with the system size L . The upper bound on temperature is the same criterion of Point (1). The lower bound is unique to this point and requires some care: the relevant size L is the size over which the chemical potential may be considered fixed: here, roughly the region of space over which μ varies by an amount $\sim t$. For small L (compared to the cloud size R_{TF}) centered around a point a distance r from the trap center, this is $L/R_{\text{TF}} \sim \frac{1}{2} \frac{R_{\text{TF}}}{r} \frac{t}{\mu_c}$ where μ_c is the central chemical potential. The precise value of L depends on where in the trap the phase transition occurs, but typical values are $L \sim R_{\text{TF}} \sim 50d$ for the $n < 1$ SF to $n = 1$ MI transition and $L \sim .1R_{\text{TF}} \sim 5d$ for the $n = 1$ MI to $n > 1$ SF. The former case gives a multiple order-of-magnitude separation of scales to ensure universality (even under less optimistic criterion). The latter case is more difficult, but we will see that the quantum criticality manifests, at least qualitatively, in this case as well and future advances in trap engineering and cooling can enable quantitative measurements of criticality even in this very demanding case. Finally, this criterion will ensure that the local-density approximation is valid and may be used to extract information about the homogeneous system's quantum criticality from measurements of the trapped system.

Point (5).—Absorption imaging produces column integrated properties, and these often wash out crucial features of the system's local properties. In principle, by taking advantage of the trap symmetries in many cases, one can reconstruct the local density via an inverse Abel transform. However, this introduces undesirable levels of noise, and consequently could prevent measurement of the local properties crucial to measuring quantum criticality. However, this sometimes may

be circumvented by extremely accurate signals and extensive averaging (Ketterle), novel reconstruction algorithms (Mueller), or by using 2D systems, removing the column integration altogether (Chin, Greiner, others, ...). The latter is perhaps the most appealing, since 2D systems are below the upper critical dimension — $d = 3$ for many quantum critical theories — and it is consequently in reduced dimensions that the quantum critical behavior is most interesting. For initial tests with the dilute Bose and Fermi gas-to vacuum phase transitions, it may be possible to obtain local results even in 3D gases simply by looking at the edge of the cloud.

If any doubts remain regarding the observability of the quantum critical region in cold atoms, Sections 14.3 and 14.5 explicitly demonstrate observability for the trivial non-interacting fermions QCP (via exact essentially analytic calculations) and the $d = 2$ Bose-Hubbard model (via worm algorithm quantum Monte Carlo), even for small traps and particle number. We point out that by the Jordan-Wigner transformation, the non-interacting fermion results imply observability also for the $d = 1$ Bose-Hubbard model.

14.2 General construction to eliminate unmeasurable non-universal parameters

14.2.1 Universal scaling functions from feasible cold atoms observables: density profiles

Near the quantum critical point low energy observables take on scaling forms [121]. To be concrete we consider the density and the compressibility — we will consider the most general case at the end of this section. To be precise, we consider the density n_{QC} of the field describing quantum criticality. In general the particle

density n may include an additional, non-universal contribution, but this non-universal contribution is often easy to exactly and analytically evaluate, or to measure, so it may be subtracted out. An example of this is worked out in Sec. 14.5 for the case of the Bose-Hubbard model. On general scaling grounds, the density n_{QC} in d -dimensions satisfies

$$n_{QC}(\beta, \mu) = \beta^{-d/z} \Phi(\beta\mu) \quad (14.5)$$

for dynamic exponent z , some universal function Φ , which depends only on the universality class of the phase transition and a prefactor to convert from energy to length units (e.g., the effective mass or velocity characterizing the QCP).

At this point it may appear that we should be able to collapse the data simply by plotting $n\beta^{d/2}$ versus $\beta\mu$, obtaining Φ . However, μ is experimentally inaccessible for a fundamental reason: μ is not a low-energy observable, but rather is a “bare” parameter of the effective quantum critical theory. For example, the chemical potential associated with the dilute Bose gas fixed point describing the Mott insulator to superfluid phase transition is not simply related to the true chemical potential of the corresponding Bose-Hubbard model at that point in the phase diagram. (One can approximately calculate, microscopically, the relation. I have carried this out in unpublished work omitted from this thesis.)²

The normal route to overcoming the fundamental inability to measure μ is to relate μ (or whatever observable tunes one through the quantum critical point) to some observable. Often this is done by relating it to the zero-temperature gap at the same value of the coupling constants [121]. Here, however, it is infeasible

²Only in the very special case of the actual dilute Bose gas to vacuum transition occurring at the edge of cold bosonic clouds can we identify μ as the physical chemical potential of the microscopic theory; however, even in this case it is difficult to measure: we must do something such as measuring the tails and fitting them to Gaussians at finite temperature and central chemical potential and extracting the central chemical potential from that (from which the local chemical potentials can be deduced). Achieving good signal to noise for accurate measurements is challenging.

to measure the gap due to the lack of local spectroscopic probes, and is possibly difficult even to reach a sufficiently low temperature to measure it in principle. Instead, we suggest using the compressibility κ as a second observable, which may be obtained by spatially differentiating the density profile. Recently, data quality has become sufficiently good to extract the derivatives; better analysis techniques are expected to further improve the situation.

The compressibility satisfies

$$\kappa(\beta, \mu) = \beta^{-(d/z-1)} \Psi(\beta\mu) \quad (14.6)$$

for some Ψ . Consequently, we can invert Eq. (14.5) to write

$$\beta\mu = \Phi^{-1}(n(\beta, \mu)\beta^{d/z}) \quad (14.7)$$

so that

$$\kappa(\beta, \mu) = \beta^{-(d/z-1)} \Xi(n\beta^{d/z}) \quad (14.8)$$

where

$$\Xi(x) \equiv \Psi(\Phi^{-1}(x)). \quad (14.9)$$

14.2.2 Universal collapse between different universal curves associated with varying values of effective quantum critical parameters

It is worth clarifying the meaning of the term “universal” when applied to scaling functions such as Ξ above. The function is universal in the sense that when one is given a quantum critical point and explores the physics near it by varying the two relevant variables — here, the chemical potential μ and temperature T — the

physics is governed by a function of a single variable, giving a non-trivial scaling collapse.

An extension of this is possible. This notion of universal collapse says nothing about the relationship of scaling functions of distinct quantum critical points, even if they are in the same universality class. In fact, with a little more work it is possible to collapse all the data between these. The method above fails because Φ , Ψ , and Ξ depend on effective parameters characterizing the quantum critical theory: for example, the dilute gas transitions are characterized by an effective mass m^* and the $O(2)$ model is characterized by an velocity c . In general, this is a parameter to convert between length and energy units. The values of these parameters clearly depend on the quantum critical point being studied, and will vary between QCP's even in the same universality class. Fortunately, because the scaling curves depend on this parameter only in a prefactor to ensure the rest of the expression — written in energy units by convention — has the correct physical units (more general scaling functions, for example, spectra, can include these parameters in the arguments as well, to convert between energy and length units)

Because of the simple structure of the dependence on these parameters (that is, they just give a prefactor), it is possible to achieve a fully universal collapse between all QCP's in same universality class, by determining the scale by fitting the overall scale of universal scaling functions (the collapse is still non-trivial despite this one parameter fit) and or by obtaining the scale from auxiliary measurements (spectra, etc.).

14.2.3 Most general observables

Similar results apply for all low energy observables, not just the density associated with the quantum critical field. There is one key difference for other observables: if they involve the order parameter field they may display scaling with temperature more general than that of Eq. (14.5). This is associated with the “anomalous dimension” of the operators: the scaling of the fields with temperature in order to obtain finite field-correlators. Associated with this are non-universal prefactors to the scaling function. The anomalous scaling presents no problem — one simply finds the appropriate power of temperature to find the anomalous dimension (similar to using the above analysis to find the dynamical exponent). Similarly, the non-universal prefactor is no different than the prefactors encountered above.

14.3 Simple example: non-interacting fermi liquid to vacuum quantum phase transition and verification of LDA results explicitly for non-interacting fermions

In this section we discuss a trivial quantum phase transition: the transition from the vacuum to a Fermi gas for spinless, non-interacting fermions. The relevant grand canonical Hamiltonian describing this is

$$H = \int d\mathbf{k} \left(\frac{\hbar^2 k^2}{2m} - \mu \right) f_{\mathbf{k}}^\dagger f_{\mathbf{k}} \quad (14.10)$$

where $f_{\mathbf{k}}$ is a fermionic annihilation operators for particles with momentum \mathbf{k} . In cold atomic systems this is the full microscopic Hamiltonian for a spin-polarized gas; the gas is non-interacting because the interaction potential is an s -wave δ -function. More generally, any interactions are irrelevant near this point. The phase transition occurs at $T = 0, \mu = 0$.

There are two reasons we discuss this transition: (1) because of its triviality, it is easy to investigate the relevant issues for studying quantum criticality with cold atoms, especially the harmonic trap and finite particle number. This specific calculation complements Sec. 14.1's general analysis. (2) This transition is experimentally relevant. Firstly, and most trivially, the edge of clouds of spin polarized or non-interacting fermions naturally realize this phase transition and could serve as testing ground and calibration of the concepts in this paper. A less trivial application of the theory would be to add a weak interaction; this may be treated perturbatively, and is conjectured to describe the high temperature Mott/metal crossover [121, 202, 203], which has recently been observed in cold atoms experiments [204, 205].

Finally, we can gain insight and confidence in our techniques from this since many of the generic features (e.g., scaling forms) encountered in this context survive at much less trivial quantum critical points. Finally, the $d = 1$ hard core Bose-Hubbard model maps exactly onto non-interacting *lattice* spinless fermions via the Jordan-Wigner transformation, as shown in Sec. 14.5.2, so our analysis of the trap and finite particle number directly applies to the dilute limit of that model as well.

14.3.1 Universal scaling collapse for finite particle number and with a trap

We consider the exact solution to the trapped, few particle problem, calculating the density profiles and applying Sec. 14.2's universal rescaling procedure, although it is exact only in the local density (Thomas-Fermi) approximation. Then we apply the LDA to calculate the density profiles, and compare to the analysis of our few particle, trapped systems to see how well universal scaling functions of few

particle systems match those in the thermodynamic limit. We shall see they agree satisfactorily, showing that our general arguments of Sec. 14.1 apply well in this case.

Near the quantum phase transition (and, for this special case, everywhere) the density takes the single parameter universal form

$$n(\mu) = -\mathcal{C}\beta^{-d/2}f_{d/2}(-e^{\beta\mu}) \quad (14.11)$$

where $f_{d/2}$ is the appropriate polylogarithm and the constant \mathcal{C} is

$$\mathcal{C} \equiv (2\pi m)^{d/2}. \quad (14.12)$$

As shown in Sec. 14.2, we should consider $\kappa\beta^{-1/2}$ as a function of $n\beta^{1/2}$. The compressibility is defined as

$$\kappa \equiv \frac{\partial n}{\partial \mu}, \quad (14.13)$$

which may be calculated in the LDA from the trapped system's density via

$$\kappa = -\frac{\partial n}{\partial r} \frac{1}{m\omega^2 r}. \quad (14.14)$$

For non-interacting one dimensional fermions, differentiating the above gives

$$\kappa\beta^{d/2-1} = -\mathcal{C}f_{d/2-1}(-e^{\beta\mu}) \quad (14.15)$$

while $n = -\mathcal{C}\beta^{-d/2}f_{d/2}(-e^{\beta\mu})$, inverts to

$$-e^{\beta\mu} = f_{d/2}^{-1}\left(-\frac{n\beta^{d/2}}{\mathcal{C}}\right) \quad (14.16)$$

so that

$$\kappa\beta^{d/2-1} = -\mathcal{C}f_{d/2-1}\left[f_{d/2}^{-1}\left(-\frac{n\beta^{d/2}}{\mathcal{C}}\right)\right]. \quad (14.17)$$

Consequently, plotting $\kappa\beta^{d/2-1}$ versus $n\beta^{d/2}$ will yield the universal curve Ξ_f with

$$\Xi_f(x) = -\mathcal{C}f_{d/2-1}\left[f_{d/2}^{-1}\left(-\frac{x}{\mathcal{C}}\right)\right]. \quad (14.18)$$

This will collapse density profiles for different temperatures, for example. Moreover, phase transitions characterized with different values of \mathcal{C} (that is, mass) will also collapse if one accounts for this by either having auxiliary knowledge of \mathcal{C} (mass) or upon fitting this single parameter.

Fig. 14.2 shows a comparison of various exact and trapped density profiles for $N = 5$ particles for $d = 1$, suggesting that that even in this case of extremely few particles, the harmonic trap and finite particle number of cold atomic systems are not a severe obstacle to studying quantum criticality. results. We show the LDA results in 2D and 3D for comparison, as a guide to the significantly different shapes of the universal curves experiments would observe in higher dimension.

14.4 Dilute Bose gas vacuum to superfluid phase transition

Consider the weakly interacting dilute Bose gas, described by the Hamiltonian

$$\begin{aligned}
 H = & \int d\mathbf{k} \left(\frac{\hbar^2 k^2}{2m} - \mu \right) b_{\mathbf{k}}^\dagger b_{\mathbf{k}} \\
 & + \frac{2\pi\hbar^2 a}{m} \int d\mathbf{r} b_{\mathbf{r}}^\dagger b_{\mathbf{r}}^\dagger b_{\mathbf{r}} b_{\mathbf{r}}, \tag{14.19}
 \end{aligned}$$

with m the particle mass, $b_{\mathbf{k}}$ the bosonic annihilation operator for particles with momentum \mathbf{k} and $b_{\mathbf{r}}$ the bosonic annihilation operator for particles with position \mathbf{r} , and (in the 3D case) a the 3D s -wave scattering length. Besides the bosonic statistics, the presence of interactions is the only difference with the fermion case considered previously. Similar to the earlier case of the vacuum-to-Fermi gas transition, this system undergoes a vacuum-to-superfluid transition at $\mu = 0$. Again, as in the non-interacting fermion case, our motivations are twofold: (1) the model's simplicity allows us to explicitly explore the effects of the trap, finite particle number, and regime of universality, while providing a testbed for our analysis techniques. This model will further demonstrate the feasibility of observing quantum

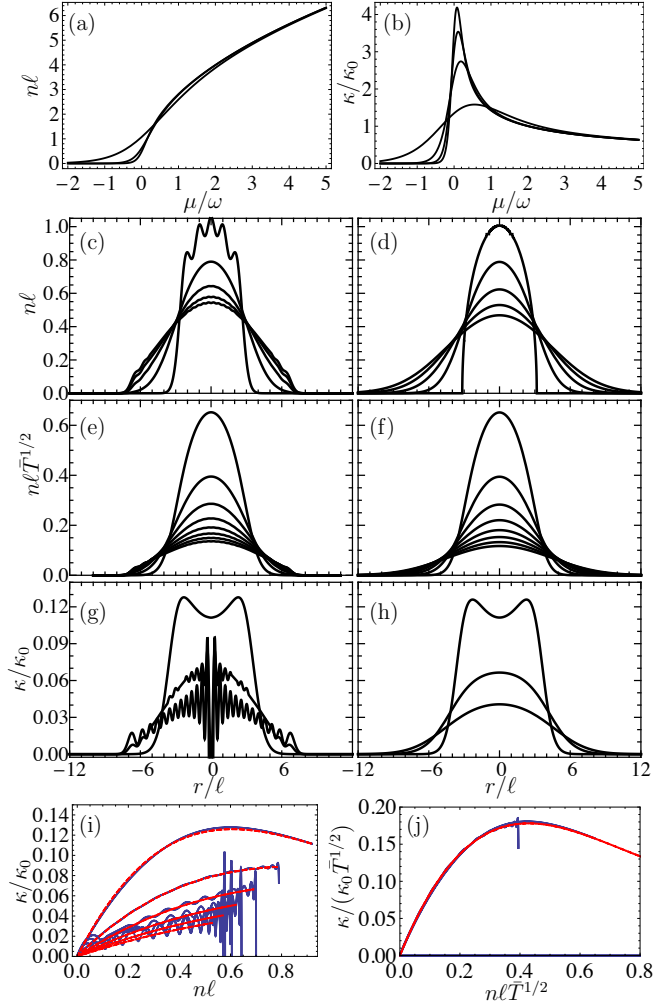


Figure 14.2: (a) Density, for temperatures $T = 2, 6, 10\omega$ and (b) compressibility for $d = 1$ non-interacting fermions as a function of μ , for temperatures $T = 2, 6, 10, 14\omega$. (c) Exact $N = 5$ particle density profile $n(r)$, in harmonic oscillator units $\ell \equiv \sqrt{1/(m\omega)}$ with m the fermion mass and ω the trap frequency (setting $k_B = \hbar = 1$ as usual), for temperatures $T = 0, 4, 8, 12, 16\omega$ compared with (d) LDA (Thomas-Fermi). (e,f) Same as (c,d) but with rescaled densities $\beta^{-1/2}n(r)$ replacing $n(r)$ to show universality near the $\mu = 0$ quantum critical point, for temperatures $T = 4, 8, 12, 16\omega$. (g) Exact $N = 5$ particle compressibility profile $\kappa(r)$ rescaled by $\kappa_0 \equiv 1/(\omega\ell)$ for temperatures $T = 2, 4, 6, \dots, 16\omega$ compared with (h) LDA. (i) Exact $N = 5$ particle κ vs n , demonstrating shape and temperature dependence of this curve for temperatures $T = 2, 4, \dots, 12\omega$, compared with LDA. (j) Exact $\kappa\beta^{1/2}$ for $N = 5$ particles, showing universal scaling collapse at every temperature (solid lines), compared with the thermodynamic limit (red dashed), for temperature $T = 2, 4, 6\omega$.

critical behavior in cold atomic systems. (2) The phase transition has a number of cold atoms experimental realizations, and has been realized in $d = 1, 2$, and 3. Moreover, despite its simplicity, unlike the non-interacting fermion case there already are some open questions in $d = 2$ regarding quantitative calculation of dynamic observables, which may be studied using cold atoms. We highlight these open questions below (see, for example, Sec. 15.0.4).

Here we will treat the cases of dimensions $d = 1$ and $d = 2$. Rather, than directly study this transition, it will be treated as a special case of the Bose-Hubbard phase transitions studied in the Sec 14.5: there, the vacuum-superfluid physics is identical to the dilute Bose gas as long as the average distance between particles is much greater than the lattice spacing. Moreover, the Mott-superfluid transitions will be in the same universality class as long as the system is sufficiently far away from the Mott lobe tip.

We will use an exact analytic solution for the $d = 1$ dilute Bose gas, a special case of the results of Section 14.5.2, and in $d = 2$ calculate the exact numerical solution via worm algorithm quantum Monte Carlo, a special case of the results of Section 14.5.3.

Even though by the standards of quantum critical phenomena, this is a textbook, fairly “trivial” quantum phase transition, open questions remain regarding its quantitative dynamics and regime of applicability. Unlike the static quantities computed above, no method — analytic or numerical — exists to quantitatively compute the dynamic properties of the system in $d = 2$ (despite the fact that this is the upper critical dimension!). Although since the system is at its upper critical dimension, the order parameter dynamics should be described using standard quantum critical analyses (perturbation theory to integrate out non-zero Matsubara frequencies to obtain an effective classical model, then approximating), this

has several shortcomings in practice. First, the full quantum critical scaling limit occurs for small $R/(k_B T)$ with R the characteristic energy of the excitations, but one finds 16% errors expected from finite $R/(k_B T)$ with R the characteristic energy of the excitations (this estimate uses static observables, where corrections to the theory can be computed) [196]. Even larger discrepancies exist between theory and experiments on dimerized quantum antiferromagnets: factors of $\approx 2-6$ in the excitations' energies and widths [196]. Secondly, since we are in the upper critical dimension, although the computed corrections due to non-zero $R/(k_B T)$ formally disappear as T/Λ becomes very small, with Λ the UV cutoff, $R/(k_B T)$ vanishes quite slowly (this is due to being in the upper critical dimension): even at energies 10^{-300} lower than experimentally relevant decreases only by a factor of $\approx 2!$

Some possible sources of the factor-of- $\approx 2-6$ discrepancy are (1) experimental error (considered unlikely, as these are well characterized), (2) non-universal behavior, (3) neglect of quantum-ness in QC eqs of motion (but this is estimated to be only 16%), or (4) interactions being insufficiently small.

These are all questions which could be investigated in cold atoms, even for this “trivial” transition. This gives us some hint that for less trivial phase transitions, the range of high-impact, near term open questions is exceedingly larger. Some are extensions of the questions here. For example: To what extent is the assumed quasiclassicality of the equations of motion for the effective classical model valid? (This is guaranteed only for small ϵ below the upper critical dimension, and at low temperature) Closely related, how valid are expansions (small- ϵ , large- N)? What is the range of universality? Other questions are even more fundamental, and some will be explicitly discussed for the finite-density $O(2)$ rotor model (“ $O(2) + \mu$ model”) and the Mott/metal transition later.

14.5 Bose-Hubbard model

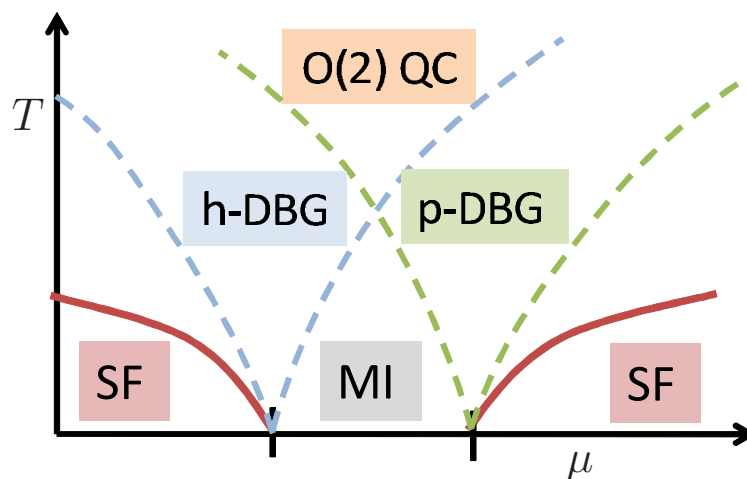


Figure 14.3: The intricate quantum critical crossovers near the Mott lobe tip, governed by the “ $O(2) + \mu$ ” model of Eq. (14.23) physics. Near the tip, the dilute gas of quasiparticles — on the larger μ side of the tip — and the dilute gas of quasiholes — on the lower μ side of the tip — can both be important. Very near each of the transitions, the system is described by the corresponding dilute Bose gas quantum phase transition of quasiparticles or quasiholes, in the universality class of Eq. (14.21). At intermediate temperatures, both excitations occur and are symmetric on the relevant energy scales, with quantum criticality there described by the $O(2)$ model of Eq. (14.22).

The Bose-Hubbard model, described by the Hamiltonian,

$$H_{\text{BH}} = -t \sum_{\langle i,j \rangle} b_i^\dagger b_j + \sum_i \left[\frac{U}{n_i} (n_i - 1) - \mu n_i \right] \quad (14.20)$$

with b_i bosonic annihilation operators for site i , t the nearest-neighbor tunneling rate, $\sum_{\langle i,j \rangle}$ indicating a sum over nearest neighbor pairs, U the on-site interaction energy (and we have Legendre transformed to include a chemical potential μ) is the one of simplest lattice models displaying a quantum phase transition [76], with both superfluid and Mott insulator states separated by a second order quantum phase transition, demonstrated at zero and finite temperature in Fig. 14.1. Ultracold bosonic atoms in optical lattices realize this model [77], and this is probably the most intensely studied strongly correlated system in cold atoms. Experiments

have explored the physics in dimension $d = 1, 2, 3$ with many observables including single-site resolved density profiles and density-density correlations (noise spectra), time of flight images, rf spectra, modulation spectra, Bragg spectra, and some basic transport probes.

The quantum critical physics of the system is quite rich. Depending on where in the phase diagram one is the way the phase transition is traversed, the transition can be in either of two universality classes [76, 121]: the dilute Bose gas universality class, with universal physics described by the dilute Bose gas (DBG) effective action

$$S_{\text{bg}}[\phi] = \int_0^\beta d\tau \int d\mathbf{r} \left[\phi^*(\mathbf{r}) \left(i\partial_\tau - \mu - \frac{\nabla^2}{2m} \right) \phi(\mathbf{r}) + \frac{u}{2} |\phi(\mathbf{r})|^4 \right], \quad (14.21)$$

with ϕ a bosonic field (periodic with period β in τ in the path integral language) — simply converting the Hamiltonian of Eq. (14.19) into the language of action, giving the parameters new names — or in the $O(2)$ rotor model universality class described by the effective action

$$S_{O(2)}[\phi] = \int_0^\beta d\tau \int d\mathbf{r} \left[\phi^*(\mathbf{r}) \left(-\partial_\tau^2 + r - c^2 \nabla^2 \right) \phi(\mathbf{r}) + \frac{u}{2} |\phi(\mathbf{r})|^4 \right]. \quad (14.22)$$

Note that the only distinction between these two universality classes is whether the time derivative comes in linearly or squared (although this has a significant impact on the physics). The former effective theory undergoes a phase transition at $\mu = 0$ while the latter undergoes a phase transition at a critical coupling $r = r_c$. We emphasize that the parameters appearing in the effective Hamiltonians need bear no simple relation to the microscopic Hamiltonian parameters: for example, the chemical potential in Eq. (14.21) has no simple relation (in fact, is undetermined by) the physical chemical potential of the Bose-Hubbard model.

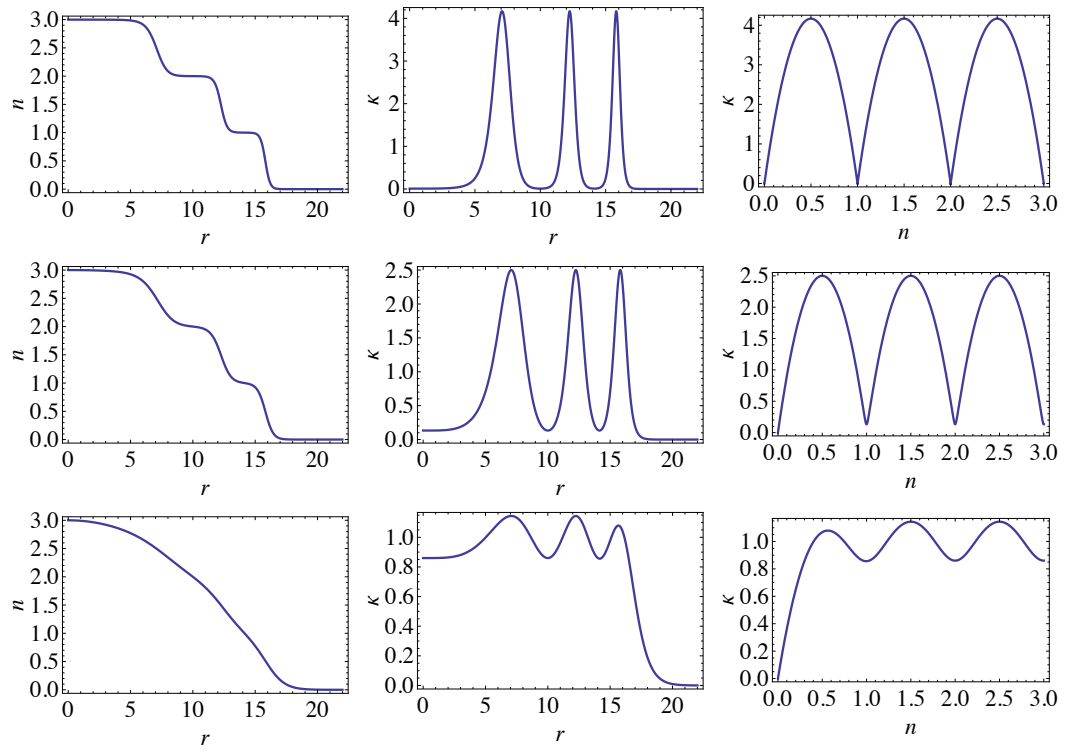


Figure 14.4: Left to right: n vs r , κ vs. r , and κ vs. n for $t = 0$ at various temperatures. From top to bottom, the plots are for $T/U = 0.06, 0.1$, and 0.25 . This represents the non-universal, non-critical contributions to the density that must be subtracted to give an appropriate quantum critical analysis.

The behavior of the density determines which theory describes observables as we cross the phase transition along some trajectory: if the phase transition is associated with a kink in the density at the phase transition, it is in the DBG universality class, while if the density is pinned, it is in the $O(2) + \mu$ universality class. Except at the Mott lobe “tips” (transition at the largest tunneling t/U for each lobe), the phase transition will be described by the DBG universality class, as there is always a density kink. At the Mott lobe tip, a single path in the t/U - μ/U plane satisfies the criteria to be described by the $O(2)$ rotor model. If the $O(2)$ point’s physics were restricted to this singular trajectory in the phase diagram, it would be essentially irrelevant, requiring infinite tuning to observe. In contrast to this, there is a sense in which this $O(2)$ theory controls the physics in a larger window around the lobe tip. Fig. 14.3 gives a cartoon of the physics underlying this. Mathematically, one finds that the theory with action

$$S_{O(2)+\mu}[\phi] = \int_0^\beta d\tau \int d\mathbf{r} \left[-\phi^*(\mathbf{r}) \left(\partial_\tau - \frac{\mu}{2} \right)^2 \phi(\mathbf{r}) - c^2 \phi^*(\mathbf{r}) \nabla^2 \phi(\mathbf{r}) + \frac{u}{2} |\phi(\mathbf{r})|^4 \right]. \quad (14.23)$$

describes the physics for a window of the t/U - μ/U plane near the Mott lobe tip. Note that for non-zero values of μ in this “ $O(2) + \mu$ ” theory, the model displays a μ -tuned transition in the DBG universality class, while for $\mu = 0$ the system undergoes a u -tuned phase transition in the $O(2)$ universality class. Physically, this model is the $O(2)$ model in the presence of a finite density, or equivalently breaking of the $O(2)$ symmetry. There are two basic consequences of this physics: (1) the dilute Bose gas transitions near the tip have their location universally determined by the $O(2)$ theory, as well as the DBG’s coupling constants, and (2) although these DBG transitions near the tip work up to some temperature T_1^* , they break down above this temperature. Above this temperature (but still well below the ultimate UV cutoff) the physics is that of the $O(2)$ model with $\mu = 0$.

This is illustrated in Fig. 14.3.

The physics of this latter model, especially the low-frequency transport, has open qualitative questions, despite the fact that this is a quite conventional, textbook quantum phase transition, described by a local symmetry breaking order parameter [121, 199]. Cold atoms offers an opportunity to greatly improve our understanding of these problems. We shall demonstrate the feasibility and construct the basic analysis techniques for static observables in this section.

14.5.1 Bose-Hubbard model in general quantum critical context and relating quantum critical fields to microscopic variables

To properly analyze density profiles of the Bose-Hubbard model, we must relate this observable to the variables occurring in the effective quantum field theory of the problem. This is a generic task in analyzing quantum phase transitions, and for the Bose-Hubbard model may be done straightforwardly, explicitly, and exactly. Specifically, the average density is

$$\langle n \rangle = \langle n \rangle_{\text{OS}} - \frac{\partial \mathcal{F}_{\text{QC}}}{\partial \mu} \quad (14.24)$$

where \mathcal{F}_{QC} is the free energy associated with the order parameter field fluctuations described by the effective low energy quantum critical theory (dilute Bose gas or O(2) rotor), obtained by a Hubbard-Stratonovitch transformation to decouple sites[121], and $\langle n \rangle_{\text{OS}}$ is the $t = 0$, on-site value for the density

$$\langle n \rangle_{\text{OS}} = \frac{\sum_n n e^{-\beta \epsilon_n}}{\sum_n e^{-\beta \epsilon_n}} \quad (14.25)$$

with

$$\epsilon_n \equiv \frac{U}{2} n(n-1) - \mu n. \quad (14.26)$$

The sums of Eq. (14.25) converge rapidly, so that a few terms generally suffice.

The scaling arguments we have previously utilized apply to the quantum critical theory, but not to the $t = 0$ terms. The $t = 0$ terms must be subtracted from experimental observables in order for the arguments of preceding sections to apply. Fig. 14.4 shows plots of the density profiles, compressibility profiles, and compressibility versus κ for $t = 0$.

14.5.2 $d = 1$

Here we discuss the quantum criticality of the $d = 1$ Bose-Hubbard model and the analysis of its universal properties relevant to cold atoms. In particular, we consider $\kappa T^{1/2}$ vs $nT^{-1/2}$ universal scaling curves. We content ourselves with the hardcore limit $U \gg \{t, \mu, T\}$ where simple analytic expressions exist.

In the hardcore limit, the only possible site fillings are $n = 0, 1$. The Hilbert space thus naturally maps one-to-one to spinless lattice fermions (where higher occupations are suppressed by the Pauli exclusions principle). The Bose-Hubbard Hamiltonian maps to a fermion Hamiltonian via the Jordan-Wigner transformation to a new set of Fermi operators:

$$f_i = \left[\prod_{j < i} (1 - 2b_j^\dagger b_j) \right] b_j \quad (14.27)$$

One may, using the boson commutation relations of the b 's and b^\dagger 's, straightforwardly verify the fermion anticommutation relations for the f_j 's. In terms of these fermionic operators, the Bose-Hubbard model Hamiltonian is

$$H = -t \sum_i \left[c_{i+1}^\dagger + \text{H.c.} - \mu c_i^\dagger c_i \right], \quad (14.28)$$

a *non-interacting* fermion problem. From this, observables that are local in real space, such as density may be straightforwardly evaluated. Our interest here is

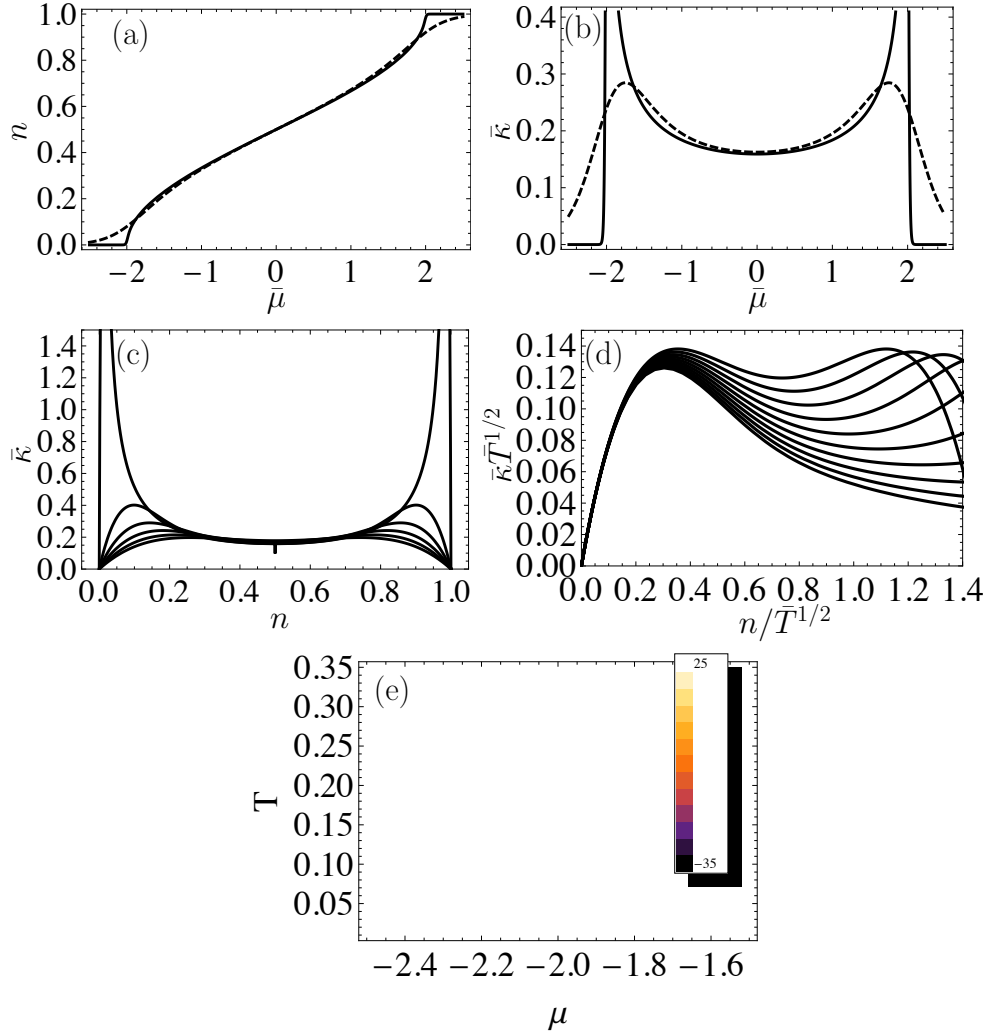


Figure 14.5: Thermodynamics and universal scaling analysis of quantum criticality, applicable to density profiles, of the 1D Bose-Hubbard model. Figs. (a) and (b) show density and compressibility versus the chemical potential for temperatures $\bar{T} \equiv T/t = 0.01, 0.06, 0.11, \dots, 0.46$, which is clearly non-universal. Figs. (c) and (d) show $\bar{\kappa}\bar{T}^{1/2}$ versus $n/\bar{T}^{1/2}$. A universal window at low densities and low temperatures is made apparent by this analysis. The shape of this curve is controlled by the universal quantum critical theory. The exponents necessary to collapse also reveal the dynamic critical exponent. There is an additional universal region near $n = 1$, and the universal scaling analysis can be applied there as well by plotting $\kappa T^{1/2}$ vs $(1 - n)T^{-1/2}$. We omit this analysis because this problem possesses a symmetry so that it is exactly equivalent to the analysis near $n = 0$ shown here. Here, \bar{x} is the variable x rescaled by the appropriate power of t to make it dimensionless. (e) Logarithmic derivative $\frac{1}{n} \frac{dn}{dT}$ — roughly the “power” characterizing the temperature dependence — in the μ - T plane, showing a quantum critical fan of constant power corresponding to power law dependence of the density in the quantum critical fan. This is a standard type of plot when examining quantum critical materials.

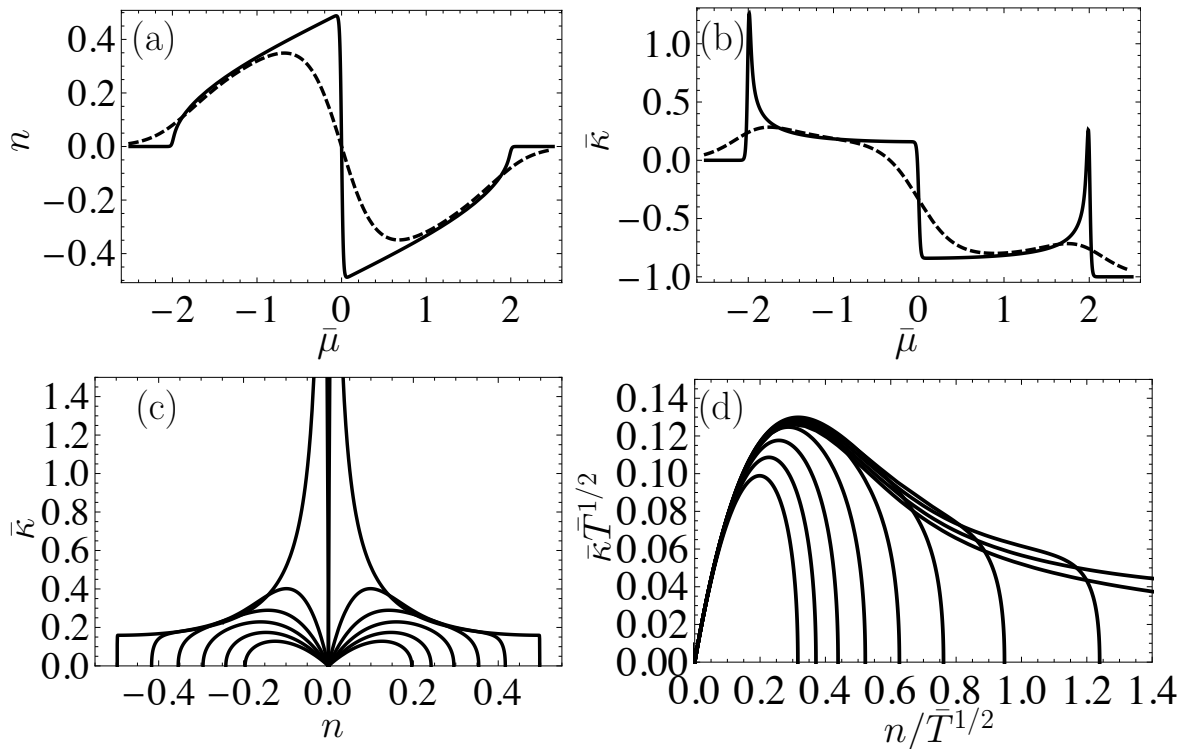


Figure 14.6: Same as Fig. 14.6, but with $t = 0$ densities subtracted off prior to analysis to reveal only universal contributions (here only, we use the same symbols — e.g., n and κ — to denote the quantities with the $t = 0$ parts subtracted off). Thermodynamics and universal scaling analysis of quantum criticality, applicable to density profiles, of the 1D Bose-Hubbard model. Figs. (a) and (b) show density and compressibility versus the chemical potential for temperatures $\bar{T} \equiv T/t = 0.01, 0.06, 0.11, \dots, 0.46$, which is clearly non-universal. Figs. (c) and (d) show $\bar{\kappa} \bar{T}^{1/2}$ versus $n/\bar{T}^{1/2}$. A universal window at low densities and low temperatures is made apparent by this analysis. The shape of this curve is controlled by the universal quantum critical theory. The exponents necessary to collapse also reveal the dynamic critical exponent. We omit the analysis near $n = 1$ because this problem possesses a symmetry so that it is exactly equivalent to the analysis near $n = 0$ shown here. Here, \bar{x} is the variable x rescaled by the appropriate power of t to make it dimensionless.

in the density n and compressibility κ . From Eq. (14.27), the bosonic density operator in the fermionic representation is simply the fermionic density:

$$n_i = f_i^\dagger f_i. \quad (14.29)$$

To calculate thermal expectation values of n , we want to sum over the Boltzmann weighted energy eigenstates of Eq. 14.28. The eigenstates are simply seen by Fourier transforming the non-interacting fermion Hamiltonian, which then has dispersion

$$\epsilon_k = -2t \cos(ka) - \mu \quad (14.30)$$

for momentum k and lattice constant a . The finite temperature expectation value of the density is thus

$$\langle n \rangle = \frac{1}{2\pi} \int_{-\pi}^{\pi} dp \frac{1}{\exp[-\beta(2t \cos p + \mu)] + 1}, \quad (14.31)$$

which is numerically straightforward to integrate. The compressibility κ is simply a derivative of this. The results for the density and compressibility as a function of μ are shown in Fig. 14.5. In this visualization (and in the closely related density profiles within the LDA $n_{\text{trap}}(r) = n [\mu_0 - (m\omega^2/2)r^2]$, the universality of the quantum criticality is hidden. Fig. 14.5 also demonstrates our analysis — plotting $\bar{\kappa}\bar{T}^{1/2}$ vs $n\bar{T}^{-1/2}$, which is extractable from experimentally measured density profiles. These curves show a window of universality at low excitation densities (that is, near physical densities $n = 0$ and $n = 1$) around the quantum phase transition, explicitly demonstrating that universal curves may be constructed from density profiles.

The regime of collapse in Fig. 14.5 also provides a nice demonstration of the range of the phase diagram over which the physics is universal and controlled by the quantum critical theory. Fig. 14.6 shows the same analysis, subtracting off the

$t = 0$ densities. A naive estimate, similar to that performed in Sec. 14.1, would take the universal window to extend to $(\mu - \mu_c) \sim t$ (at low temperatures), or equivalently to densities $(n - n_c) \sim 0.3$. This is basically confirmed by Fig. 14.5; indeed, exploring lower temperatures (not shown) reveals that at sufficiently low temperatures, deviations in this regime are at most a few percent.

Including the bosons' trapping potential in this mapping to non-interacting fermions gives the same trapping potential for fermions, and allows us to apply earlier results to show few particles, harmonic trap presented no fundamental obstacles to observing quantum criticality. The only difference is now that there is a UV cutoff from the lattice, but (we find) that this creates no problems, and in fact was mimicked by the hard energy cutoff applied in our results for non-interacting fermions.

As a final aside, note that it is simple to extend this discussion to models with longer range tunnelings or, equivalently, arbitrary band structures.

14.5.3 $d \geq 2$

Method and accuracy analysis.—To calculate the properties of 2D lattice bosons we have employed worm algorithm quantum Monte Carlo, as implemented in ALPS. This algorithm samples observables by sampling paths in configuration space and imaginary time, as with path integral Monte Carlo. However, it works in the grand canonical ensemble, allowing for efficient calculation of superfluid properties (and imaginary time dynamics). The method converges to exact solutions. The main error sources (which may be reduced at the expense of computational time) are: (1) finite size errors, (2) statistical sampling errors, and (3) systematic equilibration errors. We have checked each of these error sources, finding that finite size effects dominate, but are quite small. We address each in turn.

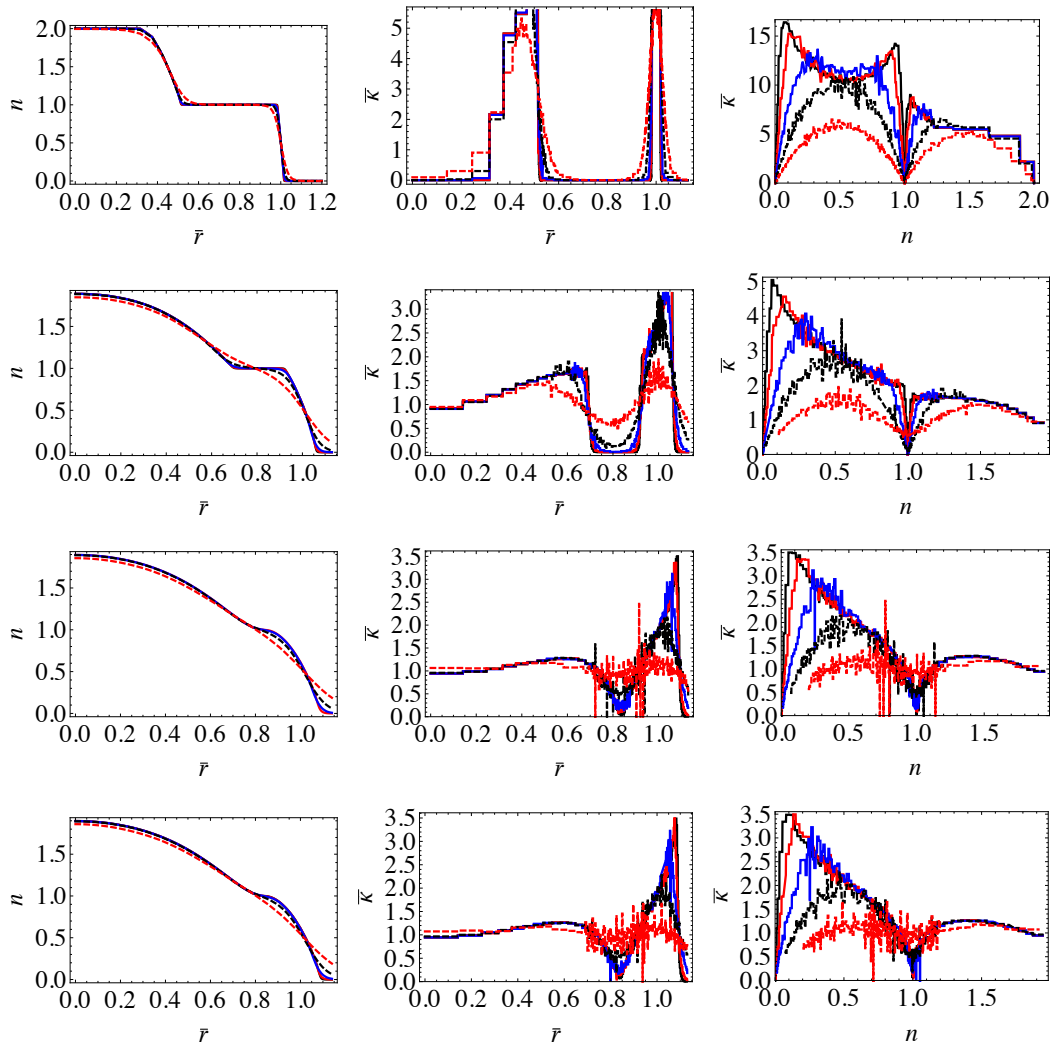


Figure 14.7: Density profiles, compressibility profiles, and compressibility versus density, conventional experimental visualizations extracted from density profiles. Top to bottom: $t/U = 0.01, 0.014, 0.0585, 0.0593$. Each graph shows temperature $T = t/4, t/2, t, 2t$, and $4t$ in black (solid), red (solid), blue (solid), black (dashed), and red (dashed), respectively. See Fig. 14.8 for an analysis bringing out and comparing the universal behavior.

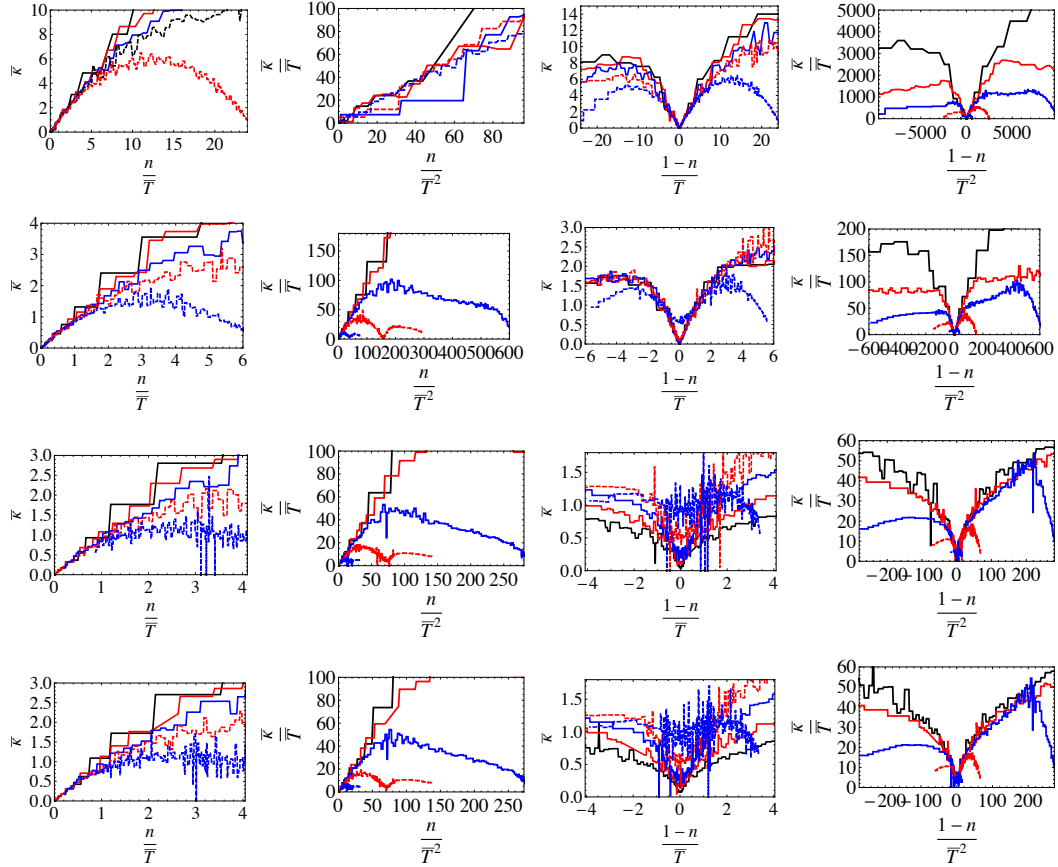


Figure 14.8: Rescaled compressibility versus density scaling curves. Top to bottom: $t/U = 0.01, 0.04, 0.0585, 0.0593$. The tip of the Mott lobe is $(t/U)_c = 0.0593$ in the thermodynamic limit [1]. Left to right: (i) rescaling appropriate to DBG transition near $n = 0$, (ii) rescaling appropriate to $O(2)$ transition near $n = 0$, (iii) rescaling appropriately to DBG near $n = 1$, and (iv) rescaling appropriate to $O(2)$ near $n = 1$. Universality persists to temperatures $T \sim t \sim 2t$, and over a more limited regime of the scaling curve at higher temperatures, as is expected. Each graph shows temperature $T = t/4, t/2, t, 2t$, and $4t$ in black (solid), red (solid), blue (solid), black (dashed), and red (dashed), respectively. The universal collapse or lack thereof is able to distinguish between the $O(2)$ and DBG universality classes, and the $O(2)$ emerges near the tip of the Mott lobe.

(1) Specifically, throughout our analysis we use a $L \times L$ square lattice with $L = 10$, and have spot checked these with $L = 25$ and $L = 50$ calculations, finding only few percent deviations between the $L = 10$ and $L = 25$ calculations for even the most challenging points of our simulation. Refs. [1, 206] have found similar conclusions through a more sophisticated analysis.

(2) We achieve a negligible statistical error, typically a tenth of a percent (less than the point size/line thickness even in critical region).

(3) Before the measurement phase of the Monte Carlo sampling there is an initial equilibration phase. We use a binning analysis to analyze the extent to which the system has equilibrated and to find the autocorrelation time, and thus the extent to which the statistical error bars are valid. We find throughout that these errors are comparable to the statistical errors, perhaps somewhat larger near the critical points.

Finally, we checked the effect of the harmonic trap by direct simulation. Similar to the non-interacting fermion and $d = 1$ Bose-Hubbard results, we find that for more than a few particles, the LDA approximation to the density profiles is adequate for the physics we desire.

Discussion of results.—Figs. 14.7 and 14.8 show extensive examples of the behavior of density profiles — and quantities extracted from them — across the quantum phase transition. Figs. 14.9 and 14.10 show the same analysis with the $t = 0$ part subtracted off. We use various tunnelings $t/U = 0.01, 0.04, 0.0585, 0.0593$ to illustrate the crossover between the DBG and $O(2)$ universality classes — the former is expected to apply for the first two tunnelings and the latter for the second two [1, 206]. The rescaled curves are rescaled so that at the lowest temperature shown — $T = t/4$ in each case — the range of physical densities is the same: to $n - n_c = 0.06$. This means that the density range on the horizontal axes at the

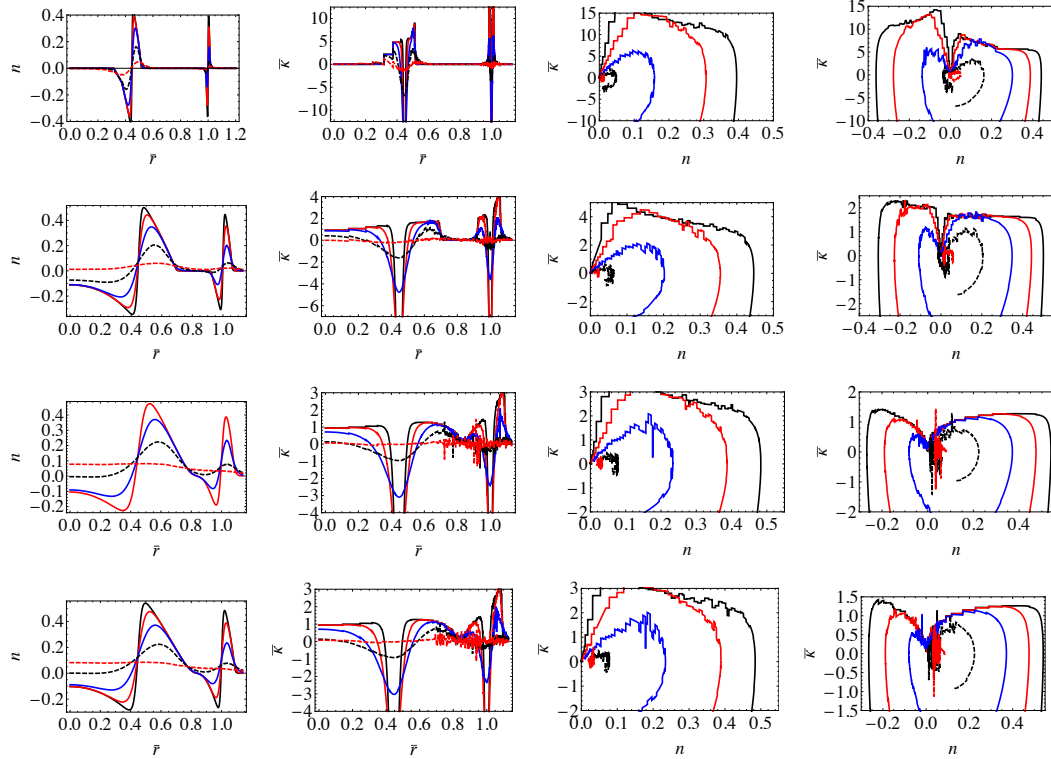


Figure 14.9: Density profiles, compressibility profiles, and compressibility versus density, conventional experimental visualizations extracted from density profiles, with contributions from $t = 0$ subtracted off to yield only the density contribution from low energy, universal fluctuations. Beware: we use identical symbols here (and only here and in Fig. 14.10 to indicate the quantities after subtraction. Top to bottom: $t/U = 0.01, 0.014, 0.0585, 0.0593$. Each graph shows temperature $T = t/4, t/2, t, 2t$, and $4t$ in black (solid), red (solid), blue (solid), black (dashed), and red (dashed), respectively. See Fig. 14.8 for an analysis bringing out and comparing the universal behavior. Note that except for the subtraction, this figure is identical to Fig. 14.7, except the last column has been split into two columns, for the transitions near $n = 0$ ($\mu \in (-0.35, 0.0)$, left) and $n = 1$ ($\mu \in (0.0, 1.0)$, right), to avoid clutter.

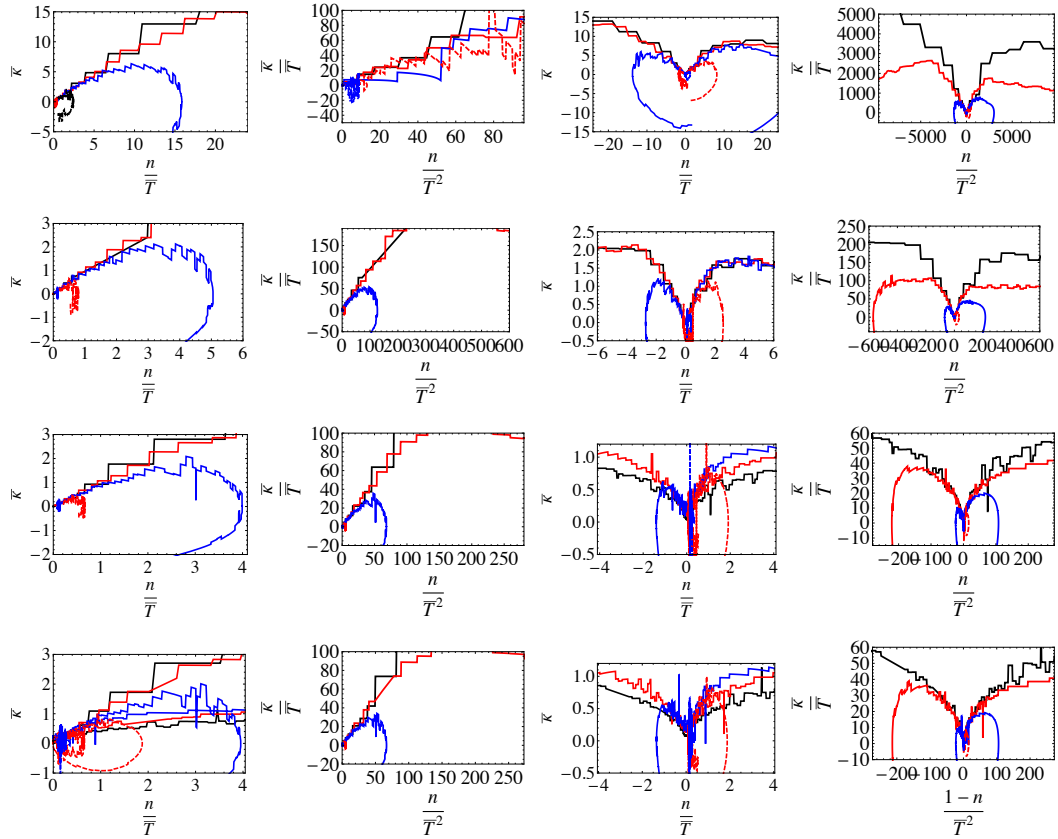


Figure 14.10: Rescaled compressibility versus density scaling curves. Top to bottom: $t/U = 0.01, 0.04, 0.0585, 0.0593$. The tip of the Mott lobe is $(t/U)_c = 0.0593$ in the thermodynamic limit. Left to right: (i) rescaling appropriate to DBG transition near $n = 0$, (ii) rescaling appropriate to $O(2)$ transition near $n = 0$, (iii) rescaling appropriately to DBG near $n = 1$ ($\mu \in (-0.35, 0.0)$), and (iv) rescaling appropriate to $O(2)$ near $n = 1$ ($\mu \in (0.0, 1.0)$). Universality persists to temperatures $T \sim t \sim 2t$, and over a more limited regime of the scaling curve at higher temperatures, as is expected. Each graph shows temperature $T = t/4, t/2, t, 2t$, and $4t$ in black (solid), red (solid), blue (solid), black (dashed), and red (dashed), respectively. The universal collapse or lack thereof is able to distinguish between the $O(2)$ and DBG universality classes, and the $O(2)$ emerges near the tip of the Mott lobe. Note that except for the subtraction, this figure is identical to Fig. 14.8.

highest shown temperature ($T = 4t$) is 0.96 in the plots rescaled according to DBG universality and is 15 in the plots rescaled according to the $O(2)$ universality.

The conclusion of this analysis is consistent with our earlier examinations of non-interacting fermions and the $d = 1$ Bose-Hubbard model: by themselves, n and κ non-universal, but nevertheless QC manifests itself in density profiles for realistic system parameters and temperatures, and our analysis enables exploration of this behavior. In the DBG universality class — $t/U = 0.01, 0.04$ — universal collapse occurs with rescalings appropriate to this class, and *not* the $O(2)$ class. Similarly, in the $O(2)$ universality class — $t/U = 0.0585, 0.0593$ — the opposite is true: universal collapse occurs with rescalings appropriate to this class, and *not* the DBG class. Thus, density profiles are sufficiently powerful to distinguish between these universality classes, the key difference here being the dynamic exponents of $z = 1$ and $z = 2$, respectively. Such an analysis should directly be able to resolve a controversy regarding the Mott-metal crossover for lattice fermions, discussed in Sec. 15.0.5.

Another observation is quite important and promising for the study of quantum critical behavior in cold atoms, regarding the observability of classical criticality near the quantum phase transition. The actual finite temperature phase transition — e.g., between the NF and SF in Fig. 14.1 — manifests a singularity in the scaling function that is governed by *classical* critical theory (that is a subcase of, and universally controlled by, the quantum phase transition in proximity of the QCP). Others have argued that this singularity is observable [207] and observed it in other systems, such as the dilute Bose gas [208]. Since this is a small portion of the universal quantum critical scaling functions, this implies that the overall scaling structure of quantum criticality is observable if the classical criticality is. Indeed, in our simulations, the classical singularity is unresolved due to insufficient

resolution of μ 's, noise, and finite size effects, yet the quantum critical collapse is readily apparent.

As an aside, note that in addition to evaluating compressibility by derivatives, one may also evaluate it by density fluctuations from the numerics.

Chapter 15

The next steps in exploring quantum criticality in cold atoms

Here we have focused on the observable properties of fairly simple, and certainly conventional, quantum phase transitions since: (1) they allowed us to treat the effects of finite particle number and harmonic trap, and (2) cold atoms experiments are most advanced in realizing these transitions. In the cases discussed, the experimental data necessary to extract information about the quantum critical properties — high resolution density profiles in the appropriate parameter regime — largely already exists and needs only to be properly analyzed. However, even in simple cases, there remain open quantitative questions, as well as general questions, such as the breakdown of the universality, which cold atoms may explore these questions.

Beyond this, there is a much richer set of properties — especially dynamic observables — and less understood quantum phase transitions of great importance in condensed matter, such as those lacking a description in terms of a local order parameter. These are also ripe for exploration in ongoing and future cold atom experiments. Indeed, cold atoms systems offer opportunities to settle long-standing questions about these systems. We briefly mention a sampling of such properties and phase transitions that will be important in the immediate future.

15.0.4 Other observables: spectroscopy

Dynamics offer particularly dramatic manifestations of quantum criticality. The theory for these, especially the low frequency ($\omega/T \ll 1$) dynamics in the quantum critical regime is fundamentally much more difficult less developed than the static

properties treated so far. Even expansions from unphysical parameter values (ϵ expansions, large- N expansions), strictly valid only for values much less than those physically occurring (e.g, $\epsilon = 2$ or $N = 2$), require substantial numerical work (classical Monte Carlo integration of solutions to the equations of motion) coupled with sophisticated analytic arguments developed only a decade ago in order to obtain just the leading order results for dynamics. Thus, dynamic cold atoms probes will be particularly fruitful to explore.

A final general point regarding the utility of cold atoms in probing quantum critical dynamics is worth noting. In the quantum critical region, the characteristic time scale is set by the temperature. However, in condensed matter experiments, this corresponds to terahertz frequencies even at cryogenic temperatures, and consequently the dynamical properties are difficult to probe over the relevant energy range, requiring for example neutron scattering. In contrast, typical thermal frequencies in cold atoms are below kilohertz and are easily accessible using a variety of RF, microwave, and optical probes.

In cold atoms, the single particle spectral function is not generally accessible. Indeed, locally resolved spectroscopies are somewhat more difficult than density profiles. However, rf spectroscopy is relatively easier, and the requisite technology already is in place in the majority of cold atoms experiments. It has also been shown to experimentally provide much information about BEC (especially in hydrogen, e.g. Ref. [83]), bosonic optical lattice systems [85], and strongly interacting fermions. An extension of our independent theoretical investigations in the Bose-Hubbard model [107, 119], together with earlier work on finite temperature superfluids [104, 110], suggest that it can usefully be applied to investigating systems across quantum phase transitions.

Here we qualitatively sketch our expectations for the finite temperature prop-

erties of spectra quite generally. The key point is that delta functions (quasiparticle peaks) characterizing response at a single momentum in the low temperature phases are broadened to non-quasiparticle peaks in the quantum critical regime. From a single spectrum, it is difficult to say whether broadening is due to this or various technical artifacts such as finite bandwidth of a pulse, however. The key observation is that there is a universal scaling collapse analogous to that of the density profiles:

$$I(\omega, \mathbf{k}, T, g) = f\left(\frac{\omega}{T}, \frac{\mathbf{k}}{T^{1/z}}, \frac{g^\nu}{T}\right) \quad (15.1)$$

for a general spectra $I(\omega, \mathbf{k})$ and universal scaling function f at frequency ω and momentum \mathbf{k} , with the coupling constant g crossing the phase transition. Thus, by varying a single parameter, especially the temperature, one should be able to check for the universal scaling collapse signifying quantum criticality (and ruling out other physical effects or technical artifacts).

15.0.5 Other phase transitions

First, we will give a laundry list of completed or ongoing experiments in cold atoms that display quantum criticality, often much less understood than the examples above, in some cases offering no description in terms of a local order parameter. Secondly, we will identify two directions in which immediate progress is possible on fundamentally important puzzles.

Transitions observed or being presently focused on in the community (that were not discussed above) are (1) transitions between various magnetic states spinor gases, including a possible “supersolid” state with coexisting spin density wave order and superfluidity, (2) the polarized Fermi gas FFLO to normal fluid transition in 1D and higher dimensional systems, (3) transitions between fractional quantum Hall states, (4) various Fermi-Hubbard model transitions including

antiferromagnetic-normal, nematic-normal, and possible superconducting-normal phase transitions among others. It is worth pointing out that, as with the phases themselves, the characteristic temperatures to achieve universal physics are lower for these last phase transitions; for example, for the antiferromagnet, the exchange energy $J = t^2/U$ sets the dispersion bandwidth of the characteristic excitations, and thus the scale for universality, analogous to t for the boson superfluid-Mott insulator or Mott-metal transitions. Other interesting transitions are (5) the “Stoner instability” from a Fermi liquid to a ferromagnet (here in a highly non-equilibrium context) [209] and (6) the many experiments involving disorder. These are just some exciting examples, and many more are accessible in cold atoms experiments.

An interesting point observation has been Bill Phillips’s group’s observation in a dilute Bose gas of behavior intermediate to the normal fluid and vacuum, superficially consistent with the appearance of quantum criticality. Further analysis and exploration would be interesting [210].

Some current experiments on lattice bosons have near single site resolution or nearly so [70, 73], and reach the lowest temperatures of lattice experiments, making them one place to look for immediate progress. Indeed, the published density profiles of Cheng Chin’s group should suffice to see for deep lattices the universal quantum critical collapse developed in this paper, and unpublished data should allow exploration of the crossover from the dilute Bose gas to $O(2)$ rotor module universality class. Seeing this would provide an experimental proof of principle of observation of non-trivial quantum criticality in cold atoms. RF or other spectra may then be used in this system to probe the spectra, whose structure in the 2D $O(2) + \mu$ class — despite its conventionality and simplicity — is a fundamental, unsolved problem in quantum critical dynamics.

A second avenue of pursuit concerns a much less simple quantum phase tran-

sition occurring in lattice fermion experiments. In the longer term, there are a plethora of possible low temperature phases and crossovers. However, already in the regime already explored by the Bloch [205] and Esslinger groups [204] it may be possible to impact a controversy. Specifically, at higher temperatures than t^2/U , any spin physics is washed out, including all the low temperature phases. However, up to temperature scales $T \sim t$, the system will ostensibly undergo a universal *crossover* between a spin-disordered Mott state to a metal as a function of doping or lattice depth. Naively, one expects that in analogy with the Bose-Hubbard model, the quantum criticality is that associated with the vacuum-to-Fermi liquid transition (the weakly repulsively interacting analog of the non-interacting fermion problem we solved): in the Mott state there are thermally excited, gapped quasiparticles on an insulating Mott background and in the Fermi liquid, there is the usual gapless quasiparticle dispersion. This model has a dynamical critical exponent $z = 2$. However, sophisticated numerical investigations at half filling in the insulator suggest that $z = 4$, as would occur if, say, the quasiparticle mass diverged at the transition.

Using analysis techniques similar to those developed here for the Bose-Hubbard model, one can examine the value of the dynamic exponent, distinguishing between $z = 2$ and $z = 4$, and looking for any crossover between universality classes in the phase diagram. By checking for universal scaling collapse, one can also evaluate whether the traditional concept of quantum criticality even applies in this region. One caveat is that due to the candidate values of the dynamical exponent, the transition is inevitably in or above the upper critical dimension, and this will require slight extension of our methods, using standard perturbative results [121].

Chapter 16

Part 5: Systems other than cold atoms

Although the bulk of this thesis concentrates on cold atomic gases, I have also worked in other areas of condensed matter physics. In graduate school, this has largely been in low temperature fluids and solids. The following chapters discuss some results I've obtained on these systems: (1) collisional properties of degenerate spin-polarized hydrogen adsorbed on helium films (**Chapter 17**), (2) anomalous behavior of atomic hydrogen defects in molecular hydrogen quantum solids (**Chapter 18**), and (3) possible scenario for supersolidity, inspired by experiments on solid hydrogen and helium (**Chapter 19**).

The systems studied here, especially the quantum solids, are in many ways the antithesis of cold atoms. In contrast to the simple, known, model Hamiltonians realized in cold atoms, in low temperature solids even the composition is frequently inhomogeneous, complicated, and unknown. This complexity opens up a richness of physics but at the cost of being unsure if the basic models of the situation are correct. A theme in my work has been to try to give general constraints on possible theories to explain the phenomena, to give scenarios to explain behavior, and to make falsifiable predictions to test these theories.

Chapter 17

Film mediated interactions alter correlations and spectral shifts of hydrogen adsorbed on helium films

*This chapter was adapted from “Influence of Film-Mediated Interactions on the Microwave and Radio Frequency Spectrum of Spin-Polarized Hydrogen on Helium Films” by Kaden R. A. Hazzard and Erich J. Mueller, published in Physical Review Letters **101**, 165301 (2008).*

The work presented in this Chapter gives a mechanism which is expected to reduce, potentially dramatically, the collision probability of two spin-polarized hydrogen atoms adsorbed on a helium film. This was motivated by experiments by Ahokas *et al.* which observed anomalously small collisional shifts. Refs. [211, 212] revealed that a symmetry missed in the original work is likely responsible for the reduction, however our mechanism is still relevant affects other observable properties: atomic recombination rates, other spectral lines, and suggests that the cloud will collapse at sufficiently low temperatures.

17.1 Abstract

We argue that helium film-mediated hydrogen-hydrogen interactions dramatically reduce the magnitude of cold collision shifts in spin-polarized hydrogen adsorbed on a helium film. The magnitude of the reduction varies considerably across the possible range of experimental parameters, but this effect can consistently explain a two orders of magnitude discrepancy between previous theory and recent experiments. It can also qualitatively explain the anomalous dependence of the cold collision frequency shifts on the ^3He covering of the film. The mediated interac-

tion is attractive, suggesting that the gas will become mechanically unstable before reaching the Kosterlitz-Thouless transition unless the experiment is performed in a drastically different regime, for example with a much thicker helium film.

17.2 Results

Two-dimensional (2D) dilute, spin polarized hydrogen is a quantum fluid that is actively studied by both the cold atom and low temperature communities. One driver of this interest is belief that 2D hydrogen can support a superfluid-normal Kosterlitz-Thouless transition, which crosses over to Bose-Einstein condensation (BEC) as the confinement length in the third-dimension is increased. The relatively large particle density and light mass give a high BEC temperature. Since the hydrogen-hydrogen interaction potential is accurately known, it is widely believed that one will be able to quantitatively compare theory and experiment.

Despite this quantitative understanding of dilute hydrogen, experiments on spin-polarized hydrogen adsorbed on a helium film display a cold collision frequency shift that is two orders of magnitude smaller than theory predicts [213]. This suggests that the helium, though traditionally considered inert, significantly affects the hydrogen. Here we show that a helium mediated interaction alters the hydrogen collision properties and resultantly reduces the cold collision shift. The exact magnitude of this shift depends on experimental parameters such as the helium film thickness. For some reasonable estimates of these parameters, we find that the magnitude of this reduction is sufficient to eliminate the discrepancy. Using these same estimates, we find a counterintuitive dependence of the shift on the ^3He concentration, just as seen in the experiments. We do not, however, find quantitative agreement with the shift's magnitude.

As elaborated below, Ahokas *et al.* [213] measure a two-photon radio frequency

(rf)-microwave absorption spectrum. These experiments are in the “cold collision” regime [48], where the thermal de Broglie wavelength is longer than the interaction’s effective range, resulting in extremely sharp spectral lines, which are shifted by interactions. These shifts are important: they limit the performance of technologies (hydrogen masers [214, 215] and atomic clocks [87]) and are versatile probes. For example, related spectral shifts were used to diagnose BEC in 3D spin polarized hydrogen [83], identify Mott insulating shells in optical lattices [85], and reveal pair structure in Fermi gases [216, 217]. Future experiments will rely on these techniques to explore ever more exotic phenomena.

Experimental details.—Ahokas *et al.* [213] study a 2D hydrogen gas bound by van der Waals forces at a distance $\zeta \sim 5\text{\AA}$ above a helium film, working in a uniform magnetic field $B = 4.6T$. They produce a cloud with more than 99% of the atoms initially in the lowest hyperfine state $|1\rangle$. Letting $|s_e s_n\rangle$ be the state with electron spin s_e and nuclear spin s_n , one finds $|1\rangle = \cos\theta |\downarrow\uparrow\rangle - \sin\theta |\uparrow\downarrow\rangle$, with $\theta = 5.5 \times 10^{-3}$. Driving a transition to state $|2\rangle = \cos\theta |\uparrow\downarrow\rangle + \sin\theta |\downarrow\uparrow\rangle$, the experimentalists measure spectra by counting the number of transferred atoms for a given probe detuning. They vary temperature, 2D hydrogen density, and the He film’s ^3He concentration from negligible to 10^{14} cm^{-2} .

Calculating spectra.—Neglecting, for now, the helium film’s degrees of freedom, the hydrogen’s Hamiltonian is

$$H = \sum_{j,\mathbf{k}} \epsilon_{j,\mathbf{k}} \psi_{j,\mathbf{k}}^\dagger \psi_{j,\mathbf{k}} + \sum_{\substack{i,j \\ \mathbf{k},\mathbf{p},\mathbf{q}}} \frac{V_{ij,\mathbf{q}}}{2} \psi_{j,\mathbf{p}}^\dagger \psi_{i,\mathbf{k}}^\dagger \psi_{i,\mathbf{k}+\mathbf{q}} \psi_{j,\mathbf{p}-\mathbf{q}} \quad (17.1)$$

where $\psi_{j,\mathbf{k}}^\dagger$ are bosonic creation operators for momentum $\hbar\mathbf{k}$ and internal state j ; $\epsilon_{j,\mathbf{k}} = \hbar^2 k^2 / 2m + \delta_j - \mu_j$ is the free dispersion relation of the effectively 2D, mass m hydrogen, including the internal energy δ_j and chemical potential μ_j ; $V_{ij,\mathbf{k}}$ is the Fourier space interaction potential between atoms in states i and j ; and \hbar is the reduced Planck’s constant.

In the rotating wave approximation the probe's Hamiltonian is $H_P = \Omega_P \sum_{\mathbf{k}} e^{-i(\omega - (\mu_2 - \mu_1))t} \psi_{2,\mathbf{k}}^\dagger \psi_{1,\mathbf{k}} + \text{H.c.}$ The rf and microwave photons transfer negligible momentum. Given that the range of the the potential ($\sim 1\text{\AA}$) is significantly less than the 2D interparticle separation ($\sim 100\text{\AA}$), the rf/microwave spectrum remains a delta function [48], with a shift given by [104]

$$\delta\omega = \frac{\hbar^2}{m} g_2(0) [f_{12}(q_T) - f_{11}(q_T)] \sigma_1, \quad (17.2)$$

where $g_2(r) \equiv \langle \psi_1^\dagger(r) \psi_1^\dagger(0) \psi_1(0) \psi_1(r) \rangle / \langle \psi_1^\dagger(0) \psi_1(0) \rangle^2$, $f_{ij}(q_T)$ is the i - j scattering amplitude evaluated at the system's characteristic momenta $\hbar q_T$, and $\sigma_1 \equiv \langle \psi_1^\dagger(0) \psi_1(0) \rangle$ is the 2D density. Here $q_T = \sqrt{m k_B T} / \hbar$ is proportional to the thermal momentum, where k_B is Boltzmann's constant. In a dilute thermal gas $g_2(0) = 2$. A similar formula holds in 3D, where $f_{ij} = 4\pi a_{ij}$ with a_{ij} the 3D scattering length.

In quasi-2D, where kinematics are 2D but the 3D scattering length a is much less than the perpendicular confinement length, we can construct a 2D interaction that reproduces the low-energy scattering properties. Assuming harmonic confinement with oscillation frequency ω_{osc} , the effective 2D scattering amplitude is [218, 51]

$$f = 2\sqrt{2\pi} \frac{\hbar^2}{l/a - (1/\sqrt{2\pi}) \log(\pi q_T^2 l^2)} \quad (17.3)$$

where $l = \sqrt{\hbar/(m\omega_{\text{osc}})}$ is the length scale of z -axis confinement of the hydrogen gas. Following Ref. [213]'s discussion, the characteristic length scale for the confinement in their experiments is $l_0 = \sqrt{2\pi} l = \hbar/\sqrt{2mE_a} \sim 5\text{\AA}$ where E_a is the adsorption energy of the hydrogen on the helium film. The spectral shift is then

$$\delta\omega = \frac{4\pi\hbar^2}{m} \left[\frac{1}{l_0/a_{12} - \log(q_T^2 l_0^2/2)} - \frac{1}{l_0/a_{11} - \log(q_T^2 l_0^2/2)} \right] g_2(0) \sigma_1. \quad (17.4)$$

If $\{a_{11}, a_{12}\} \ll l_0$ this reduces to the simpler form

$$\delta\omega = \frac{4\pi\hbar^2}{m} g_2(0) (a_{12} - a_{11}) \frac{\sigma_1}{l_0}, \quad (17.5)$$

as for a 3D gas with density σ_1/l_0 .

The spectral shift predicted by Eq. (17.5) is one hundred times larger than experiment. We will show that this discrepancy is consistent with the corrections found by including the hydrogen-hydrogen interaction mediated by the helium film, V_{med} . Although V_{med} is state-independent, it alters $\delta\omega$ by reducing the probability that two particles are close enough to feel the spin dependent V_{ij} . Remarkably, even an attractive V_{med} can reduce this overlap [105].

Helium film-mediated interaction.—Wilson and Kumar derive a hydrogen-only effective action [219] assuming that (i) the helium film's excitations are non-interacting, (ii) the hydrogen-helium interaction potential is modeled as a van der Waals potential, $V_{\text{H-He}}(r) = -(6\Lambda_0/n\pi)r^{-6}$ with Λ_0 controlling the potential's strength, n is the helium density, and r is the 3D distance between the hydrogen and helium atoms, (iii) the hydrogen confinement length l_0 is significantly smaller than the hydrogen-helium separation ζ , and (iv) retardation effects can be neglected. We define the total hydrogen density operator $\rho_t(\rho) \equiv \sum_j \psi_j^\dagger(\rho)\psi_j(\rho)$ where ρ is the atomic coordinate projected onto the plane of the 2D film. Then Fourier transforming Ref. [219]'s effective Hamiltonian gives

$$H_{\text{eff}} = H - \frac{1}{2} \iint d^2\rho d^2\rho' \rho_t(\rho)\rho_t(\rho')V_{\text{med}}(\rho - \rho') \quad (17.6)$$

with mediated pair interaction

$$V_{\text{med}}(\mathbf{R}) = V_0 \bar{V}_{\lambda/\zeta}(\mathbf{R}/\lambda), \quad (17.7)$$

$$V_0 \equiv \frac{2\delta^2}{\pi^3 \lambda^2 M C_3^2} \quad (17.8)$$

defining $\delta \equiv 6\Lambda_0\phi_g/n\zeta^4$, $\lambda \equiv \sqrt{\frac{1}{MC_3^2}} \left(\frac{1}{2M} + \frac{\beta d_0}{n} \right)$, and $\phi_g \equiv \sqrt{nd_0}$, where C_3 is the film's third sound speed, d_0 is the helium film thickness, M is the helium mass, and β is the film surface tension (estimates of parameters in experiments are given

later). The non-dimensionalized potential \bar{V}_ξ is found to be

$$\bar{V}_\xi(x) = \iint d^2\bar{\rho} d^2\bar{\rho}' \bar{A}(\bar{\rho})\bar{A}(\bar{\rho}')\bar{G}_F\left(\frac{\mathbf{x} + \bar{\rho} + \bar{\rho}'}{\xi}\right), \quad (17.9)$$

where ξ is an argument of V_ξ , and we define

$$\bar{A}(x) \equiv \frac{1}{(1+x^2)^3} \quad \text{and} \quad \bar{G}_F(x) \equiv K_0(x), \quad (17.10)$$

with K_0 the zeroth modified Bessel function of the second kind. Note that $A(\rho) = -(12\phi_g\Lambda_0/\pi n\zeta^6)\bar{A}(\rho/\zeta)$ is the hydrogen-helium van der Waals interaction at a separation ρ and $G_F(\rho) = (n/2d_0\pi\beta)\bar{G}_F(\rho/\lambda)$ is the helium film's Green's function. We numerically compute $\bar{V}_\xi(x)$ as a function of x and ξ . Typical results are shown in Fig. 17.1(a).

Spectral line shifts with mediated potential.—To evaluate spectral shifts via Eq. (17.2), we calculate the scattering amplitude of $V_{\text{tot}} = V_{ij} + V_{\text{med}}$. Since the range of the bare hydrogen-hydrogen potential r_{eff} is much smaller than the range of V_{med} , we may replace V_{tot} with $V'_{\text{tot}} = V'_{ij} + V_{\text{med}}$, where V'_{ij} is an arbitrary short range potential reproducing V_{ij} 's scattering amplitude. This replacement requires that the relative momentum $k_0 \sim \sqrt{|2mV_{\text{med}}(0)|}/\hbar$ of the particles when they reach the bottom of the attractive potential V_{med} satisfies $k_0 r_{\text{eff}} \ll 1$, which is well-satisfied. The same conditions allow us to use a boundary condition in place of V'_{ij} , chosen to reproduce V'_{ij} 's scattering amplitude [105]. We numerically solve the resulting two-particle Schrödinger equation with potential V'_{tot} .

We use the following estimates in our calculations, taken from Refs. [220, 219, 213]: $l_0 \sim 5\text{\AA}$, $a_t = 0.72\text{\AA}$, $a_s = 0.17\text{\AA}$, $\lambda \sim 50\text{\AA}$, $C_3 \sim 1\text{ m/s}$, $q_T \sim (30\text{\AA})^{-1}$, $\delta \sim 0.265\sqrt{\hbar^2 MC_3^2/2m}$, and $\zeta \sim 5\text{\AA}$. These are typically known within a factor of two.

Figure 17.1(b) shows the $|1\rangle$ - $|1\rangle$ and $|1\rangle$ - $|2\rangle$ scattering amplitudes as a function of the mediated interaction strength, with all other parameters fixed at their typical

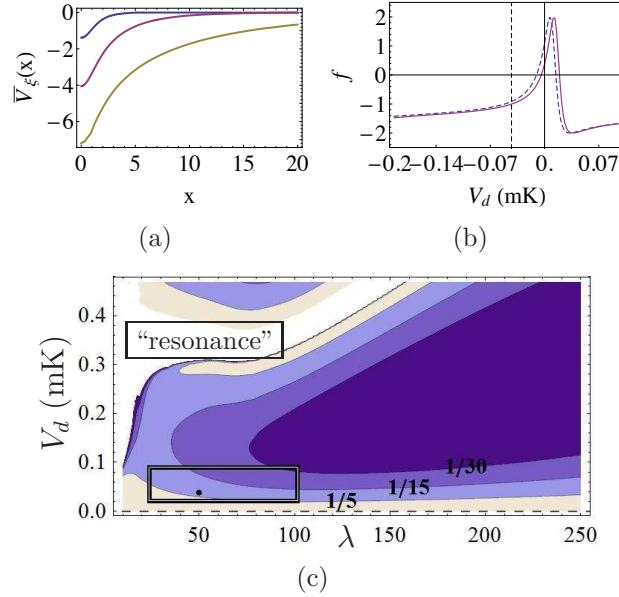


Figure 17.1: (a) Rescaled mediated potential as a function of interparticle separation divided by λ , as given by Eq. (17.9), with $\xi = 1, 4, 15$ from top to bottom. (b) Scattering amplitudes f as a function of mediated potential depth factor $V_d \equiv (2\delta^2)/(\pi^3\lambda_0^2MC_3^2) = V_0(\lambda/\lambda_0)^2$ with $\lambda_0 \equiv 50\text{\AA}$, for the triplet (dashed) and singlet (solid) scattering channels. Vertical lines indicate V_d for the typical parameters given in the text (dashed line) and for $V_d = 0$ (solid). The divergences near $V_d = 0$ have been rounded off for display. (c) Contour plot of the factor by which V_{med} reduces the frequency shift as a function of λ and V_d . Typical values of parameters are shown by the black dot, while factor of two variations comprise the interior of the black rectangle. The contour plot is hidden in the white “resonance” region (far away from the relevant regime), where the scattering amplitude diverges.

values. The two vertical lines correspond to zero mediated potential and typical mediated potential strengths.

Fig. 17.1(c) shows the factor by which the mediated potential reduces the spectral shift $\delta\omega$, relative to $\delta\omega$ in the absence of the mediated potential, as a function of the potential depth and the characteristic length λ . The black box denotes the range of scattering amplitudes consistent with known parameters. A black dot indicates our best estimate of typical experimental parameters. Fig. 17.1(c) shows that for our best estimate of parameters, the mediated potential reduces $\delta\omega$ by a factor of 7, while a nearly 30-fold decrease is possible within the range of experimental parameters. The reductions we quote are due solely to the mediated potential. Compared with the analysis in [213], there is an additional 40% reduction of $\delta\omega$ simply by using the more accurate formula of Eq. (17.2) in place of the approximation Eq. (17.5). Thus the observed reduction in the cold collision frequency shift is consistent with our predictions.

³He film.—Our theory also accounts for unexpected effects of adding ³He to the film’s surface. Since adding ³He reduces the hydrogen surface adsorption energy, one would naively expect an increase in the confinement length, decrease in density, and decrease in spectral shift. Instead, adding ³He with surface density $\sim 10^{14} \text{ cm}^{-2}$ leads to an observed 25% *increase* in the shift. Our theory predicts such an increase, but with larger magnitude.

The ³He driven change in the adsorption energy E_a modifies the mediated interaction by increasing the confinement length l by $\sim 2-10\%$ and by increasing ζ , the distance of the gas to the helium surface. The fractional change in ζ should be comparable to the fractional change in l , and we take these to be equal. We find a 200-400% increase of frequency shifts upon adding ³He.

This reduction can be understood by the following simple argument, which

focuses on the dependence of V_0 on l . Eq. (17.8) shows that the mediated potential roughly scales as $V_{\text{med}} \propto 1/\zeta^8 \propto 1/l^8$, so a 2–10% increase of l yields a ~ 15 –53% decrease of the mediated potential strength, moving the dashed line in Fig. 17.1(b) to the right by 15–53%, leading to a drastic increase in the shift. This simple argument omits the $1/l$ factor in $\delta\omega$, due to the decreased 3D density, and $\bar{V}_{\lambda/\zeta}$'s dependence on l , but as our more detailed calculations show these effects are insufficient to compensate.

Validity of Approximations.—We have made a number of approximations. Here we enumerate the most important ones, and discuss which ones need to be addressed in the future through a more sophisticated theory.

The most severe approximation we made is to follow Ref. [219], and neglect retardation in the induced potential. Such effects are relevant when the phase speed of the hydrogen excitations ω/k becomes large compared to C_3 at characteristic speeds $\sqrt{k_B T/m}$ and energies $k_B T$. For $T \sim 50$ mK as in the experiments, $\omega/k \sim 5$ m/s. In comparison, typical third sound speeds are $C_3 \sim 1$ m/s, so we expect retardation corrections may be significant. Including the frequency dependence in calculating the spectral shift is challenging, requiring solution of a coupled set of 2D partial differential equations for each ω . We expect that a sharp spectral peak survives, but with reduced spectral weight.

Additionally, given the long length-scale of the mediated potential, we should also critically examine the assumption that only the long-wavelength limit of the s -wave phase shift is needed to evaluate the cold collision frequency shift. Eq. (17.2) requires that the areal interparticle distance ($n_{2D}^{-1/2}$) is larger than the effective range of the potential R_e . Since $R_e \sim 250 \text{ \AA}$ and $n_{2D}^{-1/2} \sim 100$ – 300 \AA , the approximation with only the $k = q_T$ s -wave scattering shift may not be sufficiently accurate. Similarly, the thermal wavelength is $\lambda_T \sim 30 \text{ \AA}$ while the cold collision

regime strictly requires $\lambda_T \gg R_e$. This can smear out spectral lines somewhat, although since $\lambda_T \sim R_e$ and the potential is rather shallow, the spectral lines may remain quite sharp. Here retardation helps us, as the slower moving atoms are the dominant contributors to the spectral peak, and these have a substantially larger de Broglie wavelength – a factor of 5 for the fastest contributing atoms.

Finally, we have neglected mass renormalization coming from virtual desorption-adsorption processes. This approximation is well-justified since the desorption process is relatively slow [221, 222], implying that the mass is renormalized by at most a few percent [220].

Conclusions.—In summary, we have shown that incorporating the helium surface into the theory of the hydrogen gas provides a significant renormalization of spectral shifts, in addition to a $\sim 40\%$ reduction from previous estimates by properly treating the quasi-2D nature of the hydrogen. For a reasonable parameter range these shifts are consistent with experimental observations. In addition, we have shown that adding ^3He to the helium film increases spectral shifts, in agreement with experiment and in contrast to the naive theory.

While the mediated interaction provides a consistent explanation of the experimental observations, it is likely that it is not the whole story. A 3D control experiment finds an ill-understood reduction of $\delta\omega$ relative to theory in the 3D gas [223]. (Note: since the publication of the original paper, this control experiment has been invalidated.) The same physics is likely to be also playing a role in 2D. Given the known uncertainty in the experimental parameters, it would be quite reasonable for the mediated interaction to be responsible for only a fraction of the observed shift.

We have found that the helium surface induces an *attractive* interaction between the hydrogen atoms. It is useful to speculate on what other physical effects this

interaction can cause. For example, can it drive a mechanical instability? While thermal pressure will stabilize the gas at the temperatures currently being studied, we believe that as the temperature is lowered that a “collapse” might occur, similar to the ones seen in atomic gases [224, 225, 226]. Importantly, the Kosterlitz-Thouless transition requires repulsive interactions, so the mediated interaction may eliminate the possibility of achieving superfluidity without significantly altering experimental parameters, for example by increasing the helium film thickness.

Finally, we point out possible ramifications of our theory to ultracold atomic gases and elsewhere. The key to our findings is that in quasi-2D, infinitesimal attractive interactions generate zero energy scattering resonances. These are pushed to finite positive energy by the 3D interaction, but a genuine 2D interaction easily overwhelms the effects of the 3D interaction. One can imagine our present theory applying to quasi-2D fermi-bose or bose-bose mixtures where one system mediates an interaction for the other species. Interestingly, similar physics might arise in layered systems: one layer effectively mediates an interaction in adjacent layers – incorporating these effects in a consistent manner could lead to dramatically modified interaction properties for each layer.

Acknowledgments.—KH thanks Neil Ashcroft, Sourish Basu, Stefan Baur, Dan Goldbaum, Jarno Järvinen, Joern Kupferschmidt, and Sophie Rittner for conversations, and especially Sergei Vasiliev and Dave Lee for an introduction to Ref. [213]’s experiments. This material is based upon work supported by the National Science Foundation through grant No. PHY-0758104.

Chapter 18

Molecular hydrogen solids

This chapter was adapted from “Atomic H in molecular H₂ crystals: candidate theories of experimental anomalies” by Kaden R. A. Hazzard and Erich J. Mueller, to be submitted to Physical Review B.

18.1 Abstract

Recent experiments in solid molecular hydrogen populated with atomic hydrogen defects demonstrate a number of spectroscopic and dynamic features which are not easily explained. We develop a few phenomenologies and microscopic mechanisms which might account for the data and general constraints on theories purported to explain the data. Finally, using these theories we make predictions for future experiments.

18.2 Introduction and motivation

Quantum solids are a fascinating class of matter. These materials display a competition between localization and zero-point fluctuations. A quantum solid is characterized by its Lindemann ratio: the ratio of the fluctuations in the atomic positions to the interatomic spacing. Virtually all classical solids melt upon reaching a Lindemann ratio around 0.1. Electron Wigner crystals, solid ⁴He and ³He (at pressures around 30 bar), and solid hydrogen provide notable exceptions with Lindemann ratios of 0.3, 0.28, 0.34, and 0.18, respectively [227, 228, 229]. In these crystals, quantum zero-point motion leads to novel phenomena: supersolid ⁴He [230, 231, 232, 233, 234], tunneling in solid hydrogen [235], Wigner crystals, and the recently observed anomalous spectral properties of atomic hydrogen in

solid molecular hydrogen [236, 237, 238]. Here we theoretically study the last system, giving a critical evaluation of scenarios of Bose-Einstein condensation of atomic hydrogen defects. We make testable predictions for these scenarios.

Solid hydrogen is the only observed molecular quantum crystal. Many rotational order/disorder transitions have been proposed and observed in this material [239]. The phenomenology of H₂ solids is even more interesting when atomic H defects are introduced [236, 240, 238].

Recent experiments in low-temperature ($T \sim 150\text{mK}$) solid molecular hydrogen, populated with large densities ($n \sim 10^{18}\text{cm}^{-3}$) of atomic hydrogen defects, observe unexplained internal state populations [236, 238]. Ahokas *et al.* [236] provocatively conjectured that the anomalies may be related to Bose-Einstein Condensation (BEC) of the atomic defects. Here our goal is to explore and constrain this and related scenarios.

18.3 Experiments

We review Ref. [236]’s experimental apparatus, results, and observed anomalies.

18.3.1 General introduction: physics of atomic hydrogen embedded in solid hydrogen

Hyperfine structure of atomic hydrogen. Fig. 18.1 shows the level structure for a H atom in a $B = 4.6\text{T}$ magnetic field, similar to that used in the experiments of interest [236]. At these large fields, the levels break into two nearly degenerate pairs. Levels within a pair are separated by radio frequencies and the pairs are separated by microwave frequencies. The electronic spin in states a and b is aligned with the magnetic field and is anti-aligned in the other states.

$$\begin{array}{c}
 \overline{\quad} |d\rangle = |\uparrow \uparrow\rangle \\
 \overline{\quad} |c\rangle = \cos \theta |\uparrow \downarrow\rangle + \sin \theta |\downarrow \uparrow\rangle \\
 \overline{\quad} |b\rangle = |\downarrow \downarrow\rangle \\
 \overline{\quad} |a\rangle = \cos \theta |\downarrow \uparrow\rangle - \sin \theta |\uparrow \downarrow\rangle
 \end{array}$$

Figure 18.1: Hyperfine level diagram for hydrogen atom in a strong magnetic field, where $\theta = 3 \times 10^{-3}$. Arrows denote electron (no-slash arrow) and nuclear (slashed arrow) spin projections.

Ahokas *et al.* [236] observe that within the solid hydrogen matrix the atomic hydrogen's spectra is modified. The a-d energy splitting decreases while the b-c energy splitting increases by the same amount.

Spectroscopy of atomic hydrogen. Spectroscopies are commonly used to probe the level structure and occupations of atomic levels. Nuclear magnetic resonance (NMR) in the linear response regime reveals information about level splittings and relative populations of the a and b level pair or the c and d level pair. Electron spin resonance (ESR) does the same for the b and c and the a and d level pairs. Finally, Ahokas *et al.* [236] use a third spectroscopy, a combination of NMR and ESR — electron-nuclear double resonance (ENDOR) — to drive a two photon transition between a and c or b and d states. This allows one to monitor the ESR signal to obtain information about the a - b pair. In addition to applying these in the linear response regime, one can drive these transitions strongly and look at saturation effects.

Molecular hydrogen. At these temperatures, two states of molecular hydrogen are relevant: the “para” and “ortho” states. In all cases, the electrons are in a symmetric bonding orbital and the electronic spins are consequently anti-aligned. In the “para” or “p-” configuration the relative nuclear wavefunction ψ is symmetric under exchanging nuclei and the nuclear spins form a singlet. In the “ortho”

or “o-” configuration ψ is antisymmetric and the nuclear spins form a triplet.

In the ground state of solid hydrogen, the molecules are “para”. However, the “ortho” state is long lived: experimentally a 1% change of ortho- concentration requires hours at low temperatures [239]. This can be a source of heating in experiments with an energy $\Delta/k_B = 170$ K released per conversion. In the experiments of Ahokas *et al.* [236] the exact quantity of o-H₂ is unknown, but given the growth technique it is likely to be at least ten percent.

At standard pressure the p-H₂ in the solid is highly spherical: interaction with neighboring H₂ negligibly distorts the p-H₂. Modeling the hydrogen-hydrogen interactions by their vacuum values quite accurately describes quantities such as the speed of sound [239]. If sufficient ortho-hydrogen is present, orientational ordering transitions may occur around 1K. The models we consider do not rely upon any orientational ordering. Depending on sample-preparation conditions, either hcp or fcc crystals may be produced [239].

Atomic hydrogen in the solid lattice. The motion of atomic hydrogen in molecular hydrogen has been widely studied [235]. Both thermally activated and quantum tunneling contribute to defect motion, but quantum tunneling dominates at these low temperatures (the two dominant tunneling pathways have energy barriers of 4600K and 100K). One motivation for these studies is to explore the possibility of Bose-Einstein condensation of these defects. This is conceptually related supersolidity driven by condensation of vacancies.

Kumada [235] argues on the basis of experimental data that the exchange reaction $H + H_2 \rightarrow H_2 + H$ is the dominant diffusion mechanism at low temperatures. Other tunneling pathways are possible, including correlated, collective relaxation and “physical” diffusion.

Ahokas *et al.* [236] achieve populations of 50ppm H defects in their solid, and

argue that H sits at substitutional sites. The observed lifetime of these defects was weeks. The dominant decay mechanism should be the recombination of two hydrogen defects. One therefore expects that this rate is determined by the diffusion rate of the defects. The long lifetime is therefore inconsistent with the diffusion rates predicted by phonon assisted tunneling. One possible explanation is the suppression of tunneling by the strain-induced mismatch of energy levels between neighboring sites [241, 242].

Crystal growth. Ahokas *et al.* [236] grow solid hydrogen from a gas of electron-spin polarized metastable hydrogen atoms, which undergo two-hydrogen recombination to form molecules. Two-body recombination is allowed due to wall-collisions carrying off the excess momenta. This grows H₂ solid layer-by-layer from at a rate of 0.5-1 molecular layer per hour. After ~ 1 week, a quartz microbalance revealed a film thickness of 150 ± 1 layers,¹

18.3.2 Anomalies and experimental results

Ref. [236] observed four anomalies: (1) several orders-of-magnitude too fast “Overhauser” relaxation, (2) a non-Boltzmann a-b population ratio, (3) saturation of a-b spectroscopic line is fails to give a 1:1 population ratio, and (4) recombination rates are extremely low. Items 2 and 3 will be our main focus.

Overhauser relaxation. The *c* to *a* relaxation is expected to be extremely small at the 4.6T fields of the experiments. This can be seen from the small mixing angle $\theta \approx 3 \times 10^{-3}$ illustrated in Fig. 18.1. The mixing angle appears in the states as $|a\rangle = \cos\theta |\downarrow\uparrow\rangle - \sin\theta |\uparrow\downarrow\rangle$, and $|b\rangle = \cos\theta |\uparrow\downarrow\rangle - \sin\theta |\downarrow\uparrow\rangle$. Any c-a decay mechanism by photon emission is suppressed by θ^α with [243] $\alpha \gtrsim 1$. Ahokas *et al.* [236] observe no such suppression: the c-a line decays with a time constant of

¹private communication with Jarno Järvinen

$\lesssim 5$ s, similar to the d-a decay time.

Equilibrium populations. The polarization

$$p \equiv \frac{n_a - n_b}{n_a + n_b} \quad (18.1)$$

characterizes the a and b state population. Assuming a Boltzmann distribution $n_a/n_b = \exp(\Delta_{ab}/T)$ where $\Delta_{ab} \approx 43$ mK is the difference in energies between the b and a states, one expects $p = 0.14$ at 150 mK. On the contrary, Ahokas *et al.* [236] measure $p = 0.5$.

When a strong rf or microwave field is used to drive the population away from this measured polarization, the system returns to this non-Boltzmann value on a time scale of ~ 50 hours.

Saturation of a-b line. An extremely strong rf field should saturate the a:b line, driving the population ratio to 1:1, or $p = 0$. Ahokas *et al.* [236] obtained a minimum of $p = 0.2$ at high excitation powers. This saturated population ratio was independent of the applied rf power (for sufficiently large power).

Low recombination rates. As previously described, at 150mK Ahokas *et al.*'s [236] recombination rate is much smaller than expected, negligible on a time scale of weeks. In contrast, at $T = 1$ K their recombination rates are consistent with previous studies [242].

Hole burning. Ahokas *et al.* applied a magnetic field gradient and a rf field to saturate the a-b line in a millimeter sized region of the sample. The spectral hole recovered in a time similar to that in the homogeneous case, indicating that the nuclear spin-relaxation is somewhat faster than spin migration. This would seem to indicate that the atomic hydrogen defects are immobile on regions much larger than a millimeter.

18.4 Scenarios

In this section we evaluate the previously proposed scenarios for these phenomena and suggest a new one. For each scenario, we present the idea, examine its consistency with Ahokas *et al.*'s[236] experiments, consider possible microscopic mechanisms, and *give testable predictions*.

18.4.1 Bose statistics and Bose-Einstein condensation

Idea

Ahokas *et al.* [236] suggested Bose-Einstein condensation (BEC) as a possible mechanism to explain the departure from the Boltzmann distribution. In a BEC the lowest energy mode becomes “macroscopically occupied.”

Hydrogen BEC would lead to excess $|a\rangle$ state population, as observed. Since the H's are effectively bosons in a lattice, they should condense at some temperature. Neglecting interactions, the BEC transition temperature T_c for a homogeneous system of spinless particles with density ρ and effective mass m^* is

$$T_c = \left(\frac{\rho}{\zeta(3/2)} \right)^{2/3} \frac{2\pi\hbar^2}{k_B m}. \quad (18.2)$$

Here ζ is the Riemann zeta function; $\zeta(3/2) \approx 2.61$ [244]. Including the b states is straightforward and makes only small changes. This estimate is accurate when Δ_{ab} is large, while if $\Delta_{ab} = 0$ one would divide the density by a factor of 2.

Phenomena explainable

This scenario can in principle explain the non-Boltzmann equilibrium ratio n_b/n_a . It can not provide an explanation of the inability to saturate the a - b line, the slow recombination, or the fast Overhauser cross-relaxation.

Consistency with experiment

Transition temperature and densities. As reported in Ahokas *et al.* [236], for density $\rho \sim 10^{18} \text{cm}^{-3}$ and effective mass m^* similar to bare mass m , the ideal Bose gas transition temperature in EQ. (18.2) is $T_c \sim 30 \text{mK}$, far below the experimental temperature. To address this inconsistency Ahokas *et al.* [236] suggest that phase separation may concentrate the defects to locally higher densities. For example, if the defects phase separated so that their density was $\rho \sim 3 \times 10^{19} \text{cm}^{-3}$, then even with $m^* = m$ the transition temperature would be $T_c = 170 \text{ mK}$, and one would reproduce the observed ratio of n_a/n_b at $T = 150 \text{ mK}$. Such a powerful concentrating mechanism would have additional consequences, such as increased recombination rates.

In the following subsection we use the experimental hole-burning data to constrain the effective mass, finding that it is sufficiently large to completely rule out simple Bose-Einstein condensation of defects at the experimental temperatures.

Estimate of effective mass. We expect that the effective mass m^* of the defects is much higher than that of the free atoms. Here we bound the effective mass by considering Ahokas *et al.*'s measurement of the lifetime of a localized spectral hole. They found that a $w \sim 0.2 \text{mm}$ hole persisted for $\tau_{\text{pers}} > 50 \text{hours}$. Our argument will relate macroscopic motion (which fills in the spectral hole) to microscopic motion (the defect tunneling). We assume diffusive motion, where the characteristic time between collisions is longer than a tunneling time.

There are at least three mechanisms by which the spectral hole can heal: the excited atoms can spontaneously undergo a transition back to the a -state, spin exchange collisions can lead to spin diffusion, or a -state atoms can diffuse back into that region of space. Neglecting all but the last process gives us an upper

bound on the atomic diffusion constant D ,

$$D \lesssim \frac{w^2}{\tau_{\text{pers}}} \approx 10^{-8} \text{cm}^2/\text{s}. \quad (18.3)$$

Throughout this argument we will aim to produce an order-of-magnitude estimate, and use the symbol “ \sim ” to indicate that we neglect constants of order unity. This diffusion constant can be related to the microscopic collision time τ_{coll} and the mean velocity v by

$$D \sim v\ell. \quad (18.4)$$

with ℓ the mean free path. In the effective mass approximation, one would expect thermal effects to yield a mean velocity $v \sim \sqrt{k_B T/m^*}$. Thus the fact that in any physical situation with lattice spacing $d \sim 3\text{\AA}$ [239], the mean free path must satisfy $\ell \gtrsim d$ together with Equation (18.3) gives an upper bound on the effective mass of

$$m^* \gtrsim k_B T \left(\frac{d}{10^{-8} \text{cm}^2/\text{s}} \right)^2 \approx 10^8 \text{amu}. \quad (18.5)$$

This effective mass is several orders of magnitude too large to allow BEC at experimentally relevant temperature scales. This argument has neglected interactions and inhomogeneities: phase separation or some “local” BEC’s that are uncoupled, thus disallowing global transport, would invalidate the arguments leading to our bound.

Microscopic mechanism

Microscopic estimates of tunneling matrix elements are beyond the scope of this work. If they are as large as implied, then condensation is ruled out. On the other hand, it is plausible that the tunneling matrix elements are much smaller, on the order of the bare mass. This would imply that our simple picture of a hole recovery

in a microscopically homogeneous system is incorrect. More careful estimates of the tunneling are thus desirable to distinguish these scenarios.

Experimental predictions

Polarization temperature dependence. Perhaps the most easily testable prediction of this model is the temperature dependence of the polarization, $p = (n_a/n_b - 1)/(n_a/n_b + 1)$ with

$$\frac{n_a}{n_b} = \frac{\int d^3k n(\epsilon_a(\mathbf{k})/(k_B T))}{\int d^3k n(\epsilon_b(\mathbf{k})/(k_B T))} \quad (18.6)$$

with $n(x) \equiv 1/(e^x - 1)$. The dispersion of atoms in state j is $\epsilon_a(\mathbf{k}) \approx \hbar^2 k^2/2m^*$, and $\epsilon_b(\mathbf{k}) \approx \hbar^2 k^2/2m^* + \Delta_{ab}$, where Δ_{ab} is the b-a energy difference. Above the BEC transition temperature T_c , the integrals yield

$$\frac{n_a}{n_b} = \frac{g_{3/2}(e^{\mu/T})}{g_{3/2}(e^{(\mu-\Delta_{ab})/T})} \quad (18.7)$$

where $g_\alpha(x) = \sum_j x^j/j^\alpha$ is the polylog function and μ is self-consistently determined to set N , for a homogeneous, three-dimensional gas. The same expression holds in dimension d with $3/2$ replaced by $d/2$. Below $T = T_c$, one instead finds

$$\frac{n_a}{n_b} = \left(\frac{T_c}{T}\right)^{3/2} \frac{\zeta(3/2) + g_{3/2}(e^{-\Delta_{ab}/T_c})}{g_{3/2}(e^{-\Delta_{ab}/T})} - 1. \quad (18.8)$$

While the effective mass sets the density at T_c , it does not appear in this expression. The polarization depends only on Δ_{ab}/T and T/T_c . To produce the observed $n_a/n_b = 3$ at $T = 150\text{mK}$, one needs $T_c = 170\text{mK}$.

Fig. 18.2 shows $p(T)$ for Boltzmann and Bose condensed (assuming $T_c = 200\text{mK}$) gases. Accurately measuring $p(T)$ would clearly distinguish Bose and Boltzmann statistics.

Equation (18.7) shows that Bose statistics can affect the ratio n_a/n_b even if the system is non-condensed. However, Eq. (18.7) bounds $n_a/n_b <$

$\zeta(3/2)/g_{3/2}(e^{-\Delta_{ab}/T}) = 2.3$, which is insufficient to explain the experimentally observed $n_a/n_b = 3$.

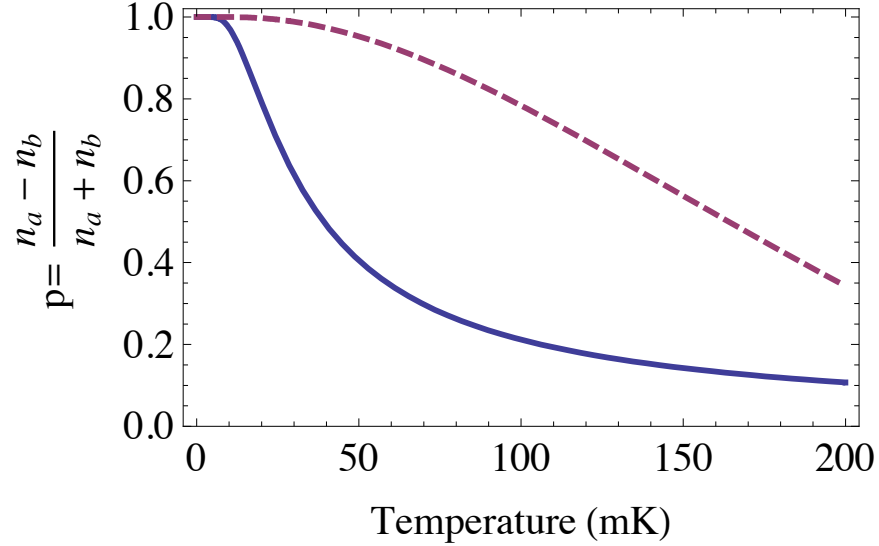


Figure 18.2: The polarization versus temperature for the Boltzmann case (solid line) and the Bose-condensed case (dashed line), from Eq. 18.8.

Transport. A second signature of BEC is superflow. For example, the sample could be incorporated into a torsional oscillator, providing a measurement of a possible nonclassical moment of inertia I : below T_c , the superflow decouples from the cell, and I decreases. Mounting the sophisticated hydrogen growth and measurement equipment in an oscillator would be challenging, as would the difficulty of working with such small samples.

Bimodal Cold Collision Shifts. The b-c spectra can reveal BEC. In particular, interactions shift spectral lines since hydrogen interactions are different for different spins. Insofar as the interaction may be described as zero energy and s-wave – reasonable, given the diluteness of the gas compared to microscopic length scales at sufficiently low temperatures – the shift is [110, 104, 244, 83]

$$\delta\omega = \frac{4\pi\hbar^2}{m}g_2(0)(a_{\uparrow\downarrow} - a_{\downarrow\downarrow})\langle n \rangle \quad (18.9)$$

where $g_2(\mathbf{r}) \equiv \langle \psi^\dagger(\mathbf{r})\psi^\dagger(0)\psi(0)\psi(\mathbf{r}) \rangle / \langle n \rangle^2$ and $\langle n \rangle$ is the average density. The key

is that for a noninteracting BEC $g_2(0) = 1$ while for a normal gas $g_2(0) = 2$. Thus, a finite-temperature condensate displays a characteristic double-peaked spectrum. This may be robust even with severe inhomogeneity. For example, this technique revealed BEC in magnetically *trapped* spin-polarized hydrogen gas [83].

Thermodynamics and collective excitations. The BEC phase transition can in principle be directly observed by monitoring thermodynamic quantities such as specific heat. Due to the small number of H atoms, the signal should be quite small. Similarly, the presence of a superfluid component would lead one to expect a second-sound mode, which could be excited (for example) via localized heating of the sample.

18.4.2 *Local Bose-Einstein condensation*

Idea

Next we pursue the idea of “local BEC”, where the defects congregate in small disconnected regions, each of which contains a condensate, but which have no relative phase coherence.

Phenomena explainable

This model can explain the non-Boltzmann ratio n_b/n_a , and the slow transport observed in the hole burning experiments. It does not provide an explanation of the slow recombination, failure to saturate, or fast Overhauser relaxation.

Consistency with experiment

The arguments from Section 18.4.1 about the polarization go through without change. The slow recovery in the hole burning experiment is readily explained if the disconnected condensates are smaller than 0.1mm. Furthermore, local clusters

are naturally expected if there is the dramatic sort of concentrating mechanism described in Section 18.4.1.

Microscopic mechanism

An attractive interaction between defects can lead to clustering. A long distance phonon mediated attraction is expected for this system. Inhomogeneities in the molecular sample, or its environment could also lead to clustering. For example, it has been observed that the ortho and para molecules phase separate. Furthermore, the sample sits on a surface may introduce strain into the crystal.

Experimental predictions

The temperature dependence calculated for global BEC is unchanged for local BEC, and one again expects a double-peaked ESR spectrum. Jointly observing these would provide a “smoking gun” for local BEC. Also, at sufficiently cold temperatures the puddles phase lock giving a global BEC. The transition temperature would be effectively zero, however, since atoms would have to tunnel macroscopic distances between concentrated regions. The concentration of $H\uparrow$, regardless of BEC, may be diagnosed by examining the dipolar shift of spectral lines due to H-H interactions.

18.4.3 Nuclear spin dependent Density-of-states

Idea

If the degeneracy of the a and b states were g_a and g_b , one would expect that $n_a/n_b = (g_a/g_b)e^{\beta\Delta_{ab}}$. Thus if a mechanism could be found to enhance (g_a/g_b) , then one could explain the observed ratio of n_a/n_b . Assuming such a relative

enhancement of the density of states, a strong RF field would lead to a saturated ratio $(n_a/n_b)_{\text{sat}} = g_a/g_b$.

Phenomena explainable

Both the equilibrium n_a/n_b and the RF saturated $(n_a/n_b)_{\text{sat}}$ can be explained by this model. We also provide a scenario whereby the Overhauser relaxation is enhanced. Within this model, the low recombination rates would be a consequence of the defects being immobile.

Consistency with experiment

At strong excitation powers the polarization $p = (n_{\text{tot},a} - n_b)/(n_{\text{tot},a} + n_b)$ saturates to

$$p_{\text{sat}} = \frac{g - 1}{g + 1} \quad (18.10)$$

where $g \equiv g_a/g_b$. Meanwhile, the thermal polarization is

$$p_{\text{therm}} = \frac{g \exp(\Delta_{ab}/(k_B T)) - 1}{g \exp(\Delta_{ab}/(k_B T)) + 1} \approx \frac{g - 0.75}{g + 0.75} \quad (18.11)$$

where the last equation holds for Ref. [236]'s experiments, where $\Delta_{ab} = 43\text{mK}$ and $T = 150\text{mK}$. If one takes $g = 2$ one finds $p_{\text{sat}} = 0.33$ and $p_{\text{therm}} = 0.45$. Ref. [236] experimentally finds $p_{\text{sat}} = 0.2$ and $p_{\text{therm}} = 0.5$. Contrast this with the naive expectation of $p_{\text{sat}} = 0.5$ and $p_{\text{therm}} = 0.14$.

Microscopic mechanism

There are very few mechanisms whereby the molecular hydrogen matrix can change the degeneracies of the atomic hydrogen hyperfine states. The most plausible direction to look in to produce such a mechanism, would be to consider nuclear spin dependent interactions with *o*-H₂. Such interactions can be produced through

spin-orbit coupling in the presence of a bias magnetic field. Hybridization of the molecular and atomic levels could in principle lead to sufficiently drastic rearrangements of the hyperfine states to affect their degeneracy. Such a strong interaction would presumably have other spectroscopic implications, such as a severe renormalization of the a - b splitting. The experiments observe an a - b splitting is changed by only 0.1% compared to its vacuum value.

If there is significant hybridization of the atomic and molecular states, then the symmetry which forbids the a - c transition would generically be broken. This would be a source of the fast Overhauser relaxation.

Experimental predictions

Most mechanisms of this sort would lead to a nearly temperature independent g , at sufficiently low temperature. Thus one would predict that the saturation polarization would be independent of temperature, and the equilibrium ratio should scale exponentially: $n_a/n_b \propto e^{\beta\Delta_{ab}}$. Any given microscopic mechanism will presumably have spectroscopic consequences, including implications for the molecular levels of the o -H₂. Finally one would expect the effect to depend on the concentration of o -H₂, leading to slow temporal changes (on the order of days) as the sample undergoes ortho-para conversion.

18.5 Other observations and speculations

Here we give two additional observations which are relevant for understanding these experiments. We hope that these can stimulate further theoretical and experimental developments.

Superfluidity due to ortho-para clusters While the superfluid explanations proposed in Sections 18.4.2 are speculative, there is precedence for superfluid

phenomena in molecular hydrogen. In particular Ceperley *et al.* have shown that the surface of small p-H₂ clusters in a vacuum is superfluid [245] using numerically exact Quantum Monte Carlo calculations, and Cazorla *et al.* have similarly shown that on small length scales 2D p-H₂ has superfluid correlations [246]. Analogous effects are predicted for defects in solid ⁴He, including grain boundaries, dislocations, and amorphous regions [247, 248, 249]. Hence, a natural related phenomena would be superfluidity at the interface of o- and p-H₂ clusters or in the p-H₂ clusters themselves. It is possible that this H₂ superflow couples with the atomic *H*.

This picture of superfluid flow in solid molecular hydrogen also been explored in experiments. Torsional oscillator measurements by Clark *et al.* [250] found that at temperatures below 200mK the moment of inertia of the solid hydrogen drops slightly. A blocked annulus experiment ruled out the possibility of global superfluidity, but a scenario with local superfluid regions is consistent with the observations.

Magnetic ordering. Finally we point out that a magnetic ordering transitions — for example nuclear ferromagnetism — would alter the ratio of *a*-state to *b*-state population. Although such an ordering would significantly shift the energy required to excite atoms between *a* and *b*, the population ratio would obey Boltzmann statistics with a renormalized splitting, $n_a/n_b = e^{-\beta\Delta'_{ab}}$. The experiments directly measure Δ'_{ab} , finding this relationship is violated. At this point we cannot rule out the possibility that a more complicated form of magnetic ordering could explain the observations.

18.6 Summary

We reviewed the unexplained phenomena seen in experiments of Ahokas *et al.* [236]. We enumerated a number of possible mechanisms which could be involved in pro-

ducing the observed phenomena. In particular, we gave detailed consideration to the idea, first introduced in Ref. [236] that the non-Boltzmann ratio n_a/n_b may be due to Bose-Einstein condensation of atomic hydrogen. We conclude that global Bose-Einstein condensation is not consistent with other experimental observations.

Although we present several other scenarios, we find that none of them are wholly satisfactory. Although some of the phenomena can be explained by local BEC, it fails to provide a mechanism for the unexpected saturation population $(n_a/n_b)_{\text{sat}}$ when a strong RF field is applied. We do find that all of the phenomena would be consistent with a nuclear spin dependent density of states. However, we are unable to provide a microscopic mechanism for this density of states.

Ultimately, substantial experimental work will be necessary to clarify the situation. Our arguments make a strong case that measuring the polarization's temperature dependence is a promising first step, and suggests other experimental signatures — especially in transport and spectral features — that would clarify the phenomena.

During the preparation of this paper, new results came out from Ahokas *et al.* [240], which introduced new mysteries. In particular they observe substantial density and substrate dependence of the population ratio n_a/n_b . All of our considerations remain valid, with the additional clue that whatever the underlying mechanism is, it must involve the surface of the sample, and be sensitive to density. For example, the formation of superfluid domains could be influenced by the substrate, or magnetic impurities in the substrate could interact with atomic hydrogen, leading in some way to the unexpected density of states.

Acknowledgments. We would like to acknowledge discussions with David Lee, Järno Jarvinen, Sergei Vasiliev, and Cyrus Umrigar.

Chapter 19

Helium and hydrogen (super?)solids

19.1 Background

Supersolidity is a counterintuitive phenomena where a solid — a substance resistant to shear — also allows superflow — dissipationless flow to pressure gradients. The discovery of anomalous rotational properties in ^4He was consistent with supersolidity, but further investigation indicated that the simple pictures that had been developed were insufficient to account for the data.

This work was largely carried out 2005-2006, when a broad range of new experimental results complemented the pioneering torsional oscillator studies, and tried to account for many of the seemingly contradictory observations. It outlines a scenario that could be consistent with all of those observations — but makes no claim of any substantial likelihood of correctness. At best, I hoped to stimulate a simpler, more complete account of the phenomena.

In the time since this period, many additional experiments have been performed and some of the experimental “facts” have been called into question. Thus, although the scenario was constructed for consistency with the data at the time, the experimental state of the art makes it unclear whether it is consistent with the most up to date observations.

Regardless, the scenario is interesting as a possible manifestation of supersolidity in disordered systems: in particular, it connects microscopic calculations (see Ref. [230] and references therein) with the macroscopic behavior probed in experiments, and due to these ideas and this connection may be useful in other contexts.

19.2 Abstract

A phenomenology of a particular model of disordered supersolidity is developed (in conjunction with the notes in supersolid-geometry). It is related to proposals of superfluid defects — dislocations, grain boundaries, and amorphous regions — but develops a picture of the macroscopic, experimental properties of the system starting from these microscopic considerations. The essence of the idea is that superflow may exist in large disordered regions, and that the supersolid feature observed in torsional oscillator experiments corresponds to the point where these become globally phase coherent, even though the superflow *within* the domains is already present at higher temperatures. The experimental consequences of this are fleshed out and found to be consistent with the present state of experiments.

19.3 Introduction

A number of conundrums surround supersolid ^4He . As some notable examples: one finds a drastic *increase* in T_c with ^3He doping, a mysteriously similar non-classical rotational susceptibility in H_2 which shows none of the other signals of superflow, frequency dependence of the transition temperature and velocity dependence, and the absence of large thermodynamic features (e.g., heat capacity peak) one expects to be associated with superfluidity. We describe a model of defects that are superfluid even at much higher temperatures than the supersolid transition, but become globally coherent only at the supersolid transition temperature T_c . This theory allows a good understanding of all these experimental mysteries.

Other unexplained experimental features exist: the geometry dependence of the supersolid fraction, an anomalously low critical velocity, absence of dc flow, low-temperature specific heat and pressure data, and anomalous shear modulus

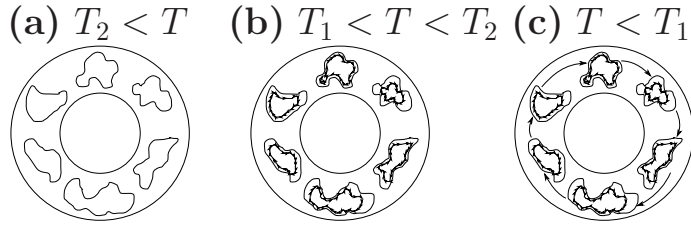


Figure 19.1: Our model’s basic idea. **(a)** The solid at $T > T_2$ before any superflow develops. There are two distinct types of regions: those that support superflow at low temperatures (SF) and those that will not (NSF). It is likely that T_2 is larger than the solidification temperature so that the domains are *always locally superfluid* in the solid. **(b)** The state of the system after cooling through one phase transition to a temperature $T_1 < T < T_2$: within each of the SF regions, a superflow develops. However, no global phase coherence is present. **(c)** The state of the system after cooling to $T < T_1$: global phase coherence has developed, and superflow occurs throughout the system.

stiffening at the supersolid transition. While our theory is not necessarily linked with each of these, none of these results are inconsistent with our ideas.

Figure 19.1 illustrates the basic idea of our model graphically. In words, it is that there exist two phase transitions, at T_1 and T_2 with $T_1 < T_2$. Some domains of the solid turn into independent supersolid domains (domains that support superflow of some kind) as the temperature is lowered below T_2 , with superflow allowed within each domain. Then, upon further cooling below T_1 , phase coherence develops between the independent superfluid regions allowing a global superflow. **It is likely that the *local* superfluidity occurs at all temperatures in the solid, in which case there will be no observable T_2 “transition”.**

Given the robustness of the transition — it is relatively independent of sample and geometry — it is necessary that the links connecting the supersolid regions are somehow robust, most likely independent defects (as opposed, say, to just tunneling through a barrier).

Before examining its consequences, it is worth seeing what this theory is and what it is not. It is not an *ab-initio* theory predicting the mechanism of supersolidity. Rather, it takes as given the point of view advocated by many that that

there are regions of the crystal which can maintain superflow. From this, it derives the macroscopic observable quantities, in the process clarifying several puzzling experiments. We now turn to these mysteries individually.

19.4 Torsional oscillator NCRI.

Torsional oscillator experiments are a classical test of superflow. Basically, a cell of some geometry is oscillated at a frequency ω about its center – an annulus, as assumed in the illustration in Figure 19.1, a cylinder, and an extruded rectangular cell have all been used in the study of supersolid helium and hydrogen. As $\omega \rightarrow 0$, elementary hydrodynamics shows that a normal fluid will follow the walls of the container, as for a solid. However, for a system with a finite superflow, as $\omega \rightarrow 0$, a finite fraction of the sample does not oscillate with the walls and the effective moment of inertia is less than that of the system without superflow.

In these experiments, the system is driven on-resonance with a lock-in amplifier. The period is $T \propto \sqrt{I}$. So as the resonance frequency changes, one can infer the change in I and hence the amount of superflow. Furthermore, the amplitude at resonance is proportional to the quality factor Q . Thus the loss via the Q factor and the moment of inertia via T may be measured.

19.5 Two supersolid features.

At each of T_1 and T_2 we expect to see a period drop going from high to low temperature, however **we suspect that T_2 may be above the solidification temperature, and thus non-visible.** Even if T_2 is below the solidification temperature, the feature will be observable only in very large annuli, as small disconnected regions give only a small contribution to the superflow. The square

cell Cornell experiments have indeed seen two features, the higher temperature of which has yet to be explained, although this is probably an artifact. For reference, these occur at roughly 150 mK and 1 K. There are hints that Goodkind’s ultrasound attenuation and soundspeed data also sees a high-temperature transition, as well, though the data is not easy to interpret.

For small domains of characteristic size r , the period drop associated with the high-temperature feature gives an apparent supersolid fraction going as $(r/R)^2$ where R is the radius of the cell. (This calculation appears elsewhere.) Thus in annuli, one has a limit for r (it can’t be larger than the annular width) and hence a very small limit on the apparent supersolid fraction.

19.6 Blocked annulus torsional oscillators

Blocking an annular cell prevents global superflow. Some superflow pattern will be established in the cell that leads to a moment of inertia reduction, but it will be much less than the naive “fraction of superflow equals fraction of mass decoupling” that applies in the unblocked case. Typical cases for current annular geometries involve a period drop for the blocked that is roughly $\sim 1/100$ of the unblocked geometry, though the blocked apparent supersolid fraction can be as large as ~ 0.5 of the unblocked fraction for a very large annulus.

When the annulus is blocked, the isolated superfluid regions, whose condensation is associated with T_2 , are going to be hardly affected. On the other hand, the superflow *around* the annulus associated with the tunneling between the independent regions occurring below T_1 , will be unable to establish its usual flow pattern.

Consequently, if prior to blocking there is a visible transition at T_2 , then upon blocking, the period drop for the transition at T_1 should decrease roughly in ac-

cordance with a blocked uniform superflow, while the period drop at T_2 should change negligibly. Experimentally, such a drop is indeed observed in ^4He for the T_1 transition. In Section 19.8 we argue that this phenomenon explains Chan's H_2 solid results in a natural way.

19.7 Dissipation peaks

All experiments observe a dissipation peak accompanying the period drop. Such a dissipation maximum is not expected in the context of the usual superfluid transition. However, such a feature is a standard characteristic of the two-dimensional Kosterlitz-Thouless transition occurring in superfluid films. This suggests that – in some respects – the flow could be two-dimensional.

Several recent works, both theoretical and experimental, have shown that grain boundaries in ^4He support superflow, giving a natural candidate for two-dimensional flow. The transition in the grain boundaries then may account for the dissipation feature. Moreover, two-dimensional systems have a relatively smeared out period drop; this is also present in the supersolid experiments, but this may arise also due to a disorder-induced smearing of transition temperatures.

Nevertheless, a mechanism with solely two-dimensional flow is hard to reconcile with the large supersolid fractions recently observed by RR. In order to understand this better, it is worth examining the experimental correlation between dissipation and apparent supersolid fraction. Although RR were able to increase the supersolid fraction by orders-of-magnitude through quenching and restricting the sample geometry, the dissipation does not increase commensurately. This suggests that in samples with more than a few percent supersolid fractions, a substantial portion comes from non-two-dimensional objects, while two-dimensional objects account for a respectively larger portion at smaller supersolid fractions. Although the dissi-

pation feature is not required by our theory, it gives one ostensible interpretation.

19.8 H₂ experiments.

In Chan’s paper on the molecular H₂ solid experiments, a transition of some kind is observed at roughly 120 mK. This period drop over a hundred mK is remarkably similar to the supersolid transition, and thus a *natural* way of interpreting the experiment is to identify it as a supersolid transition of some kind.

However, there are at least five mysterious aspects of this experiment:

- The signal does not disappear after blocking the annulus.
- The temperature of the measured ⁴He T_1 transition coincides with that of H₂ – as measured by the de Boer and Lindemann parameters, ⁴He is “more quantum” and thus presumably should have a higher transition temperature.
- There is no critical velocity up to 500 $\mu\text{m/s}$ in H₂.
- The feature is not present when HD is substituted for H_2 .
- There is no dissipation maximum in the H₂ data, while there is for the T_1 transition in ⁴He.

The present analysis can account for all of these phenomena, relate parameters to the ⁴He experiments, and make “easily” testable predictions. In a moment we will account for these observed effects.

In Chan’s paper, they attempt to explain some of these mysteries via clustering of ortho- and para-hydrogen in specific locations of the cell. However, this theory is somewhat unnatural in providing no reason that the effect and transition temperature are so similar to the ⁴He transition, nor does it provide a reason the cluster would occur in the requisite extreme manner. There is also a serious difficulty

with the clustering explanation proposed in the preprint in that *it is impossible to account for the magnitude of the effect* by clustering: even the most extreme clustering falls short. Our theory does not suffer these defects.

Let’s examine the first of the mysteries, that **the superflow fails to disappear upon blocking the annulus. Such a feature is expected within a theory of disordered domains**, when one is above the global coherence transition. The observed feature, then, would be associated with the “ T_2 ” feature.

Next, **the experimental feature disappears if HD is substituted for H_2 , consistent with our theory, since HD is a fermion**, consistent with our picture, but not easily with other pictures.

Finally we will consider the transition temperatures. The Lindemann ratio and the de Boer parameter are, in this context, ways of characterizing the “quantumness” of a solid. The former is defined as the ratio of the zero-point root-mean-displacement of an atom of the solid to the interatomic spacing. “Classical solids” have a more or less universal ratio of around 10% for melting. H_2 and 4He , the two atomic quantum solids, have Lindemann ratios of 18% and 26%, respectively, in their stable ground states. Importantly, 4He has a larger Lindemann ratio and hence is “more quantum” – we would thus expect the supersolid transition at a *higher* temperature than H_2 .¹ The de Boer parameter also supports this reasoning: it is defined as $\Lambda \stackrel{\text{def.}}{\equiv} \frac{h}{\sigma\sqrt{m\epsilon}}$, with σ the equilibrium spacing of the fit Lennard-Jones potential and ϵ the the dissociation energy. For intuition, note that the de Boer parameter is essentially capturing the same thing as the Lindemann ratio: it is the ratio of the length scale associated with the dissociation energy – $h/\sqrt{m\epsilon}$ – to the interatomic spacing σ ; they are simply different ways of viewing the same physics of zero-point fluctuations. For H_2 and 4He , the de Boer parameters are 1.7 and

¹Assuming that the mechanism – defects carrying superflow, etc. – in the H_2 is analogous to that in 4He .

2.6, respectively. Again, ^4He is “more quantum,” with greater zero point motion, and hence should show superflow at a higher temperature.

In short, this suggests that H_2 should become a supersolid at a lower temperature than ^4He , in stark contrast to the observations, where they occur at roughly the same temperature. In light of the arguments earlier in this section, this becomes less puzzling however: we should not compare the feature in H_2 with the usual ^4He supersolid feature, but rather with the a “ T_2 ” feature. Assuming $T_{2,^4\text{He}} \sim 1\text{K}$, very roughly on the order of the melting temperature, we see that the transition temperature observed in H_2 is indeed significantly lower than the corresponding transition in ^4He .

The Lindemann ratios of ^4He and H_2 provide a simple estimate of the ratio of their respective transition temperatures. The zero point motion of the atoms is the standard deviation of position for that atom; taking a simple cosine as a model for the lattice potential for simplicity allows one to calculate the Wannier functions as a function of lattice depth and spacing; then given the experimental values of lattice spacing and Lindemann ratio we can determine the lattice depth, giving a complete characterization of the potential from which we calculate the hopping energy of nearest neighbors. Then, the hopping energy/rate must be on the order of the transition temperature, since it is the only energy scale in the (non-interacting) system. Carrying out this procedure produces a ratio of transition temperature

$$\frac{T_{^4\text{He}}}{T_{\text{H}_2}} \sim 2.1$$

in rough agreement with the observed factor of 4 or 5. We would not consider taking such a simplistic, toy estimate seriously if it weren’t for the fact that it gives results in qualitative agreement with experiment.

Next, **the theory accounts for the apparent lack of a critical velocity**

in \mathbf{H}_2 . In an annulus of radius R with oscillation frequency and amplitude of angle oscillation Θ_0 , the angle of the system is $\Theta(t) = \Theta_0 \sin(\omega t)$, while the rim velocity as a function of time is $v_{\text{rim}}(t) = \Theta_0 R \omega \cos(\omega t)$. We can assume this velocity to be uniform throughout the sample for a thin annulus. The maximal velocity is then $v_{\text{m}} = \Theta_0 R \omega$. It is a standard feature of the theory of superflow that the superflow disappears when the superflow moves relative to the background wall and normal fluid with a velocity greater than a critical velocity v_c . In the usual case of uniform superflow in the annulus, this corresponds to

$$v_{\text{m}} = v_c. \tag{19.1}$$

However, in the case of present interest, where individual domains support superflows locally, but without global coherence, the flow velocity relative to the background is clearly not v_{m} . [[In supersolid-geometry-v3, I solved the hydrodynamic equations; I will use this in what follows.]] To calculate the velocity relative to the background (cell and normal solid), it is easiest to work in the rotating reference frame where the background doesn't move. We know that the hydrodynamic solution for the superflow of a circular domain in the lab frame, being irrotational, yields a flow that translates in space, but has no rotation about the center of mass. So in the rotating frame the center of mass is stationary, and there is rotation of the flow about the center of mass. In the rotating frame, this rotation goes through an *angle* that is the same in magnitude and opposite in orientation to the angle traversed in the lab frame by the domain's center of mass. If the circular domain has radius r , then, the angle of the domain's flow is $\Theta_{\text{dom}} = -\Theta_0 \sin(\omega t)$ and maximal velocity in the domain relative to the background is thus $v_{\text{dom}} = \Theta_0 r \omega$. The critical velocity occurs then at $v_{\text{dom}} = v_c$. Comparing this with Equation 19.1, we see that **the critical oscillation velocity in the disconnected case is enhanced by a factor of R/r to the connected case.**

This can be re-phrased in an illuminating way: in the connected case the breakdown of superflow happens at

$$v_m = v_c; \tag{19.2}$$

in the disconnected case it occurs as

$$v_m = (R/r)v_c. \tag{19.3}$$

Define a frequency v_m/R and a critical frequency $\Omega_c \stackrel{\text{def.}}{\equiv} v_c/r$: then we see that **the critical breakdown of superflow in the disconnected case occurs at a critical *frequency* Ω_c independent of the system geometry, rather than the usual critical *velocity*.**

Applied to the case of H_2 experiments, we see that the apparent critical velocity will be enhanced by a factor $R/r > 5.6$ relative to the true critical velocity (since the domain radius must be at most half of the annular width). Additionally considering that the $10 - 100 \mu\text{m/s}$ critical velocity in ^4He is abnormally low, **one does not expect a breakdown of flow in H_2 up to $500 \mu\text{m/s}$ within the theoretical picture we presented.**

It is also worth estimating the true supersolid fraction of the domains needed in order to generate the apparent global supersolid fraction of < 0.1 percent. It is clear that the ratio of the apparent supersolid fraction in this picture to the “true” supersolid fraction (i.e., the supersolid fraction if things were globally connected; the fraction of the system that is in the microscopic state associated with superflow) is the same as the ratio of the high-temperature feature’s period drop to the total

period drop (calculated elsewhere)². This is

$$\frac{\rho_{\text{app}}}{\rho_{\text{true}}} = \frac{1}{1 + 2 \left(\frac{R}{r}\right)^2}.$$

Because the circular domains can have radii no larger than the annular width divided by two, we then know that this ratio is smaller than 0.015; so in order to obtain the observed apparent fraction of $\sim 0.1\%$, one needs a not unreasonable domain supersolid fraction of $\sim 7\%$. Indeed, larger have been observed in ^4He by RR. Nevertheless, the NCRI decreases rapidly with decreasing domain size, so if our mechanism is correct, the domains are very near their maximum size and the “true” supersolid fraction is at least a few percent.

Actually, there are some caveats to the limits argued in the last couple paragraphs: the apparent supersolid fraction generated by this mechanism can be higher than estimates. Most importantly, the cell is constructed with radial channels and a central fill line; the majority of the feature’s magnitude can be accounted for by assuming there is a superflow in the radial channels and *nowhere* in the annulus or fill line – clearly such a flow would not disappear upon blocking the radius.³

19.9 Annealing

Our theory should make qualitative predictions for the annealing results, as well. I have not completely pursued this, but some qualitative things are worth pointing out that may be related to the experiments that observed two features: the early Rittner-Reppy experiments. The theory presented here should be essentially

²That is, the most specialized formula given, assuming that the geometry factor is one, all the clusters participate in the globally connected cluster, and that there is no supersolidity immediately upon solidification; while these are *assumptions* in the case of calculating the ratio of period drops, in calculating the apparent to “true” supersolid fraction they are simply the right parameters to do this.

³I did this estimate using Kelken Chang’s calculation in a rectangular cell.

correct, but the interpretation of these experiments is unclear; nonetheless, we see the predictions are in qualitative agreement with the experiments.

Given only the basic picture of Figure 19.1, and given that the supersolid transitions can be annealed away, our theory establishes the qualitative annealing behavior of each transition and the differences in behavior between them. Let's go through some of the types of arguments I have in mind.

19.10 Frequency dependence

In contrast with typical theories involving disorder and glassy dynamics predict a frequency dependence of the superflow fraction below the transition temperature, the Rutgers experiments — in oscillators with two simultaneous resonant frequencies — have showed a fraction independent of frequency. However, they displayed at least two intriguing features: (1) at finite T a frequency-dependent critical velocity (in contrast to usual superflow) that becomes frequency independent at low T , and (2) an intriguing shift of T_c with frequency.

Both anomalies are consistent with our model with dislocation links — or more generally, any fluctuating links. At zero temperature, the links are froze and one probes the intrinsic dynamics of the superflow. One then sees a frequency-independent critical *velocity* as expected. At higher temperatures however, the links become more easily displaced, and the finite frequency probes the dynamics of the links as well as the superflow, so one no longer observes a strictly frequency-independent velocity dependence of the superflow fraction.

Similarly analyzing the frequency dependent T_c in our model, the links dynamics give a frequency dependence to the amount of time spent near domains, and hence to the effective tunnelling rate, and consequently temperature. This physics is qualitatively captured in *usual* response properties via a Debye relaxation or

Cole-Davidson law.

It should be possible to make precise predictions within our theory regarding the magnitude of such shifts, once one commits to a specific model of the links between domains. This would provide a very direct experimentally testable prediction.

19.11 Thermodynamics: specific heat & pressure

First, let's start by reviewing the experimental status of thermodynamic measurements in ^4He . **There are two sides to the mysteries: on the one hand, there is no heat capacity feature at the supersolid transition, as there would be in a naive theory of Bose-Einstein condensation; on the other hand, there *is* some rather peculiar behavior going on at temperatures well below the supersolid transition,** with the pressure varying as $P \sim T^2$ and the specific heat either going as $C \sim T$ or having a feature interpretable in terms of an “excess specific heat.” Also, there is an absence of any pressure signature of the transition along the melting curve.

Let's start with the second mystery. The relations $P \sim T^2$ and $C \sim T$ are a generic feature of systems with a non-zero density of states at zero energy. **Systems with disorder generally will have a non-zero density of states at zero energy, so both the specific heat and pressure temperature dependencies are expected from our theory.** This is consistent with, but hardly unique to, our theory — virtually any theory involving disorder will naturally be consistent with these results.

The more interesting observation is the absence of a specific heat peak. Consider an ordinary superfluid; upon cooling through the superfluid transition, a fraction of the liquid goes from carrying the usual entropy of a liquid to carrying no entropy, since the superfluid component exists in a single quantum state. This

generates a peak feature at the superfluid transition temperature as defined via the mass decoupling/non-classical rotational inertia. However, in our phenomenology, at the supersolid transition each domain has a fully developed superflow, with only global coherence absent. More precisely, for usual superfluidity, above the transition *each particle* has a few degrees of freedom associated with it, and hence the entropy drop upon fully developing superfluidity is on the order of k_B times the number of particles; here, above the transition, the entropy is determined by noting that *each domain* will have only a few states associated with it and hence the entropy drop from this point to fully developed globally coherent superflow is on the order of k_B times the number of *domains*. **Since the number of domains is drastically less than the number of particles, there should be essentially no specific heat feature.**

19.12 ^3He doping

Yet another very puzzling feature of the ^4He experiments is that there supersolid feature occurs at *higher* temperatures as one *increases* the (fermionic) ^3He concentration from the isotopically pure sample. The supersolid fraction increases as well for small ^3He concentrations, before decreasing starting at concentrations around 100 parts per billion. Contrast this to a superfluid where such small amounts of ^3He doping have little effect, and where the first noticeable effects are a *decrease* in superfluid fraction and transition temperature.

We can very tentatively suggest a semi-quantitative explanation of these facts within our theory. Let's adopt a more specific picture than we have previously: consider that the ^3He serves as a nucleation site for the domains; this is physically plausible since the ^3He is distinct from the ^4He and has a lower mass, and hence greater zero-point fluctuations, creating pressure gradients near the ^3He and

presumably a nucleation site for disorder. We have been assuming that there is a backbone connecting these domains (perhaps a grain boundary network).

We will examine two, essentially distinct, mechanisms for the physics of the links: (1) a model of frozen links where T_c is associated with the tunneling rate through the links and (2) a model of dynamic links where T_c is associated with the binding of links to domains. Each give adequate descriptions of the data, although the latter agrees remarkably well.

19.12.1 Frozen link model

In a model with domains connected by a backbone of links, the tunneling rate between the domains to be

$$\Gamma = t_c^2 G \tag{19.4}$$

where t_c is a matrix element for tunneling from a domain onto the backbone and where G is the matrix element for propagating along the backbone from the location of one domain to another. For a two-dimensional condensed system the Green's function to propagate from a point \mathbf{x}_1 to \mathbf{x}_2 is proportional to $1/\sqrt{d}$ with the d the distance between domains

$$d \stackrel{\text{def.}}{\equiv} \sqrt{|\mathbf{x}_1 - \mathbf{x}_2|}, \tag{19.5}$$

basically from probability conservation. (Perhaps this happens even in a non-condensed system, so long as the particles propagate ballistically; i.e., the mean free path is longer than the distance between domains). Then the tunneling rate between two domains is

$$\Gamma \propto 1/\sqrt{d}. \tag{19.6}$$

For the simple model with amorphous regions nucleating near ^3He , we can obtain d from the domain ^3He density. If the ^3He is uniformly distributed, then

$d \propto n_{d\text{He}}^{1/3}$ On the other hand, it is known that ^3He likes to cluster around surfaces or possibly due to the elastic strain, grain boundaries as well. In this case, $d \propto n_{d\text{He}}^{1/3}$.

Then

$$\Gamma \propto n_{^3\text{He}}^x \quad (19.7)$$

with $n_{^3\text{He}}$ the ^3He density and $x = 1/6$ for uniform distribution of ^3He and $x = 1/4$ for uniform distribution along a two-dimensional object. The prediction is shown in Figure 19.2; we see that the prediction is quite good for both power laws, but especially for the $x = 1/4$. (Notice that the graph is a log-log plot spanning five decades of concentration!). This is an interesting conclusion as fractional power laws for temperature versus concentration are generally non-trivial.

19.12.2 Dynamic link model

In this model, the supersolid transition T_c occurs when the links (most likely dislocations) bind to the domains. One such cause could be dislocation links binding to amorphous regions, in turn nucleated on ^3He sites. Such physics is essentially equivalent to E. Kim *et al.*'s model for dislocation- ^3He interaction turned on its head: now there are more or less static domains associated with the ^3He to which vibrating dislocations are pinned. As E. Kim *et al.* argue, the transition temperature for this pinning is

$$T_c = -2E_B \left(\ln \left[\frac{x_3^2 L_{\text{IP}}^3 E_B}{4\mu b^6} \right] \right)^{-1} \quad (19.8)$$

where E_B is the binding energy of the dislocation to the domain, L_{IP} is the distance between intrinsic pinning nodes of the dislocation network, μ is the ^4He bulk shear modulus, and b is the magnitude of the dislocation's Burger's vector. Figure 19.2 shows this fit, taken from (Kim *et al.*, PRL 2008;100(6):065301); it is in good

agreement with the data. The fitting parameters also yielded physically reasonable values.

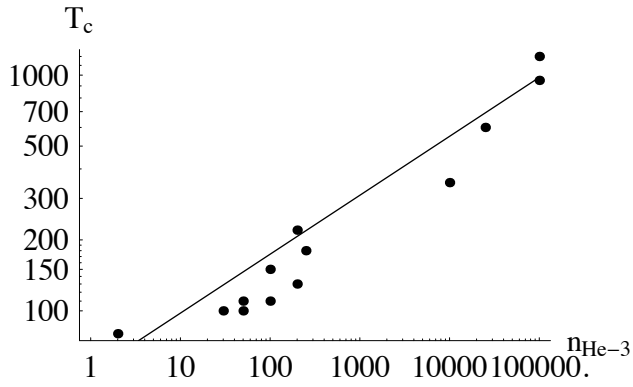
Note that while this formula was given in Kim *et al.*, that they offered no explanation of how it leads to the observed “supersolid” features. Here we note that it may signify the temperature at which local superflow becomes global, due to the binding of links that support superflow between domains.

Regardless of the mechanism considered, **the maximum temperature which the supersolidity has reached is roughly the theoretically predicted values for defects** (generally between 0.5K and 1.5K for grain boundaries, glassy regions/supercooled liquid, etc. **This is what is expected if increasing ^3He brings the domains closer together.**

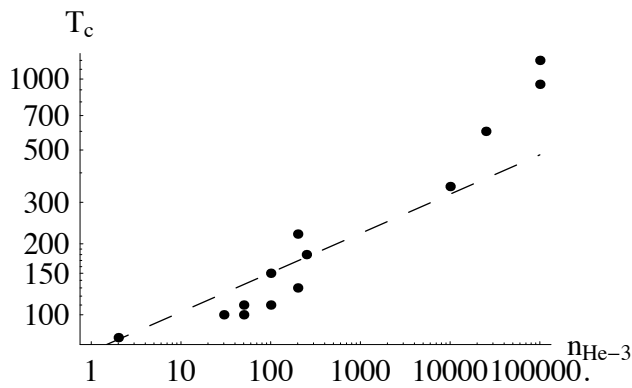
19.13 Anomalous critical velocity

The theoretical critical velocity in known supersolid region candidates (grain boundaries, glassy regions, etc.) is on the order of 1m/s. However, the experimentally observed critical velocity as measured in the torsional oscillator experiments is between 10 and 100 $\mu\text{m/s}$.

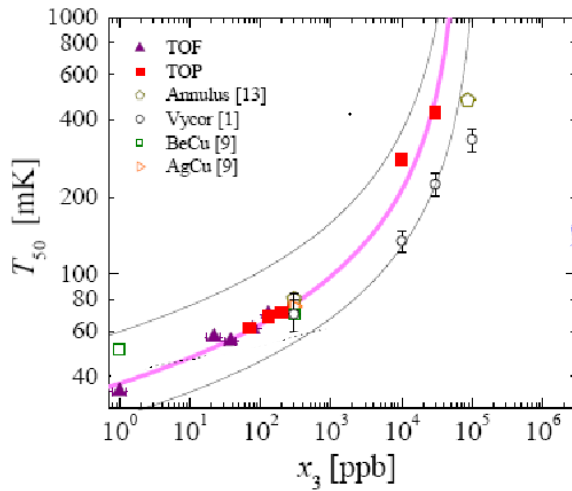
One idea consistent with our theory is that this reduction is simply due to a variety of orientations of line or plane defects that carry supercurrent. Then in order to give the appropriate velocity v_{osc} in the oscillatory frame, defect which are oriented an angle θ out of this plane will have velocity along them of $v_{\parallel} = v_{\text{osc}} / \cos \theta$, so that the superflow will breakdown at a critical $v_{\text{osc}} / \cos \theta$. Since $v_{\parallel} > v_{\text{osc}}$, the apparent critical velocity will be higher than the critical velocity for flow along the defect.



(a)



(b)



(c)

Figure 19.2: The critical temperature (in mK) versus ^3He concentration (in parts per billion) on a log-log plot. Solid line: $x = 1/4$ static links prediction (see text); Dashed line $x = 1/6$ static links prediction. (Points are copied by hand out of Moses's proposal.) The color figure is from Kim *et al.* and compares various experimental T_c 's with Eq. (19.8), our prediction for T_c (solid pink line).

19.14 dc flow

Here we try to understand some of the distinctions between different classes of dc flow experiments within our theory; in particular why do experiments observe no dc superflow?

The basic idea comes from UMass in a vivid slogan: one cannot squeeze a fluid from a stone. Basically, any externally applied pressure that would drive flow need not be transferred to the fluid carried by the defects, if the defects are strong enough to support a pressure gradient across them, to “protect” the superflow.

If this is the case, the addition of a reservoir of superfluid to the left will allow indefinite mass flow (interestingly, so would the superfluidity of the left surface) but this is not present in the Beamish experiments. Such an experiment is carried out by the UMass group, with inconclusive results.

19.15 Shear

Day and Beamish have observed a characteristic stiffening of the solid at low temperatures, with an appropriately rescaled shear modulus displaying an essentially identical feature as the torsional oscillator period drop. A proposed interpretation is that this is a dislocation pinning phenomena. Indeed, this this hints that the picture presented above that the ^3He concentration dependence of T_c comes from binding of dislocations to ^3He or amorphous regions. In this case, one expects the binding, etc. to continue even in the absence of superflow (e.g., for ^3He). This is observed in experiment is consistent with our theoryfs.

19.16 Implications for mechanism

We have interspersed two arguments: first, those regarding the most general theory and secondly, postulating more particular mechanisms. In the process, a consistent, specific mechanism emerged: local ^3He -induced 3D defects supporting superflow — perhaps superglass — that anneal away, connected by a lower dimensional — perhaps dislocation or grain boundary — backbone (in ^4He that is; the domains remain disconnected in H_2), but most of the theory is relatively independent of this.

19.17 Future directions

On both sides of the supersolid transition, each domain is supporting a finite superflow. At the low-temperature transition, enough links support superflow that a globally connected cluster forms. Moreover, it is most plausible that all of these links begin to connect at roughly the same critical temperature, given the robustness of the transition temperature to sample-to-sample variation, annealing, and sample geometry.

Such a system is, at least qualitatively, described by a Bose-Hubbard model or, equivalently, coupled Josephson junctions on an irregular graph where the vertices represent superfluid domains and the edges represent tunnel-coupling between the domains. Note that this is a Bose-Hubbard model with many particles, perhaps millions, per site, but this does not change the analysis qualitatively. For reference, Figure 19.3 sketches the phase diagrams at zero and finite temperature are provided. Figure 19.3b illustrates discusses possible effects of temperature in this model.

From such a model one might be able to predict off-resonant frequency de-

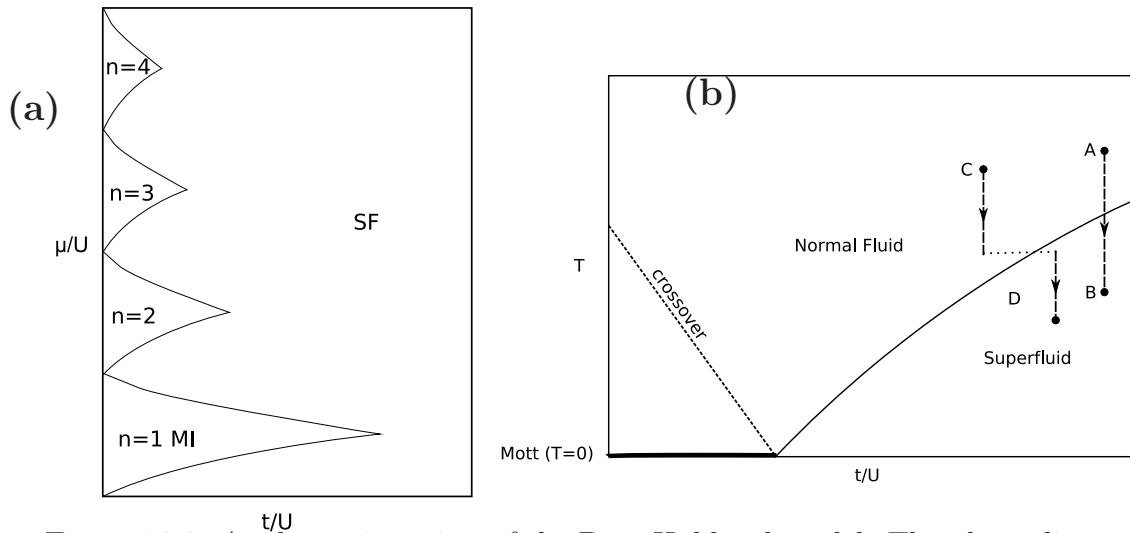


Figure 19.3: A schematic review of the Bose-Hubbard model: The phase diagrams for the Hubbard or coupled Josephson junction model. Here t is the tunneling rate, μ is the chemical potential, U is a measure of the interaction strength between particles on the same site, and T is the temperature. The “ $n = x$ ” states are the x -particle per lattice site Mott insulating states. **(a)** Zero-temperature phase diagram, consisting of Mott insulating lobes with integer fillings and a superfluid phase; presumably the supersolid phase is far from the Mott lobes. **(b)** The finite temperature phase diagram, with a normal fluid and a superfluid phase. While $A \rightarrow B$ would be a cooling path for a system directly described by the Hubbard model, our theory associate a more indirect path in t/U with the experimental cooling, as illustrated by the path $C \rightarrow D$.

pendence of the observations, and design novel experiments to more precisely test the ideas presented in these notes, for example in the multi-frequency oscillator experiments.

19.18 Discussion

Implications for mechanism.—We have interspersed two arguments: first, those regarding the most general theory and secondly, postulating more particular mechanisms. In the process, a consistent, specific mechanism emerged: local ^3He -induced 3D defects supporting superflow — perhaps superglass — that anneal away, connected by a lower dimensional — perhaps dislocation or grain boundary — backbone (in ^4He that is; the domains remain disconnected in H_2), but most of the

theory is relatively independent of this.

Future directions.—On both sides of the supersolid transition, each domain is supporting a finite superflow. At the low-temperature transition, enough links support superflow that a globally connected cluster forms. Moreover, it is most plausible that all of these links begin to connect at roughly the same critical temperature, given the robustness of the transition temperature to sample-to-sample variation, annealing, and sample geometry.

Such a system is, at least qualitatively, described by a Bose-Hubbard model or, equivalently, coupled Josephson junctions on an irregular graph where the vertices represent superfluid domains and the edges represent tunnel-coupling between the domains. Note that this is a Bose-Hubbard model with many particles, perhaps millions, per site, but this does not change the analysis qualitatively. For reference, Figure 19.3 sketches the phase diagrams at zero and finite temperature are provided. Figure 19.3b illustrates discusses possible effects of temperature in this model.

From such a model one might be able to predict off-resonant frequency dependence of the observations, and design novel experiments to more precisely test the ideas presented in these notes.

Conclusions.—Despite its phenomenological nature, we see our picture clears up a number of experimental mysteries and, if verified, it offers a method of examining microscopic parameters. Through this last feature, it may shed light on the *microscopic* mechanism of superflow, and a plausible suggestion for the mechanism has been given here in terms of amorphous regions connected by a grain boundary or surface “backbone.”

KH acknowledges stimulating discussions with S. Basu, J. Beamish, K. Shirahama, N. Prokof'ev, and J. Sethna. We are especially grateful for discussions

and receiving (at the time) unpublished results from A. Rittner, J. Reppy, and M. Chan.

APPENDIX A

RELATING SCATTERING AMPLITUDES AND T -MATRIX

I will derive how the scattering amplitude is related to the T -matrix. First, I will derive the equation satisfied by the scattered amplitude, and show that this is the same as the Lippmann-Schwinger equation satisfied by the T -matrix. This allows me to relate the scattering length a to the T matrix at zero momentum.

To see that the scattering amplitude and the T -matrix satisfy this equation, we use the definition of the scattering amplitude along with the fact that ψ satisfies the Schrödinger equation. Since in momentum space ψ satisfies

$$\frac{k^2}{m}\psi(\mathbf{k}) + \frac{1}{\Omega} \sum_{\mathbf{k}'} V(\mathbf{k} - \mathbf{k}')\psi(\mathbf{k}') = E\psi(\mathbf{k}). \quad (\text{A.1})$$

with Ω the volume of space. For our potential,

$$\frac{k^2}{m}\psi(\mathbf{k}) + \frac{4\pi a}{m\Omega} \sum_{\mathbf{k}'} \psi(\mathbf{k}') = E\psi(\mathbf{k}). \quad (\text{A.2})$$

The scattering wavefunction for incoming wavevector \mathbf{k} is defined so that

$$\psi_{\mathbf{k}}(\mathbf{k}') = \psi_{0,\mathbf{k}}(\mathbf{k}') + \psi_{\text{scat},\mathbf{k}}(\mathbf{k}') \quad (\text{A.3})$$

where $\psi_{0,\mathbf{k}}$ is the wavevector \mathbf{k} solution to the Schrödinger equation for $a = 0$.

Thus,

$$\begin{aligned} \frac{k'^2}{m} [\psi_{0,\mathbf{k}}(\mathbf{k}') + \psi_{\mathbf{k},\text{scat}}(\mathbf{k}')] + \sum_{\mathbf{k}''} V(\mathbf{k}'' - \mathbf{k}') (\psi_{0,\mathbf{k}}(\mathbf{k}') + \psi_{\mathbf{k},\text{scat}}(\mathbf{k}')) \\ = \frac{k^2}{m} (\psi_{0,\mathbf{k}}(\mathbf{k}') + \psi_{\mathbf{k},\text{scat}}(\mathbf{k}')) \end{aligned} \quad (\text{A.4})$$

so since $\psi_{0,\mathbf{k}}(\mathbf{k}') = \delta_{\mathbf{k},\mathbf{k}'}$, we obtain

$$\left[\frac{k^2 - k'^2}{m} \right] \psi_{\mathbf{k},\text{scat}}(\mathbf{k}') - \sum_{\mathbf{k}''} V(\mathbf{k}'' - \mathbf{k}') \psi_{\mathbf{k},\text{scat}}(\mathbf{k}'') = V(\mathbf{k} - \mathbf{k}'). \quad (\text{A.5})$$

The Lippmann-Schwinger equation, Eq. (2.28), was derived in Section 2.2.1; the “on-shell” part with $E = k^2/m$ is

$$\begin{aligned} T(\mathbf{k}, \mathbf{k}') &= V(\mathbf{k} - \mathbf{k}') \\ &+ \frac{1}{\Omega} \sum_{\mathbf{k}''} V(\mathbf{k}' - \mathbf{k}'') ((k^2 - k''^2)/m + i\delta)^{-1} T(\mathbf{k}, \mathbf{k}', E). \end{aligned} \quad (\text{A.6})$$

Comparing Eqs. (A.5) and (A.6) we see the

$$T(\mathbf{k}, \mathbf{k}') = \left(\frac{k^2 - k'^2}{m} \right) \psi_{\mathbf{k},\text{scat}}(\mathbf{k}'). \quad (\text{A.7})$$

This establishes the desired relationship between T and ψ_{scat} .

Finally, I relate the low-momentum behavior of the T -matrix to the scattering length. At $k = 0$, Fourier transforming Eq. (A.7) with respect to \mathbf{k}' gives

$$\psi_{\mathbf{k}=0,\text{scat}} = -\frac{mT(0,0)}{4\pi r}. \quad (\text{A.8})$$

In the current notation, the scattering length was defined by $\psi_{\mathbf{k}=0,\text{scat}} = -a/r$, so we see that

$$T(0,0) = 4\pi a/m. \quad (\text{A.9})$$

This is the desired relationship between the scattering length and the T -matrix.

APPENDIX B

WARD IDENTITIES IN THE RF SPECTRUM FOR THE BOSE-HUBBARD MODEL: VERTEX CORRECTIONS, SYMMETRIES, AND CONSERVATION LAWS.

B.1 Abstract

I derive a symmetry inherited relationship between the vertex function and Green's function, for rf spectra of the Bose-Hubbard model. This is somewhat non-trivial in this context. We start with Ward identities enforcing this symmetry, and then construct an approximation which satisfies these Ward identities by writing the rf spectra in terms of single particle Green's functions plus vertex corrections.

B.2 Introduction and motivation

We have previously calculated the rf spectra of the Bose-Hubbard model using a Lehmann representation method — this assumes that the rf spectra excites single quasiparticle-quasihole excitations. However, this approach fails to satisfy the symmetries with the two channel's scattering lengths are equal, due to the neglect of interactions between the excited quasiparticle and quasihole (vertex corrections).

Here we derive an approximation which remedies this problem.

The Ward identities/vertex corrections derived are applicable regardless of the starting point of the approximation used to obtain the single particle Green's functions: for example, we may use the Lehmann representation introduced in our other document, a full mean field Green's function, or an RPA green's function which includes quadratic fluctuations. This will be carried out in other notes.

B.3 Homogeneous gas: no lattice

B.3.1 Setup

We start with the Hamiltonian for our system, which consists of a gas with two hyperfine states $\alpha = 1, 2$. The gas will initially be entirely in the $\alpha = 1$ state.

First we define $\psi_\alpha(\mathbf{r})$ to be the boson annihilation operator at position \mathbf{r} in state α , and notate

$$\psi(\mathbf{r}) = \begin{pmatrix} \psi_1(\mathbf{r}) \\ \psi_2(\mathbf{r}) \end{pmatrix}. \quad (\text{B.1})$$

Then the Hamiltonian is

$$H = H_1 + H_2, \quad (\text{B.2})$$

with H_1 and H_2 defined immediately below.

The single particle Hamiltonian H_1 is given by

$$H_1 = \sum_\alpha \int d^3r \psi^\dagger(\mathbf{r}) \left(- \sum_\alpha \frac{D_\alpha^2}{2m} + V(\mathbf{r}) \right) \psi(\mathbf{r}) \quad (\text{B.3})$$

where the sum over α runs over the three spatial components with

$$D_\alpha \equiv \frac{\partial}{\partial r_\alpha} - ig\sigma \cdot \mathbf{A}_\alpha(\mathbf{r}, t). \quad (\text{B.4})$$

Here σ is the vector of Pauli matrices,

$$\sigma = \begin{pmatrix} \sigma^{(x)} \\ \sigma^{(y)} \\ \sigma^{(z)} \end{pmatrix} \quad (\text{B.5})$$

with

$$\sigma^{(x)} = \begin{pmatrix} 0 & 1 \\ 1 & 0 \end{pmatrix} \quad (\text{B.6})$$

$$\sigma^{(y)} = \begin{pmatrix} 0 & -i \\ i & 0 \end{pmatrix} \quad (\text{B.7})$$

$$\sigma^{(z)} = \begin{pmatrix} 1 & 0 \\ 0 & -1 \end{pmatrix}. \quad (\text{B.8})$$

We use the superscript notation for the 3-vector direction determining the Pauli matrix, so we reserve subscripts for the $SU(2)$ indices. In the physical scenario of interest, the gauge field is $\mathbf{A}_\alpha = 0$; however, we include it as our formal derivation of the Ward identities requires it.

The interaction Hamiltonian H_2 is given by

$$H_2 = \sum_{\alpha,\beta} \frac{U_{\alpha,\beta}}{2} \int d^3r \psi_\alpha^\dagger(\mathbf{r}) \psi_\beta^\dagger(\mathbf{r}) \psi_\beta(\mathbf{r}) \psi_\alpha(\mathbf{r}) \quad (\text{B.9})$$

and

$$U_{\alpha,\beta} = \frac{4\pi\hbar^2}{m} a_{\alpha,\beta} \quad (\text{B.10})$$

where $a_{\alpha,\beta}$ is the 3D scattering length. Note that the covariant derivative D_α is a 2×2 matrix operator.

When the interaction coefficients are equal, that is $U_{11} = U_{12} = U_{21} = U_{22}$, the Hamiltonian is symmetric under a global $SU(2)$ transformation $e^{i\sigma \cdot \Lambda}$ where Λ is

an arbitrary 3-vector. As a consequence of this symmetry, the rf spectra will be a single delta function peaked at the vacuum energy splitting Δ .

We would like to ensure that our approximations satisfy this symmetry requirement (which is connected to conservation laws), and this is the bulk of what is explored in these notes.

B.3.2 Showing covariance of kinetic energy

In order to ensure our approximations satisfy the $SU(2)$ invariance requirement, it will turn out to be necessary to first promote the global $SU(2)$ transformation to a local gauge transformation. The field transformation is

$$\psi(\mathbf{r}, t) \rightarrow \psi'(\mathbf{r}, t) = e^{i\sigma \cdot \mathbf{\Lambda}(\mathbf{r}, t)} \psi(\mathbf{r}, t), \quad (\text{B.11})$$

and in this section we calculate the corresponding transformation of the $SU(2)$ gauge field that ensures the covariant derivative is, in fact, covariant under the following $SU(2)$ gauge transformation.

Rather than working with the general gauge transformation, it will suffice to work with infinitesimal gauge transformations $\mathbf{\Lambda}$. Then the field transformation law is then

$$\psi(\mathbf{r}, t) \rightarrow \psi'(\mathbf{r}, t) = [1 + i\sigma \cdot \mathbf{\Lambda}(\mathbf{r}, t)] \psi(\mathbf{r}, t) + O(\Lambda^2). \quad (\text{B.12})$$

The covariant derivative then transforms as

$$D_\alpha \rightarrow D'_\alpha = \frac{\partial}{\partial r_\alpha} - ig\sigma \cdot \mathbf{A}'_\alpha(\mathbf{r}, t), \quad (\text{B.13})$$

defining \mathbf{A}'_α , which we now compute. The covariance of the derivative is determined by requiring

$$D'_\alpha = e^{i\sigma \cdot \mathbf{\Lambda}(\mathbf{r}, t)} D_\alpha e^{-i\sigma \cdot \mathbf{\Lambda}(\mathbf{r}, t)}, \quad (\text{B.14})$$

as this implies that

$$[\psi'(\mathbf{r}, t)]^\dagger (D'_\alpha)^2 \psi'(\mathbf{r}, t) = \psi^\dagger(\mathbf{r}, t) D_\alpha^2 \psi(\mathbf{r}, t). \quad (\text{B.15})$$

Computing the right hand side of Eq. (B.14) gives

$$D'_\alpha = D_\alpha + i[\sigma \cdot \mathbf{\Lambda}(\mathbf{r}, t), D_\alpha] \quad (\text{B.16})$$

working here, and henceforth, to the lowest appropriate order in $\mathbf{\Lambda}$. We compute this commutator by acting with it on a test function:

$$i[\sigma \cdot \mathbf{\Lambda}(\mathbf{r}, t), D_\alpha] f(\mathbf{r}, t) = i \left[\sigma \cdot \mathbf{\Lambda}(\mathbf{r}, t), \left(\frac{\partial}{\partial r_\alpha} - ig\sigma \cdot \mathbf{A}_\alpha(\mathbf{r}, t) \right) \right] f(\mathbf{r}, t) \quad (\text{B.17})$$

$$= i \left\{ \left[\sigma \cdot \mathbf{\Lambda}(\mathbf{r}, t), \frac{\partial}{\partial r_\alpha} \right] - ig[\sigma \cdot \mathbf{\Lambda}(\mathbf{r}, t), \sigma \cdot \mathbf{A}_\alpha(\mathbf{r}, t)] \right\} f(\mathbf{r}, t) \quad (\text{B.18})$$

The first term is

$$\left[\sigma \cdot \mathbf{\Lambda}(\mathbf{r}, t), \frac{\partial}{\partial r_\alpha} \right] f(\mathbf{r}, t) = \left(\sigma \cdot \mathbf{\Lambda}(\mathbf{r}, t) \frac{\partial f(\mathbf{r}, t)}{\partial r_\alpha} - \sigma \cdot \frac{\partial (\mathbf{\Lambda}(\mathbf{r}, t) f(\mathbf{r}, t))}{\partial r_\alpha} \right) \quad (\text{B.19})$$

$$= -\sigma \cdot \frac{\partial \mathbf{\Lambda}(\mathbf{r}, t)}{\partial r_\alpha} f(\mathbf{r}, t) \quad (\text{B.20})$$

The second term of Eq. (B.18) is simplified by noticing that

$$[\sigma \cdot \mathbf{v}, \sigma \cdot \mathbf{w}] = 2i\sigma \cdot (\mathbf{v} \times \mathbf{w}) \quad (\text{B.21})$$

and consequently the commutator in Eq. (B.18) is

$$[\sigma \cdot \mathbf{\Lambda}(\mathbf{r}, t), \sigma \cdot \mathbf{A}_\alpha(\mathbf{r}, t)] = 2i\sigma \cdot (\mathbf{\Lambda}(\mathbf{r}, t) \times \mathbf{A}_\alpha(\mathbf{r}, t)). \quad (\text{B.22})$$

Putting these together, Eq. (B.18) yields

$$D'_\alpha = D_\alpha - i\sigma \cdot \left(\frac{\partial \mathbf{\Lambda}}{\partial r_\alpha} - 2g\mathbf{\Lambda}(\mathbf{r}, t) \times \mathbf{A}_\alpha(\mathbf{r}, t) \right) \quad (\text{B.23})$$

Thus we see that to maintain covariance, upon gauge transforming the atom field ψ by Eq. (B.11) the $SU(2)$ gauge field \mathbf{A}_α must transform, for infinitesimal $\mathbf{\Lambda}$, as

$$\mathbf{A}_\alpha \rightarrow \mathbf{A}'_\alpha = \mathbf{A}_\alpha + \frac{1}{g} \frac{\partial \mathbf{\Lambda}}{\partial r_\alpha} - 2\mathbf{\Lambda}(\mathbf{r}, t) \times \mathbf{A}_\alpha(\mathbf{r}, t). \quad (\text{B.24})$$

B.3.3 Partition function in path integral representation, including sources

To derive the Ward identity, we will introduce the partition function for our system, and consider the consequences of its symmetries. We include source terms in the action, so that we may obtain Green's functions by differentiating the partition function with respect to the sources. In the bosonic coherent state path integral description of the system, using the usual notation for the integrals and integration measure, the partition function Z is defined as

$$Z[J, J^*, \mathbf{W}_\mu] = \int \mathcal{D}\psi \mathcal{D}\mathbf{A}_\alpha e^{-(S[\psi, \psi^*, \mathbf{A}_\alpha] + S_J[J, J^*, \mathbf{W}_\mu; \psi, \psi^*, \mathbf{A}_\alpha])/\hbar}. \quad (\text{B.25})$$

with the (imaginary time) action S defined by

$$\begin{aligned} S[\psi, \psi^*, \mathbf{A}_\alpha] &= \int_0^\beta d\tau \left\{ \int d^3r \left[\psi^\dagger(\mathbf{r}, \tau) \left(\hbar \frac{\partial}{\partial \tau} - \mu \right) \psi(\mathbf{r}, \tau) \right] + H[\psi, \psi^*, \mathbf{A}_\alpha] \right\} \end{aligned} \quad (\text{B.26})$$

Note that $\mu = \begin{pmatrix} \mu_1 & 0 \\ 0 & \mu_2 \end{pmatrix}$ is a 2×2 matrix here, and the source action S_J defined as

$$\begin{aligned} S_J[J, J^*, \mathbf{W}_\mu; \psi, \psi^*, \mathbf{A}_\alpha] &= \int_0^\beta d\tau \int d^3r \left[J^*(\mathbf{r}, t) \psi(\mathbf{r}, \tau) + \psi^*(\mathbf{r}, \tau) J(\mathbf{r}, \tau) + \sum_\alpha \mathbf{W}_\alpha \cdot \mathbf{A}_\alpha \right] \end{aligned} \quad (\text{B.27})$$

Note that in the path integral, we have allowed \mathbf{A}_α to fluctuate, which it doesn't in the original problem.

B.3.4 Partition function under $SU(2)$ transformations

We would like to know how the partition function transforms under $SU(2)$ gauge transformations. There are three relevant parts: (1) the integration measure

$\mathcal{D}\psi\mathcal{D}\mathbf{A}_\alpha$, (2) the system action S , and (3) and the source S_J .

Integration measure

Atom field integration measure.—The integration measure $\mathcal{D}\psi$ is trivially invariant under $SU(2)$ gauge transformations, since the field transformation is unitary. A little more explicitly, note that $\mathcal{D}\psi$ is defined as

$$\mathcal{D}\psi = \prod_{\mathbf{r},\tau} [d\psi_{\mathbf{r},\tau}^* d\psi_{\mathbf{r},\tau}]. \quad (\text{B.28})$$

This is okay formally, though from a mathematical standpoint it might be more rigorous to define the equivalent measure in Fourier space. Then under the field transformation $\psi'(\mathbf{r}, \tau) = e^{i\sigma\cdot\mathbf{\Lambda}(\mathbf{r},\tau)}\psi(\mathbf{r}, \tau)$ we have

$$\mathcal{D}\psi \rightarrow \mathcal{D}\psi' = \prod_{\mathbf{r},\tau} [d\psi_{\mathbf{r},\tau}^* e^{-i\sigma\cdot\mathbf{\Lambda}(\mathbf{r},\tau)} e^{i\sigma\cdot\mathbf{\Lambda}(\mathbf{r},\tau)} d\psi_{\mathbf{r},\tau}] \quad (\text{B.29})$$

$$= \prod_{\mathbf{r},\tau} [d\psi_{\mathbf{r},\tau}^* d\psi_{\mathbf{r},\tau}] \quad (\text{B.30})$$

$$= \mathcal{D}\psi, \quad (\text{B.31})$$

showing that the field integration measure $\mathcal{D}\psi$ is invariant under $SU(2)$ transformations.

Gauge field integration measure.—We only know and care about the gauge field's transformations under infinitesimal transformations, we will only consider the integration measure transformations to $O(\mathbf{\Lambda})$. Explicitly, the integration measure

$$\mathcal{D}\mathbf{A}_\alpha = \prod_{\mathbf{r},\tau,\alpha} [dA_\alpha(\mathbf{r}, \tau)] \quad (\text{B.32})$$

with $d\mathbf{v}$ shorthand for $\prod_j dv_j$ when \mathbf{v} is a vector and v_j are the components of \mathbf{v} . (Again it might mathematically be more proper to work in Fourier space, but this should suffice for our purposes.) Recapitulating Eq. (B.24),

$$\mathbf{A}_\alpha \rightarrow \mathbf{A}'_\alpha = \mathbf{A}_\alpha + \frac{1}{g} \frac{\partial \mathbf{\Lambda}}{\partial r_\alpha} - 2\mathbf{\Lambda}(\mathbf{r}, t) \times \mathbf{A}_\alpha(\mathbf{r}, t), \quad (\text{B.33})$$

Intuitively, \mathbf{A}_α is shifted by the $\frac{1}{g} \frac{\partial \mathbf{A}}{\partial r_\alpha}$ term, and since $\mathbf{\Lambda} \times \mathbf{A}_\alpha$ is perpendicular to \mathbf{A}_α , it is an infinitesimal rotation of \mathbf{A} , and thus the integration measure will be invariant.

Formally, we can show this a little more explicitly. It is helpful to rewrite the transformation of Eq. (B.33) so that \mathbf{A}'_α is an operator acting on \mathbf{A}_α . This is found by representing the cross product in components, and yields

$$\mathbf{A}'_\alpha(\mathbf{r}, \tau) = \frac{1}{g} \frac{\partial \mathbf{A}(\mathbf{r}, \tau)}{\partial r_\alpha} + (1 + 2\mathcal{M})\mathbf{A}_\alpha(\mathbf{r}, \tau). \quad (\text{B.34})$$

with

$$\mathcal{M} \equiv \begin{pmatrix} 0 & \Lambda_z & -\Lambda_y \\ -\Lambda_z & 0 & \Lambda_x \\ \Lambda_y & -\Lambda_x & 0 \end{pmatrix}. \quad (\text{B.35})$$

Then, since $\frac{1}{g} \frac{\partial \mathbf{A}(\mathbf{r}, \tau)}{\partial r_\alpha}$ is a constant shift for each component integrated over (and we are integrating over all space, and $1 + 2\mathcal{M}$ is a linear transformation, each term in the integration measure of Eq. (B.32) transforms as

$$d\mathbf{A}_\alpha(\mathbf{r}, \tau) \rightarrow d[\mathbf{A}'_\alpha(\mathbf{r}, \tau)] = \frac{1}{|\det(1 + 2\mathcal{M})|} d\mathbf{A}_\alpha(\mathbf{r}, \tau). \quad (\text{B.36})$$

The determinant of $(1 + 2\mathcal{M})$ is

$$\det(1 + 2\mathcal{M}) = 1 + 4\Lambda^2 + O(\Lambda^4), \quad (\text{B.37})$$

so to the $O(\Lambda)$, the determinant is 1 and

$$d\mathbf{A}_\alpha(\mathbf{r}, \tau) \rightarrow d[\mathbf{A}'_\alpha(\mathbf{r}, \tau)] = d\mathbf{A}_\alpha(\mathbf{r}, \tau). \quad (\text{B.38})$$

Hence, the integration measure for the gauge field \mathbf{A}_α is invariant under $SU(2)$ gauge transformations, as claimed.

System action

Likewise, the system action $S[\psi, \psi^*, \mathbf{A}_\alpha]$ is invariant under $SU(2)$ gauge transformations. To see this note that the chemical potential term is manifestly invariant, and we showed the kinetic energy is invariant in Section B.3.2. All that remains is the interaction energy. Defining $n_\alpha \equiv \psi_\alpha^\dagger \psi_\alpha$ and $n \equiv \sum_\alpha n_\alpha$, the interaction term is

$$\sum_{\alpha, \beta} U_{\alpha, \beta} \psi_\alpha^\dagger \psi_\beta^\dagger \psi_\beta \psi_\alpha = \sum_{\alpha, \beta} U_{\alpha, \beta} \psi_\alpha^\dagger n_\beta \psi_\alpha \quad (\text{B.39})$$

$$= \sum_{\alpha, \beta} U_{\alpha, \beta} n_\alpha (n_\beta - \delta_{\alpha\beta}) \quad (\text{B.40})$$

$$= U \left[\sum_{\alpha, \beta} n_\alpha n_\beta - \sum_\alpha n_\alpha \right] \quad (\text{B.41})$$

$$= Un(n-1). \quad (\text{B.42})$$

Source action

The source action $S_J[J, J^*, \mathbf{W}_\alpha; \psi, \psi^*, \mathbf{A}_\alpha]$ varies under $SU(2)$ transformations, unlike the system action S and the integration measure $\mathcal{D}\psi \mathcal{D}\mathbf{A}$.

The source action S_J transforms as

$$S_J[J, J^*, \mathbf{W}_\alpha; \psi, \psi^*, \mathbf{A}_\alpha] \rightarrow S'_J[J, J^*, \mathbf{W}_\alpha; \psi, \psi^*, \mathbf{A}_\alpha] = S_J + \delta S_J \quad (\text{B.43})$$

with

$$\begin{aligned} \delta S_J = & \int_0^\beta d\tau \int d^3r \left\{ iJ^*(\mathbf{r}, t) \sigma \cdot \boldsymbol{\Lambda}(\mathbf{r}, \tau) \psi(\mathbf{r}, \tau) - i\psi^*(\mathbf{r}, \tau) \sigma \cdot \boldsymbol{\Lambda}(\mathbf{r}, \tau) J(\mathbf{r}, \tau) \right. \\ & \left. + \sum_\alpha \mathbf{W}_\alpha(\mathbf{r}, \tau) \cdot \left[\frac{1}{g} \frac{\partial \boldsymbol{\Lambda}(\mathbf{r}, \tau)}{\partial r_\alpha} - 2\boldsymbol{\Lambda}(\mathbf{r}, t) \times \mathbf{A}_\alpha(\mathbf{r}, t) \right] \right\}, \quad (\text{B.44}) \end{aligned}$$

which follows immediately from expanding $\psi'(\mathbf{r}, \tau) \doteq [1 + i\sigma \cdot \boldsymbol{\Lambda}(\mathbf{r}, \tau)] \psi(\mathbf{r}, \tau)$ and substituting \mathbf{A}_α 's transformation in the definition of S_J in Eq. (B.27).

B.3.5 Consequences of $SU(2)$ invariance of the partition function

The partition function is invariant under $SU(2)$ gauge transformations of the fields ψ and \mathbf{A}_α . This follows by considering a path integral of an arbitrary functional of the fields $f[\psi, \psi^*, \mathbf{A}_\alpha]$:

$$\mathcal{I} = \int \mathcal{D}\psi \mathcal{D}\mathbf{A}_\alpha f[\psi, \psi^*, \mathbf{A}_\alpha]. \quad (\text{B.45})$$

Consider the behavior under an $SU(2)$ gauge transformation of the integrand, f ,

$$\begin{aligned} & \int \mathcal{D}\psi \mathcal{D}\mathbf{A}_\alpha f \left[e^{i\sigma \cdot \Lambda} \psi, \psi^* e^{-i\sigma \cdot \Lambda}, \mathbf{A}_\alpha + \frac{1}{g} \frac{\partial \Lambda}{\partial r_\alpha} - 2\Lambda \times \mathbf{A}_\alpha \right] \\ &= \int \mathcal{D}(e^{-i\sigma \cdot \Lambda} \psi') \mathcal{D} \left[\mathbf{A}'_\alpha - \frac{1}{g} \frac{\partial \Lambda}{\partial r_\alpha} + 2\Lambda \times \mathbf{A}_\alpha \right] f[\psi', (\psi')^*, \mathbf{A}'_\alpha]. \end{aligned} \quad (\text{B.46})$$

Now, we can rename the integration variables ψ' to ψ and \mathbf{A}'_α to \mathbf{A}_α , and recognize the integration measure as the that after a gauge transformation generated by $-\Lambda$, which is invariant under this transformation, by our argument in Section B.3.4. Hence, since the (suppressed) integration limits are also invariant under the $SU(2)$ transformation. Consequently, Eq. (B.46) shows that

$$\begin{aligned} & \int \mathcal{D}\psi \mathcal{D}\mathbf{A}_\alpha f \left[e^{i\sigma \cdot \Lambda} \psi, \psi^* e^{-i\sigma \cdot \Lambda}, \mathbf{A}_\alpha + \frac{1}{g} \frac{\partial \Lambda}{\partial r_\alpha} - 2\Lambda \times \mathbf{A}_\alpha \right] \\ &= \int \mathcal{D}\psi \mathcal{D}\mathbf{A}_\alpha f[\psi, \psi^*, \mathbf{A}_\alpha], \end{aligned} \quad (\text{B.47})$$

and applying this to the path integral expression for the partition function, shows that the partition function is invariant under $SU(2)$ gauge transformations:

$$Z' = Z. \quad (\text{B.48})$$

As a consequence, certain expectation values are constrained to satisfy a relation with the source fields; we derive this relation now. This relation will follow

by computing Z' , the partition function after $SU(2)$ gauge transforming the integrand, in a second way by Taylor expanding the transformed partition function Z' for infinitesimal gauge transformations. Using the transformations of the actions and integration measures derived above, we find

$$Z'[J, J^*, \mathbf{W}_\mu] = \int \mathcal{D}\psi \mathcal{D}\mathbf{A}_\alpha e^{-(S+S_J+\delta S_J)/\hbar} \quad (\text{B.49})$$

$$= \int \mathcal{D}\psi \mathcal{D}\mathbf{A}_\alpha e^{-(S+S_J)/\hbar} \left[1 - \frac{\delta S_J}{\hbar} \right] \quad (\text{B.50})$$

$$= Z \left[1 - \frac{\langle \delta S_J \rangle}{\hbar} \right], \quad (\text{B.51})$$

where we have defined

$$\langle \mathcal{O} \rangle \equiv \frac{1}{Z} \int \mathcal{D}\psi \mathcal{D}\mathbf{A}_\alpha \mathcal{O}. \quad (\text{B.52})$$

Eq. (B.51) that in order to satisfy the identity of Eq. (B.48), we must have

$$\langle \delta S_J \rangle = 0. \quad (\text{B.53})$$

Inserting δS_J from Eq. (B.44), this gives

$$0 = \int_0^\beta d\tau \int d^3r \left\{ iJ^*(\mathbf{r}, t) \boldsymbol{\sigma} \cdot \boldsymbol{\Lambda}(\mathbf{r}, \tau) \phi(\mathbf{r}, \tau) - i\phi^*(\mathbf{r}, \tau) \boldsymbol{\sigma} \cdot \boldsymbol{\Lambda}(\mathbf{r}, \tau) J(\mathbf{r}, \tau) + \sum_\alpha \mathbf{W}_\alpha(\mathbf{r}, \tau) \cdot \left[\frac{1}{g} \frac{\partial \boldsymbol{\Lambda}(\mathbf{r}, \tau)}{\partial r_\alpha} - 2\boldsymbol{\Lambda}(\mathbf{r}, t) \times \mathcal{A}_\alpha(\mathbf{r}, t) \right] \right\} \quad (\text{B.54})$$

where we have defined

$$\phi(\mathbf{r}, \tau) \equiv \langle \psi(\mathbf{r}, \tau) \rangle, \quad (\text{B.55})$$

$$\mathcal{A}_\alpha(\mathbf{r}, \tau) \equiv \langle \mathbf{A}_\alpha(\mathbf{r}, \tau) \rangle. \quad (\text{B.56})$$

Now, we would like to eliminate the integrals in Eq. (B.54), by choosing the $\boldsymbol{\Lambda}(\mathbf{r}, \tau)$ to be delta functions, and to pick out the a 'th component of the equation. To facilitate this, we handle differentiating the delta function by integrating by

parts and dropping the boundary term:

$$\begin{aligned} & \int_0^\beta d\tau \int d^3r \mathbf{W}_\alpha(\mathbf{r}, \tau) \cdot \left(\frac{\partial \boldsymbol{\Lambda}(\mathbf{r}, \tau)}{\partial r_\alpha} \right) \\ &= - \int_0^\beta d\tau \int d^3r \left(\frac{\partial \mathbf{W}_\alpha(\mathbf{r}, \tau)}{\partial r_\alpha} \right) \cdot \boldsymbol{\Lambda}(\mathbf{r}, \tau). \end{aligned} \quad (\text{B.57})$$

Furthermore, because we would like to factor our expression into $\boldsymbol{\Lambda} \cdot (\dots)$, we rewrite the cross product with the identity

$$\mathbf{W}_\alpha \cdot (\boldsymbol{\Lambda} \times \mathcal{A}_\alpha) = \boldsymbol{\Lambda} \cdot (\mathcal{A}_\alpha \times \mathbf{W}_\alpha). \quad (\text{B.58})$$

Then using $\boldsymbol{\Lambda}(\mathbf{r}, \tau) = \hat{a} \delta(\mathbf{r}) \delta(\tau)$, Eq. (B.54) is

$$\begin{aligned} 0 &= iJ^*(\mathbf{r}, t) \sigma^{(a)} \phi(\mathbf{r}, \tau) - i\phi^*(\mathbf{r}, \tau) \sigma^{(a)} J(\mathbf{r}, \tau) \\ &\quad - \sum_\alpha \left[\frac{1}{g} \frac{\partial W_{\alpha,a}(\mathbf{r}, \tau)}{\partial r_\alpha} + 2 (\mathcal{A}_\alpha(\mathbf{r}, t) \times \mathbf{W}_\alpha(\mathbf{r}, \tau))_a \right]. \end{aligned} \quad (\text{B.59})$$

This equation is the consequence of the $SU(2)$ symmetry relating expectation values of observables, ϕ and \mathcal{A} , in the presence of sources, J and \mathbf{W}_μ .

B.3.6 Connected Green's functions and effective action

We now turn to using the relation of expectation values implied by Eq (B.59) into a relation between the exact Green's functions and one-particle irreducible vertex function which we need for the rf spectra calculation. First, we need to introduce the connected Green's functions' generating functional and the effective action, which we carry out in this section.

Connected Green's functions generating function

We define F implicitly by $Z = e^{-F/\hbar}$ so that

$$F = -\hbar \log Z. \quad (\text{B.60})$$

Then by the usual arguments, since Z is the generating function of Green's functions — both disconnected and connected — it follows that W is the generating function of connected Green's functions.

It is worth pointing out the simplest example of this:

$$\frac{\delta F}{\delta J(\mathbf{r}, \tau)} = -\frac{\hbar}{Z} \frac{\delta Z}{\delta J(\mathbf{r}, \tau)} \quad (\text{B.61})$$

$$= -\frac{\hbar}{Z} \int \mathcal{D}\psi \mathcal{D}\mathbf{A}_\alpha \left(-\frac{\psi^*(\mathbf{r}, \tau)}{\hbar} \right) e^{-(S+S_J)/\hbar} \quad (\text{B.62})$$

$$= \langle \psi^*(\mathbf{r}, \tau) \rangle \quad (\text{B.63})$$

$$= \phi^*(\mathbf{r}, \tau), \quad (\text{B.64})$$

where the functional derivative of Z follows immediately from Eqs. (B.25) and (B.27). Similarly

$$\frac{\delta F}{\delta J^*(\mathbf{r}, \tau)} = \phi^*(\mathbf{r}, \tau), \quad (\text{B.65})$$

$$\frac{\delta F}{\delta \mathbf{W}_\alpha(\mathbf{r}, \tau)} = \mathcal{A}_\alpha(\mathbf{r}, \tau). \quad (\text{B.66})$$

Effective action from the connected Green's functions' generating function

We define the effective action as the Legendre transform of the connected Green's functions' generating function F . To make this precise, we will write J , J^* , and \mathbf{W}_α as a notational shorthand for

$$J = J(\phi, \phi^*, \mathcal{A}_\alpha) \quad (\text{B.67})$$

$$J^* = J^*(\phi, \phi^*, \mathcal{A}_\alpha) \quad (\text{B.68})$$

$$\mathbf{W}_\alpha = \mathbf{W}_\alpha(\phi, \phi^*, \mathcal{A}_\alpha) \quad (\text{B.69})$$

$$(\text{B.70})$$

which are defined by inverting the expressions for ϕ , ϕ^* , and \mathcal{A}_α as a function of the sources. Then the effective action is

$$\begin{aligned} \Gamma[\phi, \phi^*, \mathcal{A}_\alpha] &= F[J, J^*, \mathbf{W}_\mu] \\ &\quad - \int d^4\xi \left\{ J^*(\xi)\phi(\xi) + \phi^*(\xi)J(\xi) + \sum_\alpha \mathbf{W}_\alpha(\xi) \cdot \mathcal{A}_\alpha(\xi) \right\} \end{aligned} \quad (\text{B.71})$$

and we have introduced the 4-vector notation

$$\xi \equiv (t, \mathbf{r}). \quad (\text{B.72})$$

An important relationship obeyed by the effective action is that the functional derivatives of Γ evaluated, evaluated at a given average field, give the sources necessary to generate that average field:

$$J(\xi) = -\frac{\delta\Gamma}{\delta\phi^*(\xi)}, \quad (\text{B.73})$$

$$J^*(\xi) = -\frac{\delta\Gamma}{\delta\phi(\xi)}, \quad (\text{B.74})$$

$$\mathcal{W}_\alpha(\xi) = -\frac{\delta\Gamma}{\delta\mathcal{A}_\alpha(\xi)}. \quad (\text{B.75})$$

We demonstrate this relationship for J , and the derivation for the other sources follow analogously. From the definition in Eq. (B.71), we have

$$\begin{aligned} \frac{\delta\Gamma}{\delta\phi^*(\xi)} &= \frac{\delta F}{\delta\phi^*(\xi)} - J(\xi) \\ &\quad - \int d^4\xi \left[\frac{\delta J^*(\xi)}{\delta\phi^*(\xi)}\phi(\xi) + \phi^*(\xi)\frac{\delta J(\xi)}{\delta\phi^*(\xi)} + \sum_\alpha \left(\frac{\delta\mathbf{W}_\alpha(\xi)}{\delta\phi^*(\xi)} \right) \cdot \mathcal{A}_\alpha(\xi) \right] \\ &= \int d\xi' \left[\frac{\delta F}{\delta J(\xi')} \frac{\delta J(\xi')}{\delta\phi^*(\xi)} + \frac{\delta F}{\delta J^*(\xi')} \frac{\delta J^*(\xi')}{\delta\phi^*(\xi)} + \sum_\alpha \frac{\delta F}{\delta\mathbf{W}_\alpha(\xi')} \frac{\delta\mathbf{W}_\alpha(\xi')}{\delta\phi^*(\xi)} \right] \\ &\quad - J(\xi) - \int d^4\xi \left[\frac{\delta J^*(\xi)}{\delta\phi^*(\xi)}\phi(\xi) + \phi^*(\xi)\frac{\delta J(\xi)}{\delta\phi^*(\xi)} + \sum_\alpha \left(\frac{\delta\mathbf{W}_\alpha(\xi)}{\delta\phi^*(\xi)} \right) \cdot \mathcal{A}_\alpha(\xi) \right] \\ &= -J(\xi), \end{aligned} \quad (\text{B.76})$$

where the first step is just the chain rule, and the last step follows from Eqs (B.64), (B.65), and (B.66). This confirms Eq. (B.73), and Eqs (B.74) and (B.75) follow analogously.

Effective action in terms of one-particle irreducible Green's functions

We introduced the effective action Γ , which is constructed so that its functional derivatives yield the one-particle irreducible response functions (although we used the alternative definition in terms of the Legendre transform above, the connection is shown in, e.g., Negele and Orland). Namely one obtains

$$\begin{aligned} \Gamma = & - \int d^4\xi_1 d^4\xi_2 \phi^*(\xi_2) G^{-1}(\xi_2, \xi_1) \phi(\xi_1) \\ & + \sum_{\alpha, \beta, \gamma} \int d^4\xi_1 d^4\xi_2 d^4\xi_3 \phi_\alpha^*(\xi_1) \phi_\beta(\xi_2) \mathbf{A}_{\gamma, \mathbf{a}}(\xi_3) [\Gamma_a^\gamma(\xi_1, \xi_2, \xi_3)]_{\alpha, \beta} \\ & + O(\phi^4, A^2) \end{aligned} \tag{B.77}$$

where G^{-1} is the operator inverse of the exact one particle Green's function and Γ_a^α is the one-particle irreducible exact vertex operator coupling the gauge field to particle-hole excitations. We conform to the unfortunate notation with two distinct Γ 's, following the rest of the world. Note that G is a 2×2 matrix here due to the two spin components. One may obtain the general form of the equation via Taylor expansion of Γ and symmetry considerations; showing the terms are the appropriate one-particle irreducible Green's functions (see Negele and Orland) takes a little more work.

B.3.7 Real space Ward identities

To obtain the real space Ward identities, we will translate Eq. (B.59) into an equation involving functional derivatives with respect to average fields of the effective action, which will give us the desired relation between the Green's functions and vertex function via Eq. (B.77).

Eq. (B.59), evaluated at ξ_3 , becomes

$$\begin{aligned}
& -i \frac{\delta\Gamma}{\delta\phi(\xi_3)} \sigma^{(a)} \phi(\xi_3) + i \phi^*(\xi_3) \sigma^{(a)} \frac{\delta\Gamma}{\delta\phi^*(\xi_3)} \\
& = \sum_{\alpha} \left\{ \frac{1}{g} \left[\frac{\partial}{\partial r_{\alpha}} \left(\frac{\delta\Gamma}{\delta\mathcal{A}_{\alpha}(\xi_3)} \right) \right] + 2 \left[\mathcal{A}_{\alpha}(\xi_3) \times \left(\frac{\delta\Gamma}{\delta\mathcal{A}_{\alpha}(\xi_3)} \right) \right] \right\}_a. \quad (\text{B.78})
\end{aligned}$$

Now is also an appropriate time to note that the source field \mathcal{A} is zero for the physical situation — we no longer need additional derivatives with respect to \mathcal{A} , so we can do this, yielding

$$\begin{aligned}
& -i \frac{\delta\Gamma}{\delta\phi(\xi_3)} \sigma^{(a)} \phi(\xi_3) + i \phi^*(\xi_3) \sigma^{(a)} \frac{\delta\Gamma}{\delta\phi^*(\xi_3)} \\
& = \frac{1}{g} \sum_{\alpha} \left[\frac{\partial}{\partial r_{\alpha}} \left(\frac{\delta\Gamma}{\delta\mathcal{A}_{\alpha}(\xi_3)} \right) \right]_a. \quad (\text{B.79})
\end{aligned}$$

In order to relate the Green's functions to the vertex functions, we want to have second and third derivatives of Γ , so we act on Eq. (B.78) with $\delta^2 / [\delta\phi_{\alpha}^*(\xi_1) \delta\phi_{\beta}(\xi_2)]$; the equation remains valid since it holds for arbitrary fields ϕ and ϕ^* . This gives

$$\begin{aligned}
& \frac{\delta^2}{\delta\phi_{\alpha}^*(\xi_1) \delta\phi_{\beta}(\xi_2)} \left\{ -i \frac{\delta\Gamma}{\delta\phi(\xi_3)} \sigma^{(a)} \phi(\xi_3) + i \phi^*(\xi_3) \sigma^{(a)} \frac{\delta\Gamma}{\delta\phi^*(\xi_3)} \right\} \\
& = \frac{1}{g} \sum_{\mu} \left[\frac{\partial}{\partial r_{\mu}} \left(\frac{\delta^3\Gamma}{\delta\phi_{\alpha}^*(\xi_1) \delta\phi_{\beta}(\xi_2) \delta\mathcal{A}_{\mu}(\xi_3)} \right) \right]_a. \quad (\text{B.80})
\end{aligned}$$

Evaluating this, retaining only the non-zero terms as implied by Eq. (B.77), we obtain

$$\begin{aligned}
& -i \frac{\delta^2\Gamma}{\delta\phi_{\alpha}^*(\xi_1) \delta\phi(\xi_3)} \sigma^{(a)} \frac{\delta\phi(\xi_3)}{\delta\phi_{\beta}(\xi_2)} + i \frac{\delta\phi^*(\xi_3)}{\delta\phi_{\alpha}^*(\xi_1)} \sigma^{(a)} \frac{\delta^2\Gamma}{\delta\phi_{\beta}(\xi_2) \delta\phi^*(\xi_3)} \\
& = \frac{1}{g} \sum_{\mu} \left[\frac{\partial}{\partial r_{\mu}} \left(\frac{\delta^3\Gamma}{\delta\phi_{\alpha}^*(\xi_1) \delta\phi_{\beta}(\xi_2) \delta\mathcal{A}_{\mu}(\xi_3)} \right) \right]_a \quad (\text{B.81})
\end{aligned}$$

so that

$$\begin{aligned}
& \sum_{\nu, \mu} \left\{ i G_{\alpha, \nu}^{-1}(\xi_1, \xi_3) \sigma_{\nu, \mu}^{(a)} \delta_{\mu\beta} \delta(\xi_3 - \xi_2) - i \sigma_{\mu, \nu}^{(a)} G_{\nu, \beta}^{-1}(\xi_3, \xi_2) \delta_{\mu, \alpha} \delta(\xi_3 - \xi_1) \right\} \\
& = \frac{1}{g} \sum_{\mu} \frac{\partial}{\partial r_{\mu}} [\Gamma_a^{\mu}(\xi_1, \xi_2, \xi_3)]_{\alpha, \beta}. \quad (\text{B.82})
\end{aligned}$$

so

$$\begin{aligned} \sum_{\nu} \left\{ iG_{\alpha,\nu}^{-1}(\xi_1, \xi_3) \sigma_{\nu,\beta}^{(a)} \delta(\xi_3 - \xi_2) - i\sigma_{\alpha,\nu}^{(a)} G_{\nu,\beta}^{-1}(\xi_3, \xi_2) \delta(\xi_3 - \xi_1) \right\} \\ = \frac{1}{g} \sum_{\mu} \frac{\partial}{\partial r_{\mu}} [\Gamma_a^{\mu}(\xi_1, \xi_2, \xi_3)]_{\alpha,\beta}. \end{aligned} \quad (\text{B.83})$$

This is the desired real space Ward identity.

In the physical case, we take the sources to zero and consequently the Green's functions become diagonal in the spin space, so that

$$G_{\nu,\mu}(\xi, \xi') = \delta_{\nu,\mu} G_{\nu}(\xi, \xi'). \quad (\text{B.84})$$

Then Eq. (B.83) becomes

$$\begin{aligned} iG_{\alpha}^{-1}(\xi_1, \xi_3) \sigma_{\alpha,\beta}^{(a)} \delta(\xi_3 - \xi_2) - i\sigma_{\alpha,\beta}^{(a)} G_{\beta}^{-1}(\xi_3, \xi_2) \delta(\xi_3 - \xi_1) \\ = \frac{1}{g} \sum_{\mu} \frac{\partial}{\partial r_{\mu}} [\Gamma_a^{\mu}(\xi_1, \xi_2, \xi_3)]_{\alpha,\beta}. \end{aligned} \quad (\text{B.85})$$

B.3.8 Fourier space Ward identities

Vector form

Since the rf probe of interest naturally oscillates at fixed frequency and wavevector, and since our Ward identities decouple into independent algebraic equations in Fourier space, we now Fourier transform Eq. (B.85). It first pays to take advantage of the fact we are dealing with a translationally invariant system, so we may use

$$G(\xi, \xi') = G(\xi - \xi') \quad (\text{B.86})$$

and

$$[\Gamma_a^{\mu}(\xi, \xi', \xi'')] = [\Gamma_a^{\mu}(\xi - \xi'', \xi' - \xi'')]. \quad (\text{B.87})$$

Next we calculate the Fourier transforms for these translationally invariant functions, defining our Fourier conventions in the process. We start with G^{-1} :

$$\begin{aligned}
\iint d^4\xi d^4\xi' e^{i(k_1\xi+k_2\xi')} G_\alpha^{-1}(\xi - \xi') &= \int d^4\bar{\xi} \int d^4\xi' e^{i(k_1(\bar{\xi}+\xi')+k_2\xi')} G_\alpha^{-1}(\bar{\xi}) \\
&= \left[\int d^4\xi' e^{i(k_1+k_2)\xi'} \right] \int d^4\bar{\xi} e^{ik_1\bar{\xi}} G_\alpha^{-1}(\bar{\xi}) \\
&= (2\pi)^4 \delta(k_1 + k_2) G_\alpha^{-1}(k_1) \tag{B.88}
\end{aligned}$$

where we defined

$$G(k) \equiv \int d\xi e^{ik\xi} G(\xi) \tag{B.89}$$

as our Fourier convention here. Similarly, for $[\Gamma_a^\mu]$, we find

$$\begin{aligned}
\iiint d^4\xi_1 d^4\xi_2 d^4\xi_3 e^{i(k_1\xi_1+k_2\xi_2+k_3\xi_3)} [\Gamma_a^\mu(\xi_1 - \xi_3, \xi_2 - \xi_3)] \\
&= \iiint d^4\bar{\xi}_1 d^4\bar{\xi}_2 d^4\xi_3 e^{i[k_1(\bar{\xi}_1+\xi_3)+k_2(\bar{\xi}_2+\xi_3)+k_3\xi_3]} [\Gamma_a^\mu(\xi_1 - \xi_3, \xi_2 - \xi_3)] \\
&= \left[\int d^4\xi_3 e^{i(k_1+k_2+k_3)\xi_3} \right] \iint d^4\bar{\xi}_1 d^4\bar{\xi}_2 e^{i(k_1\bar{\xi}_1+k_2\bar{\xi}_2)} [\Gamma_a^\mu(\bar{\xi}_1, \bar{\xi}_2)] \\
&= (2\pi)^4 \delta(k_1 + k_2 + k_3) [\Gamma_a^\mu(k_1, -k_2)] \tag{B.90}
\end{aligned}$$

where we use the Fourier convention

$$[\Gamma_a^\mu(k_1, -k_2)] = \iint d\xi d\xi' e^{i(k_1\xi-k_2\xi')} [\Gamma_a^\mu(\xi_1, \xi_2)]. \tag{B.91}$$

With these Fourier transforms, we integrate both sides of Eq. (B.85) against $\iiint d^4\xi_1 d^4\xi_2 d^4\xi_3 e^{i(k\xi_1-k'\xi_2-q\xi_3)}$ (this convention should be somewhat natural when

we deal with the rf spectra), which yields

$$\begin{aligned} & \iiint d^4\xi_1 d^4\xi_2 d^4\xi_3 e^{i(k\xi_1 - k'\xi_2 - q\xi_3)} \\ & \quad \times \left\{ iG_\alpha^{-1}(\xi_1, \xi_3) \sigma_{\alpha,\beta}^{(a)} \delta(\xi_3 - \xi_2) - i\sigma_{\alpha,\beta}^{(a)} G_\beta^{-1}(\xi_3, \xi_2) \delta(\xi_3 - \xi_1) \right\} \\ & = \iiint d^4\xi_1 d^4\xi_2 d^4\xi_3 e^{i(k\xi_1 - k'\xi_2 - q\xi_3)} \left\{ \frac{1}{g} \sum_\mu \frac{\partial}{\partial r_{3,\mu}} [\Gamma_a^\mu(\xi_1, \xi_2, \xi_3)]_{\alpha,\beta} \right\} \end{aligned} \quad (\text{B.92})$$

$$\begin{aligned} & \Rightarrow \iiint d^4\xi_1 d^4\xi_2 \\ & \quad \times \left\{ e^{i(k\xi_1 - (k'+q)\xi_2)} G_\alpha^{-1}(\xi_1 - \xi_2) \sigma_{\alpha,\beta}^{(a)} - e^{i((k-q)\xi_1 - k'\xi_2)} \sigma_{\alpha,\beta}^{(a)} G_\beta^{-1}(\xi_1 - \xi_2) \right\} \\ & = \frac{1}{g} \iiint d^4\xi_1 d^4\xi_2 d^4\xi_3 e^{i(k\xi_1 - k'\xi_2 - q\xi_3)} \left\{ \sum_\mu q_\mu [\Gamma_a^\mu(\xi_1 - \xi_3, \xi_2 - \xi_3)]_{\alpha,\beta} \right\} \end{aligned} \quad (\text{B.93})$$

So that using our Fourier transform conventions and results, we obtain

$$G_\alpha^{-1}(k) \sigma_{\alpha,\beta}^{(a)} - \sigma_{\alpha,\beta}^{(a)} G_\beta^{-1}(k - q) = \frac{1}{g} \sum_\mu q_\mu [\Gamma_a^\mu(k, k - q)]_{\alpha,\beta}. \quad (\text{B.94})$$

Eq. (B.94) is the complete Ward identities in Fourier space.

Ward identities written into individual components

Next, we write out the individual components ($a = x, y, z$, $\alpha = 1, 2$, and $\beta = 1, 2$) of Eq. (B.94) to better see their structure and to more easily work with them.

These are

$$G_1^{-1}(k) - G_2^{-1}(k - q) = \frac{1}{g} \sum_\mu q_\mu [\Gamma_x^\mu(k, k - q)]_{12} \quad (\text{B.95})$$

$$G_2^{-1}(k) - G_1^{-1}(k - q) = \frac{1}{g} \sum_\mu q_\mu [\Gamma_x^\mu(k, k - q)]_{21} \quad (\text{B.96})$$

$$-iG_1^{-1}(k) + iG_2^{-1}(k - q) = \frac{1}{g} \sum_\mu q_\mu [\Gamma_y^\mu(k, k - q)]_{12} \quad (\text{B.97})$$

$$iG_2^{-1}(k) - iG_1^{-1}(k - q) = \frac{1}{g} \sum_\mu q_\mu [\Gamma_y^\mu(k, k - q)]_{21} \quad (\text{B.98})$$

$$G_1^{-1}(k) - G_1^{-1}(k - q) = \frac{1}{g} \sum_\mu q_\mu [\Gamma_z^\mu(k, k - q)]_{11} \quad (\text{B.99})$$

$$-G_2^{-1}(k) + G_2^{-1}(k - q) = \frac{1}{g} \sum_\mu q_\mu [\Gamma_z^\mu(k, k - q)]_{22}. \quad (\text{B.100})$$

and

$$\begin{aligned}
\sum_{\mu} q_{\mu} [\Gamma_x^{\mu}(k, k - q)]_{11} &= \sum_{\mu} q_{\mu} [\Gamma_x^{\mu}(k, k - q)]_{22} = \sum_{\mu} q_{\mu} [\Gamma_y^{\mu}(k, k - q)]_{11} \\
&= \sum_{\mu} q_{\mu} [\Gamma_y^{\mu}(k, k - q)]_{22} = \sum_{\mu} q_{\mu} [\Gamma_z^{\mu}(k, k - q)]_{12} \\
&= \sum_{\mu} q_{\mu} [\Gamma_z^{\mu}(k, k - q)]_{21} = 0.
\end{aligned} \tag{B.101}$$

This is the complete set of Fourier-space, component-by-component Ward identities.

The important Ward identities for rf spectra are Eqs. (B.95), (B.96), (B.97), and (B.98).

Ward identities separated into non-interacting vertex plus corrections

In calculations it is useful to separate expressions into those which apply to a non-interacting system plus terms from the interactions. We now carry this out for the Green's functions. By using the definition of the self energies Σ_{α} , namely

$$G_{\alpha}^{-1}(k) = G_{0,\alpha}^{-1}(k) + \Sigma_{\alpha}(k) \tag{B.102}$$

where $G_{0,\alpha}$ is the component α non-interacting system's Green's function. We will similarly define the non-interacting vertex $[\gamma_a^{\mu}]_{\alpha,\beta}$ and interaction correction $[\Delta\Gamma_a^{\mu}]_{\alpha,\beta}$: $\Gamma_a^{\mu} = \gamma_a^{\mu} + \Delta\Gamma_a^{\mu}$, defining

$$G_{0,1}^{-1}(k) - G_{0,2}^{-1}(k - q) = \frac{1}{g} \sum_{\mu} q_{\mu} [\gamma_x^{\mu}(k, k - q)]_{12} \tag{B.103}$$

$$G_{0,2}^{-1}(k) - G_{0,1}^{-1}(k - q) = \frac{1}{g} \sum_{\mu} q_{\mu} [\gamma_x^{\mu}(k, k - q)]_{21} \tag{B.104}$$

$$-iG_{0,1}^{-1}(k) + iG_{0,2}^{-1}(k - q) = \frac{1}{g} \sum_{\mu} q_{\mu} [\gamma_y^{\mu}(k, k - q)]_{12} \tag{B.105}$$

$$iG_{0,2}^{-1}(k) - iG_{0,1}^{-1}(k - q) = \frac{1}{g} \sum_{\mu} q_{\mu} [\gamma_y^{\mu}(k, k - q)]_{21} \tag{B.106}$$

$$G_{0,1}^{-1}(k) - G_{0,1}^{-1}(k - q) = \frac{1}{g} \sum_{\mu} q_{\mu} [\gamma_z^{\mu}(k, k - q)]_{11} \tag{B.107}$$

$$-G_{0,2}^{-1}(k) + G_{0,2}^{-1}(k - q) = \frac{1}{g} \sum_{\mu} q_{\mu} [\gamma_z^{\mu}(k, k - q)]_{22}. \tag{B.108}$$

Eqs. (B.95), (B.96), (B.97), (B.98), (B.99), and (B.100) then imply

$$\Sigma_1(k) - \Sigma_2(k - q) = \frac{1}{g} \sum_{\mu} q_{\mu} [\Delta\Gamma_x^{\mu}(k, k - q)]_{12} \quad (\text{B.109})$$

$$\Sigma_2(k) - \Sigma_1(k - q) = \frac{1}{g} \sum_{\mu} q_{\mu} [\Delta\Gamma_x^{\mu}(k, k - q)]_{21} \quad (\text{B.110})$$

$$-i\Sigma_1(k) + i\Sigma_2(k - q) = \frac{1}{g} \sum_{\mu} q_{\mu} [\Delta\Gamma_y^{\mu}(k, k - q)]_{12} \quad (\text{B.111})$$

$$i\Sigma_2(k) - i\Sigma_1(k - q) = \frac{1}{g} \sum_{\mu} q_{\mu} [\Delta\Gamma_y^{\mu}(k, k - q)]_{21} \quad (\text{B.112})$$

$$\Sigma_1(k) - \Sigma_1(k - q) = \frac{1}{g} \sum_{\mu} q_{\mu} [\Delta\Gamma_z^{\mu}(k, k - q)]_{11} \quad (\text{B.113})$$

$$-\Sigma_2(k) + \Sigma_2(k - q) = \frac{1}{g} \sum_{\mu} q_{\mu} [\Delta\Gamma_z^{\mu}(k, k - q)]_{22}. \quad (\text{B.114})$$

B.4 Lattice (single band)

B.4.1 Setup

We now turn to the case of interacting bosons in a lattice and examine the consequences of $SU(2)$ gauge invariance for the matter-gauge field interaction vertex. The arguments will follow completely analogously to the case without a lattice. I will be a little less pedantic in my presentation here.

The two component Bose-Hubbard Hamiltonian

$$H = H_1 + H_2 \quad (\text{B.115})$$

with

$$H_1 = -t \sum_{\langle i,j \rangle} c_i^{\dagger} e^{a_{ij}(t)} c_j + \sum_j c_j^{\dagger} (V_j - \mu) c_j \quad (\text{B.116})$$

and

$$H_2 = \sum_j \left(\sum_{\alpha,\beta} \frac{U_{\alpha\beta}}{2} c_{j,\alpha}^{\dagger} c_{j,\beta}^{\dagger} c_{j,\beta} c_{j,\alpha} \right). \quad (\text{B.117})$$

In these equations, $\sum_{\langle i,j \rangle}$ is a sum over nearest neighbors i and j , V_j is the on-site trapping potential, μ is the chemical potential (both V_j and μ are 2×2 matrices),

$U_{\alpha\beta}$ are the interaction parameters, c_j is defined as

$$c_j = \begin{pmatrix} c_{j,1} \\ c_{j,2} \end{pmatrix}. \quad (\text{B.118})$$

with $c_{j,\alpha}$ the Bose annihilation operator for a particle at site j in internal state α , and a_{ij} a 2×2 matrix corresponding to an externally imposed $SU(2)$ lattice gauge field.

Again, as in the continuum case, a vacuum energy splitting between states $\alpha = 1$ and $\alpha = 2$ may be canonically transformed away. Also, we will ignore the V_j trapping potential, as in the continuum case.

B.4.2 Showing covariance of kinetic energy

The Hamiltonian H in Eq. (B.115) is invariant under $SU(2)$ transformations; this follows exactly as in the continuum case for each term except the kinetic term. Imposing invariance on the kinetic term will define the transformation rules of the gauge field. That is, we promote our global $SU(2)$ symmetry $c_j \rightarrow c'_j = e^{i\sigma \cdot \mathbf{A}_j} c_j$ to a local gauge symmetry:

$$c_j(t) \rightarrow c'_j(t) = e^{i\sigma \cdot \mathbf{A}_j(t)} c_j. \quad (\text{B.119})$$

The ‘‘covariant derivative’’ kinetic term,

$$T_{ij} \equiv c_i^\dagger e^{i\sigma \cdot \mathbf{a}_{ij}} c_j \quad (\text{B.120})$$

in the Hamiltonian then transforms as

$$T_{ij} \rightarrow T'_{ij} = \left(c_i^\dagger e^{-i\sigma \cdot \mathbf{A}_i(t)} \right) e^{i\sigma \cdot \mathbf{a}_{ij}(t)} \left(e^{i\sigma \cdot \mathbf{A}_j(t)} c_j \right). \quad (\text{B.121})$$

We will work only to lowest order in the infinitesimal $SU(2)$ gauge transformations \mathbf{A}_j , so that, using the BCH formula, this transformation is

$$T_{ij} \rightarrow T'_{ij} = c_i^\dagger e^{i\sigma \cdot \mathbf{a}'_{ij}} c_j. \quad (\text{B.122})$$

with

$$\sigma \cdot \mathbf{a}_{ij}' = \sigma \cdot \mathbf{a}_{ij} - (1/2)[i\sigma \cdot \bar{\Lambda}_{ij}(t), i\sigma \cdot \mathbf{a}_{ij}(t)] + i\sigma \cdot \delta\Lambda_{ij}(t) + O(\Lambda^2) \quad (\text{B.123})$$

with

$$\bar{\Lambda}_{ij}(t) \equiv \frac{\Lambda_i(t) + \Lambda_j(t)}{2} \quad (\text{B.124})$$

and

$$\delta\Lambda_{ij}(t) = \Lambda_i(t) - \Lambda_j(t). \quad (\text{B.125})$$

Calculating the commutator via $[\sigma \cdot \mathbf{w}, \sigma \cdot \mathbf{v}] = 2i\sigma \cdot (\mathbf{w} \times \mathbf{v})$, Eq. (B.123) gives, to $O(\Lambda^2)$,

$$\sigma \cdot \mathbf{a}_{ij}' = \sigma \cdot \mathbf{a}_{ij} + (1/2)\sigma \cdot (\bar{\Lambda}_{ij}(t) \times \mathbf{a}_{ij}(t)) + i\sigma \cdot \delta\Lambda_{ij}(t). \quad (\text{B.126})$$

Since the Pauli matrices along with the identity matrix form a complete set we can remove the $\sigma \cdot$, obtaining

$$\mathbf{a}_{ij} \rightarrow \mathbf{a}_{ij}' = \mathbf{a}_{ij} + (1/2) \cdot (\bar{\Lambda}_{ij}(t) \times \mathbf{a}_{ij}(t)) + i\delta\Lambda_{ij}(t). \quad (\text{B.127})$$

which guarantees gauge covariance. Precisely, the system is gauge invariant under the simultaneous field transformations of Eq. (B.119) and (B.127).

B.4.3 Partition function in path integral representation, including sources

The path integral, including sources so we can generate the Green's functions, is, using the usual path integral notational conventions,

$$Z[J_j^*, J_j, \mathbf{w}_{ij}] = \int \mathcal{D}c_j(\tau) \mathcal{D}\mathbf{a}_{ij}(\tau) e^{-(S+S_J)/\hbar} \quad (\text{B.128})$$

where the system sans sources action is

$$\begin{aligned}
S[c_j, c_j^*, \mathbf{a}_{ij}] &= \int_0^\beta d\tau \sum_j c_j^\dagger(\tau) \left(\frac{\partial}{\partial \tau} - \mu - \sigma \cdot \phi_j(\tau) \right) c_j(\tau) \\
&+ \int d\tau H[c_j(\tau), c_j^*(\tau), \mathbf{a}_{ij}(\tau)],
\end{aligned} \tag{B.129}$$

where we introduce the time-component of the gauge field, ϕ , and note that ϕ and the chemical potential, μ , are 2×2 matrices, and the source term is

$$\begin{aligned}
S_J[J_j, J_j^*, \mathbf{w}_{ij}, \mathbf{w}_{0j}; c_j, c_j^*, \mathbf{a}_{ij}, \phi_j] \\
&= \int_0^\beta d\tau \left[\sum_j \left(J_j^*(\tau) c_j(\tau) + c_j^*(\tau) J_j(\tau) + \mathbf{w}_j^{(0)}(\tau) \cdot \phi_j(\tau) \right) \right. \\
&\quad \left. + \sum_{\langle i,j \rangle} \mathbf{w}_{ij}(\tau) \cdot \mathbf{a}_{ij}(\tau) \right].
\end{aligned} \tag{B.130}$$

Note that to maintain covariance, ϕ obeys the transformation law

$$\phi_j \rightarrow \phi'_j = \phi_j + i \left(\frac{\partial \Lambda_j(\tau)}{\partial \tau} \right) - 2i (\phi_j(\tau) \times \mathbf{\Lambda}_j(\tau)). \tag{B.131}$$

Later, we will find it convenient to use the generating functional (I'll say "free energy") F defined by

$$F = -\hbar \log Z. \tag{B.132}$$

Whereas taking functional derivatives of Z with respect to sources generates the total Green's functions, F generates the *connected* Green's functions.

B.4.4 Action under $SU(2)$ transformations

We will soon argue that the partition function is invariant under $SU(2)$ matter and gauge field transformations of the integrand, and explore the consequences of this. To facilitate this, we determine how S , S_J , and the integration measure $\mathcal{D}c_j a_{ij}$ vary under an $SU(2)$ gauge transformation. Either by construction (e.g.,

for the kinetic terms) or the same arguments as in the non-lattice case, S and the integration measure are invariant under $SU(2)$ transformations of c_j and \mathbf{a}_{ij} . We calculate the behavior of S_J under the gauge transformation of the matter and gauge fields from Eq. (B.130). This yields

$$\begin{aligned}
S_J \rightarrow S'_J = \int d\tau \left\{ \sum_j \left[J_j^*(\tau) e^{i\sigma \cdot \Lambda_j(\tau)} c_j(\tau) + c_j^*(\tau) e^{-i\sigma \cdot \Lambda_j(\tau)} J_j(\tau) \right. \right. \\
\left. \left. + \mathbf{w}_j^{(0)}(\tau) \cdot \left(\phi_j(\tau) + i \left(\frac{\partial \Lambda_j(\tau)}{\partial \tau} \right) - 2i (\phi_j(\tau) \times \Lambda_j(\tau)) \right) \right] \right. \\
\left. + \sum_{\langle i,j \rangle} \mathbf{w}_{ij}(\tau) \cdot \left(\mathbf{a}_{ij} + i\delta \Lambda_{ij}(\tau) + \frac{1}{2} (\bar{\Lambda}_{ij}(\tau) \times \mathbf{a}_{ij}(\tau)) \right) \right\} \quad (\text{B.133})
\end{aligned}$$

Recognizing that henceforth we may set $\mathbf{a}_{ij} = 0$ and $\phi_j = 0$, since we won't be further differentiating with respect to these variables, to lowest order in $\Lambda_j(\tau)$ we have $S_J \rightarrow S'_J = S_J + \delta S_J$ with

$$\begin{aligned}
\delta S_J = \int d\tau \left\{ \sum_j \left[J_j^*(\tau) (i\sigma \cdot \Lambda_j(\tau)) c_j(\tau) + c_j^\dagger(\tau) (-i\sigma \cdot \Lambda_j(\tau)) J_j(\tau) \right. \right. \\
\left. \left. + \mathbf{w}_j^{(0)}(\tau) \cdot \left(i \frac{\partial \Lambda_j(\tau)}{\partial \tau} \right) \right] + \sum_{\langle i,j \rangle} \mathbf{w}_{ij}(\tau) \cdot (i\delta \Lambda_{ij}(\tau)) \right\}. \quad (\text{B.134})
\end{aligned}$$

Massaging Λ_j to factor in δS_J . We will soon wish to obtain an expression independent of $\Lambda_i(\tau)$ and eliminates the \sum_j and $\int D\tau$ by factoring this out of the equation and using the fact that it is arbitrary to choose it to be a spatial Kronecker delta and a time Dirac delta function. However, in order to do this, we must massage the term involving $\delta \Lambda_{ij}$, since this involves both Λ_i and Λ_j . This is the analog of the integration by parts carried out in the continuum case. The key

to the argument is to recognize that $\sum_i \sum_{j \in \text{n.n. of } i} f_{ij} = \sum_j \sum_{i \in \text{n.n. of } j} f_{ij}$. Then

$$\sum_{\langle i,j \rangle} \mathbf{w}_{ij} \cdot \delta \Lambda_{ij} = \sum_{\langle i,j \rangle} \mathbf{w}_{ij} \cdot (\Lambda_i - \Lambda_j) \quad (\text{B.135})$$

$$= \sum_i \sum_{j \in \text{n.n. of } i} \mathbf{w}_{ij} \cdot \Lambda_i - \sum_i \sum_{j \in \text{n.n. of } i} \mathbf{w}_{ij} \cdot \Lambda_j \quad (\text{B.136})$$

$$= \sum_i \sum_{j \in \text{n.n. of } i} \mathbf{w}_{ij} \cdot \Lambda_i - \sum_j \sum_{i \in \text{n.n. of } j} \mathbf{w}_{ji} \cdot \Lambda_i \quad (\text{B.137})$$

$$= \sum_{\langle i,j \rangle} (\mathbf{w}_{ij} - \mathbf{w}_{ji}) \cdot \Lambda_i. \quad (\text{B.138})$$

Consequently, this relation plus integrating the time component of the gauge field by parts, Eq. (B.134) becomes

$$\begin{aligned} \delta S_J = \int d\tau \left\{ \sum_i \left[J_i^*(\tau) (i\sigma \cdot \Lambda_i(\tau)) c_i(\tau) + c_i^*(\tau) (-i\sigma \cdot \Lambda_i(\tau)) J_i(\tau) \right. \right. \\ \left. \left. - \frac{\partial \mathbf{w}_j^{(0)}(\tau)}{\partial \tau} \cdot (i\Lambda_j(\tau)) \right] + i \sum_{\langle i,j \rangle} (\mathbf{w}_{ij}(\tau) - \mathbf{w}_{ji}(\tau)) \cdot \Lambda_i(\tau) \right\} \quad (\text{B.139}) \end{aligned}$$

B.4.5 Consequences of $SU(2)$ invariance of the partition function

The partition function Z will turn out to be invariant under $SU(2)$ transformations of its integrand, and this will constrain the field expectation values for a given value of the sources. We now demonstrate these two claims in turn.

Partition function Z is invariant under $SU(2)$ transformation of integrand

The partition function Z upon gauge transforming the integrand's fields is

$$Z \rightarrow Z' = \int \mathcal{D}c_j(\tau) \mathcal{D}\mathbf{a}_{ij}(\tau) \exp \left[- (S[c'_j, (c'_j)^*, \mathbf{a}'_{ij}]) / \hbar \right] \quad (\text{B.140})$$

with $c'_j = e^{i\sigma \cdot \Lambda_j(\tau)} c_j$, $(c_j^*)' = c_j^* e^{-i\sigma \cdot \Lambda_j(\tau)}$, and $\mathbf{a}'_{ij} = \sigma \cdot \mathbf{a}_{ij} - (1/2)[i\sigma \cdot \bar{\Lambda}_{ij}, i\sigma \cdot \mathbf{a}_{ij}] + i\sigma \cdot \delta \Lambda_{ij}$. Now, we change integration variables to

$$\tilde{c}_j = e^{-i\sigma \cdot \Lambda_j(\tau)} c_j, \quad (\text{B.141})$$

$$\tilde{c}_j^* = c_j^* e^{i\sigma \cdot \Lambda_j(\tau)}, \quad (\text{B.142})$$

$$\tilde{\mathbf{a}}_{ij} = \sigma \cdot \mathbf{a}_{ij} + (1/2)[i\sigma \cdot \bar{\Lambda}_{ij}, i\sigma \cdot \mathbf{a}_{ij}] - i\sigma \cdot \delta \Lambda_{ij} \quad (\text{B.143})$$

so that

$$Z' = \int \mathcal{D}\tilde{c}_j(\tau) \mathcal{D}\tilde{\mathbf{a}}_{ij}(\tau) \exp \left[- (S[c_j, c_j^*, \mathbf{a}_{ij}]) / \hbar \right] \quad (\text{B.144})$$

$$= \int \mathcal{D}c_j(\tau) \mathcal{D}\mathbf{a}_{ij}(\tau) \exp \left[- (S[c_j, c_j^*, \mathbf{a}_{ij}]) / \hbar \right] \quad (\text{B.145})$$

$$= Z, \quad (\text{B.146})$$

where the last step follows since the integration measure and domain are invariant under the gauge transform associated with $-\Lambda_j$. Hence, $Z' = Z$ as claimed.

Consequences of Z 's invariance

The invariance of Z under the integrand's gauge transformation implies $\langle \delta S_J \rangle = 0$ as in the continuum case. Then Eq. (B.139) gives

$$0 = \left\langle \int d\tau \left\{ \sum_i \left[J_i^*(\tau) (i\sigma \cdot \Lambda_i(\tau)) c_i(\tau) + c_i^*(\tau) (-i\sigma \cdot \Lambda_i(\tau)) J_i(\tau) - \frac{\partial \mathbf{w}_j^{(0)}(\tau)}{\partial \tau} \cdot (i\Lambda_j(\tau)) \right] + i \sum_{\langle i,j \rangle} (\mathbf{w}_{ij}(\tau) - \mathbf{w}_{ji}) \cdot \Lambda_i(\tau) \right\} \right\rangle. \quad (\text{B.147})$$

Defining the average

$$b_j(\tau) \equiv \langle c_j(\tau) \rangle, \quad (\text{B.148})$$

and noticing that Eq. (B.147) holds for arbitrary $\Lambda_{\mathbf{j}}(\tau)$, we choose $\Lambda_{\mathbf{j}}(\tau') = \Lambda \hat{\alpha} \delta_{j,s} \delta(\tau' - \tau)$ and find

$$\begin{aligned} & J_s^*(\tau) \sigma^{(a)} b_s(\tau) - b_s^*(\tau) \sigma^{(a)} J_s(\tau) \\ &= \left[\frac{\partial \mathbf{w}_s^{(0)}(\tau)}{\partial \tau} - \sum_{j \in \text{n.n. of } s} (\mathbf{w}_{s\mathbf{j}}(\tau) - \mathbf{w}_{\mathbf{j}s}(\tau)) \right]_a. \end{aligned} \quad (\text{B.149})$$

This is an expression of the relation between sources and average fields, which we will manipulate into the relevant Ward identity.

B.4.6 Effective action

Legende transform of F

We define the effective action via the Legendre transformation (and as before, this ensures it is the generating functional of the one particle irreducible Green's function and vertex functions):

$$\begin{aligned} \Gamma[b_j(\tau), b_j^*(\tau), \alpha_{\mathbf{ij}}(\tau)] &= W[J_j(\tau), J_j^*(\tau), \mathbf{w}_{\mathbf{ij}}(\tau)] \\ &\quad - \int d\tau \left\{ \sum_j \left[J_j^*(\tau) b_j(\tau) + b_j^*(\tau) J_j(\tau) + \mathbf{w}_{\mathbf{j}}^{(0)} \cdot \alpha_{\mathbf{j},\mathbf{0}} \right] \right. \\ &\quad \left. + \sum_{\langle i,j \rangle} \mathbf{w}_{\mathbf{ij}}(\tau) \cdot \alpha_{\mathbf{ij}}(\tau) \right\} \end{aligned} \quad (\text{B.150})$$

where $\alpha_{\mathbf{ij}} \equiv \langle \mathbf{a}_{\mathbf{ij}} \rangle$, $\alpha_{\mathbf{j},\mathbf{0}} \equiv \langle \phi_{\mathbf{j}} \rangle$, and $J_j(\tau)$, $J_j^*(\tau)$ and $\mathbf{w}_{\mathbf{ij}}(\tau)$ are the sources which give rise to average fields $b_j(\tau)$, $b_j^*(\tau)$, and $\alpha_{\mathbf{ij}}(\tau)$.

Following the arguments in the continuum case, Γ 's first functional derivatives are

$$\frac{\delta \Gamma}{\delta b_j(\tau)} = -J_j^*(\tau), \quad (\text{B.151})$$

$$\frac{\delta \Gamma}{\delta b_j^*(\tau)} = -J_j(\tau), \quad (\text{B.152})$$

$$\frac{\delta \Gamma}{\delta \alpha_{\mathbf{ij}}(\tau)} = -\mathbf{w}_{\mathbf{ij}}(\tau). \quad (\text{B.153})$$

Effective action in terms of one-particle irreducible functions

As discussed in Negele and Orland, one finds that the effective action is

$$\begin{aligned}
\Gamma = & - \int d\tau_1 d\tau_2 \sum_{j_1, j_2} b_{j_1}^\dagger(\tau_1) G^{-1}(j_1, \tau_1; j_2, \tau_2) b_{j_2}(\tau_2) \\
& + \int d\tau_1 d\tau_2 d\tau_3 \sum_a \sum_{\alpha, \beta} \sum_{j_1, j_2, j_3} \sum_{s \in \text{n.n. of } j_3} b_\alpha^\dagger(j_1, \tau_1) b_\beta(j_2, \tau_2) \alpha_{j_3, s}^{(a)}(\tau_3) \\
& \quad \times [\Gamma_a^{j_3, s}(j_1, \tau_1; j_2, \tau_2; j_3, \tau_3)]_{\alpha, \beta} \\
& + \int d\tau_1 d\tau_2 d\tau_3 \sum_a \sum_{\alpha, \beta} \sum_{j_1, j_2, j_3} b_\alpha^\dagger(j_1, \tau_1) b_\beta(j_2, \tau_2) \alpha_0^{(a)}(j_3, \tau_3) \\
& \quad \times [\Gamma_a^0(j_1, \tau_1; j_2, \tau_2; j_3, \tau_3)]_{\alpha, \beta} \\
& + O(b^4) + O(\alpha^2) \tag{B.154}
\end{aligned}$$

where G is the 2×2 matrix for the exact single-particle Green's function and Γ_a^{ij} is the one-particle irreducible exact vertex operator coupling the bond i - j gauge field to particle-hole excitations. We have also changed our notation slightly, with the lattice operators now putting the site index in parentheses rather than as a subscript.

B.4.7 Real space Ward identities

Eq. (B.149) will yield the Ward identities between the exact one particle irreducible vertex and the exact Green's functions by taking advantage of Eq. (B.154). First we rewrite Eq. (B.149) by using Eqs. (B.153), and evaluating everything at the position and imaginary time j_3, τ_3 :

$$\begin{aligned}
& \frac{\delta\Gamma}{\delta b(j_3, \tau_3)} \sigma^{(a)} b(j_3, \tau_3) - b^*(j_3, \tau_3) \sigma^{(a)} \frac{\delta\Gamma}{\delta b^*(j_3, \tau_3)} \\
& = \frac{\partial}{\partial\tau_3} \left(\frac{\delta\Gamma}{\delta\alpha_0^{(a)}(j_3, \tau_3)} \right) - \sum_{s \in \text{n.n. of } j_3} \left(\frac{\delta\Gamma}{\delta\alpha_{j_3, s}^{(a)}(\tau_3)} - \frac{\delta\Gamma}{\delta\alpha_{s, j_3}^{(a)}(\tau_3)} \right) \tag{B.155}
\end{aligned}$$

In order to turn this equation into one involving the irreducible vertex and Green's functions, we functionally differentiate both sides of the Equation twice. This is

valid since it holds for arbitrary values of the b 's. Then

$$\begin{aligned}
& \frac{\delta^2}{\delta b_\alpha^*(j_1, \tau_1) \delta b_\beta(j_2, \tau_2)} \left[\frac{\delta \Gamma}{\delta b(j_3, \tau_3)} \sigma^{(a)} b(j_3, \tau_3) - b^*(j_3, \tau_3) \sigma^{(a)} \frac{\delta \Gamma}{\delta b^*(j_3, \tau_3)} \right] \\
&= \frac{\delta^2}{\delta b_\alpha^*(j_1, \tau_1) \delta b_\beta(j_2, \tau_2)} \left[\frac{\partial}{\partial \tau_3} \left(\frac{\delta \Gamma}{\delta \alpha_0^{(a)}(j_3, \tau_3)} \right) \right. \\
&\quad \left. - \sum_{s \in \text{n.n. of } j_3} \left(\frac{\delta \Gamma}{\delta \alpha_{j_3, s}^{(a)}(\tau_3)} - \frac{\delta \Gamma}{\delta \alpha_{s, j_3}^{(a)}(\tau_3)} \right) \right] \quad (\text{B.156})
\end{aligned}$$

which yields

$$\begin{aligned}
& \sum_{\mu, \nu} \left[\frac{\delta^2 \Gamma}{\delta b_\alpha^*(j_1, \tau_1) \delta b_\mu(j_3, \tau_3)} \sigma_{\mu, \nu}^{(a)} \frac{\delta b_\nu(j_3, \tau_3)}{\delta b_\beta(j_2, \tau_2)} - \frac{\delta b_\mu^*(j_3, \tau_3)}{\delta b_\alpha^*(j_1, \tau_1)} \sigma_{\mu, \nu}^{(a)} \frac{\delta^2 \Gamma}{\delta b_\nu^*(j_3, \tau_3) \delta b_\beta(j_2, \tau_2)} \right] \\
&= \frac{\partial}{\partial \tau_3} \left(\frac{\delta^3 \Gamma}{\delta b_\alpha^*(j_1, \tau_1) \delta b_\beta(j_2, \tau_2) \delta \alpha_0^{(a)}(j_3, \tau_3)} \right) \\
&\quad - \sum_{s \in \text{n.n. of } j_3} \left(\frac{\delta^3 \Gamma}{\delta b_\alpha^*(j_1, \tau_1) \delta b_\beta(j_2, \tau_2) \delta \alpha_{j_3, s}^{(a)}(\tau_3)} \right. \\
&\quad \left. - \frac{\delta^3 \Gamma}{\delta b_\alpha^*(j_1, \tau_1) \delta b_\beta(j_2, \tau_2) \delta \alpha_{s, j_3}^{(a)}(\tau_3)} \right) \quad (\text{B.157})
\end{aligned}$$

so that finally

$$\begin{aligned}
& \sum_{\mu} \left[\frac{\delta^2 \Gamma}{\delta b_\alpha^*(j_1, \tau_1) \delta b_\mu(j_3, \tau_3)} \sigma_{\mu, \beta}^{(a)} \delta_{j_2, j_3} \delta(\tau_3 - \tau_2) \right. \\
&\quad \left. - \delta_{j_1, j_3} \delta(\tau_3 - \tau_1) \sigma_{\alpha, \mu}^{(a)} \frac{\delta^2 \Gamma}{\delta b_\mu^*(j_3, \tau_3) \delta b_\beta(j_2, \tau_2)} \right] \\
&= \frac{\partial}{\partial \tau_3} \left(\frac{\delta^3 \Gamma}{\delta b_\alpha^*(j_1, \tau_1) \delta b_\beta(j_2, \tau_2) \delta \alpha_0^{(a)}(j_3, \tau_3)} \right) \\
&\quad - \sum_{s \in \text{n.n. of } j_3} \left(\frac{\delta^3 \Gamma}{\delta b_\alpha^*(j_1, \tau_1) \delta b_\beta(j_2, \tau_2) \delta \alpha_{j_3, s}^{(a)}(\tau_3)} \right. \\
&\quad \left. - \frac{\delta^3 \Gamma}{\delta b_\alpha^*(j_1, \tau_1) \delta b_\beta(j_2, \tau_2) \delta \alpha_{s, j_3}^{(a)}(\tau_3)} \right). \quad (\text{B.158})
\end{aligned}$$

Evaluating the functional derivatives with Eq. (B.154) gives the real space Ward

identities

$$\begin{aligned}
& \sum_{\mu} \left[\delta_{j_1, j_3} \delta(\tau_3 - \tau_1) \sigma_{\alpha, \mu}^{(a)} G_{\mu, \beta}^{-1}(j_3, \tau_3; j_2, \tau_2) - G_{\alpha, \mu}^{-1}(j_1, \tau_1; j_3, \tau_3) \sigma_{\mu, \beta}^{(a)} \delta_{j_2, j_3} \delta(\tau_3 - \tau_2) \right] \\
&= \frac{\partial}{\partial \tau_3} \left[\Gamma_a^0(j_1, \tau_1; j_2, \tau_2; j_3, \tau_3) \right]_{\alpha, \beta} \\
&\quad - \sum_{s \in \text{n.n. of } j_3} \left(\left[\Gamma_a^{j_3, s}(j_1, \tau_1; j_2, \tau_2; j_3, \tau_3) \right]_{\alpha, \beta} - \left[\Gamma_a^{s, j_3}(j_1, \tau_1; j_2, \tau_2; j_3, \tau_3) \right]_{\alpha, \beta} \right) \quad (\text{B.159})
\end{aligned}$$

There is a further simplification, which could have been made much sooner, which yields that

$$[\Gamma^{sj}] = -[\Gamma^{js}]. \quad (\text{B.160})$$

This follows from the fact that $[\Gamma_a^{sj}]$ is the variational derivative of the effective action, $[\Gamma_a^{sj}] = \delta\Gamma/\delta\alpha_{\mathbf{s}, \mathbf{j}}^{(\mathbf{a})}$, and that $\alpha_{\mathbf{s}, \mathbf{j}}^{(\mathbf{a})} = -\alpha_{\mathbf{j}, \mathbf{s}}^{(\mathbf{a})}$ by definition. Consequently, Eq. (B.159) is

$$\begin{aligned}
& \sum_{\mu} \left[\delta_{j_1, j_3} \delta(\tau_3 - \tau_1) \sigma_{\alpha, \mu}^{(a)} G_{\mu, \beta}^{-1}(j_3, \tau_3; j_2, \tau_2) - G_{\alpha, \mu}^{-1}(j_1, \tau_1; j_3, \tau_3) \sigma_{\mu, \beta}^{(a)} \delta_{j_2, j_3} \delta(\tau_3 - \tau_2) \right] \\
&= \frac{\partial}{\partial \tau_3} \left[\Gamma_a^0(j_1, \tau_1; j_2, \tau_2; j_3, \tau_3) \right]_{\alpha, \beta} - 2 \sum_{s \in \text{n.n. of } j_3} \left[\Gamma_a^{j_3, s}(j_1, \tau_1; j_2, \tau_2; j_3, \tau_3) \right]_{\alpha, \beta} \quad (\text{B.161})
\end{aligned}$$

B.4.8 Fourier space Ward identities

As in the continuum case, the translational invariance of our system will lead to simplifications. In particular, we should look at our functions in Fourier space and use the real space translational invariance properties

$$G(\mathbf{s}_1, \tau_1; \mathbf{s}_2, \tau_2) = G(\mathbf{s}_1 - \mathbf{s}_2, \tau_1 - \tau_2), \quad (\text{B.162})$$

$$[\Gamma^0(\mathbf{s}_1, \tau_1; \mathbf{s}_2, \tau_2; \mathbf{s}_3, \tau_3)] = [\Gamma^0(\mathbf{s}_1 - \mathbf{s}_3, \tau_1 - \tau_3; \mathbf{s}_2 - \mathbf{s}_3, \tau_2 - \tau_3)], \quad (\text{B.163})$$

and

$$\begin{aligned}
& [\Gamma^{\mathbf{r}_1, \mathbf{r}_2}(\mathbf{s}_1, \tau_1; \mathbf{s}_2, \tau_2; \mathbf{s}_3, \tau_3)] \\
&= [\Gamma^{\mathbf{r}_1 - \mathbf{s}_3, \mathbf{r}_2 - \mathbf{s}_3}(\mathbf{s}_1 - \mathbf{s}_3, \tau_1 - \tau_3; \mathbf{s}_2 - \mathbf{s}_3, \tau_2 - \tau_3)]. \quad (\text{B.164})
\end{aligned}$$

We Fourier transform each of these Equations, yielding

$$\begin{aligned} & \int \int d\tau_1 d\tau_2 \sum_{\mathbf{s}_1, \mathbf{s}_2} e^{i(\mathbf{k}_1 \cdot \mathbf{s}_1 + \mathbf{k}_2 \cdot \mathbf{s}_2 + \omega_1 \tau_1 + \omega_2 \tau_2)} G^{-1}(\mathbf{s}_1 - \mathbf{s}_2, \tau_1 - \tau_2) \\ &= \int \int d\chi d\tau_2 \sum_{\ell, \mathbf{s}_2} e^{i(\mathbf{k}_1 \cdot (\ell + \mathbf{s}_2) + \mathbf{k}_2 \cdot \mathbf{s}_2) + \omega_1 (\chi + \tau_2) + \omega_2 \tau_2} G^{-1}(\ell, \chi) \end{aligned} \quad (\text{B.165})$$

$$= \int d\chi \sum_{\ell} e^{i(\mathbf{k}_1 \cdot \ell + \omega_1 \chi)} G^{-1}(\ell, \chi) \left[\int d\tau_2 \sum_{\mathbf{s}_2} e^{i((\mathbf{k}_1 + \mathbf{k}_2) \cdot \mathbf{s}_2 + (\omega_1 + \omega_2) \tau_2)} \right] \quad (\text{B.166})$$

$$= 2\pi N \delta(\mathbf{k}_1 + \mathbf{k}_2) \delta(\omega_1 + \omega_2) \int d\chi \sum_{\ell} e^{i(\mathbf{k}_1 \cdot \ell + \omega_1 \chi)} G^{-1}(\mathbf{k}_1, \omega_1) \quad (\text{B.167})$$

where we defined

$$G^{-1}(\mathbf{k}, \omega) = \int d\chi \sum_{\mathbf{s}} e^{i(\mathbf{k} \cdot \mathbf{s} + \omega \tau)} G(\mathbf{s}, \tau). \quad (\text{B.168})$$

For $[\Gamma_a^{jj}]$, we similarly obtain

$$\begin{aligned} & \int \int \int d\tau_1 d\tau_2 d\tau_3 \sum_{\mathbf{s}_1, \mathbf{s}_2, \mathbf{s}_3} e^{i(\mathbf{k}_1 \cdot \mathbf{s}_1 + \mathbf{k}_2 \cdot \mathbf{s}_2 + \mathbf{k}_3 \cdot \mathbf{s}_3 + \omega_1 \tau_1 + \omega_2 \tau_2 + \omega_3 \tau_3)} \\ & \quad [\Gamma^{\mathbf{r}_1 - \mathbf{s}_3, \mathbf{r}_2 - \mathbf{s}_3}(\mathbf{s}_1 - \mathbf{s}_3, \tau_1 - \tau_3; \mathbf{s}_2 - \mathbf{s}_3, \tau_2 - \tau_3)] \\ &= \int \int \int d\chi_1 d\chi_2 d\tau_3 \sum_{\ell_1, \ell_2, \mathbf{s}_3} e^{i(\mathbf{k}_1 \cdot (\ell_1 + \mathbf{s}_3) + \mathbf{k}_2 \cdot (\ell_2 + \mathbf{s}_3) + \mathbf{k}_3 \cdot \mathbf{s}_3 + \omega_1 (\chi_1 + \tau_3) + \omega_2 (\chi_2 + \tau_3) + \omega_3 \tau_3)} \\ & \quad \times [\Gamma^{\mathbf{r}_1 - \mathbf{s}_3, \mathbf{r}_2 - \mathbf{s}_3}(\ell_1, \chi_1; \ell_2, \chi_2)] \\ &= \int \int \int d\chi_1 d\chi_2 d\tau_3 \sum_{\ell_1, \ell_2, \mathbf{s}_3} e^{i(\mathbf{k}_1 \cdot \ell_1 + \mathbf{k}_2 \cdot \ell_2 + \omega_1 \chi_1 + \omega_2 \chi_2)} e^{i((\mathbf{k}_1 + \mathbf{k}_2 + \mathbf{k}_3) \cdot \mathbf{s}_3 + (\omega_1 + \omega_2 + \omega_3) \tau_3)} \\ & \quad \times [\Gamma^{\mathbf{r}_1 - \mathbf{s}_3, \mathbf{r}_2 - \mathbf{s}_3}(\ell_1, \chi_1; \ell_2, \chi_2)]. \end{aligned} \quad (\text{B.169})$$

Further simplification is possible by considering the superscripts on the Γ and the structure of the vertex term in the Ward identities. In particular, adapting to the notation used in this section, the indices have the form $\sum_{\mathbf{j} \in \text{n.n. of } \mathbf{s}_3} \Gamma^{\mathbf{j}, \mathbf{s}_3}$. Consequently, when we shift the summation variables by \mathbf{s}_3 , the second index vanishes, while the first goes to $\mathbf{j} - \mathbf{s}_3$. Furthermore, since the \mathbf{j} -summation runs over the nearest neighbors of \mathbf{s}_3 , the indices $\mathbf{j} - \mathbf{s}_3$ in the summation are independent

of \mathbf{s}_3 . Dropping the first index since it is zero, we have

$$\begin{aligned}
& \int \int \int d\tau_1 d\tau_2 d\tau_3 \sum_{\mathbf{s}_1, \mathbf{s}_2, \mathbf{s}_3} e^{i(\mathbf{k}_1 \cdot \mathbf{s}_1 + \mathbf{k}_2 \cdot \mathbf{s}_2 + \mathbf{k}_3 \cdot \mathbf{s}_3 + \omega_1 \tau_1 + \omega_2 \tau_2 + \omega_3 \tau_3)} \\
& \quad [\Gamma^\zeta(\mathbf{s}_1 - \mathbf{s}_3, \tau_1 - \tau_3; \mathbf{s}_2 - \mathbf{s}_3, \tau_2 - \tau_3)] \\
& = \int \int \int d\chi_1 d\chi_2 \sum_{\ell_1, \ell_2} e^{i(\mathbf{k}_1 \cdot \ell_1 + \mathbf{k}_2 \cdot \ell_2 + \omega_1 \chi_1 + \omega_2 \chi_2)} [\Gamma^\zeta(\ell_1, \chi_1; \ell_2, \chi_2)] \\
& \quad \times \left[\int d\tau_3 \sum_{\mathbf{s}_3} e^{i((\mathbf{k}_1 + \mathbf{k}_2 + \mathbf{k}_3) \cdot \mathbf{s}_3 + (\omega_1 + \omega_2 + \omega_3) \tau_3)} \right] \\
& = 2\pi N \delta_{\mathbf{k}_1 + \mathbf{k}_2 + \mathbf{k}_3} \delta(\omega_1 + \omega_2 + \omega_3) [\Gamma^\zeta(\mathbf{k}_1, \omega_1; -\mathbf{k}_2, -\omega_2)]. \quad (\text{B.170})
\end{aligned}$$

Integrating and summing against

$$\int d\tau_1 \int d\tau_2 \int d\tau_3 \sum_{\mathbf{j}_1, \mathbf{j}_2, \mathbf{j}_3} e^{i(\mathbf{k} \cdot \mathbf{j}_1 - \mathbf{k}' \cdot \mathbf{j}_2 - \mathbf{q} \cdot \mathbf{j}_3 + \omega \tau_1 - \omega' \tau_2 - \nu \tau_3)},$$

we obtain

$$\begin{aligned}
& \int \int \int d\tau_1 d\tau_2 d\tau_3 \\
& \quad \sum_{\mathbf{j}_1, \mathbf{j}_2, \mathbf{j}_3} e^{i(\mathbf{k} \cdot \mathbf{j}_1 - \mathbf{k}' \cdot \mathbf{j}_2 - \mathbf{q} \cdot \mathbf{j}_3 + \omega \tau_1 - \omega' \tau_2 - \nu \tau_3)} \sum_{\mu} \delta_{j_1, j_3} \delta(\tau_3 - \tau_1) \sigma_{\alpha, \mu}^{(a)} G_{\mu, \beta}^{-1}(j_3, \tau_3; j_2, \tau_2) \\
& - \int \int \int d\tau_1 d\tau_2 d\tau_3 \sum_{\mathbf{j}_1, \mathbf{j}_2, \mathbf{j}_3} e^{i(\mathbf{k} \cdot \mathbf{j}_1 - \mathbf{k}' \cdot \mathbf{j}_2 - \mathbf{q} \cdot \mathbf{j}_3 + \omega \tau_1 - \omega' \tau_2 - \nu \tau_3)} \\
& \quad \times \sum_{\mu} G_{\alpha, \mu}^{-1}(j_1, \tau_1; j_3, \tau_3) \sigma_{\mu, \beta}^{(a)} \delta_{j_2, j_3} \delta(\tau_3 - \tau_2) \\
& = \int \int \int d\tau_1 d\tau_2 d\tau_3 \sum_{\mathbf{j}_1, \mathbf{j}_2, \mathbf{j}_3} e^{i(\mathbf{k} \cdot \mathbf{j}_1 - \mathbf{k}' \cdot \mathbf{j}_2 - \mathbf{q} \cdot \mathbf{j}_3 + \omega \tau_1 - \omega' \tau_2 - \nu \tau_3)} \quad (\text{B.171})
\end{aligned}$$

$$\begin{aligned}
& \times \frac{\partial}{\partial \tau_3} [\Gamma_a^0(j_1, \tau_1; j_2, \tau_2; j_3, \tau_3)]_{\alpha, \beta} \\
& - \int \int \int d\tau_1 d\tau_2 d\tau_3 \sum_{\mathbf{j}_1, \mathbf{j}_2, \mathbf{j}_3} e^{i(\mathbf{k} \cdot \mathbf{j}_1 - \mathbf{k}' \cdot \mathbf{j}_2 - \mathbf{q} \cdot \mathbf{j}_3 + \omega \tau_1 - \omega' \tau_2 - \nu \tau_3)} 2 \sum_{s \in \text{n.n. of } j_3} \quad (\text{B.172})
\end{aligned}$$

$$\times [\Gamma_a^{j_3, s}(j_1, \tau_1; j_2, \tau_2; j_3, \tau_3)]_{\alpha, \beta} \quad (\text{B.173})$$

Consequently, Fourier transforming Eq. (B.161) with the advantage of this translational invariance and also using the fact that the Green's functions are diagonal,

$$G_{\alpha\beta} = \delta_{\alpha, \beta} G_{\alpha}, \quad (\text{B.174})$$

we obtain

$$\begin{aligned}
& 2\pi N \delta(\mathbf{k} - \mathbf{q} - \mathbf{k}', \omega - \nu - \omega') \left\{ \sigma_{\alpha,\beta}^{(a)} G_{\mu}^{-1}(\mathbf{k} - \mathbf{q}, \omega - \nu) - G_{\alpha}^{-1}(\mathbf{k}_1; \omega) \sigma_{\alpha,\beta}^{(a)} \right\} \\
& = (2\pi N \delta_{\mathbf{k}-\mathbf{q}-\mathbf{k}'} \delta(\omega - \nu - \omega')) i\nu \left[\Gamma_a^0(\mathbf{k}, \omega; -\mathbf{k}', -\omega') \right]_{\alpha,\beta} \\
& - 2 \iiint d\tau_1 d\tau_2 d\tau_3 \sum_{\mathbf{j}_1, \mathbf{j}_2, \mathbf{j}_3} e^{i(\mathbf{k} \cdot \mathbf{j}_1 - \mathbf{k}' \cdot \mathbf{j}_2 - \mathbf{q} \cdot \mathbf{j}_3 + \omega\tau_1 - \omega'\tau_2 - \nu\tau_3)} \quad (\text{B.175}) \\
& \times \sum_{s \in \text{n.n. of } j_3} \left[\Gamma_a^{j_3, s}(j_1, \tau_1; j_2, \tau_2; j_3, \tau_3) \right]_{\alpha,\beta}.
\end{aligned}$$

This result may be simplified further. For example, for a cubic lattice, we may exploit translational invariance to write

$$\begin{aligned}
& \iiint d\tau_1 d\tau_2 d\tau_3 \sum_{\mathbf{j}_1, \mathbf{j}_2, \mathbf{j}_3} e^{i(\mathbf{k} \cdot \mathbf{j}_1 - \mathbf{k}' \cdot \mathbf{j}_2 - \mathbf{q} \cdot \mathbf{j}_3 + \omega\tau_1 - \omega'\tau_2 - \nu\tau_3)} \\
& \quad \times \sum_{s \in \text{n.n. of } j_3} \left[\Gamma_a^{j_3, s}(j_1, \tau_1; j_2, \tau_2; j_3, \tau_3) \right]_{\alpha,\beta} \\
& = \iiint d\tau_1 d\tau_2 d\tau_3 \sum_{\mathbf{j}_1, \mathbf{j}_2, \mathbf{j}_3} e^{i(\mathbf{k} \cdot \mathbf{j}_1 - \mathbf{k}' \cdot \mathbf{j}_2 - \mathbf{q} \cdot \mathbf{j}_3 + \omega\tau_1 - \omega'\tau_2 - \nu\tau_3)} \\
& \quad \times \sum_{\zeta = \pm x, \pm y, \pm z} \left[\Gamma_a^{0, \zeta}(j_1 - j_3, \tau_1 - \tau_3; j_2 - j_3, \tau_2 - \tau_3) \right]_{\alpha,\beta} \\
& = \iiint d\tau_1 d\tau_2 d\tau_3 \sum_{\mathbf{j}_1, \mathbf{j}_2, \mathbf{j}_3} e^{i(\mathbf{k} \cdot \mathbf{j}_1 - \mathbf{k}' \cdot \mathbf{j}_2 - \mathbf{q} \cdot \mathbf{j}_3 + \omega\tau_1 - \omega'\tau_2 - \nu\tau_3)} \\
& \quad \times \sum_{\zeta = x, y, Z} \left[\Gamma_a^{0, \zeta}(j_1 - j_3, \tau_1 - \tau_3; j_2 - j_3, \tau_2 - \tau_3) \right. \\
& \quad \left. + \Gamma_a^{0, -\zeta}(j_1 - j_3, \tau_1 - \tau_3; j_2 - j_3, \tau_2 - \tau_3) \right]_{\alpha,\beta}. \quad (\text{B.176})
\end{aligned}$$

Then the final simplification comes from using translational invariance to write

$$\left[\Gamma_a^{0, -\zeta}(j_1, \tau_1; j_2, \tau_2) \right]_{\alpha,\beta} = \left[\Gamma_a^{\zeta, 0}(j_1 + \zeta, \tau_1; j_2 + \zeta, \tau_2) \right]_{\alpha,\beta} \quad (\text{B.177})$$

and the bond-reversal anti-symmetry of a_{ij} exploited earlier to write

$$\left[\Gamma_a^{\zeta, 0}(j_1 + \zeta, \tau_1; j_2 + \zeta, \tau_2) \right]_{\alpha,\beta} = - \left[\Gamma_a^{0, \zeta}(j_1 + \zeta, \tau_1; j_2 + \zeta, \tau_2) \right]_{\alpha,\beta}. \quad (\text{B.178})$$

Using this in Eq. (B.176) yields

$$\begin{aligned}
& \iiint d\tau_1 d\tau_2 d\tau_3 \sum_{\mathbf{j}_1, \mathbf{j}_2, \mathbf{j}_3} e^{i(\mathbf{k} \cdot \mathbf{j}_1 - \mathbf{k}' \cdot \mathbf{j}_2 - \mathbf{q} \cdot \mathbf{j}_3 + \omega\tau_1 - \omega'\tau_2 - \nu\tau_3)} \\
& \quad \times \sum_{s \in \text{n.n. of } j_3} [\Gamma_a^{j_3, s}(j_1, \tau_1; j_2, \tau_2; j_3, \tau_3)]_{\alpha, \beta} \\
& = \iiint d\tau_1 d\tau_2 d\tau_3 \sum_{\mathbf{j}_1, \mathbf{j}_2, \mathbf{j}_3} e^{i(\mathbf{k} \cdot \mathbf{j}_1 - \mathbf{k}' \cdot \mathbf{j}_2 - \mathbf{q} \cdot \mathbf{j}_3 + \omega\tau_1 - \omega'\tau_2 - \nu\tau_3)} \\
& \quad \times \sum_{\zeta=x,y,z} [\Gamma_a^{0, \zeta}(j_1, \tau_1; j_2, \tau_2) - \Gamma_a^{0, \zeta}(j_1 + \zeta, \tau_1; j_2 + \zeta, \tau_2)]_{\alpha, \beta} \quad (\text{B.179})
\end{aligned}$$

So finally, substituting this vertex Fourier transform, and the formulas for vertex Fourier transforms from earlier, into Eq. (B.176), we obtain

$$\begin{aligned}
\sigma_{\alpha, \beta}^{(a)} G_\mu^{-1}(\mathbf{k} - \mathbf{q}, \omega - \nu) - G_\alpha^{-1}(\mathbf{k}; \omega) \sigma_{\alpha, \beta}^{(a)} & = i\nu [\Gamma_a^0(\mathbf{k}, \omega; \mathbf{k} - \mathbf{q}, \omega - \nu)]_{\alpha, \beta} \\
& - 2 \sum_{\zeta=\hat{x}, \hat{y}, \hat{z}} (1 - e^{i\mathbf{q} \cdot \zeta}) [\Gamma_a^{0, \zeta}(\mathbf{k}, \omega; -\mathbf{k}', -\omega')]_{\alpha, \beta}. \quad (\text{B.180})
\end{aligned}$$

This is final momentum-space expression of the Ward identity for the $SU(2)$ symmetric Bose-Hubbard model. Note that as $\mathbf{q} \rightarrow 0$, it reduces to the expression obtained in the continuum — the factor of two difference is because in the lattice case we counted each bond twice. We could also write these out component-by-component, analogous to Eqs. (B.95), (B.96), (B.97), and (B.98). The form is identical, replacing the spatial q_μ 's by the $2(1 - e^{iq_\mu|\zeta})$.

B.5 Rf spectra

Given Eqs. (B.94) and (B.180), we would like to examine the consequences for the rf spectra. Although my main goal is to determine the rf spectra for the Bose-Hubbard model (which will be explained elsewhere), here we would like to check that things work for a dilute gas.

B.5.1 Rf spectra in terms of exact single particle Green's functions and interaction vertex

Pethick and Stoof's PRA, Stoof's notes, and Stoof's book give the rf spectra $I(\omega)$ as the analytic continuation of $I(i\nu_n)$ (where ν_n is a Matsubara frequency), with

$$I(i\nu_n) \propto \sum_{\omega_n} G_2(i\omega_n)G_1(i\omega_n - i\nu_n) \times [\gamma_x^0(i\omega_n, i\omega_n - i\nu_n) + \Delta\Gamma_x^0(i\omega_n, i\omega_n - i\nu_n)]_{12} \quad (\text{B.181})$$

This is a standard result for the two-particle response functions in terms of Green's functions and vertices.

We will use our results for the Green's functions G_α and vertex corrections $\Delta\Gamma$ to calculate this for the dilute gas now.

B.5.2 Non-interacting gas

In the non-interacting gas, the self energy is zero. Also, we may canonically transformed away the vacuum energy difference between states 1 and 2. Then defining the dispersion

$$\epsilon_{\mathbf{k}} = \frac{\hbar^2 k^2}{2m}, \quad (\text{B.182})$$

one finds the Green's functions

$$G_\alpha(i\omega_n) = \frac{1}{i\omega_n - \epsilon_{\mathbf{k}}}. \quad (\text{B.183})$$

Our Ward identities imply that the vertex corrections are zero since the self energies are zero and the system is $SU(2)$ symmetric. Consequently, Eq. (B.181) gives the rf spectra to be

$$I(i\nu_n) \propto \sum_{\omega_n} \frac{1}{i\omega_n - \epsilon_{\mathbf{k}}} \frac{1}{i\omega_n - i\nu_n - \epsilon_{\mathbf{k}}}. \quad (\text{B.184})$$

Working at zero temperature, so that the sums are contour integrals, we have

$$I(i\nu_n) \propto \frac{1}{i\nu_n}. \quad (\text{B.185})$$

I have taken the particle pole (from G_2) to be in the upper half of the complex plane and the hole pole (from G_1) to be in the lower complex plane.

As expected, we have an un-shifted delta function peak due to the $SU(2)$ symmetry of the problem.

B.5.3 Dilute gas: condensed and non-condensed

Condensed gas.—In the dilute, fully condensed gas, the self energies are

$$\Sigma_2 = \Sigma_1 = \frac{4\pi\hbar^2 a}{m}\rho, \quad (\text{B.186})$$

where ρ is the particle density. Again, we have $SU(2)$ symmetry and the Ward identities are zero, so the rf spectra is an unshifted delta function

$$I(i\nu_n) \propto \frac{1}{i\nu_n} \quad (\text{B.187})$$

identical to the non-interacting gas result, Eq. (B.185).

Thermal, non-condensed gas.—In the thermal gas, the self energies are

$$\Sigma_2 = \frac{8\pi\hbar^2 a_{12}}{m}\rho \quad (\text{B.188})$$

and

$$\Sigma_1 = \frac{4\pi\hbar^2 a_{11}}{m}\rho, \quad (\text{B.189})$$

where the factor of 2 in Σ_2 comes from the fact that both direct and exchange terms contribute since states 1 and 2 are distinguishable, and that all the particle density ρ is in state 1. Then at the $SU(2)$ symmetric $a_{12} = a_{11}$ point the rf spectra neglecting vertex corrections would be a delta function shifted by $\frac{4\pi\hbar^2 a}{m}\rho$. This is

important point raised by Pethick and Stoof regarding the “factor of two” anomaly of a naive mean-field result.

Just for fun, let’s see what rf spectra our vertex corrections derived from the Ward identity give for arbitrary values of a_{12} and a_{11} , even though the Ward identity is only valid for the $SU(2)$ symmetry point with $a_{12} = a_{11}$. We take the vertex correction from Eq. (B.109), noting that only the ν component of q is non-zero in an rf spectra experiment. For convenience, we also set the dispersions of each state to zero, since they are the same for the two states. Then the spectrum from Eq. (B.184) is

$$I(i\nu_n) \propto \sum_{\omega_n} G_2(i\omega_n)G_1(i\omega_n - i\nu_n) \left(1 + \frac{\Sigma_1 - \Sigma_2}{i\nu_n}\right) \quad (\text{B.190})$$

giving

$$I(i\nu_n) \propto \sum_{\omega_n} \frac{1}{i\omega_n - \Sigma_2} \frac{1}{i\omega_n - i\nu_n - \Sigma_1} \left(1 + \frac{\Sigma_1 - \Sigma_2}{i\nu_n}\right) \quad (\text{B.191})$$

$$= \frac{1}{i\nu_n - (\Sigma_2 - \Sigma_1)} \left(1 + \frac{\Sigma_1 - \Sigma_2}{i\nu_n}\right) \quad (\text{B.192})$$

$$= \frac{1}{i\nu_n}. \quad (\text{B.193})$$

This is, as it was derived to be, correct in the $SU(2)$ symmetric case, but wrong everywhere else.

A second option is to *literally* use the vertex correction at the $SU(2)$ symmetric point, $\Delta [\Gamma_x^0]_{12} = -4\pi\hbar^2 a\rho/m$, to which it evaluates there, rather than the symbolic expression. Then the rf spectra is

$$I(i\nu_n) \propto \sum_{\omega_n} \frac{1}{i\omega_n - \Sigma_2} \frac{1}{i\omega_n - i\nu_n - \Sigma_1} \left(1 + \frac{\Sigma_1}{i\nu_n}\right) \quad (\text{B.194})$$

$$= \frac{1}{i\nu_n - (\Sigma_2 - \Sigma_1)} \left(\frac{i\nu_n - \Sigma_1}{i\nu_n}\right) \quad (\text{B.195})$$

but this doesn’t help.

To summarize, while we see the derived Ward identities indeed reproduce the appropriate response function when there is $SU(2)$ symmetry, this is a trivial result. Moreover, it is not obvious how to extend this to work when the symmetry is broken, even slowly.

Note: I relied heavily on Dickerscheid, Stoof, et al.'s notes for the fermion rf spectra to derive these Ward identities.

Bibliography

- [1] B. Capogrosso-Sansone, N. V. Prokof'ev, and B. V. Svistunov, *Phys. Rev. B* **75**, 134302 (2007).
- [2] P. Coleman, *Annales Henri Poincare* **4**, 559 (2003).
- [3] N. Goldenfeld, *Lectures On Phase Transitions And The Renormalization Group*, illustrated edition ed. (Addison-Wesley, Reading, MA, 1992).
- [4] A. Altland and B. Simons, *Condensed Matter Field Theory* (Cambridge University Press, The Edinburgh Building, Cambridge CB2 8RU, UK, 2006).
- [5] P. M. Chaikin and T. C. Lubensky, *Principles of Condensed Matter Physics*, 1st ed. (Cambridge University Press, The Edinburgh Building, Cambridge CB2 2RU, UK, 2000).
- [6] J. Cardy, *Scaling and Renormalization in Statistical Physics* (Cambridge University Press, The Edinburgh Building, Cambridge CB2 2RU, UK, 1996).
- [7] J. Zinn-Justin, *Quantum Field Theory and Critical Phenomena*, 4 ed. (Oxford University Press, USA, Oxford University Press Inc., New York, 2002).
- [8] A. Zee, *Quantum Field Theory in a Nutshell: Second Edition*, 2 ed. (Princeton University Press, 41 William Street, Princeton, New Jersey 08540, 2010).
- [9] G. I. Menon, arxiv:1003.2032 (2010).
- [10] P. Turchin, *Complex Population Dynamics: A Theoretical/Empirical Synthesis (MPB-35)* (Princeton University Press, 41 William Street, Princeton, New Jersey 08540, 2003).
- [11] M. J. Keeling and P. Rohani, *Modeling Infectious Diseases in Humans and*

- Animals*, 1 ed. (Princeton University Press, 41 William Street, Princeton, New Jersey 08540, 2007).
- [12] R. M. Anderson, R. M. May, and B. Anderson, *Infectious Diseases of Humans: Dynamics and Control* (Oxford University Press, USA, New York, 1992).
- [13] O. Diekmann and J. A. P. Heesterbeek, *Mathematical Epidemiology of Infectious Diseases: Model Building, Analysis and Interpretation*, 1 ed. (Wiley, Oxford University Press Inc., New York, 2000).
- [14] D. Kondepudi and I. Prigogine, *Modern Thermodynamics: From Heat Engines to Dissipative Structures* (Wiley, Baffins Lane, Chichester, West Sussex PO19 1UD, England, 1998).
- [15] G. K. Chan, J. J. Dorando, D. Ghosh, J. Hachmann, E. Neuscamman, H. Wang, and T. Yanai, in *Frontiers in Quantum Systems in Chemistry and Physics, Progress in Theoretical Chemistry and Physics*, edited by S. Wilson, P. Grout, J. Maruani, G. Delgado-Barrio, and P. Piecuch (Springer, Netherlands, 2008), pp. 49–65.
- [16] M. J. Feigenbaum, *Journal of Statistical Physics* **21**, 669 (1979).
- [17] S. Coles, *An Introduction to Statistical Modeling of Extreme Values*, 1 ed. (Springer-Verlag, London, UK, 2001).
- [18] M. Mézard and A. Montanari, *Information, Physics, and Computation* (Oxford University Press, USA, New York, 2009).
- [19] B. S. Kerner, *Introduction to Modern Traffic Flow Theory and Control: The Long Road to Three-Phase Traffic Theory*, 1 ed. (Springer, London, UK, 2009).
- [20] S. A. Marvel, S. H. Strogatz, and J. M. Kleinberg, *Physical Review Letters* **103**, 198701 (2009).
- [21] P. W. Anderson, K. Arrow, and D. Pines, *The Economy As An Evolving Complex System* (Westview Press, USA, 1988).
- [22] W. B. Arthur and S. N. Durlauf, *The Economy As An Evolving Complex System II* (Westview Press, USA, 1997).

- [23] L. E. Blume and S. N. Durlauf, *The Economy As an Evolving Complex System, III: Current Perspectives and Future Directions (Santa Fe Institute Studies on the Sciences of Complexity)*, illustrated edition ed. (Oxford University Press, USA, New York, 2005).
- [24] S. H. Strogatz, *Sync: How Order Emerges From Chaos In the Universe, Nature, and Daily Life* (Hyperion, 77 West 66th Street, New York, New York 10023-6298, 2004).
- [25] I. Stewart and J. S. Cohen, *The Collapse of Chaos: Discovering Simplicity in a Complex World* (Penguin Books Ltd, 80 Strand, London WC2R 0R L, England, 2000).
- [26] J. Gleick, *Chaos: Making a New Science*, any rep ed. (Penguin (Non-Classics), 80 Strand, London WC2R 0R L, England, 2008).
- [27] A. Y. Kitaev, *Annals of Physics* **303**, 2 (2003).
- [28] S. A. Diddams, D. J. Jones, J. Ye, S. T. Cundiff, J. L. Hall, J. K. Ranka, R. S. Windeler, R. Holzwarth, T. Udem, and T. W. Hensch, *Physical Review Letters* **84**, 5102 (2000).
- [29] M. Fischer, N. Kolachevsky, M. Zimmermann, R. Holzwarth, T. Udem, T. W. Hensch, M. Abgrall, J. Grnert, I. Maksimovic, S. Bize, H. Marion, F. P. D. Santos, P. Lemonde, G. Santarelli, P. Laurent, A. Clairon, C. Salomon, M. Haas, U. D. Jentschura, and C. H. Keitel, *Physical Review Letters* **92**, 230802 (2004).
- [30] A. Cho, *Science* **320**, 312 (2008).
- [31] Z. Gu, M. Levin, and X. Wen, arxiv:0807.2010 (2008).
- [32] J. I. Cirac and F. Verstraete, *Journal of Physics A: Mathematical and Theoretical* **42**, 504004 (2009).
- [33] I. Bloch, J. Dalibard, and W. Zwerger, *Rev. Mod. Phys.* **80**, 885 (2008).
- [34] S. Giorgini, L. P. Pitaevskii, and S. Stringari, *Reviews of Modern Physics* **80**, 1215 (2008).
- [35] K. Maeda, G. Baym, and T. Hatsuda, *Physical Review Letters* **103**, 085301 (2009).

- [36] M. G. Alford, A. Schmitt, K. Rajagopal, and T. Schfer, *Reviews of Modern Physics* **80**, 1455 (2008).
- [37] P. Braun-Munzinger and J. Wambach, *Reviews of Modern Physics* **81**, 1031 (2009).
- [38] D. Hanneke, S. Fogwell, and G. Gabrielse, *Physical Review Letters* **100**, 120801 (2008).
- [39] M. O. Scully and M. S. Zubairy, *Quantum Optics* (Cambridge University Press, The Edinburgh Building, Cambridge CB2 8RU, UK, 1997).
- [40] S. Blatt, A. D. Ludlow, G. K. Campbell, J. W. Thomsen, T. Zelevinsky, M. M. Boyd, J. Ye, X. Baillard, M. Fouch, R. L. Targat, A. Bruschi, P. Lemonde, M. Takamoto, F. Hong, H. Katori, and V. V. Flambaum, *Physical Review Letters* **100**, 140801 (2008).
- [41] B. Barbier, M. Gargaud, H. Martin, J. Reisse, and C. de Duve, *Lectures in Astrobiology* (Springer Science & Business, London, UK, 2006), p. 556.
- [42] D. G. Andrews, *An Introduction to Atmospheric Physics*, 2nd ed. (Cambridge University Press, The Edinburgh Building, Cambridge CB2 2RU, UK, 2010).
- [43] G. Guyot, *Physics of the Environment and Climate* (John Wiley & Sons, USA, 1998).
- [44] A. Assion, T. Baumert, M. Bergt, T. Brixner, B. Kiefer, V. Seyfried, M. Strehle, and G. Gerber, *Science* **282**, 919 (1998).
- [45] W. Demtröder, *An Introduction to Atomic and Molecular Physics*, 1 ed. (Springer, London, UK, 2005).
- [46] R. Cotterill, *Biophysics: An Introduction*, 1st ed. (Wiley, Baffins Lane, Chichester, West Sussex PO19 1UD, England, 2002).
- [47] F. J. Duarte, *Tunable Laser Optics*, 1 ed. (CRC Press, 6000 Broken Sound Parkway NW, Suite 300, Boca Raton, FL 33487-2742, 2003).
- [48] C. J. Pethick and H. Smith, *Bose-Einstein condensation in dilute gases* (Cambridge University Press, The Edinburgh Building, Cambridge CB2 2RU, UK, 2001).

- [49] N. Berloff, *Physics* **2**, 61 (2009).
- [50] E. A. L. Henn, J. A. Seman, G. Roati, K. M. F. Magalhes, and V. S. Bagnato, *Physical Review Letters* **103**, 045301 (2009).
- [51] D. Petrov, D. Gangardt, and G. Shlyapnikov, *Journal de Physique IV* **116**, 5 (2004).
- [52] O. Fischer, M. Kugler, I. Maggio-Aprile, C. Berthod, and C. Renner, *Reviews of Modern Physics* **79**, 353 (2007).
- [53] C. H. Chen, S. Cheong, and A. S. Cooper, *Physical Review Letters* **71**, 2461 (1993).
- [54] G. Veeravalli, E. Kuhnle, P. Dyke, and C. J. Vale, *Physical Review Letters* **101**, 250403 (2008).
- [55] M. M. Parish, S. K. Baur, E. J. Mueller, and D. A. Huse, *Physical Review Letters* **99**, 250403 (2007).
- [56] T. Lahaye, C. Menotti, L. Santos, M. Lewenstein, and T. Pfau, *Reports on Progress in Physics* **72**, 126401 (2009).
- [57] Q. Zhou and T. Ho, arxiv:0703169 (2007).
- [58] A. J. Daley, J. M. Taylor, S. Diehl, M. Baranov, and P. Zoller, arxiv **0810.5153**, (2008).
- [59] H. J. Metcalf, P. van der Straten, and P. Straten, *Laser Cooling and Trapping*, corrected ed. (Springer, London, UK, 1999).
- [60] F. P. D. Santos, J. Lonard, J. Wang, C. J. Barrelet, F. Perales, E. Rasel, C. S. Unnikrishnan, M. Leduc, and C. Cohen-Tannoudji, *Physical Review Letters* **86**, 3459 (2001).
- [61] A. Robert, O. Sirjean, A. Browaeys, J. Poupard, S. Nowak, D. Boiron, C. I. Westbrook, and A. Aspect, *Science* **292**, 461 (2001).
- [62] A. Griesmaier, J. Werner, S. Hensler, J. Stuhler, and T. Pfau, *Physical Review Letters* **94**, 160401 (2005).

- [63] Y. Takasu, K. Maki, K. Komori, T. Takano, K. Honda, M. Kumakura, T. Yabuzaki, and Y. Takahashi, *Physical Review Letters* **91**, 040404 (2003).
- [64] S. Kraft, F. Vogt, O. Appel, F. Riehle, and U. Sterr, *Physical Review Letters* **103**, 130401 (2009).
- [65] S. Stellmer, M. K. Tey, B. Huang, R. Grimm, and F. Schreck, *Physical Review Letters* **103**, 200401 (2009).
- [66] Y. N. M. de Escobar, P. G. Mickelson, M. Yan, B. J. DeSalvo, S. B. Nagel, and T. C. Killian, *Physical Review Letters* **103**, 200402 (2009).
- [67] K. Ni, S. Ospelkaus, M. H. G. de Miranda, A. Pe'er, B. Neyenhuis, J. J. Zirbel, S. Kotochigova, P. S. Julienne, D. S. Jin, and J. Ye, *Science* **322**, 231 (2008).
- [68] A. Ashkin, *Proceedings of the National Academy of Sciences of the United States of America* **94**, 4853 (1997).
- [69] M. Ueda and Y. Kawaguchi, 1001.2072 (2010).
- [70] W. S. Bakr, J. I. Gillen, A. Peng, S. Foelling, and M. Greiner, 0908.0174 (2009).
- [71] K. D. Nelson, X. Li, and D. S. Weiss, *Nat Phys* **3**, 556 (2007).
- [72] T. Gericke, P. Wurtz, D. Reitz, T. Langen, and H. Ott, *Nat Phys* **4**, 949 (2008).
- [73] N. Gemelke, X. Zhang, C. Hung, and C. Chin, *Nature* **460**, 995 (2009).
- [74] A. A. Abrikosov, *Methods of Quantum Field Theory in Statistical Physics*, revised ed. (Dover Publications, New York, USA, 1975).
- [75] L. D. Landau and L. M. Lifshitz, *Quantum Mechanics Non-Relativistic Theory, Third Edition: Volume 3*, 3 ed. (Butterworth-Heinemann, London, UK, 1981).
- [76] M. P. A. Fisher, P. B. Weichman, G. Grinstein, and D. S. Fisher, *Phys. Rev. B* **40**, 546570 (1989).

- [77] D. Jaksch, C. Bruder, J. I. Cirac, C. W. Gardiner, and P. Zoller, *Phys. Rev. Lett.* **81**, 31083111 (1998).
- [78] N. W. Ashcroft and N. D. Mermin, *Solid State Physics*, 1 ed. (Brooks Cole, USA, 1976).
- [79] N. Prokofev, B. Svistunov, and I. Tupitsyn, *Journal of Experimental and Theoretical Physics* **87**, 310 (1998).
- [80] K. Byczuk and D. Vollhardt, *Physical Review B (Condensed Matter and Materials Physics)* **77**, 235106 (2008).
- [81] J. K. Freericks and H. Monien, *Physical Review B* **53**, 2691 (1996).
- [82] J. K. Freericks, H. R. Krishnamurthy, Y. Kato, N. Kawashima, and N. Trivedi, *Physical Review A* **79**, 053631 (2009).
- [83] D. G. Fried, T. C. Killian, L. Willmann, D. Landhuis, S. C. Moss, D. Kleppner, and T. J. Greytak, *Phys. Rev. Lett.* **81**, 38113814 (1998).
- [84] I. Bloch, *Nature Physics* **1**, 23 (2005).
- [85] G. K. Campbell, J. Mun, M. Boyd, P. Medley, A. E. Leanhardt, L. G. Marcassa, D. E. Pritchard, and W. Ketterle, *Science* **313**, 649 (2006).
- [86] C. J. Pethick and H. T. C. Stoof, *Phys. Rev. A* **64**, 013618 (2001).
- [87] K. Gibble and S. Chu, *Physical Review Letters* **70**, 1771 (1993).
- [88] C. Fertig and K. Gibble, *Physical Review Letters* **85**, 1622 (2000).
- [89] G. K. Brennen, G. Pupillo, A. M. Rey, C. W. Clark, and C. J. Williams, *Journal of Physics B: Atomic, Molecular and Optical Physics* **38**, 1687 (2005).
- [90] P. Rabl, A. J. Daley, P. O. Fedichev, J. I. Cirac, and P. Zoller, *PRL* **91**, 110403 (2003).
- [91] M. Greiner, O. Mandel, T. Esslinger, T. W. Hansch, and I. Bloch, *Nature* **415**, 39 (2002).
- [92] S. Fölling, F. Gerbier, A. Widera, O. Mandel, T. Gericke, and I. Bloch, *Nature* **434**, 481 (2005).

- [93] S. Föolling, A. Widera, T. Muller, F. Gerbier, and I. Bloch, *Physical Review Letters* **97**, 060403 (2006).
- [94] M. Greiner, O. Mandel, T. W. Hansch, and I. Bloch, *Nature* **419**, 5154 (2002).
- [95] W. Ketterle, private communication, 2007.
- [96] M. R. Matthews, D. S. Hall, D. S. Jin, J. R. Ensher, C. E. Wieman, E. A. Cornell, F. Dalfovo, C. Minniti, and S. Stringari, *Physical Review Letters* **81**, 243 (1998).
- [97] E. G. M. van Kempen, S. J. J. M. F. Kokkelmans, D. J. Heinzen, and B. J. Verhaar, *Physical Review Letters* **88**, 093201 (2002).
- [98] L. Pollet, S. Rombouts, K. Heyde, and J. Dukelsky, *Phys. Rev. A* **69**, 043601 (2004).
- [99] S. Bergkvist, P. Henelius, and A. Rosengren, *PRA* **70**, 053601 (2004).
- [100] S. Wessel, F. Alet, M. Troyer, and G. G. Batrouni, *Phys. Rev. A* **70**, 053615 (2004).
- [101] G. G. Batrouni, V. Rousseau, R. T. Scalettar, M. Rigol, A. Muramatsu, P. J. H. Denteneer, and M. Troyer, *PRL* **89**, 117203 (2002).
- [102] B. DeMarco, C. Lannert, S. Vishveshwara, and T. Wei, *PRA* **71**, 063601 (2005).
- [103] B. Capogrosso-Sansone, E. Kozik, N. Prokof'ev, and B. Svistunov, *Physical Review A (Atomic, Molecular, and Optical Physics)* **75**, 013619 (2007).
- [104] M. Öktel, T. C. Killian, D. Kleppner, and L. S. Levitov, *Phys. Rev. A* **65**, 033617 (2002).
- [105] L. Landau and E. Lifshitz, *Statistical Physics I* (Butterworth Heinemann, London, UK, 1997).
- [106] J. Stenger, S. Inouye, A. P. Chikkatur, D. M. Stamper-Kurn, D. E. Pritchard, and W. Ketterle, *PRL* **82**, 45694573 (1999).
- [107] K. R. A. Hazzard and E. J. Mueller, *Physical Review A* **76**, (2007).

- [108] K. Sun, C. Lannert, and S. Vishveshwara, Phys. Rev. A **79**, 043422 (2009).
- [109] Y. Ohashi, M. Kitaura, and H. Matsumoto, Physical Review A (Atomic, Molecular, and Optical Physics) **73**, 033617 (2006).
- [110] M. Ö. Oktel and L. S. Levitov, Phys. Rev. Lett. **83**, 69 (1999).
- [111] I. H. Deutsch and P. S. Jessen, Phys. Rev. A **57**, 19721986 (1998).
- [112] N. Dupuis and K. Sengupta, Physica B: Condensed Matter **404**, 517 (2009).
- [113] K. Sengupta and N. Dupuis, Phys. Rev. A **71**, 033629 (2005).
- [114] S. Konabe, T. Nikuni, and M. Nakamura, Physical Review A (Atomic, Molecular, and Optical Physics) **73**, 033621 (2006).
- [115] C. Menotti and N. Trivedi, Physical Review B **77**, 235120 (2008).
- [116] G. Baym, Phys. Rev. **127**, 13911401 (1962).
- [117] C. P. Slichter, *Principles of Magnetic Resonance* (Springer-Verlag, New York, London, UK, 1990).
- [118] J. T. Stewart, J. P. Gaebler, and D. S. Jin, Nature **454**, 744 (2008).
- [119] K. R. A. Hazzard and E. J. Mueller, 0907.1332 (2009).
- [120] D. A. W. Hutchinson, E. Zaremba, and A. Griffin, PRL. **78**, 18421845 (1997).
- [121] S. Sachdev, *Quantum phase transitions* (Cambridge University Press, The Edinburgh Building, Cambridge CB2 2RU, UK, 2001).
- [122] J. R. Schrieffer, *Theory Of Superconductivity*, revised ed. (Perseus Books, New York, USA, 1999).
- [123] P. G. D. Gennes, *Superconductivity Of Metals And Alloys* (Westview Press, USA, 1999).
- [124] M. Tinkham, *Introduction to Superconductivity: Second Edition (Dover Books on Physics)*, 2 ed. (Dover Publications, New York, USA, 2004).

- [125] N. R. Cooper, arXiv **arXiv:0810.4398**, (2008).
- [126] S. Viefers, Journal of Physics: Condensed Matter **20**, 123202 (14pp) (2008).
- [127] E. J. Mueller, Physical Review A **70**, 041603 (2004).
- [128] A. S. Srensen, E. Demler, and M. D. Lukin, Physical Review Letters **94**, 086803 (2005).
- [129] M. Hafezi, A. S. Srensen, E. Demler, and M. D. Lukin, Physical Review A **76**, 023613 (2007).
- [130] Y. Lin, R. L. Compton, K. Jimenez-Garcia, J. V. Porto, and I. B. Spielman, Nature **462**, 628 (2009).
- [131] K. Osterloh, M. Baig, L. Santos, P. Zoller, and M. Lewenstein, Physical Review Letters **95**, 010403 (2005).
- [132] H. P. Bchler, M. Hermele, S. D. Huber, M. P. A. Fisher, and P. Zoller, Physical Review Letters **95**, 040402 (2005).
- [133] D. R. Hofstadter, Phys. Rev. B **14**, 22392249 (1976).
- [134] D. J. Thouless, M. Kohmoto, M. P. Nightingale, and M. den Nijs, Phys. Rev. Lett. **49**, 405408 (1982).
- [135] K. W. Madison, F. Chevy, W. Wohlleben, and J. Dalibard, Phys. Rev. Lett. **84**, 806809 (2000).
- [136] N. R. Cooper, N. K. Wilkin, and J. M. F. Gunn, Phys. Rev. Lett. **87**, 120405 (2001).
- [137] P. Engels, I. Coddington, P. C. Haljan, and E. A. Cornell, Phys. Rev. Lett. **89**, 100403 (2002).
- [138] J. R. Abo-Shaer, C. Raman, J. M. Vogels, and W. Ketterle, Science **292**, 476479 (2001).
- [139] V. Schweikhard, I. Coddington, P. Engels, V. P. Mogendorff, and E. A. Cornell, Phys. Rev. Lett. **92**, 040404 (2004).
- [140] N. K. Wilkin and J. M. F. Gunn, Phys. Rev. Lett. **84**, 69 (2000).

- [141] S. Viefers, T. H. Hansson, and S. M. Reimann, Phys. Rev. A **62**, 053604 (2000).
- [142] J. Sinova, C. B. Hanna, and A. H. MacDonald, Phys. Rev. Lett. **89**, 030403 (2002).
- [143] J. W. Reijnders, F. J. M. van Lankvelt, K. Schoutens, and N. Read, Phys. Rev. Lett. **89**, 120401 (2002).
- [144] B. Paredes, P. Zoller, and J. I. Cirac, Phys. Rev. A **66**, 033609 (2002).
- [145] N. Regnault and T. Jolicoeur, Phys. Rev. Lett. **91**, 030402 (2003).
- [146] U. R. Fischer, P. O. Fedichev, and A. Recati, Journal of Physics B: Atomic, Molecular and Optical Physics **37**, S301 (2004).
- [147] T. Ho and E. J. Mueller, Phys. Rev. Lett. **89**, 050401 (2002).
- [148] N. Read and N. R. Cooper, Phys. Rev. A **68**, 035601 (2003).
- [149] M. Popp, B. Paredes, and J. I. Cirac, Phys. Rev. A **70**, 053612 (2004).
- [150] S. K. Baur, K. R. A. Hazzard, and E. J. Mueller, Physical Review A (Atomic, Molecular, and Optical Physics) **78**, 061608 (2008).
- [151] Y. Lee and Y. Lee, Phys. Rev. B **70**, 224506 (2004).
- [152] L. Radzihovsky, J. Park, and P. B. Weichman, Phys. Rev. Lett. **92**, 160402 (2004).
- [153] M. W. J. Romans, R. A. Duine, S. Sachdev, and H. T. C. Stoof, Physical Review Letters **93**, 020405 (2004).
- [154] I. M. Khalatnikov, *An Introduction to the Theory of Superfluidity* (Westview Press, USA, 2000).
- [155] X. Wen, *Quantum Field Theory of Many-body Systems: From the Origin of Sound to an Origin of Light and Electrons*, reissue ed. (Oxford University Press, New York, USA, 2007).
- [156] D. Goldbaum and E. Mueller, arxiv:0807.3609 (2008).

- [157] D. S. Goldbaum and E. J. Mueller, arxiv **arXiv:0809.2078**, (2008).
- [158] R. B. Laughlin, Physical Review Letters **50**, 1395 (1983).
- [159] R. A. Williams, J. D. Pillet, S. Al-Assam, B. Fletcher, M. Shotter, and C. J. Foot, Optics Express **16**, 16977 (2008).
- [160] N. K. Wilkin, J. M. F. Gunn, and R. A. Smith, Phys. Rev. Lett. **80**, 22652268 (1998).
- [161] N. R. Cooper and N. K. Wilkin, Phys. Rev. B **60**, R16279R16282 (1999).
- [162] B. Paredes, P. Fedichev, J. I. Cirac, and P. Zoller, Phys. Rev. Lett. **87**, 010402 (2001).
- [163] N. Goldman, I. Satija, P. Nikolic, A. Bermudez, M. A. Martin-Delgado, M. Lewenstein, and I. B. Spielman, 1002.0219 (2010).
- [164] M. Z. Hasan and C. L. Kane, 1002.3895 (2010).
- [165] S. Chu, private communication .
- [166] K. Bergmann, H. Theuer, and B. W. Shore, Rev. Mod. Phys. **70**, 10031025 (1998).
- [167] W. Petrich, M. H. Anderson, J. R. Ensher, and E. A. Cornell, Phys. Rev. Lett. **74**, 33523355 (1995).
- [168] T. Kinoshita, T. Wenger, and D. S. Weiss, Physical Review Letters **95**, 190406 (2005).
- [169] H. Muller, U. Stadtmuller, and T. Schmitt, Biometrika **74**, 743 (1987).
- [170] L. Yu and D. Fil, arxiv:0807.0726 (2008).
- [171] S. M. Girvin and A. H. MacDonald, Phys. Rev. Lett. **58**, 12521255 (1987).
- [172] N. Read, Phys. Rev. Lett. **62**, 8689 (1989).
- [173] E. Shimshoni, A. Auerbach, and A. Kapitulnik, Physical Review Letters **80**, 3352 (1998).

- [174] S. Will, T. Best, U. Schneider, L. Hackermüller, D. Lohmann, and I. Bloch, 0911.5066 (2009).
- [175] G. Mazzaella, S. M. Giampaolo, and F. Illuminati, *Phys. Rev. A* **73**, 013625 (2006).
- [176] A. Smerzi and A. Trombettoni, *Phys. Rev. A* **68**, 023613 (2003).
- [177] L. Li, J. Checkelsky, Y. Hor, C. Uher, A. Hebard, R. Cava, and N. Ong, *Science* **321**, 547 (2008).
- [178] J. Larson, A. Collin, and J. Martikainen, *Physical Review A (Atomic, Molecular, and Optical Physics)* **79**, 033603 (2009).
- [179] O. E. Alon, A. I. Streltsov, and L. S. Cederbaum, *Physical Review Letters* **95**, 030405 (2005).
- [180] P. R. Johnson, E. Tiesinga, J. V. Porto, and C. J. Williams, *New Journal of Physics* **11**, 093022 (2009).
- [181] C. Chin, private communication.
- [182] P. Barmettler, A. M. Rey, E. Demler, M. D. Lukin, I. Bloch, and V. Gritsev, *Physical Review A (Atomic, Molecular, and Optical Physics)* **78**, 012330 (2008).
- [183] L. Jiang, A. M. Rey, O. Romero-Isart, J. J. García-Ripoll, A. Sanpera, and M. D. Lukin, *Physical Review A (Atomic, Molecular, and Optical Physics)* **79**, 022309 (2009).
- [184] D. B. M. Dickerscheid, U. A. Khawaja, D. van Oosten, and H. T. C. Stoof, *Phys. Rev. A* **71**, 043604 (2005).
- [185] T. Busch, B. Englert, K. Rzazewski, and M. Wilkens, *Foundations of Physics* **28**, 549 (1998).
- [186] R. B. Diener and T. Ho, *Phys. Rev. Lett.* **96**, 010402 (2006).
- [187] H. Zhai and T. Ho, *Phys. Rev. Lett.* **99**, 100402 (2007).
- [188] M. Köhl, H. Moritz, T. Stöferle, K. Günter, and T. Esslinger, *Physical Review Letters* **94**, 080403 (2005).

- [189] L. Duan, Physical Review Letters **95**, 243202 (2005).
- [190] C. Mathy and D. A. Huse, [arxiv:0805.1507](#), .
- [191] D. M. Ceperley, Reviews of Modern Physics **67**, 279 (1995).
- [192] N. Gemelke, private communication.
- [193] L. Mathey, E. Altman, and A. Vishwanath, Physical Review Letters **100**, 240401 (2008), [undefined 10.1103/PhysRevLett.100.240401](#).
- [194] A. V. Chubukov, S. Sachdev, and J. Ye, Physical Review B **49**, 11919 (1994), copyright (C) 2009 The American Physical Society; Please report any problems to prola@aps.org.
- [195] S. Sachdev, Zeitschrift für Physik B Condensed Matter **94**, 469 (1994).
- [196] S. Sachdev and E. R. Dunkel, Physical Review B (Condensed Matter and Materials Physics) **73**, 085116 (2006).
- [197] S. A. Hartnoll, P. K. Kovtun, M. Muller, and S. Sachdev, Physical Review B (Condensed Matter and Materials Physics) **76**, 144502 (2007).
- [198] C. P. Herzog, P. Kovtun, S. Sachdev, and D. T. Son, Physical Review D (Particles, Fields, Gravitation, and Cosmology) **75**, 085020 (2007).
- [199] S. Sachdev and M. Muller, Journal of Physics: Condensed Matter **21**, 164216 (2009).
- [200] M. Köhl, H. Moritz, T. Stöferle, C. Schori, and T. Esslinger, Journal of Low Temperature Physics **138**, 635 (2005).
- [201] T. Stöferle, H. Moritz, C. Schori, M. Köhl, and T. Esslinger, Physical Review Letters **92**, 130403 (2004).
- [202] M. Imada, Journal of the Physical Society of Japan **64**, 2954 (1995).
- [203] F. F. Assaad and M. Imada, Physical Review Letters **76**, 3176 (1996).
- [204] R. Joerdens, N. Strohmaier, K. Günter, H. Moritz, and T. Esslinger, Nature **455**, 204 (2008).

- [205] U. Schneider, L. Hackermuller, S. Will, T. Best, I. Bloch, T. A. Costi, R. W. Helmes, D. Rasch, and A. Rosch, arxiv arxiv:0809.1464 (2008).
- [206] B. Capogrosso-Sansone, ebner Gne Syler, N. Prokofev, and B. Svistunov, *Physical Review A* **77**, 015602 (2008).
- [207] Q. Zhou, Y. Kato, N. Kawashima, and N. Trivedi, *Physical Review Letters* **103**, 085701 (2009).
- [208] M. Köhl, T. Donner, S. Ritter, T. Bourdel, A.ttl, F. Brennecke, and T. Esslinger, *Advances in Solid State Physics* (Springer-Berlin, Heidelberg, 2008), pp. 79–88.
- [209] G. Jo, Y. Lee, J. Choi, C. A. Christensen, T. H. Kim, J. H. Thywissen, D. E. Pritchard, and W. Ketterle, *Science* **325**, 1521 (2009).
- [210] P. Clad, C. Ryu, A. Ramanathan, K. Helmerson, and W. D. Phillips, *Physical Review Letters* **102**, 170401 (2009).
- [211] J. Ahokas, J. Jrvinen, G. V. Shlyapnikov, and S. Vasiliev, *Physical Review Letters* **101**, 263003 (2008).
- [212] A. I. Safonov, I. I. Safonova, and I. I. Lukashevich, *JETP Letters* **87**, 23 (2008).
- [213] J. Ahokas, J. Jrvinen, and S. Vasiliev, *Phys. Rev. Lett.* **98**, 043004 (2007).
- [214] R. L. Walsworth, I. F. Silvera, E. M. Mattison, and R. F. C. Vessot, *Phys. Rev. A* **46**, 24952512 (1992).
- [215] M. E. Hayden, M. D. Hürlimann, and W. N. Hardy, *Phys. Rev. A* **53**, 15891604 (1996).
- [216] C. H. Schunck, Y. Shin, A. Schirotzek, M. W. Zwierlein, and W. Ketterle, *Science* **316**, 867 (2007).
- [217] Y. Shin, C. H. Schunck, A. Schirotzek, and W. Ketterle, *Phys. Rev. Lett.* **99**, 090403 (2007).
- [218] D. Petrov and G. Shlyapnikov, *Phys. Rev. Lett.* **84**, 2551 (2000).
- [219] B. G. Wilson and P. Kumar, *Phys. Rev. B* **27**, 3076 (1983).

- [220] J. P. H. W. v. d Eijnde, C. J. Reuver, and B. J. Verhaar, Phys. Rev. B **28**, 63096315 (1983).
- [221] J. J. Berkhout and J. T. M. Walraven, Phys. Rev. B **47**, 88868904 (1993).
- [222] B. W. Statt, Phys. Rev. B **32**, 71607164 (1985).
- [223] S. Vasiliev, private communication.
- [224] C. A. Sackett, H. T. C. Stoof, and R. G. Hulet, Phys. Rev. Lett. **80**, 20312034 (1998).
- [225] E. J. Mueller and G. Baym, Phys. Rev. A **62**, 053605 (2000).
- [226] J. L. Roberts, N. R. Claussen, S. L. Cornish, E. A. Donley, E. A. Cornell, and C. E. Wieman, Phys. Rev. Lett. **86**, 42114214 (2001).
- [227] D. Ceperley, Phys. Rev. B **18**, 31263138 (1978).
- [228] C. A. Burns and E. D. Isaacs, Phys. Rev. B **55**, 57675771 (1997).
- [229] M. Nielsen, Phys. Rev. B **7**, 16261635 (1973).
- [230] N. Prof'ev, Advances in Physics **56**, 381 (2007).
- [231] E. Kim and M. Chan, Nature **427**, 225 (2004), undefined 10.1038/nature02220.
- [232] E. Kim and M. H. W. Chan, Science **305**, 1941 (2004).
- [233] A. S. C. Rittner and J. D. Reppy, Physical Review Letters **98**, 175302 (2007).
- [234] A. S. C. Rittner and J. D. Reppy, Physical Review Letters **97**, 165301 (2006).
- [235] T. Kumada, Phys. Rev. B **68**, 052301 (2003).
- [236] J. Ahokas, J. Jrvinen, V. V. Khmelenko, D. M. Lee, and S. Vasiliev, Physical Review Letters **97**, 095301 (2006).
- [237] S. Vasilyev, J. Jrvinen, V. V. Khmelenko, and D. M. Lee, AIP Conference Proceedings **850**, 81 (2006).

- [238] Nat Phys **2**, 651 (2006), 10.1038/nphys435.
- [239] I. F. Silvera, Rev. Mod. Phys. **52**, 393452 (1980).
- [240] J. Ahokas, O. Vainio, S. Novotny, J. Jrvinen, V. V. Khmelenko, D. M. Lee, and S. Vasiliev, Physical Review B **81**, 104516 (2010).
- [241] *Quantum Tunnelling in Condensed Media*, edited by Y. Kagan and A. J. Leggett (Elsevier Science, Amsterdam, North-Holland, 1992).
- [242] A. V. Ivliev, A. Y. Katunin, I. I. Lukashevich, V. V. Sklyarevskii, V. V. Suraev, V. V. Filippov, N. I. Filippov, and V. A. Shevtsov, JETP Letters **36**, 472 (1982).
- [243] N. V. Prokof'ev and G. V. Shlyapnikov, Sov. Phys. JETP **66**, 1204 (1987).
- [244] C. Pethick and H. Smith, *Bose-Einstein Condensation in Dilute Gases* (Cambridge University Press, The Edinburgh Building, Cambridge CB2 2RU, UK, 2002).
- [245] S. A. Khairallah, M. B. Sevryuk, D. M. Ceperley, and J. P. Toennies, arxiv 0612161 (2006).
- [246] C. Cazorla and J. Boronat, 0807.0307 (2008).
- [247] L. Pollet, M. Boninsegni, A. B. Kuklov, N. V. Prokof'ev, B. V. Svistunov, and M. Troyer, Physical Review Letters **98**, 135301 (2007).
- [248] M. Boninsegni, A. B. Kuklov, L. Pollet, N. V. Prokof'ev, B. V. Svistunov, and M. Troyer, Physical Review Letters **99**, 035301 (2007).
- [249] G. Söyler, B. Capogrosso-Sansone, N. V. Prokof'ev, and B. V. Svistunov, Physical Review A (Atomic, Molecular, and Optical Physics) **76**, 043628 (2007).
- [250] A. C. Clark, X. Lin, and M. H. W. Chan, Physical Review Letters **97**, 245301 (2006).